POLITECNICO DI TORINO

Master's Degree in Aerospace Engineering

Master's Degree Thesis

Conjugate Heat Transfer Analysis of a Rib-Cooled High-Pressure Turbine Vane under Pulsating Conditions

Supervisors

Prof. Daniela Anna MISUL
Prof. Simone SALVADORI

Co-Supervisors

Dr. Panagiotis GALLIS
Dr. Rosario NASTASI

Candidate

Christian PASCALE
322785

October 2025

Abstract

Numerical simulations play a pivotal role in the development and optimization of turbomachinery components. While experimental methods remain the gold standard for performance and flow analyses, their application is often constrained by factors such as fluid compressibility, elevated temperatures, diversified range of Reynolds numbers, probe intrusion into the flow field, and the difficulty of instrumentation in certain regions of the machine. In light of these limitationsand with the growing availability of computational resourcesthere is a strong incentive to refine computational models and validate their predictions against empirical data, establishing a complementary relationship between the two investigative approaches. High-fidelity simulations, in particular, enable a detailed investigation of fluid dynamic phenomena induced by structural modifications, including in regions inaccessible to direct measurement.

This thesis presents a numerical investigation into cooling strategies for a high-pressure turbine vane. The focus is on a first-stage vane subjected to unsteady thermal and pressure loads originating from a Rotating Detonation Combustor (RDC). The study begins with a comprehensive literature review, emphasizing established cooling techniques for high-pressure stator vanes. For the applied component, the selected geometry is a high-pressure vane designed at Politecnico di Torino as part of the EnaTech-RDE PRIN 2022 project. This vane, previously optimized for obtainign elevated performances in transonic operation, had been the subject of earlier studies.

An unstructured computational grid was created using Ansys Meshing, with targeted refinements in regions of high gradients. This mesh was used for two distinct computational fluid dynamics (CFD) analysis types: the initial phase included a mesh sensitivity study focused on the external flow around the vane. After achieving convergence in the key variables, three Reynolds-Averaged Navier-Stokes (RANS) simulations were conducted using the $k-\omega$ SST turbulence model: the first simulation modeled thermal interaction between the main gas path and the vane body and the next two included internal cooling channels, first in a smooth configuration, and then with inclined rib turbulators.

A comparative analysis was then conducted between the two internally cooled configurations using the Transitional $k-\omega$ SST model with a $\gamma - Re_\theta$ transition formulation. This model is particularly effective in capturing separated flow phenomena, such as those occurring between individual cooling ribs.

The final stage of the work involved a set of Unsteady Reynolds-Averaged Navier-Stokes (URANS) simulations using the same transition model. Results from these were compared

against steady-state counterparts to assess the thermal response of the solid domain relative to the transient characteristics of the fluid flow.

Contents

List of Figures

List of Tables

1 Introduction

High-pressure turbines are vital components in modern propulsion systems, operating under extreme thermal and mechanical stresses. With the advent of advanced combustion technologies such as the Rotating Detonation Combustor (RDC), turbine components are now being exposed to more severe and complex operating conditions. RDCs utilize continuously propagating detonation waves, offering significant advantages over conventional combustors in terms of thermal efficiency and system compactness. However, these benefits come at the cost of highly unsteady, spatially non-uniform exhaust flow fields, which introduce significant challenges for downstream turbine componentsparticularly stator vanes.

Located immediately downstream of the combustor, stator vanes must withstand high thermal loads resulting from elevated temperatures, fluctuating pressures, and steep gradients in flow properties. These oscillatory boundary conditions differ markedly from the steady-state assumptions typically used in conventional turbine design. Understanding how such unsteady conditions affect both the external aerodynamics and the internal thermal response of turbine vanes is essential for enabling the integration of RDCs into future aerospace propulsion systems.

This thesis investigates the performance of a high-pressure turbine vane with internal cooling, subjected to unsteady inflow conditions representative of RDC operation. Due to the complexity of accurately replicating detonative exhaust in numerical simulations, the inlet conditions were simplified to time-periodic pressure and temperature profiles, under the assumption of an already established detonation regime. This approach allowed for more numerically stable simulations while preserving the key unsteady features of RDC exhaust.

The study employs Conjugate Heat Transfer (CHT) simulations to model the coupled interaction between the internal coolant flow and the solid vane structure. Both aerodynamic and thermal performance are evaluated for multiple cooling configurations, including smooth and ribbed internal channels. Initial analyses are conducted using steady-state Reynolds-Averaged NavierStokes (RANS) simulations with the $k-\omega\ SST$ turbulence model, further enhanced by the $\gamma-Re_\theta$ transition model to capture laminar-to-turbulent effects. Subsequently, Unsteady RANS (URANS) simulations are performed using the simplified periodic inlet conditions to assess transient thermal behavior.

The primary objective of this work is to provide insights into the thermal performance of internally cooled turbine vanes operating under RDC-like inflow conditions. Special attention is given to the effects of cooling channel geometry, inflow unsteadiness, and transition modeling on the resulting surface temperature distributions and thermal loads. The outcomes of this research aim to contribute to a broader understanding of how traditional cooling strategies perform under the extreme and unsteady conditions induced by detonative combustion, potentially guiding future design adaptations for RDE-based propulsion systems.

The remainder of the thesis is organized as follows:

- **Section 2** presents the theoretical background, beginning with the fundamental Brayton cycle and an overview of detonative combustion theory. The section also introduces the governing equations for the fluid and solid domains, the CHT coupling strategy, and the numerical models employed, including turbulence and transition modeling. A review of turbine vane cooling strategies from the literature is also included.
- **Section 3** describes the computational mesh development and sensitivity study. Several mesh configurations were tested with varying levels of refinement, focusing on both the external aerodynamic domain and internal cooling passages. Particular attention is given to wall resolution strategies and mesh quality in unstructured grids.
- **Section 4** outlines the results of the steady-state RANS simulations. Three configurations are studied: an uncooled baseline case, a smooth-channel cooling case, and a ribbed-channel cooling case. Simulations were performed using the Ansys Fluent solver, with results analyzed via contour and profile plots. Additional simulations incorporating transition modeling were conducted to assess its impact on heat transfer predictions.
- **Section 5** presents the URANS simulations using time-periodic inlet conditions to replicate RDC-induced unsteadiness. The computational domain is modified to include an outlet plenum to account for potential transonic flow behavior. The chosen turbulence and transition models are retained, and the inlet frequency is set to $f = 5\ kHz$.
- **Section 6** summarizes the key findings, comparing the thermal performance of cooled and uncooled configurations, and evaluating the influence of unsteady inlet conditions on the solid temperature response. These results are discussed in the context of their implications for turbine vane design in RDC-powered systems.

2 Theoretical Background

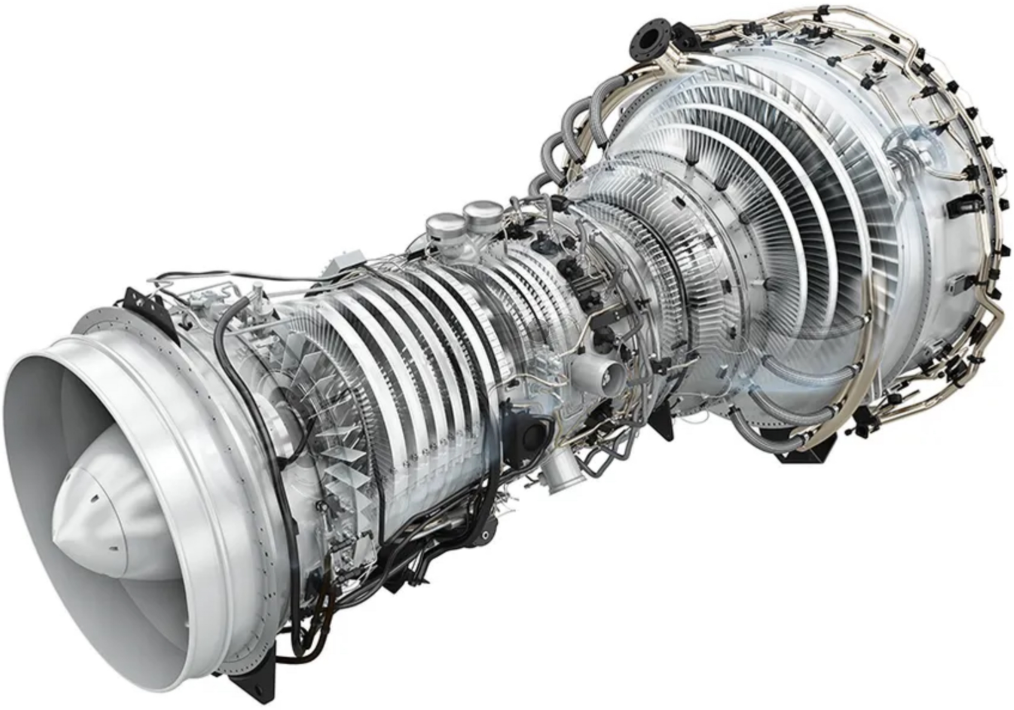

Figure 2.1: Gas Turbine Engine.

The gas turbine engine, a cornerstone of modern engineering, represents a paradigm of high power density and efficiency, fundamentally shaping both aerospace propulsion and terrestrial energy production. Its ubiquitous application, from generating propulsive thrust in aircraft to driving generators in the electrical power grid, necessitates a rigorous theoretical and computational understanding of its operational principles and performance characteristics.

The thermodynamic cycle governing the gas turbine engine is the Brayton cycle, shown in Figure 2.2, which models the behavior of the working fluidairas it undergoes a series of four distinct processes: isentropic compression, constant-pressure heat addition, isentropic expansion, and constant-pressure heat rejection. The analysis of these processes hinges on the application of fundamental thermodynamic laws, particularly the First Law

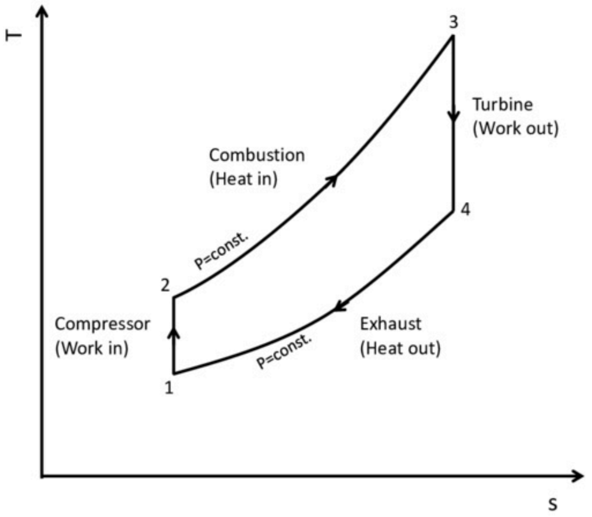

Figure 2.2: Gas Turbine Engine Brayton Cycle.

of Thermodynamics for an open system, which is expressed by the steady-flow energy equation, shown in Equation 1.

$$\dot{Q} - \dot{W}s = \dot{m}\left[(h2 - h_1) + \frac{1}{2}\left(V_2^2 - V_1^2\right) + g\left(z_2 - z_1\right)\right] \tag{1}$$

This equation, along with equations of state for ideal gases, forms the basis for determining critical variables such as pressure p, temperature T, specific enthalpy h, and specific entropy s at various stations throughout the engine. The interrelationship of these variables defines key performance parameters like the overall pressure ratio (β) and thermal efficiency (η_{th}). The functionality of the gas turbine engine is distributed among its key components. The compressor, located at the engine inlet, performs the work of compressing the air, thereby increasing its pressure and temperature. The high-pressure air then enters the combustion chamber, where fuel is introduced and ignited, resulting in a significant increase in temperature at nearly constant pressure. The resulting high-temperature, high-pressure gas is then directed to the turbine section. Following the turbine, the gas expands through a nozzle to produce thrust in propulsive applications or is exhausted to the atmosphere in power generation systems. Central to the engine's operation is the turbine, which serves the critical role of extracting energy from the high-energy gas stream. This extracted work is utilized to drive the compressor and, in most configurations, to power an external load, whether a propeller, a fan, or an electrical generator. The study of the turbine's performance is underpinned by specific aerodynamic and thermodynamic formulae. The work extracted per unit mass flow through the turbine is governed by the Euler turbomachinery equation, shown in Equation 2 where u is the blade speed and c_u is the tangential component of the absolute fluid velocity.

$$w_t = u_1 c_{u1} - u_2 c_{u2} \tag{2}$$

Furthermore, the turbine's effectiveness is characterized by its isentropic efficiency, defined by the ratio of actual work output to the ideal isentropic work output. This analysis is crucial for optimizing the engine's overall performance. This thesis will delve into the theoretical and computational aspects of these components, with a particular emphasis on the design and analysis of the turbine, to provide a holistic understanding of gas turbine engine operation and its continuous evolution.

The stator, whose fluid dynamic analysis is the central topic of this study, is the turbine section located immediately downstream of the combustor and is subjected to the primary thermal flows from it. Its main functions are the conversion of the incoming fluid's thermodynamic potential energy into kinetic energy and the straightening of the flow entering the rotating rotor with the most appropriate angle to maximize the work exchanged. The latter function is demonstrated in Figure 2.3: the velocity triangles created between the stator and the rotor of a single turbine stage are presented and show the velocity vector variation performed by the single component.

The flow acceleration occurs through the expansion of the working fluid with the consequent decrease in pressure and temperature. The geometry of the passage formed by two consecutive blades can have different configurations. For entirely incompressible flows, it takes the form of a simple convergent passage, which, in the case of transonic flows with a throat section, is transformed into a convergent-divergent nozzle. In multi-stage applications, a stator vane row is placed between two consecutive rotor stages, the coupling of which forms the so-called stage. Depending on where the pressure drops occur, there are different configurations. The two most common, as presented in Figure 2.4, are:

- impulse turbine with pressure stages, in which the energy recovery occurs with a single overall pressure drop that takes place on the stator. This configuration includes the widely used velocity compounding;

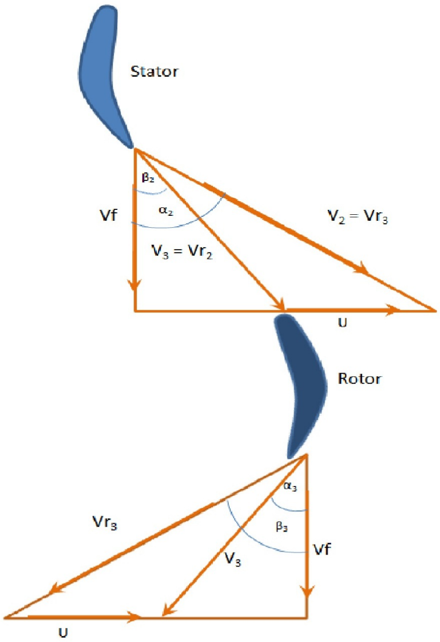

Figure 2.3: Velocity Triangles in a Stage.

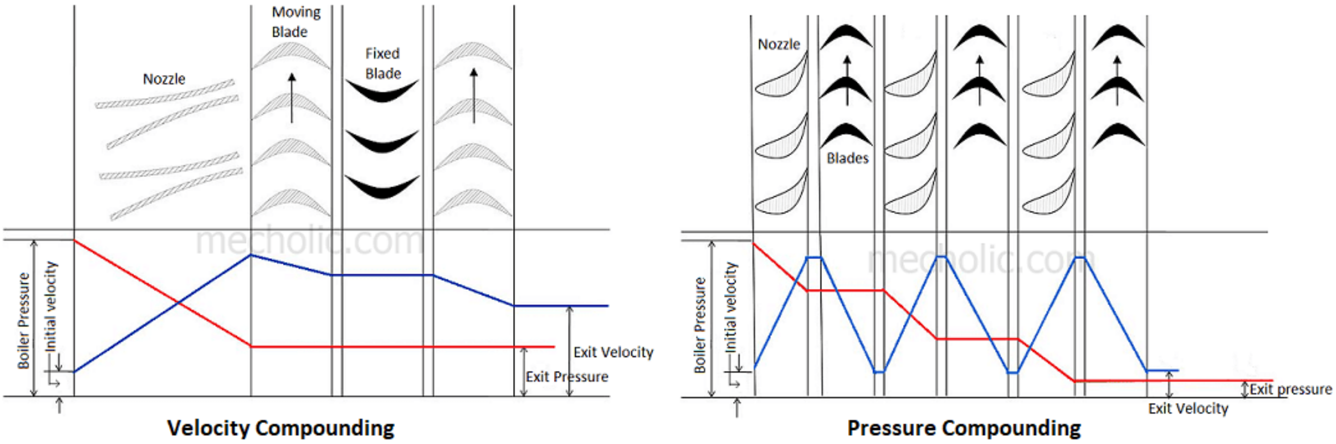

Figure 2.4: Compounding of Axial Turbines.

- reaction turbine, in which the energy recovery occurs partly on the rotor and partly on the stator, and where a degree of reaction R can be defined as:

$$R = \frac{Isentropic\ Enthalpy\ Change\ in\ Rotor}{Isentropic\ Enthalpy\ Change\ in\ Stage} = \frac{T_2 - T_3}{T_1^o - T_3^o} \tag{3}$$

where the subscripts $_1$,$_2$,$_3$ indicate the position upstream of the stator, downstream of it, and downstream of the rotor respectively, in the case of a perfect calorically perfect gas. This second category includes pressure-staged turbines.

The regime characterizing the case study is called transonic and is defined by a fluid field Mach number between $M = 0.8$ and $M = 1.2$. This regime leads to the coexistence of subsonic and supersonic zones. The specific acceleration of the flow occurs at the suction side, on the back of the blade, where a low-pressure, and consequently high-velocity, bubble is located. It is precisely these abrupt variations in thermodynamic conditions that can lead to the formation of purely viscous discontinuities concentrated in very thin regions of the flow field: shock waves. These lead to sudden changes in the thermodynamic characteristics of the field such as pressure, temperature, and consequently density, accompanied by an increase in entropy and consequent irreversible losses. The prediction of such phenomena, which could compromise the efficiency of the entire machine, is of vital importance and, therefore, is studied using numerical methods, whose complex is called Computational Fluid Dynamics or CFD.

2.1 Governing Equations

For the complex domain proposed by a turbomachinery study to be solved numerically, several fundamental physical relations must be taken into consideration: the conservation of mass, momentum, and energy, which are collected in the Navier-Stokes equations, a set of two scalar equations and one vector equation presented in Equations 3, 4, 5 in their integral form of wider applicability.

The first of these presents the concept of mass conservation applied to a volume V with an external surface S: the temporal variation of the mass present in the predefined volume domain is opposite to the mass flow exiting the domain's surface.

$$\frac{d}{dt}\iiint_V \rho\, dV + \iint_S \rho \mathbf{u} \cdot \mathbf{n} dS = 0 \tag{4}$$

Equation 5 presents the concept of momentum conservation in the three Cartesian directions. These equations, reduced to their compact form and written as a single equation, can be analyzed in their individual parts. In the term on the left side of the equals sign, the first addend indicates the temporal variation of the momentum present in the chosen volume, followed by the convective term of the conserved quantity through the domain's surface. On the right side of the equals sign, the diffusive term, a sum of the turbulent and pressure contributions, and the term responsible for the external body forces applied to the domain are summed.

$$\frac{d}{dt}\iiint_V \rho\mathbf{u}\,dV + \iint_S \rho\mathbf{u}(\mathbf{u}\cdot\mathbf{n})\,dS = \iint_S \sigma\cdot\mathbf{n}\,dS + \iiint_V \rho\mathbf{g}\,dV \tag{5}$$

Equation 6 presents the scalar equation that expresses the concept of energy conservation. This is the sum of the contributions of the temporal variation of energy in the chosen volume, the convective and diffusive terms of the conserved quantity, the heat flux, and the external forces that are applied to the volume.

$$\begin{aligned}\frac{d}{dt}\iiint_V \rho e\,dV + \iint_S \rho e(\mathbf{u}\cdot\mathbf{n})\,dS = -\iint_S \mathbf{q}\cdot\mathbf{n}\,dS + \iint_S (\sigma\cdot\mathbf{u})\cdot\mathbf{n}\,dS + \\ + \iiint_V \rho\mathbf{g}\cdot\mathbf{u}\,dV\end{aligned} \tag{6}$$

From these equations, through the Reynolds Transport Theorem and the Stokes' Theorem, presented in Equations 7 and 8 respectively, the differential form of the Navier-Stokes equations, presented in Equations 9, 10, and 11, is derived.

$$\frac{dB_{sys}}{dt} = \frac{\partial}{\partial t}\iiint_{CV} \rho b\,dV + \iint_{CS} \rho b(\mathbf{u}\cdot\mathbf{n})\,dA \tag{7}$$

$$\oint_{\partial S} \mathbf{F}\cdot d\mathbf{l} = \iint_S (\nabla\times\mathbf{F})\cdot d\mathbf{S} \tag{8}$$

The following differential forms, although simpler to solve numerically through specific methods and representing the domain best in most case studies, cannot be applied to the resolution of fluid dynamic fields that present or may present punctual discontinuities, such as shock waves. For this reason, the transonic field in our case of interest can only be solved by solvers that implement the governing equations in their strong or integral form.

$$\frac{\partial\rho}{\partial t} + \nabla\cdot(\rho\mathbf{u}) = 0 \tag{9}$$

$$\frac{\partial(\rho\mathbf{u})}{\partial t} + \nabla\cdot(\rho\mathbf{u}\mathbf{u}) = -\nabla p + \nabla\cdot\tau + \rho\mathbf{g} \tag{10}$$

$$\frac{\partial(\rho e)}{\partial t} + \nabla\cdot(\rho e\mathbf{u}) = -p(\nabla\cdot\mathbf{u}) + \nabla\cdot(k\nabla T) + \Phi \tag{11}$$

The equations presented so far form a system of five equations and seven unknowns: pressure p, density ρ, three velocity components u, v, w, temperature T, heat flux q, and internal energy e. To close the system and solve the fluid dynamic field, it is imperative to add three more equations: the ideal gas equation of state, Fourier's law, and the relationship that exists between internal energy and temperature, presented respectively in Equations 12, 13, and 14. The last relationship is presented first in its general version and then in the one applicable to calorically perfect gases, which are characterized by a constant specific heat at constant volume c_v with respect to temperature.

$$p = \rho R^* T \tag{12}$$

$$\mathbf{q} = -k \nabla T \tag{13}$$

$$e = \int c_v(T)\, dT = c_v T \tag{14}$$

From the momentum conservation equation, presented in Equations 6 and 10, the two contributions of pressure and stress forces are derived from the diffusive term through Equation 15, which demonstrates the dependence of the diffusive forces on the part normal to the wall, which is called pressure $-p\mathbf{I}$, and the shear stresses on each face expressed in the three Cartesian directions grouped in the shear stress tensor τ, which, in the case of a Newtonian fluid, takes the form presented in Equation 16.

$$\sigma = -p\mathbf{I} + \tau \tag{15}$$

$$\tau = \mu \left(\nabla \mathbf{u} + (\nabla \mathbf{u})^T - \frac{2}{3} (\nabla \cdot \mathbf{u}) \mathbf{I} \right) + \lambda (\nabla \cdot \mathbf{u}) \mathbf{I} \tag{16}$$

2.2 Viscosity Models

The chaotic and unsteady nature of turbulent flow makes the direct numerical solution of the Navier-Stokes equations computationally prohibitive for most engineering applications. To overcome this, the most common approach is the one known as the Reynolds-averaged Navier-Stokes equations or *RANS*, which is the decomposition of each flow variable into a time-averaged component and a fluctuating component with a zero mean, as shown in Equation 17.

$$\mathbf{v}(\vec{x}, t) = \mathbf{v}(\vec{x}) + \mathbf{v}'(\vec{x}, t) \tag{17}$$

Applying this approach to the full Navier-Stokes equations, their Reynolds-averaged form is deduced, with the momentum conservation shown in Equation 18. This equation contains the elements seen previously, but now applied to the time-averaged conserved quantity, with the addition of the Reynolds stress tensor $-\rho\overline{u_i'u_j'}$: a new unknown that expresses the dependency that exists between the mean motion and turbulence. This element, which has the same dimension as the shear stress tensor τ, is the main difference between the Navier-Stokes equations and RANS and is the reason why supplementary equations must be introduced to close the new system of governing equations.

$$\frac{\partial(\rho\bar{u}_i)}{\partial t}+\frac{\partial(\rho\bar{u}_i\bar{u}_j)}{\partial x_j}=-\frac{\partial\bar{p}}{\partial x_i}+\frac{\partial}{\partial x_j}\left[\mu\left(\frac{\partial\bar{u}_i}{\partial x_j}+\frac{\partial\bar{u}_j}{\partial x_i}\right)-\rho\overline{u_i'u_j'}\right]+\rho\bar{g}_i \tag{18}$$

Most turbulence models used in the industrial field are based on the Boussinesq assumption, which models the Reynolds tensor in analogy with viscous stresses, introducing a term proportional to the mean deformation tensor and is presented here in Equation 19 where the constant of proportionality is a new variable, the turbulent viscosity μ_t.

$$\tau^R=2\mu_t\mathbf{S}-\frac{2}{3}\rho k\mathbf{I} \tag{19}$$

In this work, the Menter $k-\omega\ SST$ model was used, whose conservation equations for turbulent kinetic energy k and the dissipation rate ω are reported in Equations 20 and 21. Once the conserved variables are calculated, the turbulent viscosity can be traced back in the following way $\mu_t=\rho\frac{k}{\omega}$. Noteworthy is the presence of the blending function F_1, which regulates how closely the $k-\omega\ SST$ model approaches the $k-\varepsilon$ model, which has better results in the bulk flow, or the pure $k-\omega$ model, which is better at calculating the solution at the wall. The blending function will assume a value of one at the wall and a value of zero far from it.

$$\frac{\partial(\rho k)}{\partial t}+\frac{\partial(\rho k u_i)}{\partial x_i}=P_k-\beta^*\rho k\omega+\frac{\partial}{\partial x_j}\left[(\mu+\sigma_k\mu_t)\frac{\partial k}{\partial x_j}\right] \tag{20}$$

$$\begin{aligned}\frac{\partial(\rho\omega)}{\partial t}+\frac{\partial(\rho\omega u_i)}{\partial x_i}=\alpha\frac{\omega}{k}P_k-\beta\rho\omega^2+\frac{\partial}{\partial x_j}\left[(\mu+\sigma_\omega\mu_t)\frac{\partial\omega}{\partial x_j}\right]+\\+2(1-F_1)\rho\sigma_{\omega,2}\frac{1}{\omega}\frac{\partial k}{\partial x_j}\frac{\partial\omega}{\partial x_j}\end{aligned} \tag{21}$$

The turbulence model used, however, assumes that the flow is certainly turbulent and has, therefore, exceeded the critical Reynolds number of transition. To verify these results, the four-equation model was used, which introduces the intermittency variable γ, which verifies what percentage of the flow has undergone turbulent transition in the section of interest. Two conservation equations are also introduced for intermittency γ and for the

Reynolds number based on momentum thickness Re_θ, presented in Equations 22 and 23 respectively.

$$\frac{\partial(\rho\gamma)}{\partial t}+\frac{\partial(\rho U_j\gamma)}{\partial x_j}=P_\gamma-E_\gamma+\frac{\partial}{\partial x_j}\left[\left(\mu+\frac{\mu_t}{\sigma_f}\right)\frac{\partial\gamma}{\partial x_j}\right] \tag{22}$$

$$\frac{\partial(\rho\tilde{R}e_{\theta t})}{\partial t}+\frac{\partial(\rho U_j\tilde{R}e_{\theta t})}{\partial x_j}=P_{\theta t}+\frac{\partial}{\partial x_j}\left[\sigma_{\theta t}(\mu+\mu_t)\frac{\partial\tilde{R}e_{\theta t}}{\partial x_j}\right] \tag{23}$$

2.3 Conjugate Heat Transfer

Conjugate Heat Transfer or CHT is the phenomenon at the base of the study of heat exchange between two adjacent bodies. Unlike the classic methods used for the computational study of fluids, CHT focuses on the integration between the convection that occurs in the fluid and the conduction in the solid, then dealing with the conservation of variables at the interface between the domains. The interaction that manifests continuously at the interface is a fundamental aspect for the accurate modeling of numerous engineering systems, from heat exchangers to cooling systems for electronic components.

Furthermore, this approach differs from simpler techniques based on the use of empirically calculated convective heat transfer coefficients h_c, for the direct calculation of both the distribution and the local variations of the aforementioned coefficient. This eliminates the need to rely on empirical values that would not be able to capture the complexity of some thermal fields imposed by the problem's fluid dynamics, especially in the case of unsteady phenomena. The possibility of calculating thermal exchanges without the use of a priori inputs is the reason why the CHT technique is widely used in the design of turbomachinery. In the latter, due to an increasingly high combustion temperature that exceeds the melting point of the metal alloys of which the turbine blades are composed, there is a widespread use of pneumatic cooling systems. The accuracy of temperature field predictions is of paramount importance in ensuring a correct and risk-free use of the machine.

The governing equations for the method are those that regulate the transport of energy in the single domains and at the interface between them. The fluid domains are subject to the Navier-Stokes equations, particularly analyzed in subsection 1 of this section. The propagation of heat within the solid occurs by conduction and, therefore, obeys Fourier's law, reported in Equation 24 where Q is the calculated conductive heat, k is the thermal conductivity of the material, and ∇T is an index of the temperature field non-uniformities within the solid.

$$Q=-\nabla\cdot(k\nabla T) \tag{24}$$

Equation 25 adds the unsteadiness of the temperature field to the Fourier equation reported above. The term on the left side of the equals sign, in fact, adds the influence of the material's thermal capacity C_p and the instantaneous variation of the temperature $\frac{\partial T}{\partial t}$. Sometimes referred to as the heat conduction equation, this is a simplified form of the energy equation for fluids, where the convective term is zero.

$$\rho C_p \frac{\partial T}{\partial t} = \nabla \cdot (k \nabla T) + Q \tag{25}$$

The interface between domains is the crucial point in the analysis of coupled heat exchange. The boundary conditions to be imposed at the interface are of two types: thermal equilibrium and energy conservation between the solid body and the fluid domain:

- at the common boundary, there cannot be a temperature discontinuity. Equation 26 imposes the equality of the variable on the faces common to both domains;

  $$T_{solid} = T_{fluid} \quad \text{at the interface} \tag{26}$$

- due to the principle of energy conservation, the heat flux that leaves the solid by conduction must be equal to the heat flux that enters the fluid by convection. In the absence of a heat source at the interface, the heat flux is continuous, as presented in Equation 27.

  $$q_{solid} = q_{fluid} \quad \text{at the interface} \tag{27}$$

  This relationship translates into an equality between the thermal flux by conduction in the solid and the thermal flux by convection in the fluid, as reported in Equation 28 where $\vec{n}$ is the vector normal to the interface oriented from the solid to the fluid.

  $$-\lambda_s (\nabla T_s \cdot \vec{n}) = -\lambda_f \left(\nabla T_f \cdot \vec{n} \right) \quad \text{at the interface} \tag{28}$$

The way in which the equations of the solid and fluid domains are solved together defines the simulation's coupling strategy. There are two main approaches:

- weak coupling, in which the solid and fluid domains are solved iteratively and sequentially. The information calculated by the fluid solver is transferred to the solid solver which uses it for the next iteration. Although the approach is widely used for its ease of implementation, it can present numerical instabilities and requires correction cycles to ensure convergence;

- strong coupling, in which the equations solving both domains are unified and solved simultaneously. Although the method is more complex to implement, it presents remarkable numerical robustness for complex geometries with many interaction interfaces.

The choice of which approach to use depends on the case study. For the thermo-fluid dynamic study of turbomachinery, the strong approach is preferred due to the complex thermal interactions and intricate geometries.

Furthermore, in unsteady simulations, the difference between the thermal response time of the solid and that of the fluid must be considered. The latter, due to high forced convection, react much faster to temperature variations compared to solids, which are commonly composed of metal alloys. Solving the solid and fluid at the same frequency at each time step could lead to numerical instabilities. To reduce problems of this kind, techniques such as super-cycling have been developed: at each iteration of the fluid solver, the data is passed to the solid solver which iterates multiple times. The solid, therefore, reaches a statistically significant steady temperature field without the need to increase the number of iterations of all the domains under examination. This method is very effective in scenarios where the fluid dynamics are much faster than the solid's thermal response.

2.4 Rotating Detonation Combustion

Rotating Detonation Combustion or RDC is a recently opened and explored research niche in the field of energy generation and aerospace propulsion. It offers a promising alternative to alternative combustion systems for better energy conversion and for the use of non-carbon-based fuels.

The first observations of the phenomenon date back to the dawn of space propulsion: with the increase in the size of launchers, instabilities were found that were not well analyzed after the harmful effects related to them had been overcome.

The principle on which this form of propulsion is based is the use of one or more supersonic detonation waves that travel around the channel that makes up the combustion chamber. The fuel and oxidant mixture is continuously injected into the annular space, where a single initial detonation is self-sustaining by means of the heating due to the advancing wavefront. The wave, in fact, ignites the fresh mixture it encounters, releasing the energy necessary to propagate the detonation itself and to axially accelerate the products, generating thrust.

Detonation combustion, from a thermodynamic point of view, is a "pressure gain" process. The flow pressure increases significantly, unlike deflagrative combustion which occurs with a slight pressure loss, which translates into a potential thermal efficiency up to 25% higher than conventional engines. A further advantage lies in the lack of moving parts, which reduces the complexity of manufacturing the component and increases its reliability. The high mass flow rates handled by the engine make this type of engine very compact.

Operation with a continuous and rotating wave at frequencies between $f = 1-10\ kHz$ represents a significant evolution compared to pulsed detonation engines or PDEs, which operate with pulsed thrusts in a frequency range of $f = 100-200\ Hz$. The latter also present the difficulty of repeated ignition at each cycle and the purging of the combustion chamber.

The laws that govern this pressure gain are the principles of conservation of mass, momentum, and energy described by the Rankine-Hugoniot relations applied to a reactive gas and reported in Equations 29, 30, 31 respectively, where the subscripts $_1$ *and* $_2$ represent the variables of interest calculated before and after the shock wave respectively. The result of these equations is the Rankine-Hugoniot curve that can be plotted on a pressure-volume graph, as can be seen in Figure 2.5.

$$\rho_1 u_1 = \rho_2 u_2 \tag{29}$$

$$p_1 + \rho_1 u_1^2 = p_2 + \rho_2 u_2^2 \tag{30}$$

$$h_1 + \frac{u_1^2}{2} + Q = h_2 + \frac{u_2^2}{2} \tag{31}$$

Of fundamental importance in the theory of rotating detonation is the Chapman-Jouguet or CJ condition formulated to describe the propagation velocity of a self-sustaining detonation wave. The detonation propagates at a velocity such that the reacting gases behind the shock wave reach the speed of sound. This entails a choking point that prevents expansion waves downstream of the wave from interfering with the wave itself and a consequent constant velocity of the wavefront. To trace the position of the CJ point, the Rankine relations, which impose the conservation of mass and momentum, and the Hugoniot relation, which imposes the conservation of energy, must be combined.

The equations that govern the upper CJ point, related to the generation of a detonation wave, are reported in Equations 32 and 33, where $\tilde{p}$ is the pressure ratio, $\tilde{v}$ is the density ratio, γ is the ratio of specific heats, and $\alpha = q\frac{\rho_1}{p_1}$ is a parameter that depends on the heat released in the reaction q and the upstream conditions.

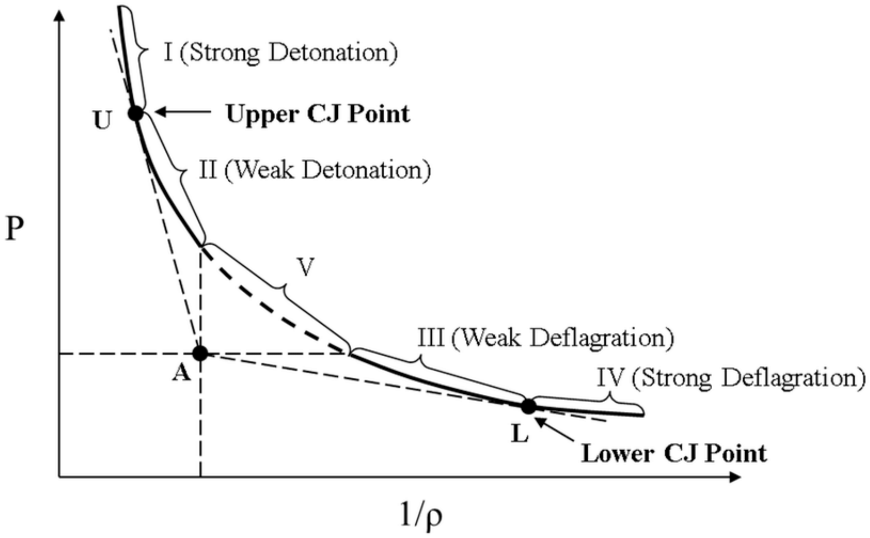

Figure 2.5: Rankine-Hugoniot Curve on Pressure-Volume Plane.

$$\tilde{p}_{+} = 1 + \alpha(\gamma - 1)\left\{1 + \left[1 + \frac{2\gamma}{\alpha(\gamma^2 - 1)}\right]^{1/2}\right\} \tag{32}$$

$$\tilde{v}_{+} = 1 + \frac{\alpha(\gamma - 1)}{\gamma}\left\{1 - \left[1 + \frac{2\gamma}{\alpha(\gamma^2 - 1)}\right]^{1/2}\right\} \tag{33}$$

The more detailed Zel'dovich-von Neumann-Döring or ZND detonation model provides a hypothesis of the internal structure of a detonation wave, overcoming the assumption of an infinitesimally thin reaction front of the Chapman-Jouguet theory. The one-dimensional ZND model describes the process in multiple phases:

1. a shock wave that compresses the unreacted gas to an extremely high pressure, known as the "von Neumann spike", where the gas is compressed but the chemical reaction has not yet begun;

2. a reaction zone, where the compressed and superheated gas enters an exothermic reaction zone at a finite velocity that accelerates the flow;

3. the CJ point, where the reaction ends and where the flow reaches the speed of sound with respect to the wavefront.

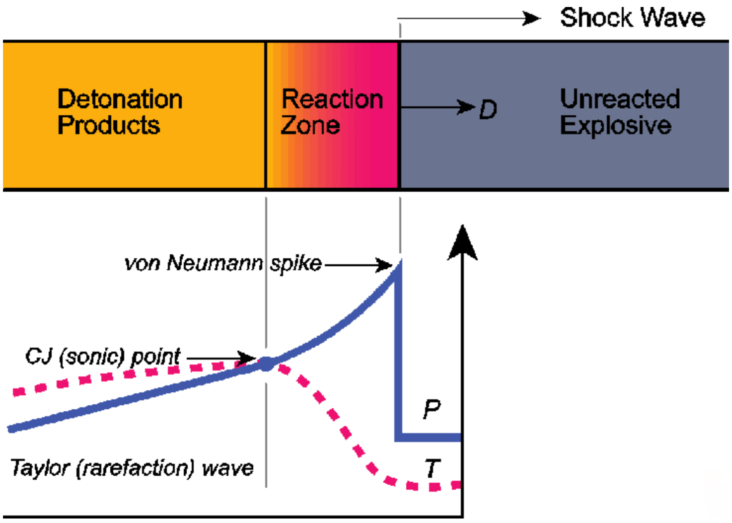

Figure 2.6: ZND Detonation Combustion Model. Chapman-Jouguet Point and von Neumann Spike are Highlighted.

The ZND model, although an effective simplification for understanding the basic physics, presents the hypothesis of unidimensionality which does not agree well with real detonations which have a complex three-dimensional structure and instabilities. Deviations from ideality, such as incomplete mixing between fuel and oxidant or the presence of secondary reactions, make theoretical models insufficient to predict the actual performance of an RDC. Studies have, in fact, shown that detonation dynamics depend strongly on the combustor geometry, which explains the need for advanced computational models to capture the nonlinear complexity of the phenomena. The fact that computational simulations and experiments on an RDE have shown extreme pressure peaks, with ratios exceeding 20:1 across the wavefront, validates the "von Neumann spike" theory.

The most promising application of this technology is its integration into turbomachinery cycles for energy generation and thrust in aerospace applications. The integration of an RDC with a conventional turbine presents challenges mainly related to the instabilities and non-uniformity of the combustor's exhaust flow. The flow entering the turbine, in fact, is characterized by high-frequency oscillations with high temperature and pressure fluctuations. The points to be observed in the design phase of a component that uses an RDC include:

- stator "unstarting", where the shock wave propagating upstream can cause

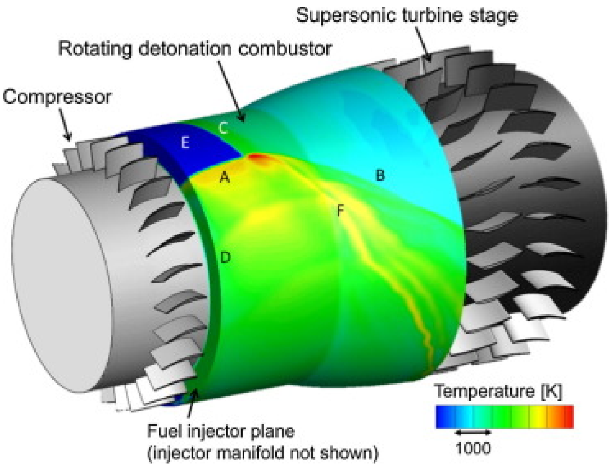

Figure 2.7: Computational Fluid Dynamic Simulation Showing Compression Wave during a Rotating Detonation Combustion.

the flow to stall through the stator passages;

- pressure losses, since the unstable interaction between blade wakes, shocks, and vortices increases entropy production and the related losses;
- flow non-uniformity, since heterogeneities in the temperature field and the turbulence of the flow entering the turbine can induce unsteady effects;

Design through fluid dynamic simulations has proven to be the most widely used tool for studying this integration. The research focuses on two main configurations that can be used for the connection between the combustor and the turbine:

- "centerbody or boattail", which uses a central shape that redirects and expands the exhaust flow to reduce its swirl angle before it reaches the turbine. This method has the advantage of eliminating unsteady losses at the cost of a potential high total pressure loss;
- "ejector mixing", where fresh bypass air is mixed with the RDC exhaust flow, dampening pressure and velocity pulsations. One study found a reduction in pressure fluctuations of 60-70% compared to the RDC outlet.

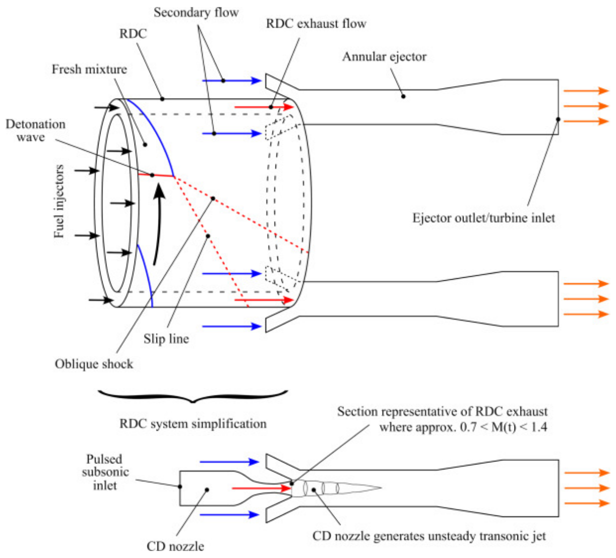

Figure 2.8: Rotating Detonation Combustor with Turbine Inlet in Ejector Mixing Configuration.

2.5 Literature Review

The first-stage stator vane is the static component that precedes the first row of rotor blades. Its function is to accelerate and deflect the high-kinetic-energy combustion gas flow towards the movable blades, converting part of its enthalpy into kinetic energy. Being the first fixed component exposed to the hottest gases, it is subject to extreme thermal and mechanical stresses. To protect the vane from these extreme operating conditions, various cooling technologies are used, schematized in Figure 2.9, among which the most common are:

- internal cooling, where cooling air taken from the compressor is made to flow inside radial or serpentine channels obtained within the blade itself;
- impingement cooling, where cooling air is conveyed into a finely perforated inner jacket through which the cooling fluid passes in the form of jets that impact the internal surface of the blade near the stagnation point of the blade;
- film cooling, where small holes, not necessarily circular in section, are drilled on the surface of the blade through which the cooling fluid is expelled, creating a film of cold fluid that isolates the blade's surface from the hot combustion gases.

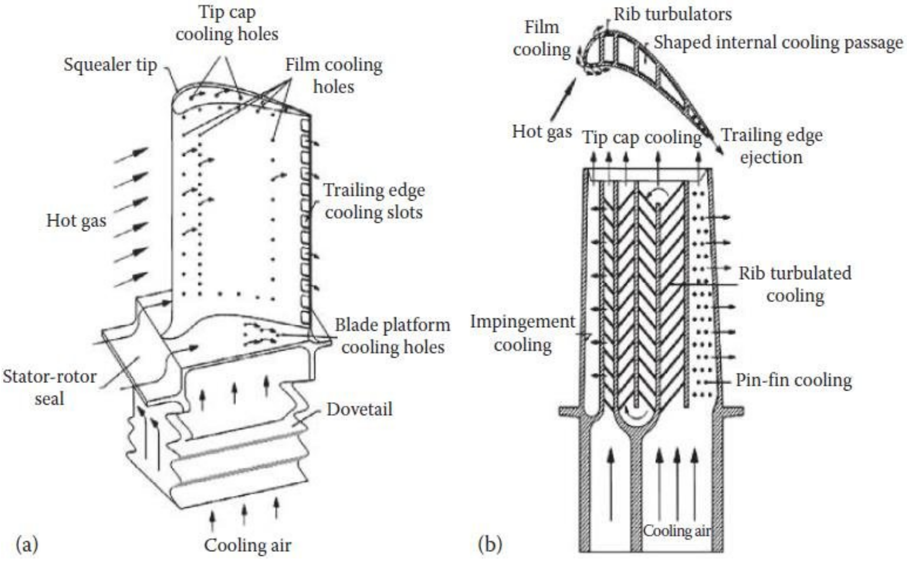

Figure 2.9: Schematic of Vane Cooling Techniques.

The non-linear interaction of the individual cooling methods is studied using fluid dynamic simulations in which particular attention is paid to the associated heat exchange.

In the present study, the rib cooling method will be highlighted and exploited. Figure 2.10 shows a diagram of the main parameters that have been varied in experiments conducted worldwide. Among these, the distance between two consecutive ribs and the ratio between the height of the single rib and the channel are the most used parameters. In

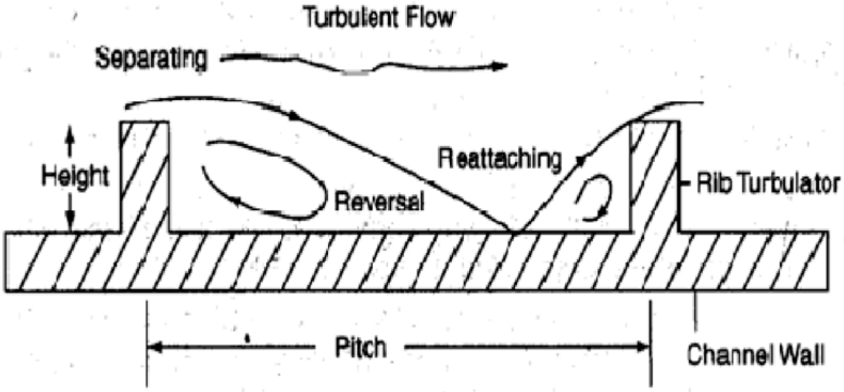

Figure 2.10: Schematic of Rib Turbolators Parameters.

the following pages, some of the experiments conducted by varying these characteristics and the geometry of the single element are presented. The latter, in fact, has undergone various configurations starting from the one simply perpendicular to the incoming flow to reach the V-shape, the W-shape, the M-shape, and the oblique arrangement at 30ř, 45ř, and 60ř.

Stator vane cooling in axial turbines is addressed primarily through ribbed, multipass, and serpentine internal cooling configurations. Yousefi et al. report that ribbed channel designs can yield up to a 25% increase in heat transfer, with a corresponding maximum metal temperature reduction of 25 K. Dees et al. demonstrate that ribbed passages may enhance external cooling effectiveness by as much as 50% compared to nonribbed configurations. Several studies, employing threedimensional conjugate heat transfer (CHT) and computational fluid dynamics (CFD) simulations, validate their models against experimental data, with temperature differences of less than 10% in some cases and uncertainties on the order of 67%. These studies consistently use turbulence models that include kepsilon variants, VelocityVorticity (V2F), and SST, while noting that the inclusion of transition effects is critical for accurate simulation.

The study conducted by Bruschewski et al., of an experimental and numerical type, has as its objective the study of a serpentine with three passages in the main body of the stator vane with the presence of turbulators and emission from the trailing edge. The numerical study compares the results from different turbulence models. The results were validated by experimental tests acquired through magnetic resonance velocimetry and thermochromic liquid crystal wall heat transfer measurement. The turbulence models used by the study were the Spalart-Allmaras model, the Menter $k-\omega\ SST$ model, the Reynolds stress method, and the calculations culminated with a Scale-Adaptive simulation.

Yousefi et al. have shown, through a three-dimensional CHT study, a 25% increase in heat transfer, accompanied by a 3% increase in the friction factor and a decrease of about 25 Kelvin in the maximum recorded temperature. Similar results were obtained by the research group of Dees et al. who compared a smooth channel configuration against one with simple ribs and found a heat transfer increase that reaches up to 50% with a lower maximum recorded temperature in the case with turbulators.

The study carried out by Fathi and Nejat found a non-linear increase in heat transfer when different cooling techniques are used. In particular, the simultaneous action of film cooling, turbulators, and impingement cooling was studied.

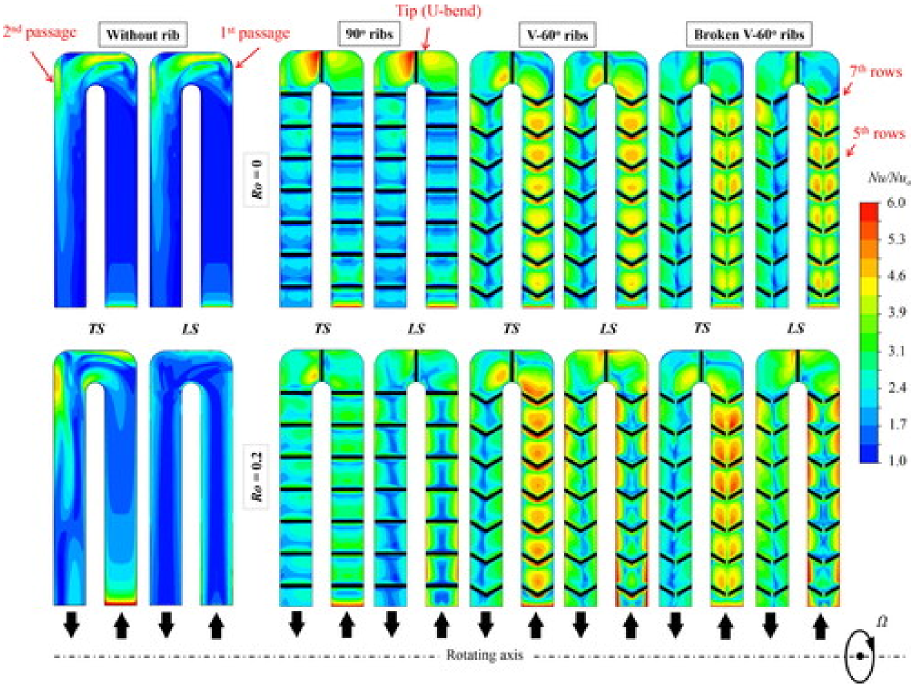

Figure 2.11: Nusselt Number Contour for Various Rib Turbolator Configurations.

Al-Qahtani et al. have shown that the curvature of the cooling serpentine causes a fluid flow separation at small radii of curvature. As shown in Figure 2.11, the group studied how the geometry of the turbulators influences heat transfer through the distribution of the normalized Nusselt number Nu. The greater heat transfer capacity that arises from turbulent mixing, which assumes the characteristics of the flow field downstream of a rearward-facing step, is evident.

Ravi et al. studied a two-pass channel with a bend in different turbulator configurations and in a Reynolds number range from 20000 to 70000. The four geometries used for the turbulator design were: straight ribs placed at 45ř, V-shaped, W-shaped, and M-shaped. The results were then validated by comparison with experiments with good data agreement. The greatest discrepancy in the data was found at the channel inlet, a sign of the importance of imposing adequate boundary conditions. As can be seen in Figure 2.12, where the wall temperature distribution is presented, the maximum heat transfer was obtained for the V-shaped geometry in the channel area and for the M-shaped geometry in the bend area. The results also show that an increase in the heat transfer coefficient is

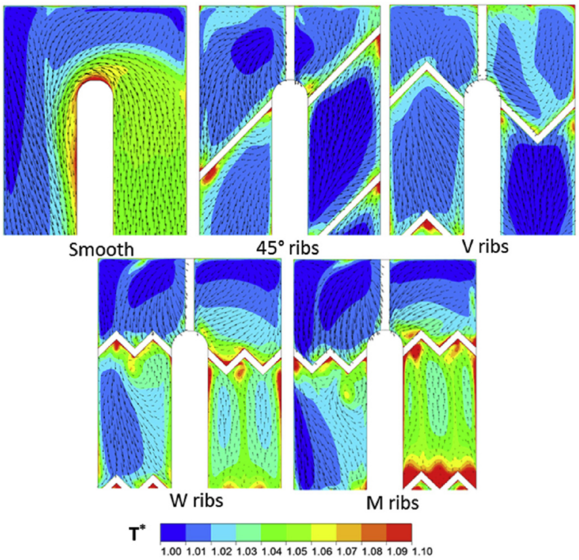

Figure 2.12: Nusselt Number Contour in Bend Region.

linked to an increase in the friction coefficient: the V-shaped configuration, in fact, proved to be the geometry with both the maximum overall heat transfer value and the pressure losses among the analyzed configurations.

Figure 2.13 presents an interesting comparison that directly links the best wall heat transfer with a local increase in turbulent energy. The higher heat transfer coefficient and, consequently, the higher Nusselt number arise from turbulent mixing phenomena.
Pin-fin arrays are a common internal cooling strategy for turbine airfoils, particularly in trailing edge regions where the geometry narrows and flow passages become highly constrained. The concept is simple: cylindrical or shaped protrusions (the pins) are placed in the coolant channel, forcing the flow to separate and reattach repeatedly. This generates strong secondary vortices, disrupts the thermal boundary layer, and thereby increases local convective heat transfer.

The effectiveness of pin-fin cooling depends strongly on the pin geometry (cylindrical, conical, or shaped pins), the spacing between them, and the Reynolds number of the coolant flow. Closely spaced arrays promote greater turbulence and surface renewal, but they also impose a significant pressure drop penalty. This trade-off is particularly important in turbine vane and blade cooling, since the coolant is bled from the compressor and any excess pressure loss translates into a performance penalty at the engine system level. Ligani studied the pin-fin cooling method, focusing on its application in the terminal part

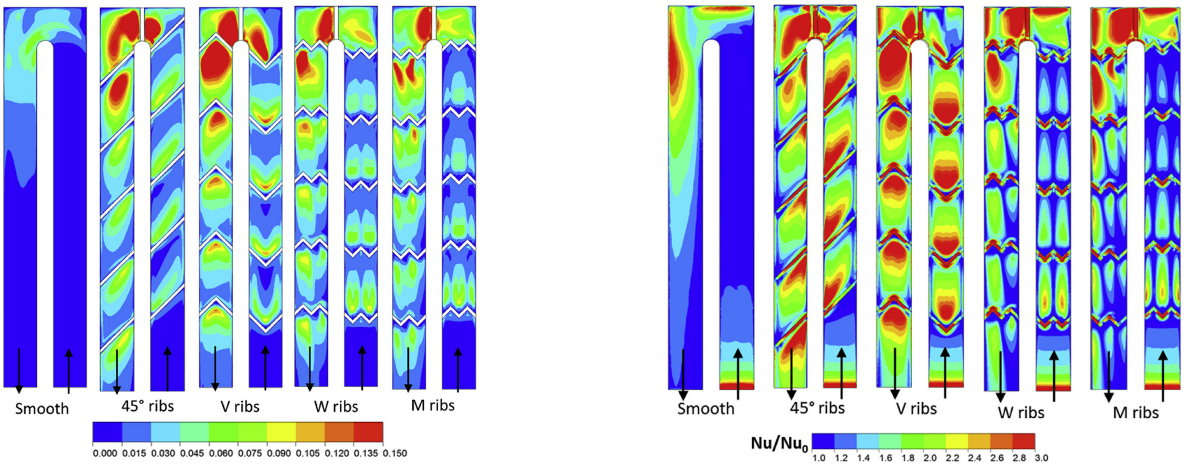

(a) (b)

Figure 2.13: Turbulent Kinetic Energy (a) and Nusselt Number (b) Contour in Ribbed Cooling Channels.

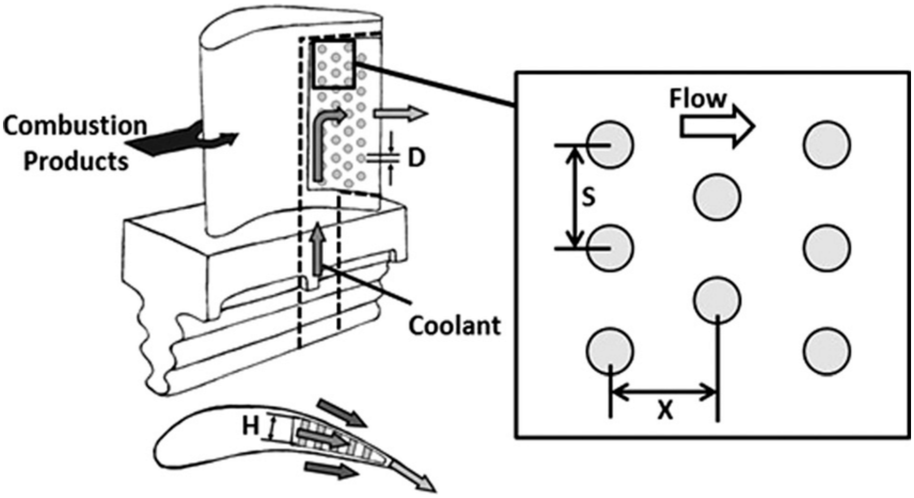

Figure 2.14: Schematic of Pin Fin Cooling Technique.

of the blade, where restricted dimensions often cause severe overheating problems (see Figure 2.14). The comparative study of different pin arrangements identified a 45ř alignment with respect to the flow direction as the most favorable, providing high heat transfer with relatively low pressure drop. The geometry of the pins themselves can vary considerablycircular, elliptical, triangular, and semicircular cross-sections have all been tested. Shapes with sharp angles, while delivering the highest heat transfer augmentation, also induce the largest pressure penalties. Spacing is another critical factor; experiments have shown that an axial pitch of approximately 2.5 times the pin diameter provides a good compromise between heat transfer enhancement and flow resistance. In practice, pin-fin arrays are most often applied in the trailing edge cavity of stator vanes or rotor blades. The trailing edge experiences high thermal loads due to thin wall sections and local acceleration of the hot gas path, but it is also structurally constrained: the narrow geometry limits the use of more elaborate cooling techniques like impingement. Pin-fins offer a relatively robust solution here, since they can be densely packed into tight spaces, provide structural reinforcement to the thin trailing edge, and still generate useful levels of heat transfer augmentation.

One persistent challenge with pin-fin cooling is flow non-uniformity. As the coolant moves through successive rows of pins, crossflow builds up and alters the jet-wake interactions that dominate local heat transfer. This means the downstream pins are often less effective than the upstream ones. To address this, research has explored pin shaping (e.g. elliptic or tapered pins) and staggered array configurations, both of which can help reduce flow blockage and improve heat transfer distribution.

Experimental studiesoften using naphthalene sublimation for mass transfer analogy or liquid crystal thermographyhave provided valuable correlations for average Nusselt numbers in pin-fin arrays. More recent CFD work has highlighted the complexity of the local flow physics, especially the role of horseshoe vortices at the pin bases and the development of secondary flows between rows. Despite decades of research, optimization in real engine geometries remains non-trivial, as the trade-off between heat transfer enhancement and pressure drop is highly case-dependent.

Figure 2.15 shows a diagram of the operation of the jet impingement cooling technique. It is one of the most effective internal cooling techniques used in the hot sections of gas turbines, and it is particularly relevant for stator vane thermal management. The method relies on directing high-velocity air jetsusually bled from the compressoronto the inner surfaces of the vane cavity. When the jet strikes the target wall, a stagnation region forms where the local heat transfer coefficient is considerably higher than in conventional channel or rib cooling. This makes it well-suited for regions exposed to steep temperature gradients.

The performance of jet impingement is largely governed by non-dimensional parameters

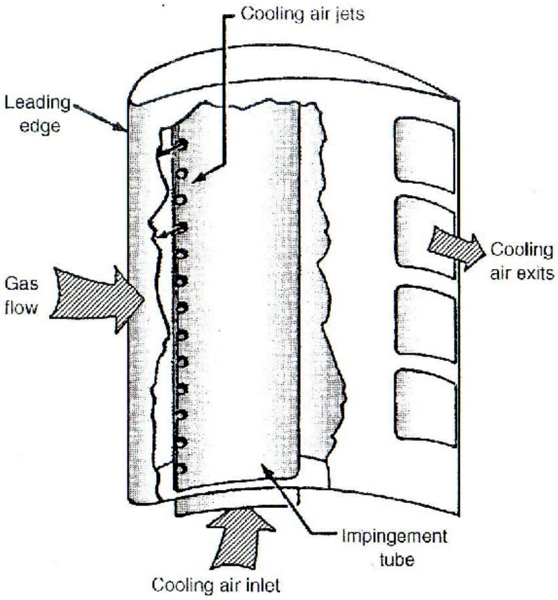

Figure 2.15: Schematic of Jet Impingement Cooling Technique.

such as the jet Reynolds number, the spacing between the jet and the impingement surface (H/D), and the arrangement of multiple jets. Small jet-to-wall distances enhance the stagnation-point heat transfer but tend to reduce uniformity downstream, especially once crossflow develops from the spent jets. In practice, this can create zones of over- and under-cooling if the jet array is not carefully designed.

For stator vanes, jet impingement is rarely applied in isolation. It is usually combined with other strategiessuch as pin-fin cooling in the trailing edge or film cooling on the external surfacebecause the vane geometry imposes complex flow constraints. The overall cooling system must balance local heat transfer enhancement against the associated pressure losses and the limited availability of compressor bleed air. In other words, the goal is not just maximum cooling effectiveness, but also efficient use of coolant mass flow to preserve engine performance. Research in this area has shown that results from canonical flat-plate jet impingement studies often do not translate directly to real vane passages. The curvature of the internal walls, the confinement of the jet, and the influence of secondary flows significantly modify the heat transfer patterns. More recent experimental campaigns (using techniques such as liquid crystal thermography or transient IR methods) and high-fidelity CFD have been directed at capturing these effects in geometries that are closer to engine reality. Some current developments include shaped or swirling jets, which aim to improve wall coverage while mitigating the negative impact of jet-to-jet interaction

3 Mesh Sensitivity Test

The first step performed was the Mesh Sensitivity Analysis. This was carried out following the schematic shown in Figure 3.1. Three meshes with different levels of refinement were used and subjected to the same boundary conditions. The results, obtained for the main fluid domain only, were then transferred to the fluid domains that form the internal cooling channels.

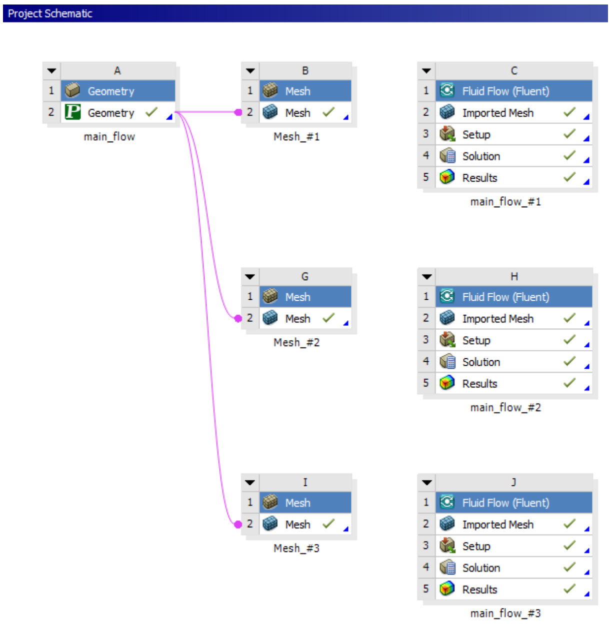

Figure 3.1: Project Schematic of Mesh Sensitivity Test.

3.1 Computational Domain

The computational domain of interest is presented in Figure 3.2. From the isometric view, it can be seen that it has a divergent trend: the geometry of the duct and the blade were derived from previous studies conducted by the same research group I belong to. The duct's purpose is to mitigate the finite span effect of the blade by introducing a divergent duct that decelerates the inlet flow at the cost of total pressure loss, which results from the creation of vortices. The result of this modification, as can be appreciated in the data post-processing, is the possibility of studying the effects at the blade's midspan as if it

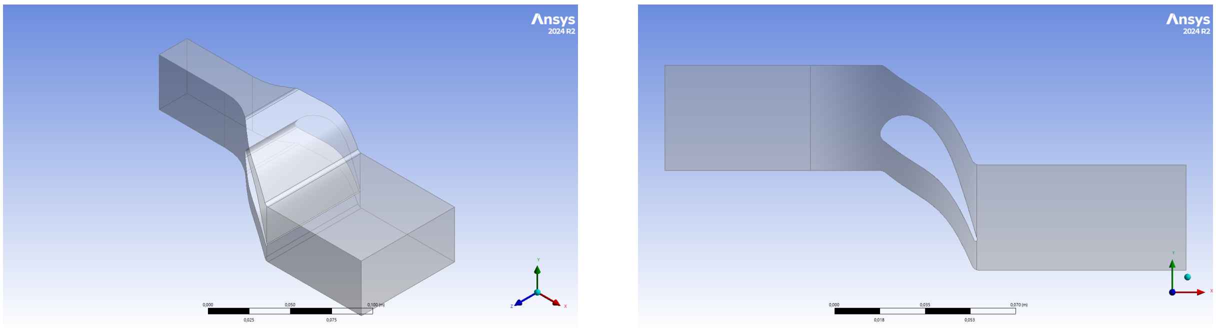

(a)

(b)

Figure 3.2: Computational Domain Used for Main Flow Study: Isometric View (a) and Top View (b).

were two-dimensional, thereby eliminating the three-dimensional effects that could arise from the interaction with the endwalls present in the computational domain. The blade, optimized by neural networks, is designed to operate in a transonic regime.

3.2 Selected Meshes

Figures 3.3, 3.4, and 3.5 show the computational grids used in both isometric and top views. Table 1 lists the parameters used for the generation of these computational grids. Following trends found in the literature for such analyses, a ratio between the average cell sizes of $r > 1.33$ was maintained, a useful value for analyses with unstructured meshes. From Mesh #1 to Mesh #3, the number of cells doubles. Although this might seem like too small an interval for such an analysis, it's important to note that the meshing starts from pre-existing computational grids used for blade optimization. These grid parameters, in fact, have proven sufficient to obtain stable variables as refinement varies.

Furthermore, in Table 1, it is shown how the average quality of the grid elements remains constant with a slight increase as the grid is refined. This behavior demonstrates

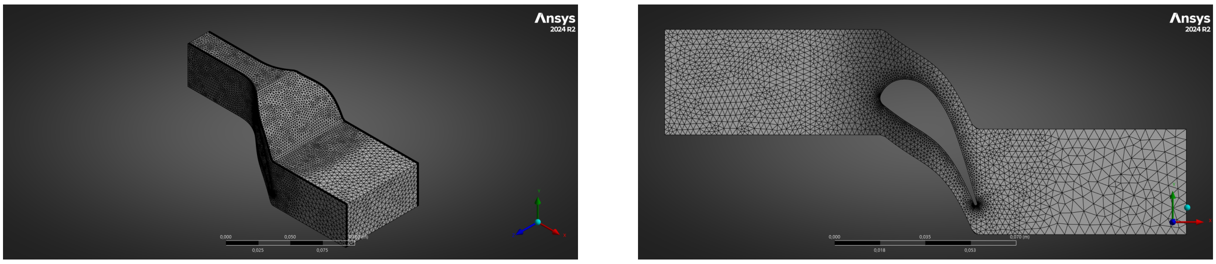

(a) (b)

Figure 3.3: Mesh #1 in Isometric (a) and Top (b) View.

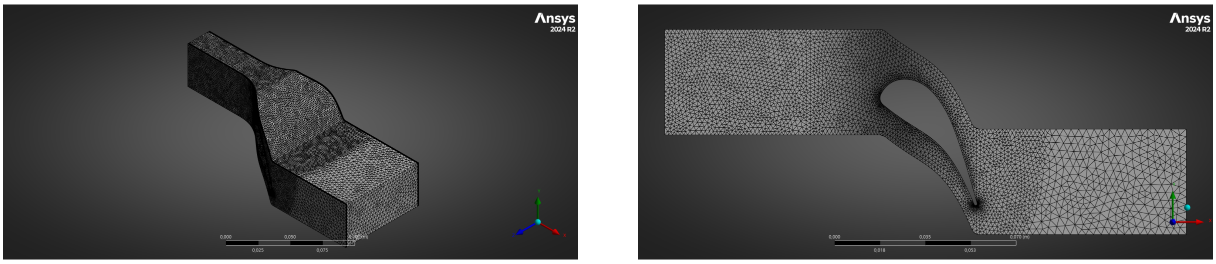

(a) (b)

Figure 3.4: Mesh #2 in Isometric (a) and Top (b) View.

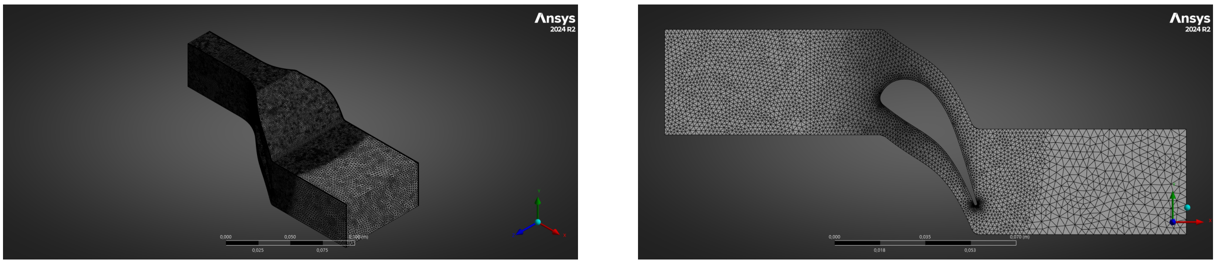

(a) (b)

Figure 3.5: Mesh #3 in Isometric (a) and Top (b) View.

that decreasing the average size of the computational cells leads to better results with more stable simulations.

The mesh metrics analyzed in Table 1 are the following:

	Mesh #1	**Mesh #2**	**Mesh #3**
Element Size [mm]	4	3	2
Refinement Size [mm]	2	1.5	1
Average Aspect Ratio [-]	1.843	1.833	1.814
Average Element Quality [-]	0.838	0.841	0.846
Average Orthogonal Quality [-]	0.771	0.776	0.784
Skewness [-]	0.227	0.223	0.214
Millions of Elements [-]	2.4	2.9	4.7

Table 1: Mesh Metrics Chosen for Sensitivity Test.

- Average Aspect Ratio, it compares the longest dimension of a cell to its shortest dimension. A value closer to one indicates a more "equilateral" cell, which is generally preferred, especially for unstructured meshes. High aspect ratios can introduce numerical errors, particularly in areas with complex flow gradients;
- Average Element Quality, a comprehensive metric that often combines aspects like aspect ratio, skewness, and orthogonality. It provides a single value to gauge the overall health of the mesh. A value closer to one signifies a high-

quality mesh;

- Average Orthogonal Quality, it measures how perpendicular a cell's face is to the line connecting the centroids of adjacent cells. Values closer to one are ideal, as a high orthogonal quality reduces numerical diffusion and improves solution stability;
- Skewness, it measures how much a cell deviates from an ideal shape. A value of zero is perfect, while a value of one indicates a degenerate cell. High skewness can lead to inaccurate results and convergence difficulties.

Mesh #1

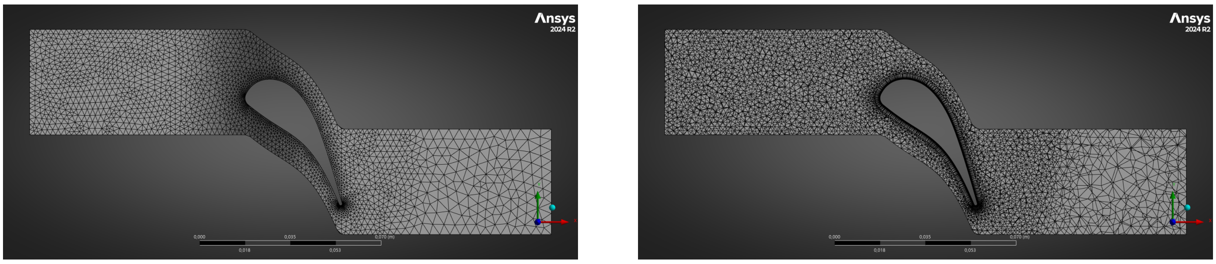
(a) (b)

Figure 3.6: Mesh #1: Top View (a) and Midspan Section (b).

Figures 3.6 to 3.9 present exemplary zones of the coarsest computational grid. We expect this to lead to the least precise solution and one more prone to discretization error.

An overview of the computational grid is shown in Figure 3.6: note the greater refinement near the section upstream of the blade and at the wall. The zone downstream of the inlet requires a higher computational resolution due to the change in geometry made to the main flow channel. Several inflation layers are present at the wall.

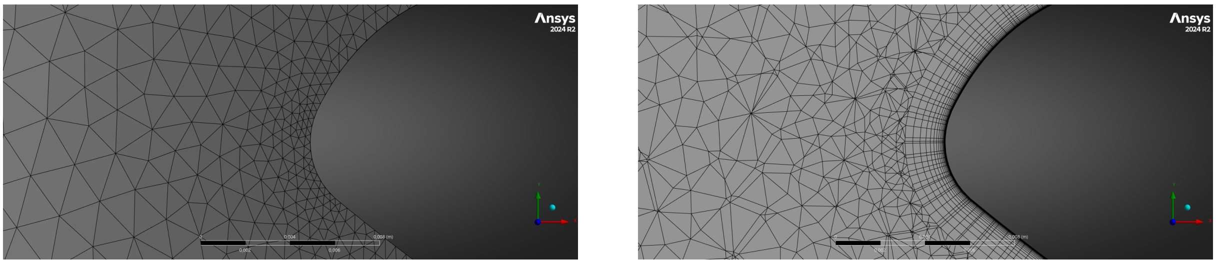
(a) (b)

Figure 3.7: Leading Edge Particular on Mesh #1: Top View (a) and Midspan Section (b).

The preliminary calculation to choose these parameters, as shown in Figure 3.8, started from the boundary conditions imposed at the domain's inlet, which were used to calculate the average Reynolds number Re_{inlet} and from which the empirical method was chosen to arrive at the desired parameters. By imposing the total pressure p^o_{inlet} and total temperature T^o_{inlet} at the inlet, a Reynolds number of $Re > 5 \cdot 10^5$ was calculated, which places the case in a turbulent regime. For this reason, the empirical Prandtl formula, $c_f = \frac{0.074}{Re^{0.2}}$, was used, which relates the Reynolds number Re to the friction coefficient c_f. From the latter, the first cell height from the wall, $\delta_1 = 0.843\ \mu m$, was determined, along with the total thickness of the layer δ_{tot}, which must reach a value as close as possible to the average size of the computational grid cells.

Figures 3.7 and 3.9 present magnifications of the blade's zones with the highest curvature, namely the leading edge and trailing edge. To best capture the geometry variation in these zones, a cell size of $l_{LE} = 0.375\ mm$ was chosen for the leading edge zone and $l_{TE} = 0.150\ mm$ for the trailing edge zone, which requires a higher resolution due to its smaller radius of curvature.

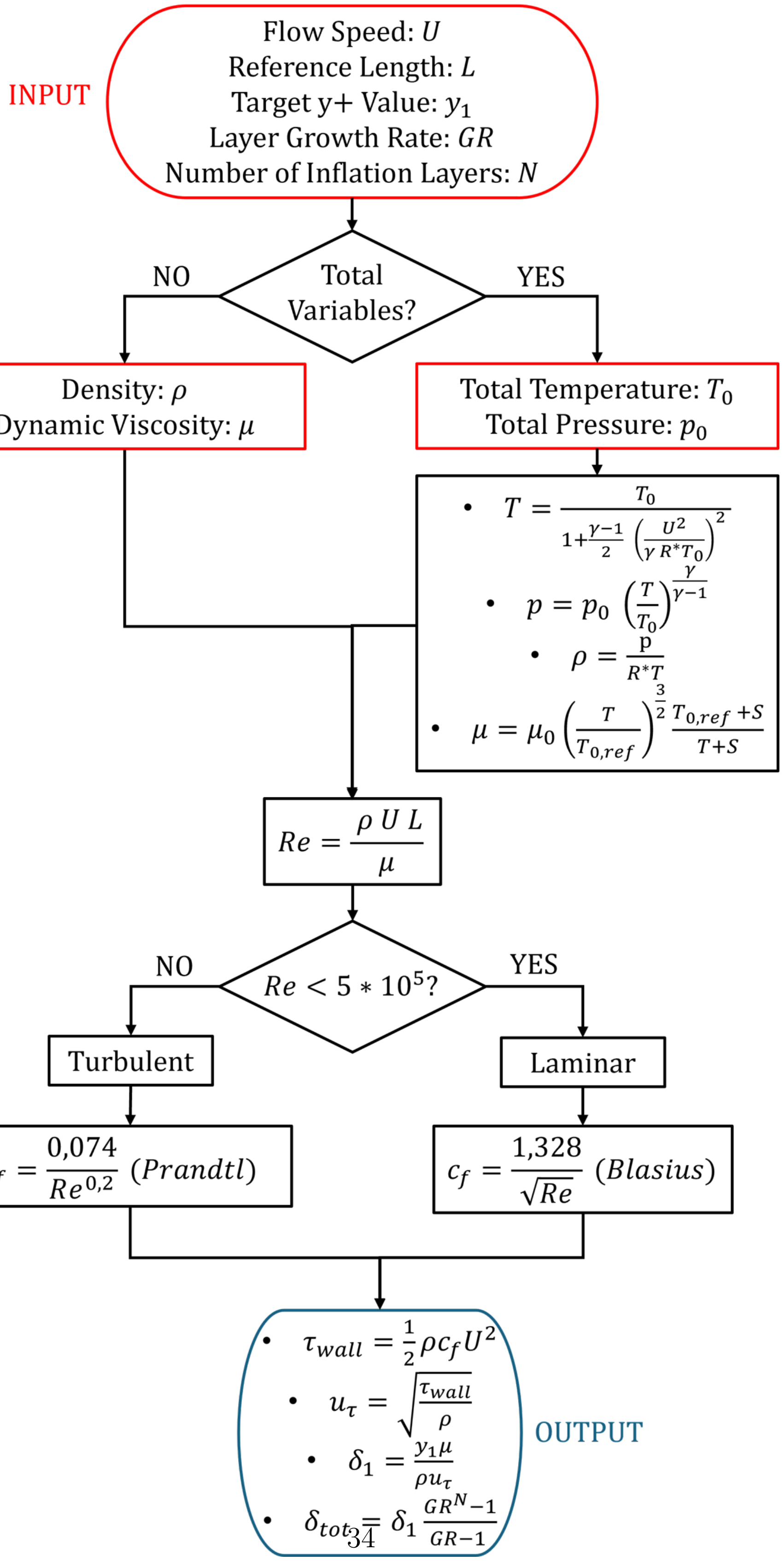

Figure 3.8: Preliminary y^+ Calculation Algorithm.

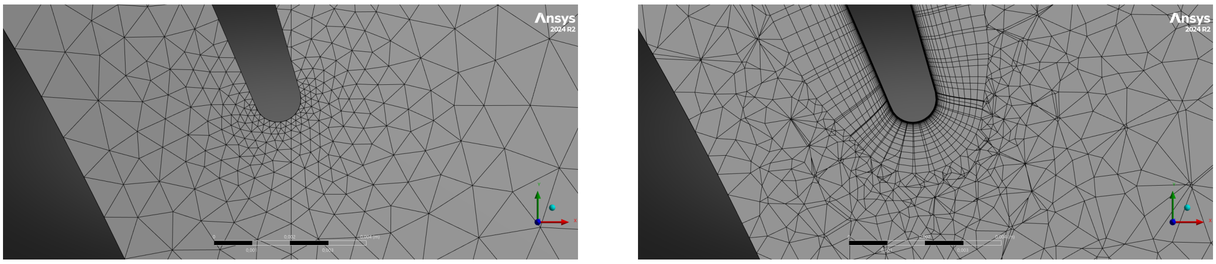

(a) (b)

Figure 3.9: Trailing Edge Particular on Mesh #1: Top View (a) and Midspan Section (b).

Mesh #2

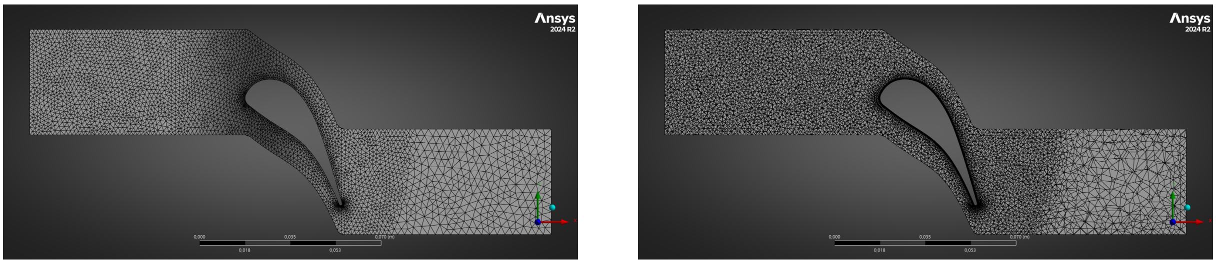

(a) (b)

Figure 3.10: Mesh #2: Top View (a) and Midspan Section (b).

In Figures 3.10 to 3.12, Mesh #2 is presented. It is generated from an average cell size of $l_2 = 3\ mm$ with a cell refinement of $l_{2,ref} = 1.5\ mm$. In Figure 3.10, the effect of the inflation layer used for the boundary layer study can be seen. Following the same procedure as for the calculation of the parameters for Mesh #1, the inflation layer was set so that the total thickness, δ_{tot}, is approximately equal to the cell size, l_2.

Figures 3.11 and 3.12 show magnifications of the computational grid at the leading and trailing edges of the blade. To best capture the profile curvature, the same parameters used for the first mesh were applied. The total number of computational cells is approximately $n_{ele} = 2.9$ million, slightly higher than the n $n_{ele} = 2.5$ million elements of the first

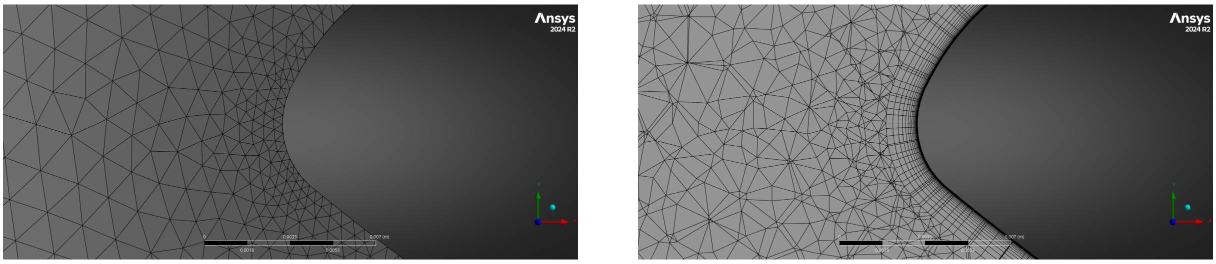

(a) (b)

Figure 3.11: Leading Edge Particular on Mesh #2: Top View (a) and Midspan Section (b).

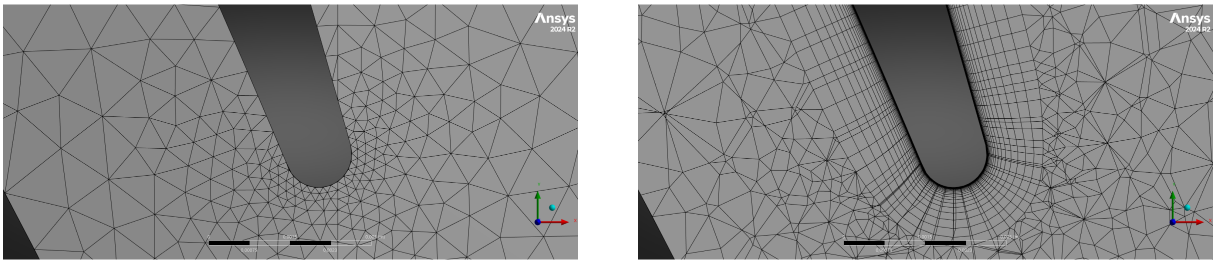
(a) (b)

Figure 3.12: Trailing Edge Particular on Mesh #2: Top View (a) and Midspan Section (b).

mesh. This small difference is attributable to the opposing effects of the decrease in the number of inflation layers and the average size of the computational cells.

Mesh #3

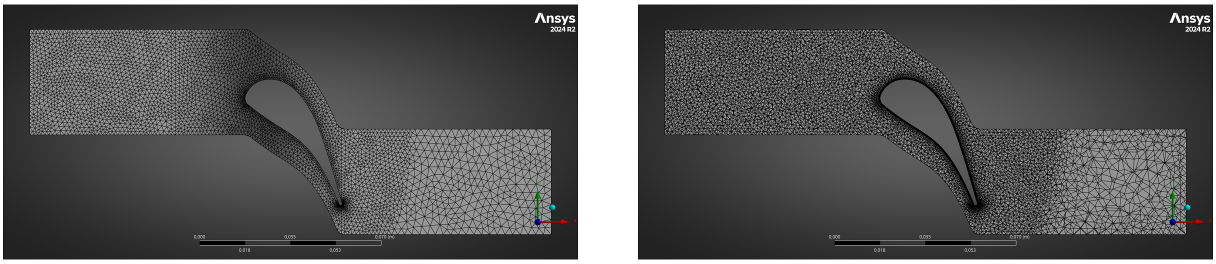

(a) (b)

Figure 3.13: Mesh #3: Top View (a) and Midspan Section (b).

In Figures 3.13 to 3.15, Mesh #3 is presented, which has the finest computational grid and will yield the results least prone to errors. The computational grid has an average cell size of $l_3 = 2\ mm$ with a refinement to $l_{3,ref} = 1\ mm$. The number of cells increases from $n_{ele} = 2.9$ to $n_{ele} = 4.7$ million, leading to a much denser discretization. The inflation layer used for the boundary layer study, visible in Figure 3.13, was chosen so that the value of $y^+ = \delta_1 \frac{u_\tau}{\nu}$, which is the height of the first cell from the wall normalized by wall variables, is $y^+ = 0.7$. This value was chosen to best calculate the heat exchange that occurs at the wall within the boundary layer, which, therefore, cannot be resolved by wall laws, but directly by the solver.

In Figures 3.14 and 3.15, magnifications are presented in the areas of maximum profile

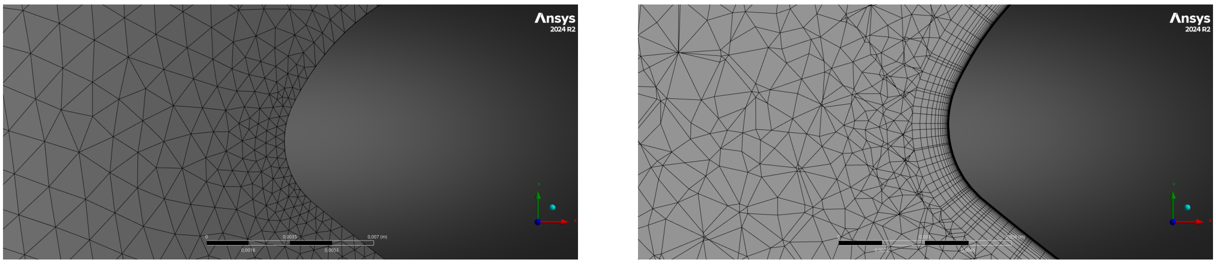

(a) (b)

Figure 3.14: Leading Edge Particular on Mesh #3: Top View (a) and Midspan Section (b)

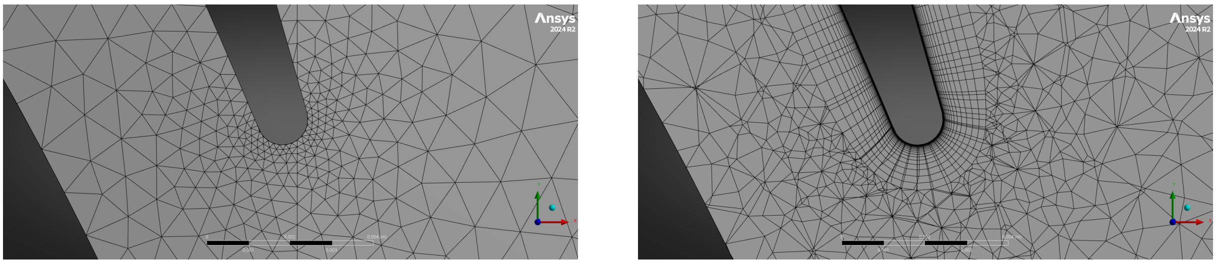

(a) (b)

Figure 3.15: Trailing Edge Particular on Mesh #3: Top View (a) and Midspan Section (b)

curvature, namely at the leading and trailing edges. In these magnifications, shown in the midspan section, it is possible to best appreciate the grid for the boundary layer study that adapts perfectly to the imposed geometry.

3.3 Boundary Conditions and Setup

	Fluid
Name	Air
Density $[kg/m^3]$	Ideal Gas Law
Heat Capacity C_p $[J/kg \cdot K]$	NASA 9-Piecewise Polynomial
Thermal Conductivity k $[W/m \cdot K]$	0.0242
Dynamic Viscosity μ $[Pa \cdot s]$	Sutherland Law
Molecular Weight $[kg/kmol]$	28.966

Table 2: Material Setup Used in Mesh Sensitivity Test.

In the following subsection, the boundary conditions and the setup used by the solver to carry out the individual simulations will be illustrated. Each simulation has the same boundary conditions in both value and type. The fluid used for the analysis, which is air, has the characteristics shown in Table 2. Since the subsequent analyses will be concerned with the heat exchange that can occur in the case of high temperatures, the model used for the characteristics of density ρ, specific heat at constant pressure C_p, and dynamic viscosity μ are temperature-dependent. Thermal conductivity k and molecular weight, on the other hand, do not undergo significant variations in the interval up to a temperature of $T = 1000\ K$: under this hypothesis, these quantities are considered constant.

In Figure 3.16, the types of boundary conditions imposed on the fluid domain are shown.

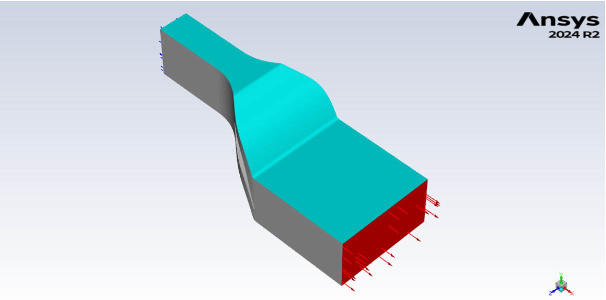

Figure 3.16: Setup of Computational Domain Used for Mesh Sensitivity Test.

Of notable importance is the light blue region: this is the wall on which the periodicity condition is imposed, which is of capital importance in the study of a linear blade row assumed to have infinite repetition. The gray walls, on the other hand, are walls with no-slip and adiabatic conditions: the latter will then be replaced by a heat exchange condition associated with a solid body which, for reasons of indifference to the mesh sensitivity analysis, was suspended from the analysis.

Table 3 reports the values of the imposed boundary conditions. They stem from the need to find a single value at which to perform the steady-state analyses used as a comparison for the unsteady ones. This is why total pressures p^o_{inlet} and temperatures T^o_{inlet} at the inlet were chosen, which result from the average of the minimum and maximum values of the periodic boundary conditions that will be used later. At the domain outlet, a gauge pressure was used that reflects the ambient pressure value in standard conditions and a backflow temperature equal to the minimum temperature of the future oscillating boundary conditions. This latter choice arose from the need to set the temperature that the fluid would have if it were sucked from the outlet: being downstream of an exhaust, the ambient temperature would have a minimum equal to the minimum of the inlet temperature. The wall boundary conditions, on the other hand, present what has already been expressed in consideration of Figure 3.16.

	Inlet	**Outlet**	**Wall**
Total Pressure [Pa]	193011	-	-
Total Temperature [K]	521.33	-	-
Gauge Pressure [Pa]	-	101325	-
Backflow Temperature [K]	-	440	-
Periodicity	-	-	Superior & Inferior
No Slip	-	-	Vane & Endwalls
Slip	-	-	-
Adiabaticity	-	-	Vane & Endwalls

Table 3: Boundary Conditions Used in Mesh Sensitivity Test.

Table 4 lists the main solver settings. For future calculations, an implicit solver will

Solver Type	Implicit Density-Based
Accuracy Order	2^{nd} Order
CFL Number	5
Initialization	Fluent Hybrid

Table 4: Solver Setup Used in Mesh Sensitivity Test.

be implemented, based on Roe's Flux Difference Splitting algorithm for its ability to better capture discontinuities, being a low-diffusive method. The choice of density-based is dictated by the transonic condition in the case under consideration: it, in fact, presents criticalities if investigated with a pressure-based method, which is more suitable for the study of incompressible flows. The accuracy was first maintained at the first order and then increased to the second order with an increment in the CFL number to 5 to ensure a faster numerical convergence. Prior to the analysis, a hybrid initialization with 10 steps, unity relaxation factors, and a threshold value of 10^{-6} was performed.

3.4 Results

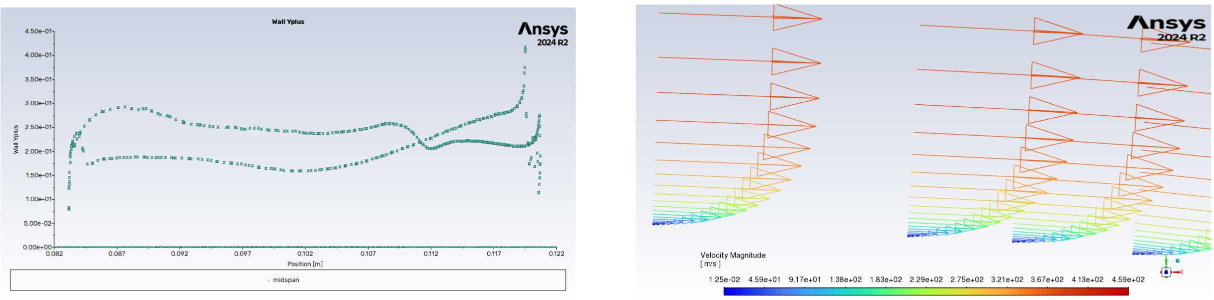

(a)

(b)

Figure 3.17: Wall $y+$ Distribution (a) and Velocity Vectors (b) Evaluated on Vane Midspan for Mesh Sensitivity Test.

In the following subsection, the results of the mesh sensitivity analysis and the consequent choice of the most suitable mesh parameters will be presented. Figure 3.17 shows the results related to the inflation layer. For the CHT study, it is crucial to have excellent quality in resolving the gradients present in the boundary layer that develops at the wall: starting from a preliminary calculated $y^+ = 0.7$, a nearly constant wall distribution was obtained with an average value of $y^+ = 0.22$, which is much better than expected. Such a striking difference between the assumed and actual values is favorable given the oscillating boundary conditions: the simulation performed here takes into consideration constant and averaged conditions, while the unsteady simulation will have to deal with higher total pressure values. This total pressure will induce a higher velocity which, in turn, will produce greater gradients at the wall that will need to be discretized with a finer grid. Staying with the steady-state case, there are also indications about the resolution level of the boundary layer: in Figure 3.17(b), in fact, one can appreciate the distribution of velocity vectors at the wall that follow a very similar trend to the theoretical reality of the phenomenon, resulting from a good discretization of the boundary layer.

Table 5 provides an overview of the results concerning the flow. The mass flow rate error was monitored as the difference between the mass flow rate at the inlet and that at the outlet of the domain. It gives an indication of the numerical convergence of the single simulation, but not of the quality of the solution itself with respect to the mesh. Instead, five variables typical of the main flow and three concerning heat exchange at the wall were monitored. The first group consists of polytropic efficiency, total-to-total pressure

	Mesh #1	Mesh #2	Mesh #3
Mass Flow Rate Error 10^{-12} kg/s	-0.9113	-4.2359	-5.6937
Polytropic Efficiency [-]	0.8603	0.8640	0.8687
Total to Total Pressure Ratio [-]	1.0933	1.0907	1.0875
Average Outlet Total Pressure [Pa]	176305	176729	177300
Average Outlet Total Temperature [K]	521.1694	521.1275	521.1177
Average Outlet Mach Number [-]	0.9251	0.9274	0.9305
Average Static Wall Temperature [K]	486.0895	486.1194	486.1583
Average Vane Static Pressure [Pa]	129506	129610	129619
Average Vane Isentropic Mach Number [-]	0.7770	0.7762	0.7761

Table 5: Mesh Sensitivity Test Results.

ratio, and the outlet average of total pressure, total temperature, and Mach number, and they show variations in line with the progressively finer discretization. The second group, consisting of the average wall static temperature, static pressure, and isentropic Mach number on the blade, show a much smaller variation than the variables of the first group, indicating the insensitivity of the solution to the mesh.

Table 6 shows the percentage variations of the two groups of variables illustrated previously. As already predicted, it can be seen that the variation of the thermal quantities is much smaller than that of the fluid dynamic ones. With the exception of the Mach number at the outlet, all other quantities in the first group show a percentage increase in the difference between Mesh #2 and Mesh #3. For this reason, further checks were carried out to ensure the convergence of the results.

Table 7 presents the results of the Richardson analysis for validating the achievement of the asymptotic range. This analysis gives us two elements: a factor related to the grid independence of the quantity in the form of a value that must approach unity, and the

	Variation between Mesh #2 & Mesh #1	**Variation between Mesh #3 & Mesh #2**
Polytropic Efficiency	+0.428%	+0.541%
Total to Total Pressure Ratio	-0.238%	-0.294%
Average Outlet Total Pressure	+0.240%	+0.322%
Average Outlet Total Temperature	-0.008%	-0.002%
Average Outlet Mach Number	+0.248%	+0.333%
Average Static Wall Temperature	+0.006%	+0.008%
Average Vane Static Pressure	+0.080%	+0.007%
Average Vane Isentropic Mach Number	-0.103%	-0.013%ă

Table 6: Mesh Sensitivity Test Results: Percentage Variation.

	GCI_{12}	GCI_{23}	**Asymptotic Range of Convergence**
Polytropic Efficiency	2.089%	1.284%	1.005
Total to Total Pressure Ratio	1.187%	0.743%	0.997
Average Outlet Total Pressure	1.154%	0.673%	1.003
Average Outlet Total Temperature	0.005%	0.002%	1.000
Average Outlet Mach Number	1.193%	0.695%	1.003

Table 7: Mesh Sensitivity Test Results: Richardson Extrapolation.

error that must be associated with each result from the current study, namely the Grid Convergence Index or GCI. The latter was calculated with a safety factor of $SF = 1.5$, consistent with aerospace applications that require narrow safety margins. The results show, as seen in the previous table, that the quantities have reached the asymptotic convergence range with a good approximation and that the error associated with the individual quantities is less than 1% for all quantities except for polytropic efficiency. This result can be accepted knowing that it requires a more stringent result than the others, stemming from the polytropic calculation.

Figures 3.18 and 3.19 show the section planes used for the analysis of the distributions of the fluid dynamic quantities of the main flow. The sections that deal with the analysis

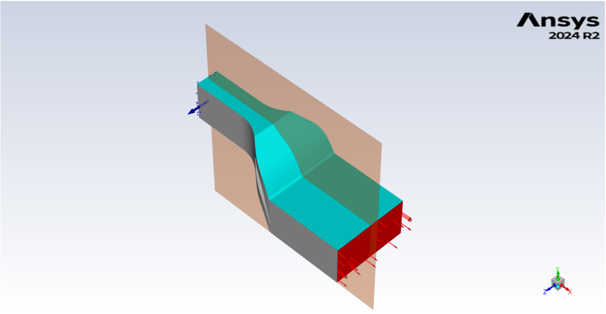

Figure 3.18: Midspan Plane Used for Mesh Sensitivity Results Evaluation.

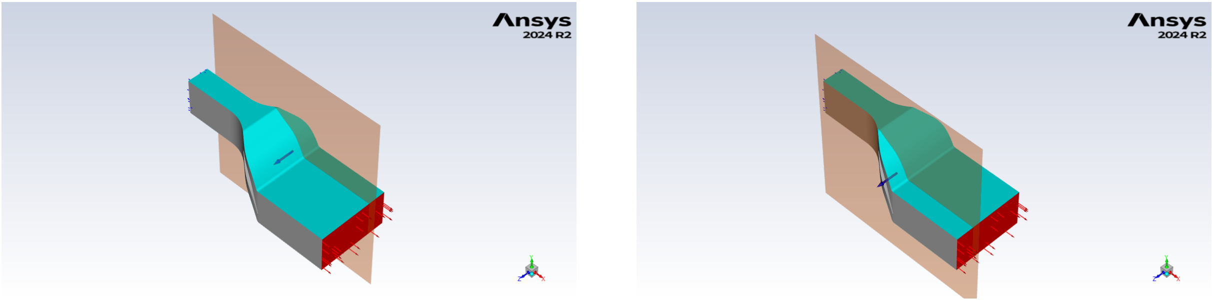

(a)

(b)

Figure 3.19: 25% Span (a) and 75% Span (b) Planes Used for Mesh Sensitivity Results Evaluation.

near the wall, namely those presented in Figure 3.19, do not follow the trend of the duct in order to obtain information on the aforementioned distributions in the wall region, where the velocity and temperature gradients create a kinematic and thermal boundary layer of considerable interest for future simulations. The cuts were therefore made at 25% and 75% of the blade's maximum width, i.e., at the trailing edge, starting from the hub, which is at a negative Z coordinate.

Mesh #1

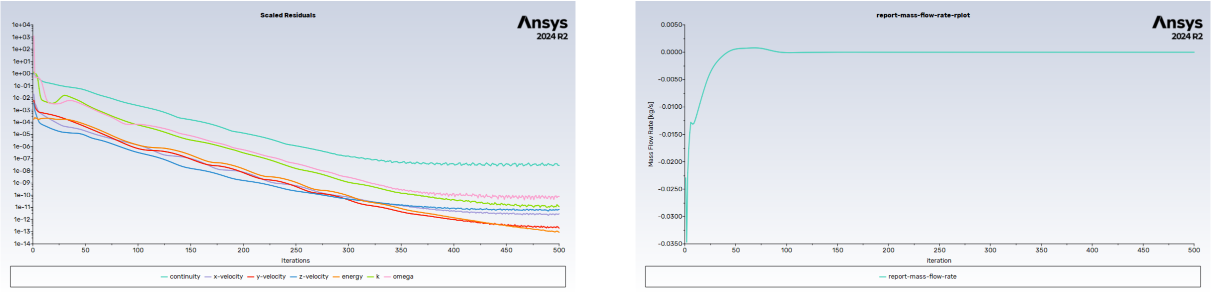

(a) (b)

Figure 3.20: Residuals (a) and Delta Mass Flow Rate (b) used for Convergence Evaluation in Mesh #1 Calculation.

Figure 3.20 shows the graphs for residuals and the difference between inlet and outlet mass flow rate. These graphs show the numerical convergence of the simulation: the derivative of the residuals with respect to the iterations is almost constant and settles on very low values, around 10^{-6} in the case of the mass equation. This hypothesis on numerical convergence is confirmed by the flatness of the line referring to the mass flow rate.

Figures 3.21 and 3.22 display the Mach number contour plots calculated at midspan and at the other two sections of interest, respectively. At midspan, there's no indication of the presence of end walls: the distribution, in fact, resembles simulations performed on two-dimensional cases, a clear sign that the main flow duct's divergence fulfilled its function of making the field more uniform. In the same value range, Figure 3.22 shows a comparison of the Mach number calculated at 25% and 75% of the vane span at the trailing edge. A careful comparison reveals subtle anomalies, which can be attributed to discretization errors of minimal entity compared to deviations from the correct symmetrical case. Further proof of the field's symmetry will be provided by the graphs showing the trends of the static pressure on the vane walls.

Figure 3.23 shows the midspan distribution of static temperature. This graph shows how the temperature increases upstream of the vane due to the decrease in velocity caused by the diverging duct geometry. This is followed by a temperature increase near the stagnation point at the leading edge of the vane and a sudden decrease for the fluid that has entered the passage between two consecutive vanes due to its converging-diverging

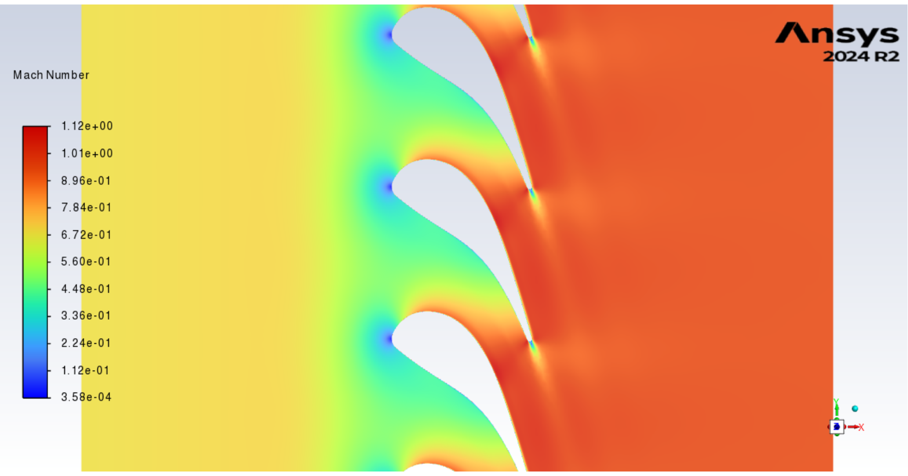

Figure 3.21: Midspan Distribution of Mach Number for Mesh #1.

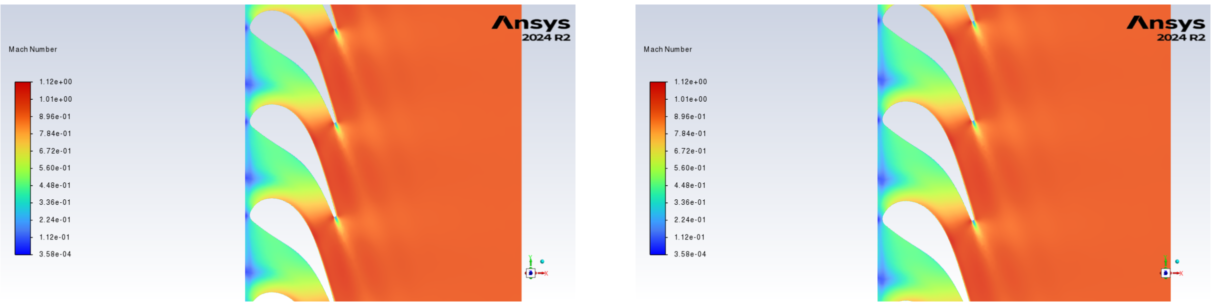

(a)

(b)

Figure 3.22: 25% Span (a) and 75% Span (b) Distribution of Mach Number for Mesh #1.

geometry, and a consequent increase in velocity and decrease in pressure. The static temperature reaches a minimum at the throat of the passage, where the velocity is at its maximum. With a subsequent compression and temperature increase, the trailing edge and thus the vane wake are reached. The typical dovetail wake originates from the trailing edge itself, with one part ending up on the suction side of the subsequent vane and the other moving towards the main flow outlet.

Figure 3.24 presents the total pressure field that developed. It is noted to be homogeneous with the flow's inlet value. Following the flow, however, a decrease in total pressure

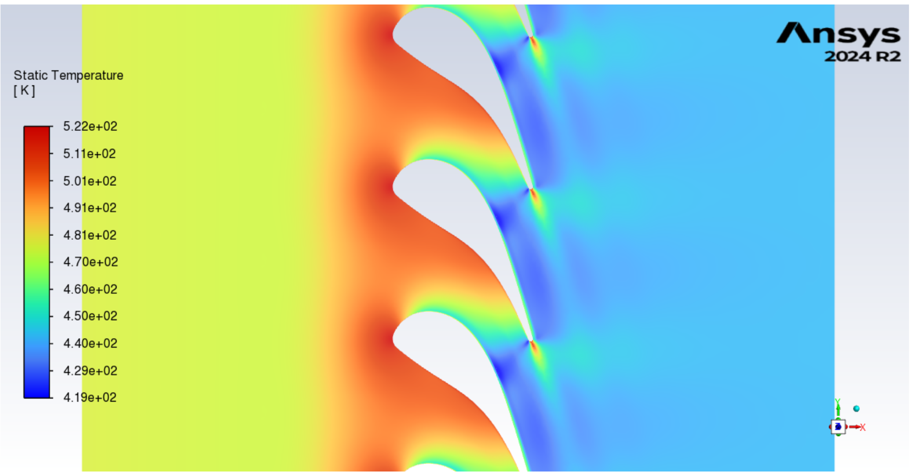

Figure 3.23: Midspan Distribution of Static Temperature for Mesh #1.

Figure 3.24: Midspan Distribution of Total Pressure for Mesh #1.

is recorded in correspondence with the vane's wake. This field gives us the valuable indication that there is no viscous discontinuity, and that all the loss generation develops downstream of the airfoil's trailing edge.

Mesh #2

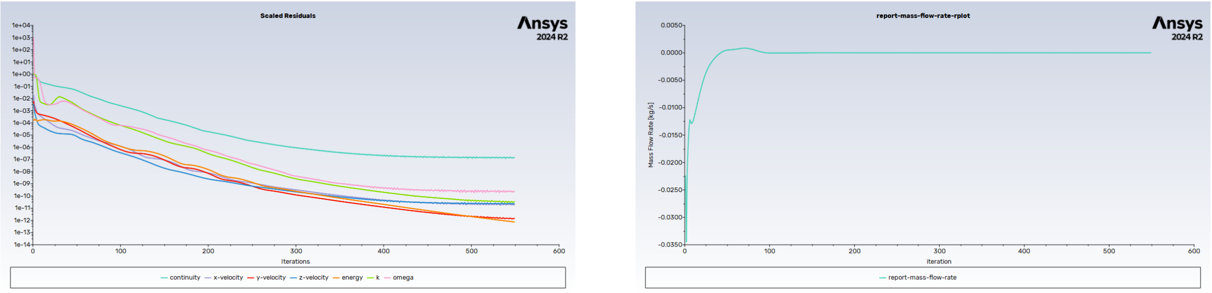

(a) (b)

Figure 3.25: Residuals (a) and Delta Mass Flow Rate (b) used for Convergence Evaluation in Mesh#2 Calculation.

Figure 3.25 presents the diagrams showing the numerical convergence of the simulation. The residuals are constant at very low values as the calculation iterations vary. The numerical convergence expressed by the residuals' trend is confirmed by the plateau created in the diagram that shows the trend of the difference between the inlet and outlet mass flow rate of the domain.

Figures 3.26 and 3.27 present the Mach number contours at midspan and at 25% and 75%

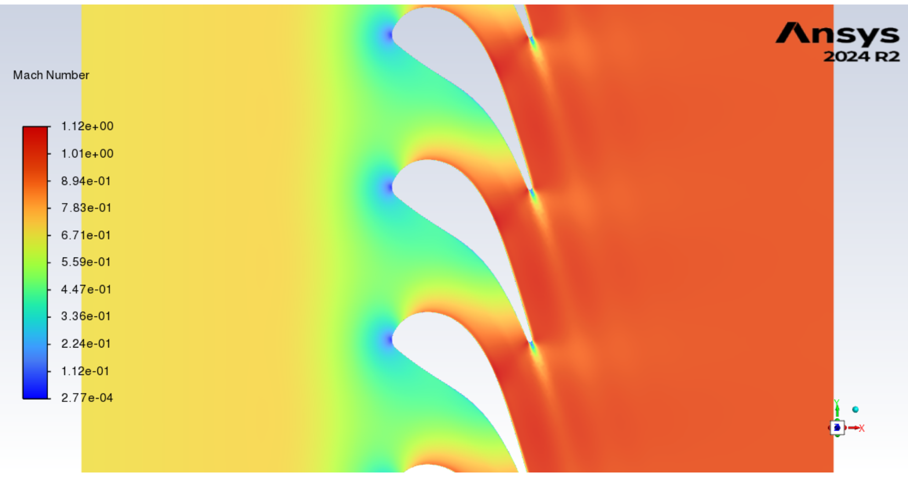

Figure 3.26: Midspan Distribution of Mach Number for Mesh #1.

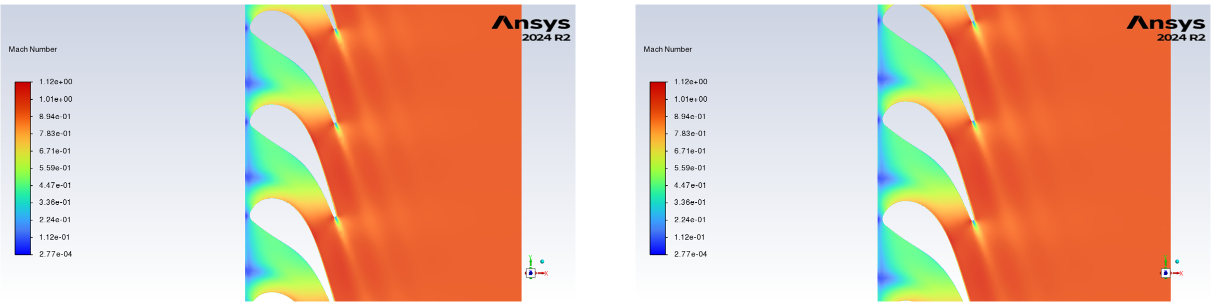

(a) (b)

Figure 3.27: 25% Span (a) and 75% Span (b) Distribution of Mach Number for Mesh #2.

of the vane span, calculated at the trailing edge. It is noted that the Mach number tends to decrease as it approaches the divergence zone of the main duct due to a sudden decrease in the calculated velocity. After passing the leading edge and entering the passage between consecutive vanes, the fluid accelerates and reaches its maximum at the throat of the converging-diverging duct. After leaving the passage, it tends to remain constant until the outlet. In this distribution, it is also possible to notice the wake originating from the vane, which locally decreases the flow's velocity. In Figure 3.27, it is noted that the trends recorded at midspan maintain their characteristics even in the vicinity of the wall. Unlike the results originating from the previous mesh, the differences have become weaker and are invisible to this comparison method.

Figure 3.28 shows the temperature distribution at midspan for Mesh #2. Here, too, the temperature variation induced by the geometry change of the duct first, and then of the passage between the vanes, is noted. The temperature reached by the outlet flow is very similar to the value calculated for the previous case and has already been considered in the dedicated subsection.

Figure 3.29 shows the total pressure distribution. It remains constant throughout the domain, highlighting the absence of any sonic shocks even with a higher level of discretization. The wake is also highlighted here by a total pressure loss that is very clear immediately downstream of the vane and then diffuses into the downstream flow.

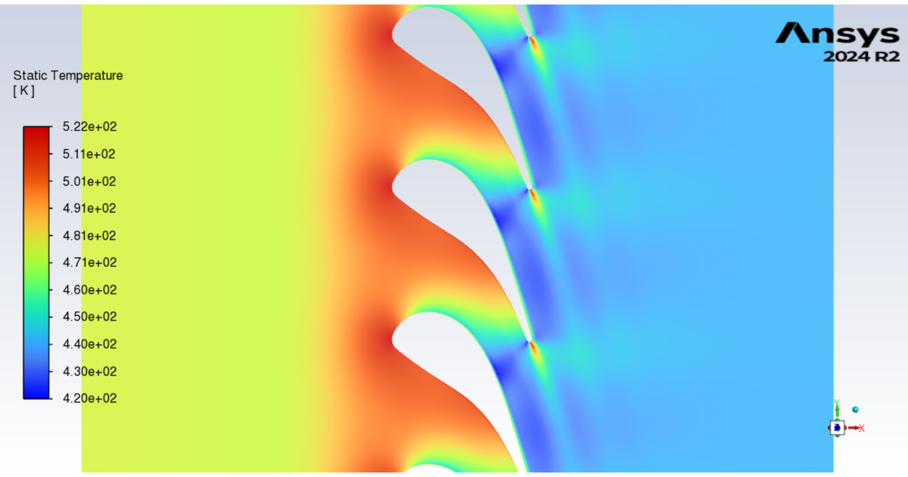

Figure 3.28: Midspan Distribution of Static Temperature for Mesh #2.

Figure 3.29: Midspan Distribution of Total Pressure for Mesh #2.

Mesh #3

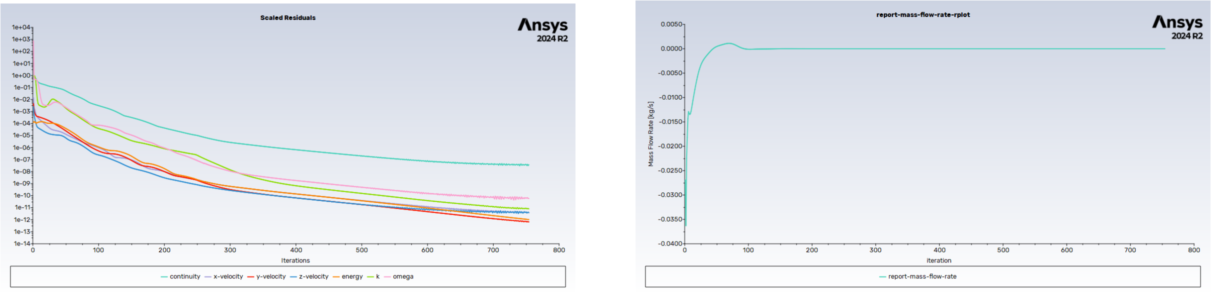

(a) (b)

Figure 3.30: Residuals (a) and Delta Mass Flow Rate (b) used for Convergence Evaluation in Mesh #3 Calculation.

Figure 3.30 presents the diagrams regarding the numerical convergence of the solution calculated on the denser Mesh #3. Looking at the residual trends, convergence was reached more slowly, which proves the higher discretization of the domain. The convergence on the mass flow rate, however, was achieved more quickly and reached values very close to zero compared to the previous cases.

Figures 3.31 and 3.32 show the Mach number distributions at midspan and in the two

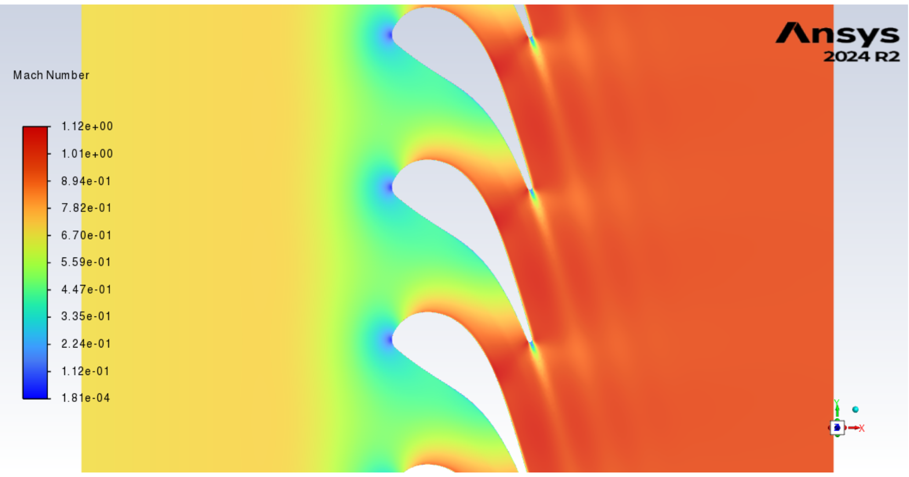

Figure 3.31: Midspan Distribution of Mach Number for Mesh #3.

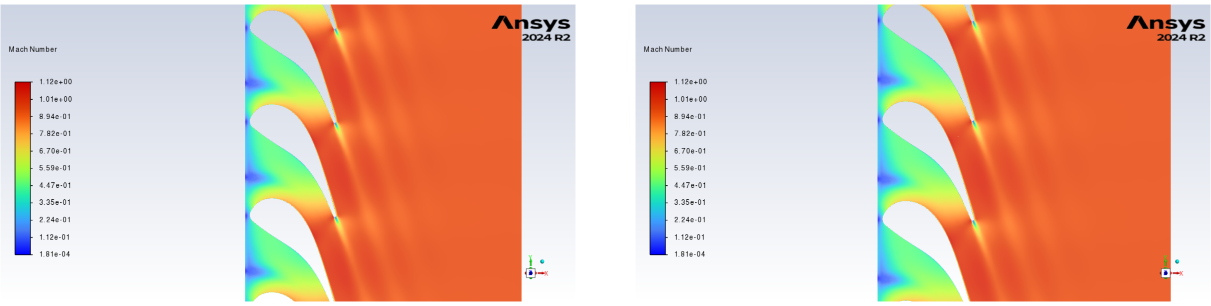

(a)

(b)

Figure 3.32: 25% Span (a) and 75% Span (b) Distribution of Mach Number for Mesh #3.

additional sections previously analyzed. The contour calculated at midspan shows the previously highlighted characteristics: a slowdown due to the main duct's geometry, a stagnation zone near the vane's leading edge, an increase in velocity in the converging-diverging passage, and a local deceleration caused by the wake that developed from the airfoil's trailing edge. Figure 3.32 shows a comparison of the distribution at 25% and 75% of the span measured at the trailing edge. The two distributions show numerous similarities, including in the wake section and the subsequent diffusion into the downstream flow.

Figure 3.33 presents the static temperature distribution for the simulation performed

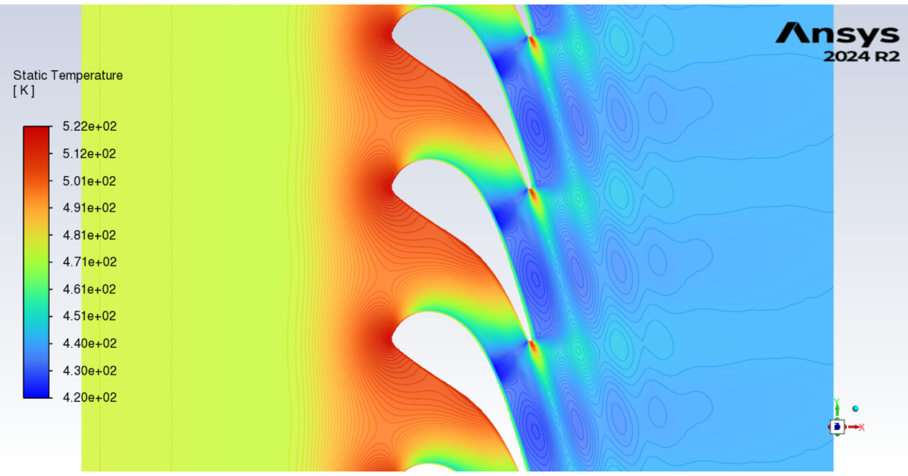

Figure 3.33: Midspan Distribution of Static Temperature for Mesh #3.

with Mesh #3. As a counterpoint to the previously seen velocity distribution, an increase in temperature due to the duct geometry and the proximity to the flow's stagnation point is also highlighted here, followed by a decrease in the inter-vane passage and a subsequent increase downstream of the airfoil wake.

Figure 3.34 shows the total pressure contour calculated at midspan. A homogeneous color corresponding to the total pressure value imposed at the inlet is noted, indicating the absence of any energy-dissipative structures. The only variation occurs in the airfoil's wake zone where, due to the no-shear layer that forms between the two flows, energy is dissipated and the total pressure drops. The wake, which is very clear immediately downstream of the vane, tends to dissipate into the body's downstream flow.

Figure 3.34: Midspan Distribution of Total Pressure for Mesh #3.

Vane Wall Static Pressure Distribution

This section reports the static pressure distributions calculated on the vane wall at midspan and in the two additional sections. The following graphs are formed from interpolated discrete data. The pressure values calculated in the two auxiliary sections are compared to verify the field's symmetry.

Figures 3.35, 3.36, and 3.37 show the static pressure distributions on the vane wall in the central section and the two auxiliary ones. A recirculation bubble is noted to develop on the upper wall of the vane in the section downstream of the maximum thickness. This phenomenon may be the result of the dovetail wake that develops at the trailing edge and is seen in the Mach number contours. This field inhomogeneity, however, does not lead to a flow separation, and the flow on the suction side manages to rejoin the flow from the pressure side. As for the sections symmetrical to the midspan, a certain agreement in values is noted, which confirms the field's symmetry. The section, having a different definition from that of the channel, presents some discrepancies from the midspan distribution: the recirculation zone and the pressure at the stagnation point are less relevant, indicating the presence of a nearby wall that causes the average velocity to decrease. In the trailing edge zone, however, the three curves almost completely overlap: the chosen section, where it intersects the vane's final part, deviates significantly from the wall, thus

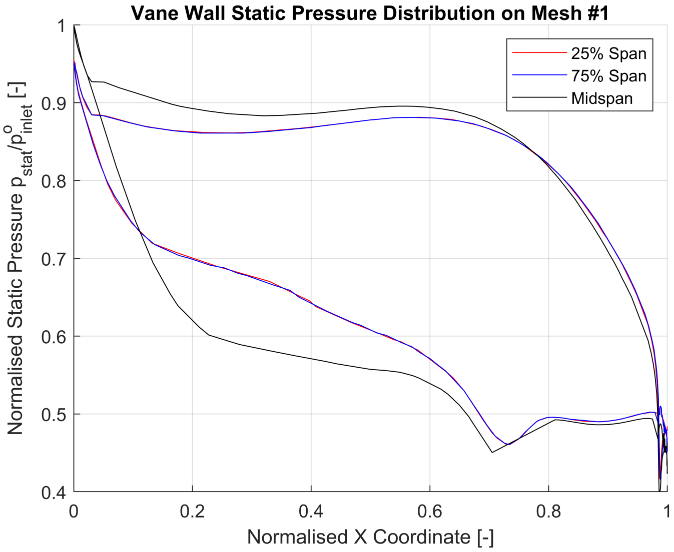

Figure 3.35: Mesh #1: Static Pressure Distribution at Midspan, 25% Span and 75% Span.

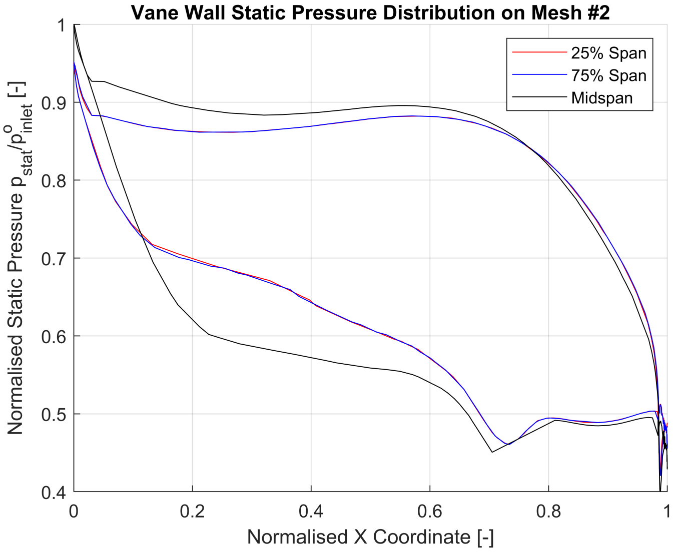

Figure 3.36: Mesh #2: Static Pressure Distribution at Midspan, 25% Span and 75% Span.

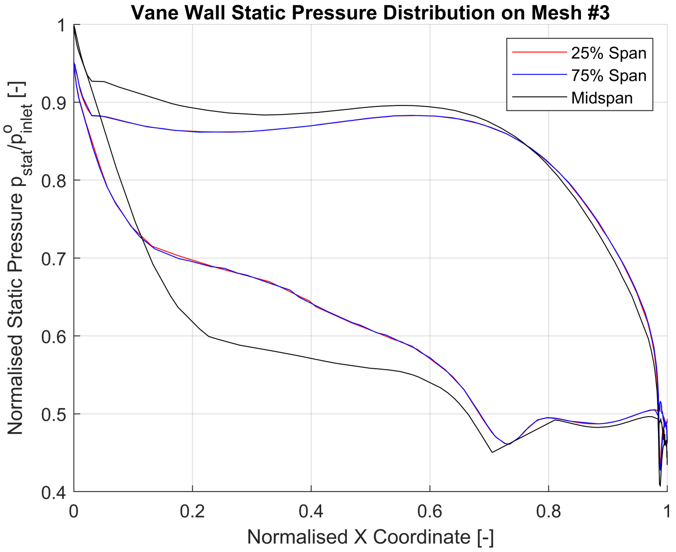

Figure 3.37: Mesh #3: Static Pressure Distribution at Midspan, 25% Span and 75% Span.

approaching midspan conditions. Figures 3.38 and 3.39 present a comparison of the pressure distributions on the vane for the same analyzed section. The difference between

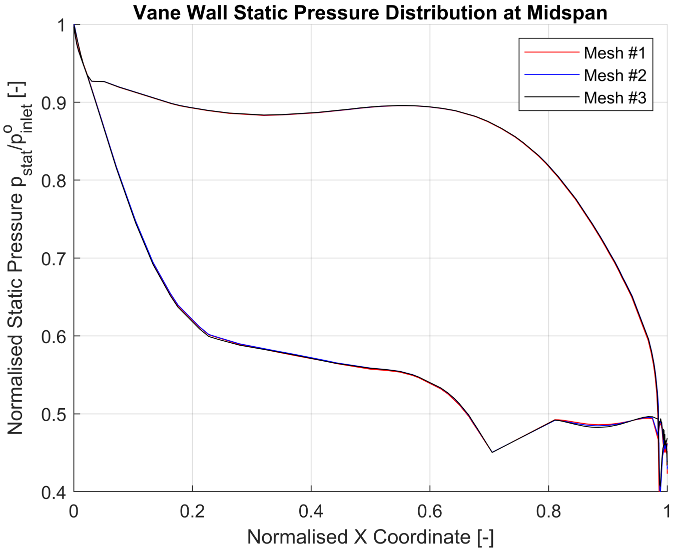

Figure 3.38: Static Pressure on Vane Midspan for Mesh #1, Mesh #2 and Mesh #3.

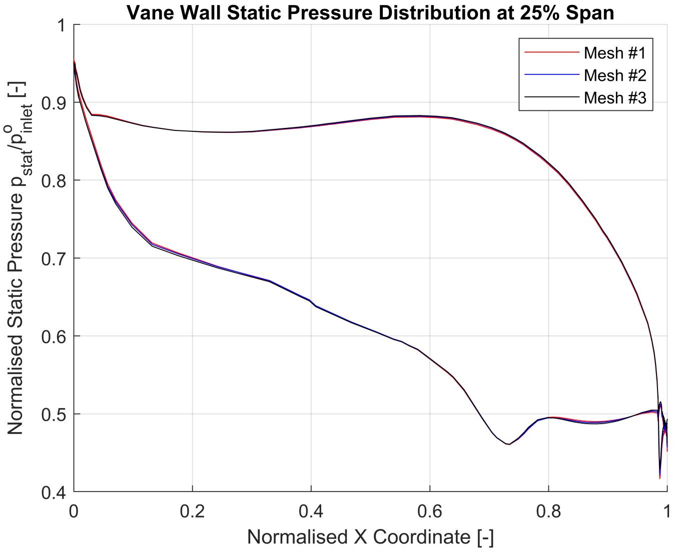

Figure 3.39: Static Pressure on Vane 25% Span for Mesh #1, Mesh #2 and Mesh #3.

the simulations performed with the meshes is minimal and decreases further with the increase in the calculation domain's discretization.

Vane Wall Static Temperature Distribution

This section reports the static temperature distributions calculated on the vane wall at midspan and in the two additional sections.

Figures 3.40, 3.41, and 3.42 show the static temperature distributions on the vane wall in the central section and the two auxiliary ones. The trend reflects the corresponding graph showing pressure but scaled for much smaller intervals. The asymmetry is more marked for this thermal variable but decreases as the discretization increases, indicating the error's dependence on the computational grid.

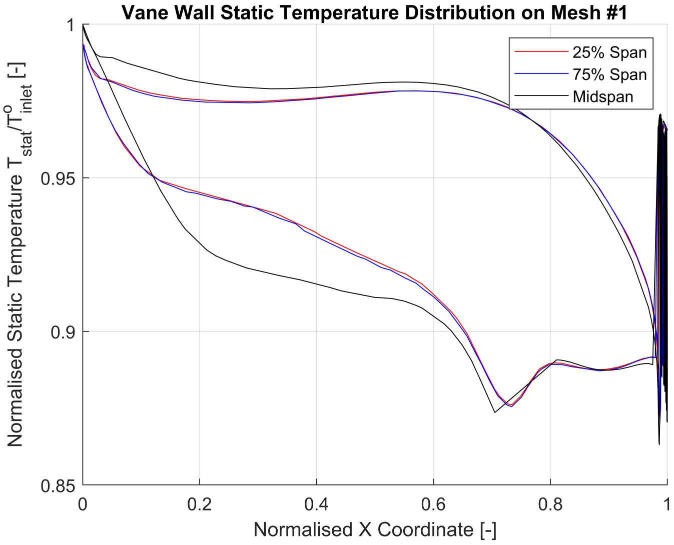

Figure 3.40: Mesh #1: Static Temperature Distribution at Midspan, 25% Span and 75% Span.

Figures 3.43 and 3.44 present a comparison of the temperature distributions on the vane for the same analyzed section. The error found on the right side of the graph is attributable to the temperature oscillations that develop at the airfoil's trailing edge.

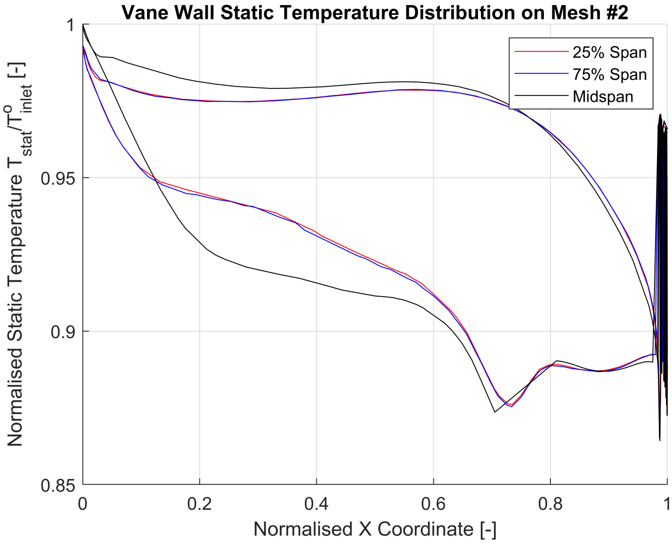

Figure 3.41: Mesh #2: Static Temperature Distribution at Midspan, 25% Span and 75% Span.

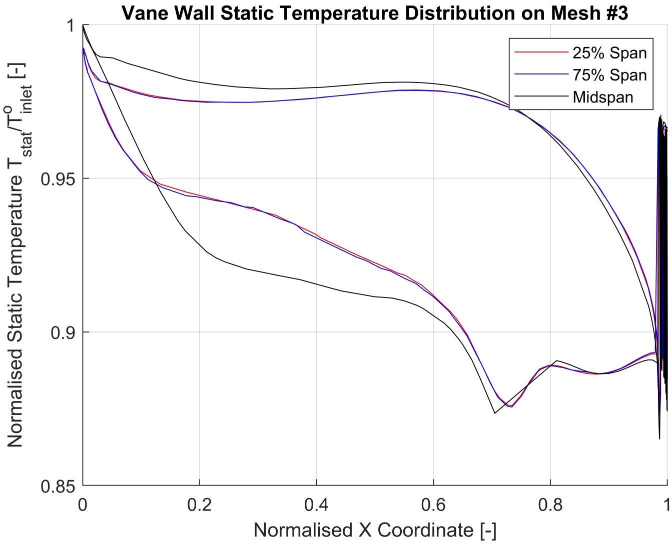

Figure 3.42: Mesh #3: Static Temperature Distribution at Midspan, 25% Span and 75% Span.

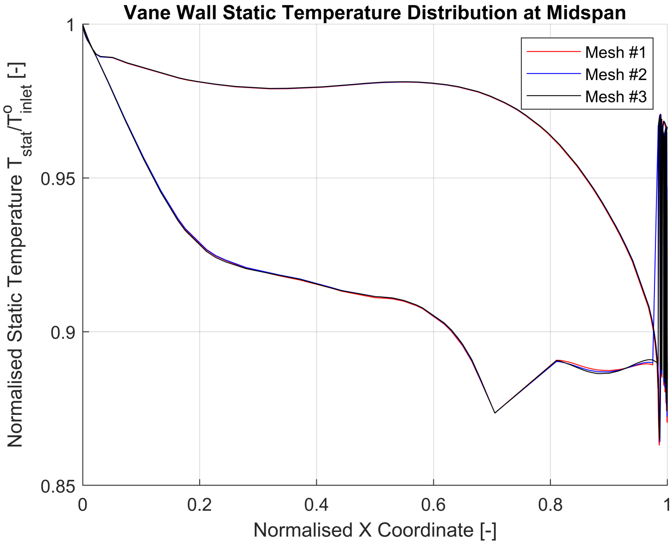

Figure 3.43: Static Temperature on Vane Midspan for Mesh #1, Mesh #2 and Mesh #3.

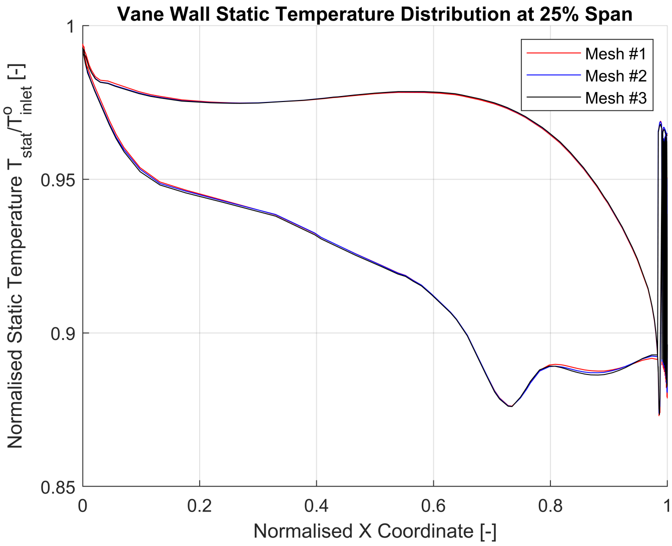

Figure 3.44: Static Temperature on Vane 25% Span for Mesh #1, Mesh #2 and Mesh #3.

4 Steady Simulations

This section details the steady-state simulations performed using the Ansys Fluent 2023 R2 suite. The Reynolds-Averaged Navier-Stokes (RANS) equations were employed, specifically adopting the $k-\omega$ SST (Shear Stress Transport) turbulence model by Menter and the $\gamma-Re_\theta$ transition model. The simulation approach is schematically represented in Figure 4.1. Starting from three distinct vane designs, the meshing parameters determined by the preceding mesh sensitivity analysis were applied to generate three separate computational meshes. For the non-cooled vane design, only the two-equation turbulence model ($k-\omega$ SST) was utilized. Conversely, to achieve more reliable results within the cooling passages, the subsequent two designs were simulated sequentially using both the two-equation turbulence model and the four-equation transition model ($\gamma-Re_\theta$ coupled with $k-\omega$ SST). The latter, more comprehensive model was omitted for the non-cooled design due to the lesser importance of accurate near-wall heat transfer resolution on the external vane surface compared to that occurring within the internal cooling channels. The results obtained with the more accurate transition model will be compared against those from the simpler two-equation model to quantify the impact of transition modeling.

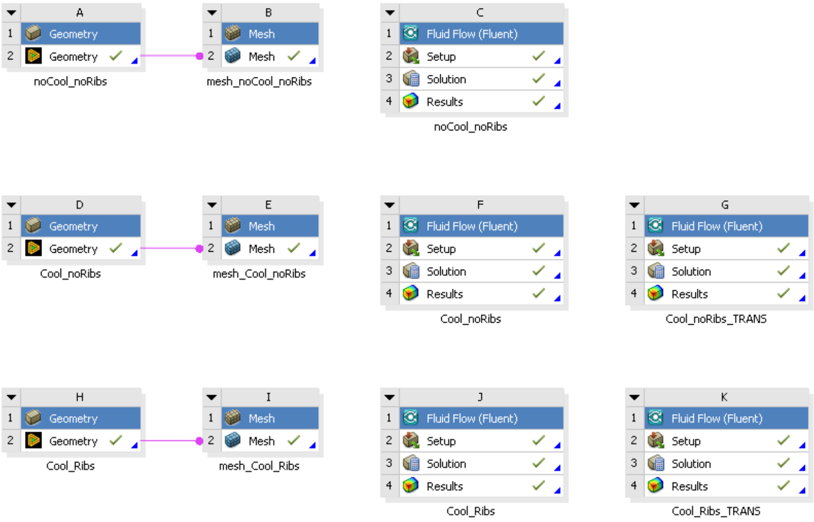

Figure 4.1: Schematic of the Steady RANS Simulations Set.

4.1 Computational Domain

Figures 4.2, 4.3, and 4.4 illustrate the computational domains employed for the steady-state simulations. The solid domain was developed starting from the main flow domain. The unprofiled surface was initially filled to create the solid vane geometry to be analyzed. The endwalls (hub and shroud) were generated by extruding the main-flow domain's outlet boundary by a thickness of $t = 5$ mm in the outward direction, creating the hub at negative Z coordinate and the shroud at positive Z coordinate, respectively.

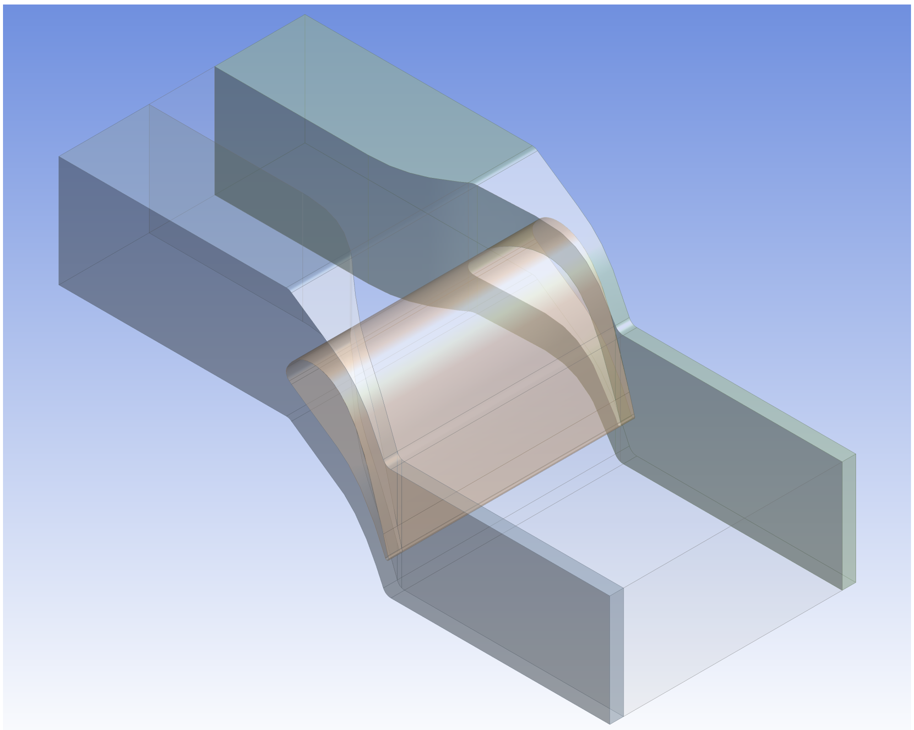

Figure 4.2: Isometric View of the Domain used for Non-Cooled Vane Steady RANS Simulation.

The internal cooling channels were defined based on the vane's aerodynamic chord, the line connecting the leading edge to the trailing edge. Internal thicknesses of $t_{in} = 2.5$ mm were maintained for both the external wall and the inter-channel walls, consistent with proportions found in literature. Three cooling channels were designed, each with varying aspect ratios and hydraulic diameters:

- the first channel, located nearest to the leading edge, has a rectangular cross-

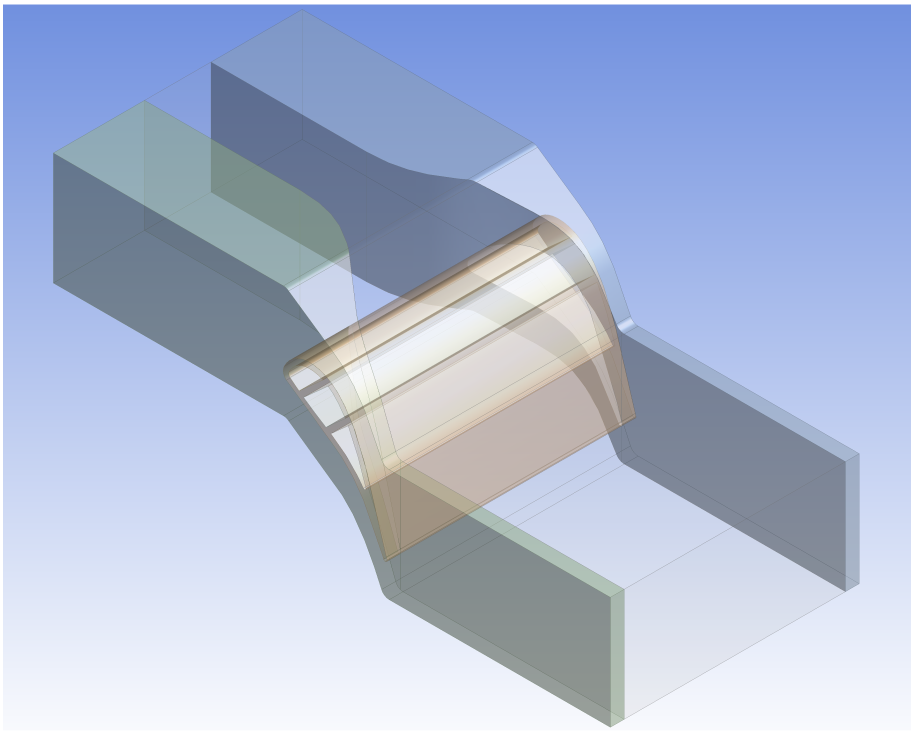

Figure 4.3: Isometric View of the Domain used for Smooth Channel Cooled Vane Steady RANS Simulation.

section where the dimension parallel to the chord L is approximately half the dimension perpendicular to it H. It is therefore characterized by an aspect ratio $\frac{L}{H} = \frac{1}{2}$ and a hydraulic diameter $D_{\text{hyd}} = 7.372$ mm;

- the second, central channel features an aspect ratio $\frac{L}{H} = 1$ and a hydraulic diameter $D_{\text{hyd}} = 10.213$ mm, making it the largest of the three;
- the third channel, situated near the vane's trailing edge, has an aspect ratio $\frac{L}{H} = 2$ and a hydraulic diameter $D_{\text{hyd}} = 6.640$ mm.

The turbulators (ribs) selected for the third design analyzed were based on literature data: a pitch-to-height ratio $\frac{P}{e} = 10$, where P is the distance between two consecutive ribs and e is their height, and an ratio $\frac{e}{D_{\text{hyd}}} = 6\%$, representing the ratio of rib height to the hydraulic diameter. This latter parameter, often considered a measure of the average surface roughness within the channels, will be used to calculate the friction factor c_f via the Moody diagram for comparison with the results obtained from the CFD analysis.

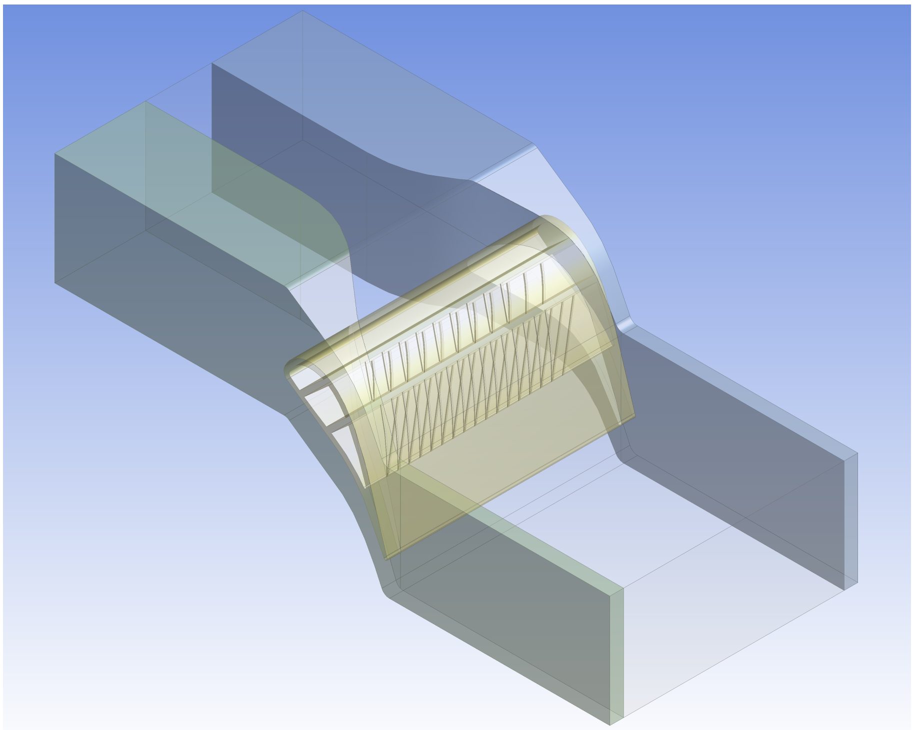

Figure 4.4: Isometric View of the Domain used for Ribbed Channel Cooled Vane Steady RANS Simulation.

4.2 Mesh Analysis

Table 8 presents the parameters used for the external flow (main flow) meshing. These values originate from the mesh sensitivity analysis and consequently produce a mesh with quality and characteristics consistent with those discussed in the preceding section. Table 9 shows the meshing parameters for the cooling fluid flowing in the internal channels. The average element size mirrors that maintained for the external flow mesh, while the local refinement in high-curvature areas retains the parameters used for the solid domain in the respective regions. Of particular note is the refinement near the turbulators: obtaining a well-resolved boundary layer that conforms to the minute geometry of the installed features is of paramount importance for accurately capturing the heat transfer enhancement. To achieve this, an inflation layer optimized for boundary layers generated by higher average velocities, yet with smaller characteristic surface structure dimensions, was employed. To mitigate potential resolution issues, a very stringent surface refinement was applied in the affected regions.

	Main Flow
Method	Tetrahedrons
Element Size [mm]	2
Refinement Size [mm]	1
Leading Edge Surface Element Size [mm]	0.375
Trailing Edge Surface Element Size [mm]	0.150
Suction & Pressure Surface Element Size [mm]	0.700
Inflation Parameters	First Layer Thickness: 0.843 μm Number of Layers: 25 Growth Rate: 1.26

Table 8: Main Flow Mesh Parameters for Steady RANS Simulations.

Table 10 reports the meshing parameters for the solid domains, specifically the hub and shroud (collectively referred to as endwalls) and the vane. When ribs are present, the average solid vane element size is reduced to $l_c = 1$ mm to achieve better resolution of the turbulators within the solid region as well. The generally larger element size in the solid

	Cooling Fluid
Method	Tetrahedrons
Element Size [mm]	1
Leading Edge Surface Element Size [mm]	0.375
Trailing Edge Surface Element Size [mm]	0.150
Suction & Pressure Surface Element Size [mm]	0.700
Rib Turbolators Interface Element Size [mm]	0.250
Inflation Parameters	First Layer Thickness: 0.843 μm Number of Layers: 25 Growth Rate: 1.225

Table 9: Cooling Fluid Channels Mesh Parameters for Steady RANS Simulations.

domain is justified by the governing equation: Fourier's law of heat conduction dictates a relatively smooth temperature gradient that is adequately resolved even with a coarser mesh. At the fluid-solid interface, a surface refinement of equal magnitude was prescribed to ensure comparable solution definition in the inter-domain zones for accurate conjugate heat transfer coupling.

	Solid Vane & Endwalls
Method	Automatic
Element Size [mm]	5
Vane Size Refinement [mm]	0.5
Leading Edge Surface Element Size [mm]	0.375
Trailing Edge Surface Element Size [mm]	0.150
Suction & Pressure Surface Element Size [mm]	0.700
Rib Turbolators Interface Element Size [mm]	0.250

Table 10: Solid Domains Mesh Parameters for Steady RANS Simulations.

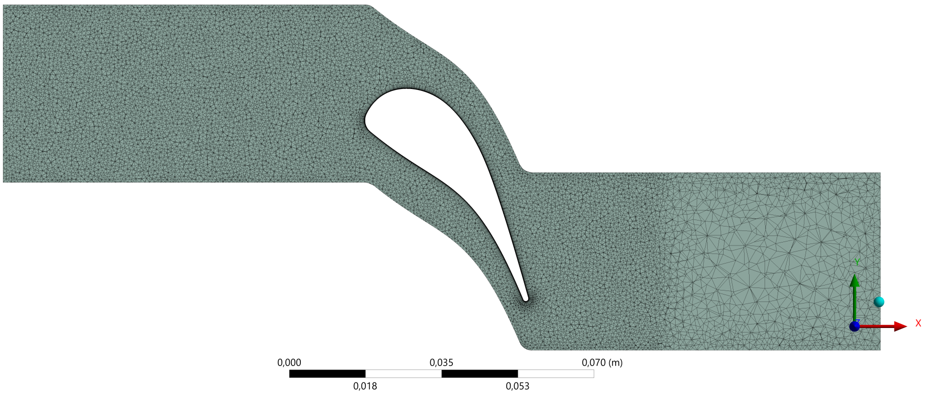

Figure 4.5: Midspan Section of the Mesh Used for Main Flow Steady RANS Simulation: Top View.

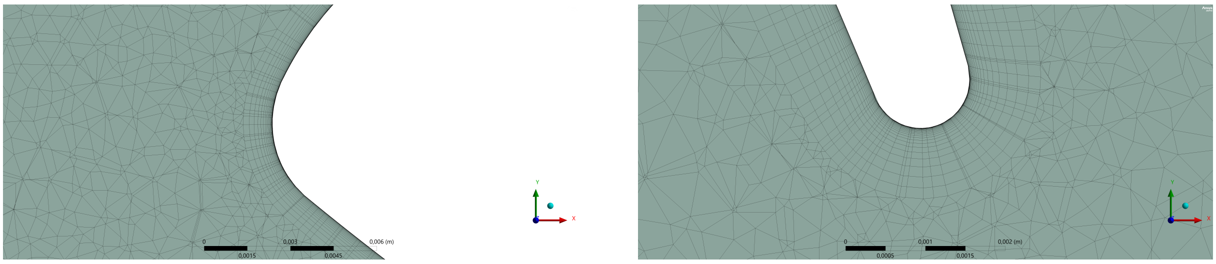

(a)

(b)

Figure 4.6: Midspan Section of the Mesh Used for Main Flow Steady RANS Simulation: Leading Edge (a) and Trailing Edge (b) Detailed View.

Figures 4.5, 4.6, and 4.7 provide an overview of the mesh utilized for the main flow domain. The midspan view highlights the zones of greatest refinement and the outlet area, which is deliberately coarser to promote numerical stability through controlled artificial viscosity. Furthermore, the boundary layer refinement near the walls is evident. To manage the steep geometric gradients at the leading and trailing edges, magnified views illustrate the effectiveness of the imposed wall refinement. Finally, the effect of the wall inflation layer on both the vane and the endwalls is shown, particularly the method used to manage the corner region formed by the solid surfaces.

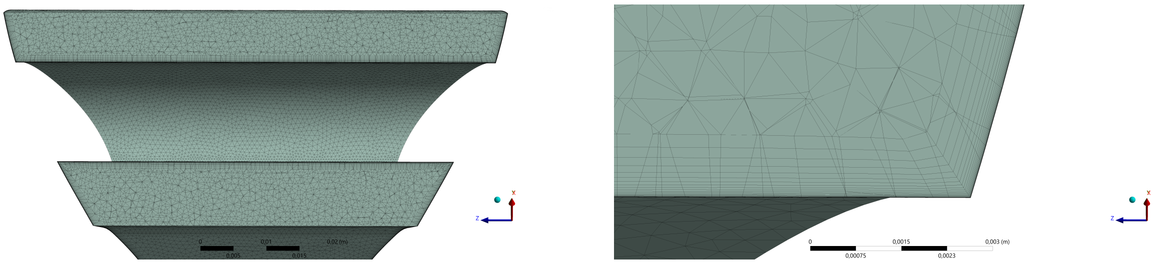

(a) (b)

Figure 4.7: Section of the Mesh Used for Main Flow Steady RANS Simulation: Vane and Endwalls Inflation Section (a) and Detailed View of the Corner Inflation (b).

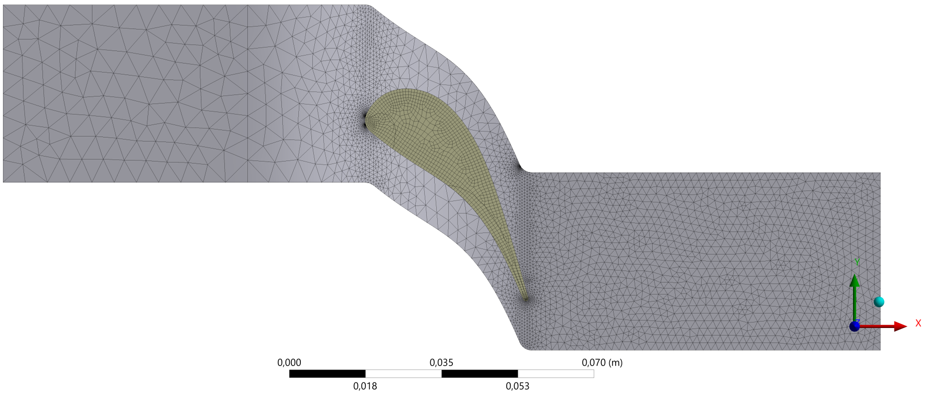

Figure 4.8: Midspan Section of the Mesh Used for Non-Cooled Vane Steady RANS Simulation: Top View.

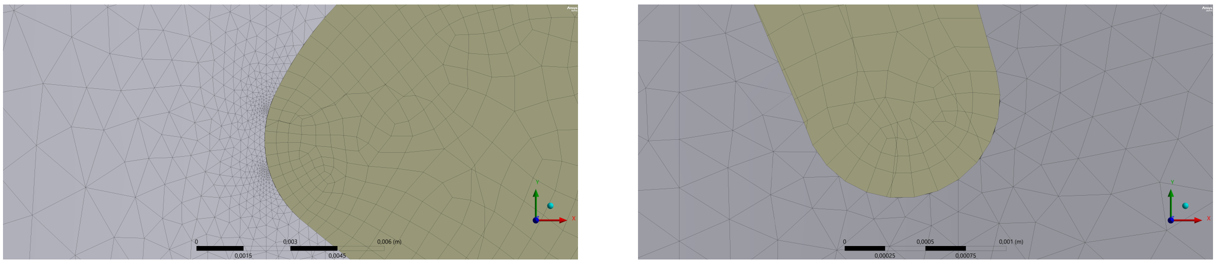

(a)

(b)

Figure 4.9: Midspan Section of the Mesh Used for Non-Cooled Vane Steady RANS Simulation: Leading Edge (a) and Trailing Edge (b) Detailed View.

Figures 4.8, 4.9, and 4.10 present the computational mesh used to discretize the solid domain for the non-cooled vane case. The absence of an inflation layer is noted, as no boundary layer analysis is required within this pure solid domain. Due to the absence of a mapped mesh between the two domains, the interface conditions will be interpolated across the surfaces of the two domains to account for the disparity in computational cells, which is standard practice in non-conformal mesh coupling.

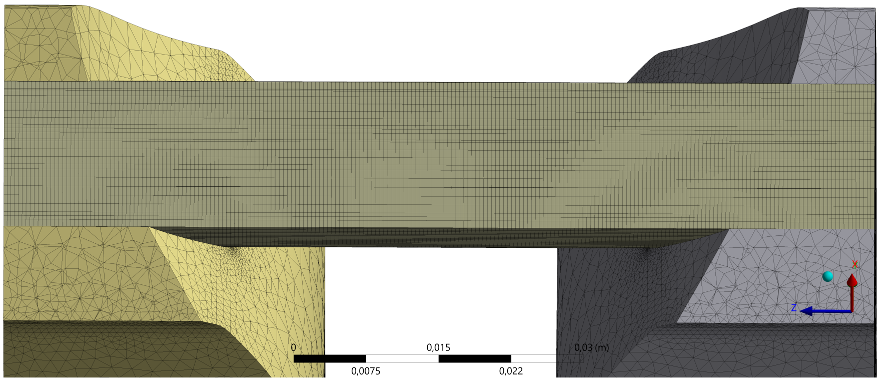

Figure 4.10: Channel Section of the Mesh Used for Non-Cooled Vane Steady RANS Simulation.

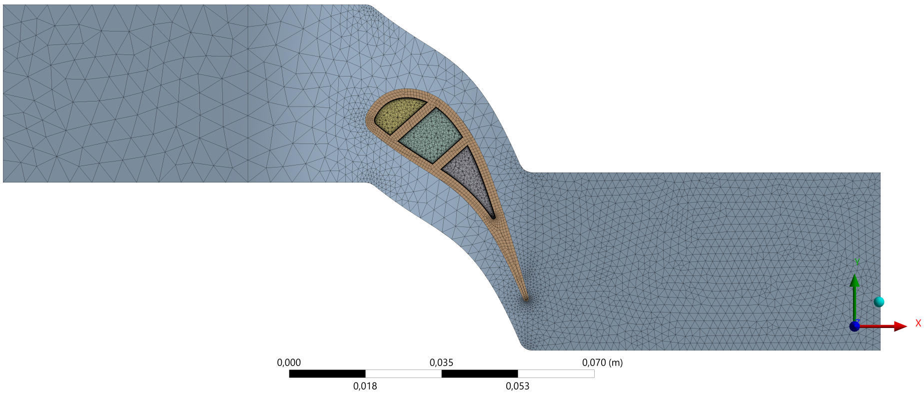

Figure 4.11: Midspan Section of the Mesh Used for Smooth Channel Cooled Vane Steady RANS Simulation: Top View.

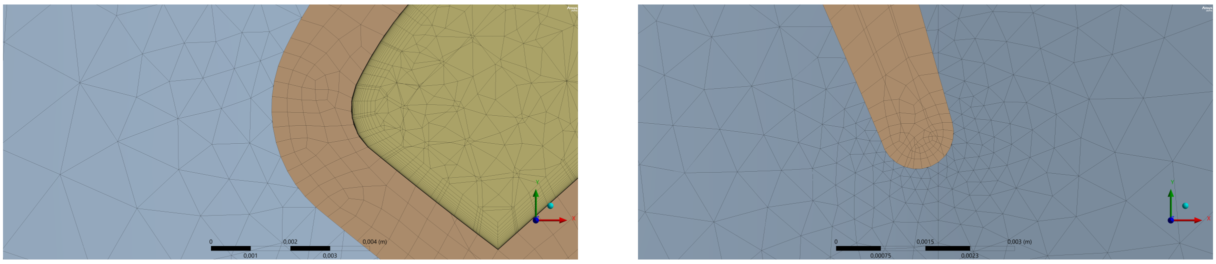

(a)

(b)

Figure 4.12: Midspan Section of the Mesh Used for Smooth Channel Cooled Vane Steady RANS Simulation: Leading Edge (a) and Trailing Edge (b) Detailed View.

Figures 4.11, 4.12, and 4.13 display the solid mesh for the smooth-channel cooled vane case. In contrast to the previously described non-cooled case, the inflation layer created to resolve the boundary layer developing within the cooling channels is now included. The velocity distribution near the wall will be further analyzed post-processing through vector visualization to assess the accuracy of the near-wall flow field.

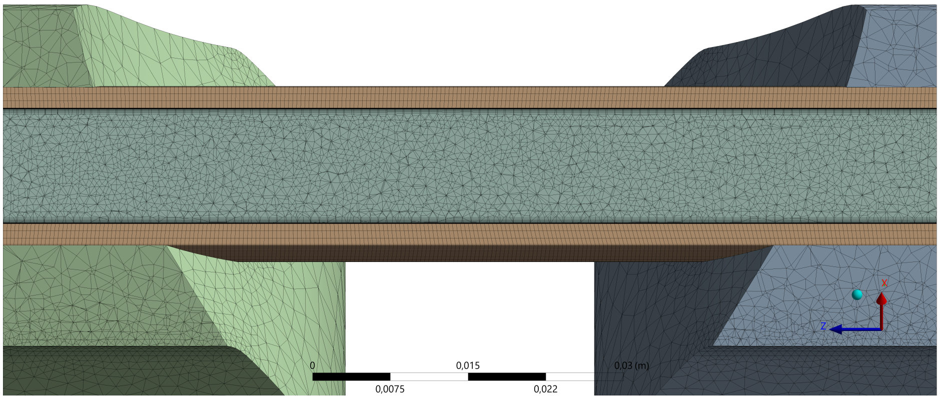

Figure 4.13: Channel Section of the Mesh Used for Smooth Channel Cooled Vane Steady RANS Simulation.

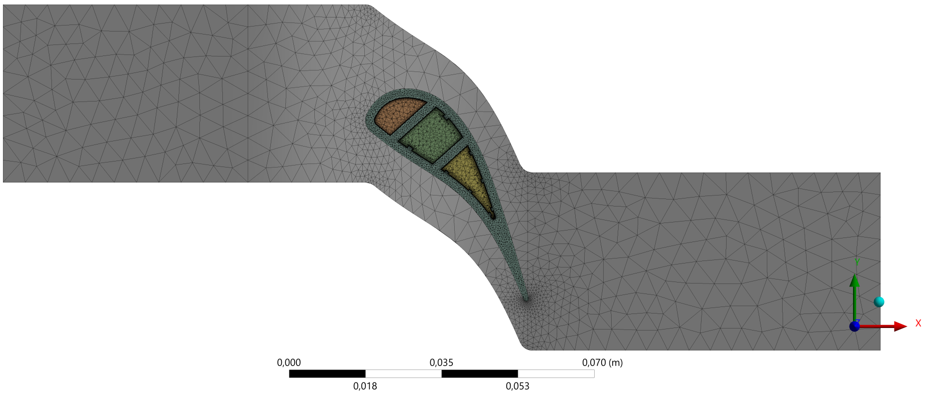

Figure 4.14: Midspan Section of the Mesh Used for Ribbed Channel Cooled Vane Steady RANS Simulation: Top View.

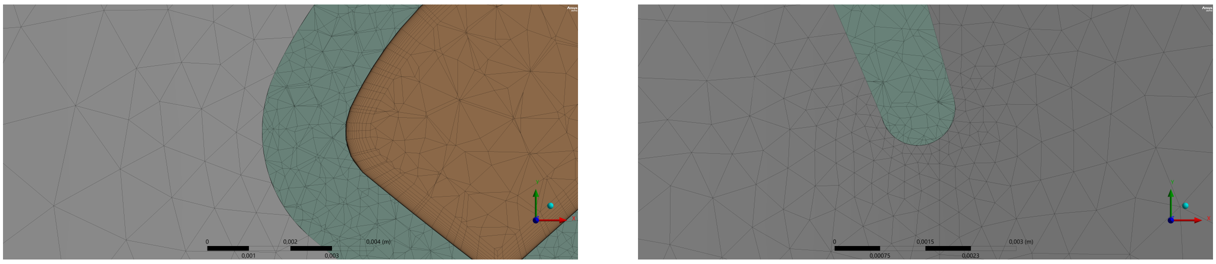

(a)

(b)

Figure 4.15: Midspan Section of the Mesh Used for Ribbed Channel Cooled Vane Steady RANS Simulation: Leading Edge (a) and Trailing Edge (b) Detailed View.

Figures 4.14, 4.15, and 4.16 present the computational grid used for the study of the ribbed-channel cooled case. In this scenario, it is critical to observe that the solid vane is more finely discretized to avoid generating excessive cell size gradients at the fluid-cooling interface, which is particularly sensitive due to the heat transfer enhancement provided by the ribs. A magnified view of the zone straddling two ribs is provided, clearly showing the mesh stretching imposed by the inflation layer, which is mitigated by the wall refinement. The inflation layer parameters will be a posteriori validated to ensure that the heat transfer driven by the near-wall temperature gradient is sufficiently resolved,

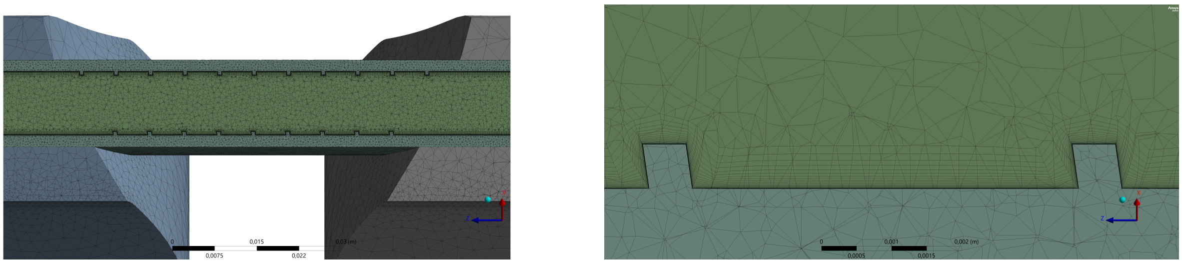

(a) (b)

Figure 4.16: Channel Section (a) and Rib Turbolators Detailed View (b) of the Mesh Used for Smooth Channel Cooled Vane Steady RANS Simulation.

typically by checking the y^+ value of the first cell center.

4.3 Boundary Conditions and Setup

This section focuses on the boundary conditions applied to the computational domain. The type and value of the imposed conditions are summarized in Table 11.

	Main Inlet	**Main Outlet**	**Coolant Inlet**	**Coolant Outlet**
Total Pressure [Pa]	193011	-	107570	-
Total Temperature [K]	521.33	-	303.15	-
Gauge Pressure [Pa]	-	101325	-	106390
Backflow Temperature [K]	-	440	-	298.15
Periodicity		Superior	Inferior	
No Slip		Vane	Endwalls	
Slip				
Adiabaticity		Vane	Endwalls	

Table 11: Boundary Conditions Used in Steady RANS Simulations.

The average values of the oscillations resulting from the use of a rotating detonation combustor(RDC) are still employed: the profile, presented in the section dedicated to unsteady simulations, shows non-zero arithmetic means for total pressure and temperature, which are imposed here as constant conditions. However, the flow inlet angle, which is imposed here as normal to the main flow inlet surface, will vary with the same frequency as the other signals in the unsteady case. Imposing a zero angle of attack for the flow allows the simulation to closely approach the case used for the mesh sensitivity analysis without significantly deviating from the unsteady case, for which this set of simulations serves as a benchmark. The final results will, in fact, be compared with the current ones to evaluate the influence of oscillations on blade cooling. The conditions imposed on the coolant flow, however, follow conditions well established in literature:

- Total inlet pressure is set to 105% of the static pressure at the vane outlet, which will allow for the future application of film cooling by mitigating the risk of backflow in the cooling holes located on the vane wall.
- The pressure ratio is set to enforce a total cooling mass flow rate of approximately 5% of the mass flow generated by the main flow, $\dot{m}_{cool,tot} = 5\%\ \dot{m}_{main}$. This condition is proven in literature to be optimal for utilizing a compressor bleed-air system without a marked loss in efficiency.

The wall boundary conditions follow what has been previously mentioned: when dealing with a blade cascade, it is inevitable to impose a periodicity condition on the upper and lower domain walls, and a no-slip condition for the walls acting as interfaces between the solid and fluid domains. The thermal wall conditions reflect the goal of performing a coupled heat transfer study, and adiabaticity is imposed on the solid walls located at the extremes of the computational domain.

The solver setup is reported in Table 12. This is a density-based solver, which is best suited for studying fluid flows in the high-subsonic and transonic regimes, as in our case, without leading to numerical instabilities in low-velocity regions thanks to the low-Mach patches included in the Ansys software. The proposed solutions adopt a second-order accuracy, keeping in mind that to stabilize a simulation with a high order of accuracy, it is often better to first calculate a solution with a lower-order of accuracy. The chosen solver uses implicit equations, which are useful for the high convergence speed of the solution at the expense of greater memory consumption and a higher computational cost. The Courant number used for the final solution is $CFL = 5$.

Solver Type	Implicit Density-Based
Accuracy Order	2^{nd} Order
Initialization	Fluent Hybrid

Table 12: Solver Setup Used in Steady RANS Simulations.

The characteristics of the materials used by the solver are reported in Table 13. The fluid material, air, uses the same variable approximation formulas as in the mesh sensitivity study. The solid material, CMSX-4, is a nickel superalloy used by NASA for experimental

	Fluid	**Solid**
Name	Air	CMSX-4
Density ρ $[kg/m^3]$	Ideal Gas Law	8700
Heat Capacity C_p $[J/kg \cdot K]$	NASA 9-Piecewise Polynomial	500
Thermal Conductivity k $[W/m \cdot K]$	0.0242	7.8
Dynamic Viscosity μ $[Pa \cdot s]$	Sutherland Law	-
Molecular Weight $[kg/kmol]$	28.966	-

Table 13: Material Setup Used in Steady RANS Simulations.

testing on various rig configurations. The use of this material is notable for the experimental study of the internally cooled C3X transonic vane, which is often cited in the literature as an exemplary case study. The value of interest for the thermal study is the material's thermal conductivity, k, which, based on an a posteriori analysis, proves to be ideal for the case study of internal cooling with smooth channels. In fact, the Biot number, Bi, calculated here as the ratio of convective heat transfer to conductive heat transfer, $Bi = \frac{h_c}{k} \cdot l_c$, where h_c is the convective heat transfer coefficient, k is the conductive heat transfer coefficient, and l_c is a characteristic length, registers a value of approximately $Bi = 0.5$ for the aforementioned case, which is perfectly consistent with literature data.

4.4 Results

In the following section, the quantitative and qualitative results of the five simulations performed will be presented. The direct comparison of the pressure and temperature distributions will be carried out in the next section.

The result of the mean wall Biot number calculation is reported in Table 14. The Biot number, defined as $Bi = \frac{h_c}{k} \cdot l_c$, where h_c is the non-dimensional convective heat transfer coefficient at the wall, l_c is an a priori chosen characteristic length (in this case, the true chord of the profile was chosen), and k is the solid's thermal conductivity constant, represents the ratio between the effects of convective and conductive heat transfer. It is noted that for the intermediate design, the Biot number $Bi = 0.5$ reflects the value found in the literature. An increase in the Biot number observed in the third design is attributed to a lower average wall temperature, which, given the same external temperature distribution outside the boundary layer, leads to greater convective heat transfer. The first design, however, approaches the flow stagnation temperature, leading to a very small difference with the temperature distribution outside the boundary layer and low convective heat transfer.

Table 15 reports the measurements of thermo-fluid dynamic quantities of interest for the five simulations performed. Specifically, the mass-averaged values at the fluid domain outlet section for three fluid dynamic quantities were recorded: total pressure p^o_{out}, static temperature T_{out}, and Mach number M_{out}. For these quantities, minimal variations are noted, which are due to the slight change in temperature that the vane imparts to the surrounding fluid. The two thermal quantities investigated are the average static temperature on the interface surface between the solid vane and the external fluid, and the average static temperature over the volume of the vane itself. A greater difference between these two values is noted across the different designs and setups implemented in the study.

Vane Design	**Heat Transfer Coefficient h_c**	**Biot Number Bi**
Non-Cooled	0.136	0.001
Smooth Channel Cooling	78.077	0.56
Ribbed Channel Cooling	102.662	0.73

Table 14: Main Flow Biot Number.

Table 16 presents the variations of the quantities calculated above with respect to the non-cooled design. As previously noted, the variation in the three fluid dynamic quanti-

	Non-Cooled Vane	**Smooth Cooling Channel Vane** $k-\omega$ SST **Model**	**Smooth Cooling Channel Vane** $\gamma-Re_\theta$ **Model**	**Ribbed Cooling Channel Vane** $k-\omega$ SST **Model**	**Ribbed Cooling Channel Vane** $\gamma-Re_\theta$ **Model**
Average Outlet Total Pressure [Pa]	179704	179763	180989	179604	180871
Average Outlet Static Temperature [K]	444.361	443.770	443.077	443.724	443.046
Average Outlet Mach Number [-]	0.942	0.943	0.948	0.942	0.948
Average Static Wall Vane Temperature [K]	519.076	492.122	484.566	486.502	472.208
Average Volume Vane Temperature [K]	519.546	477.874	472.446	472.030	459.506

Table 15: Steady RANS Simulations Results: Main Flow Variables.

ties is very limited: the largest changes occur in the Mach number calculation, which is an index of the change in the local speed of sound induced by the temperature variation that the main flow undergoes from the cooled vane. The wall heat transfer quantities, however, vary much more significantly, reaching a maximum variation in the volume-averaged value of the static temperature: specifically, the ribbed channel cooled vane design solved with the transition model. This suggests that the transition model is the most suitable for studying the effect of cooling channels on heat transfer between the vane and the surrounding main flow.

Tables 17 and 18 present the values monitored for the thermo-fluid dynamic study of

	Smooth Cooling Channel Vane $k-\omega$ SST **Model**	**Smooth Cooling Channel Vane** $\gamma-Re_\theta$ **Model**	**Ribbed Cooling Channel Vane** $k-\omega$ SST **Model**	**Ribbed Cooling Channel Vane** $\gamma-Re_\theta$ **Model**
Average Outlet Total Pressure [Pa]	+0.033%	+0.710%	-0.056%	+0.645%
Average Outlet Static Temperature [K]	-0.133%	-0.290%	-0.144%	-0.297%
Average Outlet Mach Number [-]	+0.106%	+0.633%	±0%	+0.633%
Average Static Wall Vane Temperature [K]	-5.477%	-7.122%	-6.700%	-9.925%
Average Volume Vane Temperature [K]	-8.720%	-9.970%	-10.066%	-13.066%

Table 16: Steady RANS Simulations Results: Main Flow Variables Percentage Variations with respect to Non-Cooled Design.

the cooling channels. Specifically, the trends of static temperature $T_{out,avg}$, total pressure $p^o_{out,avg}$, and velocity magnitude $|v_{out,avg}|$ averaged over the outlet surface, and static temperature and velocity averaged over the fluid volume were studied. From these quantities, the mean Reynolds number calculated on the hydraulic diameter, $Re_{D_{hyd}}$, and the percentage pressure drop developed across the cooling channels were also calculated. Only the channels that were to undergo the installation of ribs were analyzed, namely the second and third channels located in the center and towards the trailing edge of the vane, respectively.

In the first table, which refers to the second and largest cooling channel, a decrease in outlet temperature is observed when switching from the two-equation model to the transition model. This suggests an underestimation of the heat transfer and, consequently, of the channel effectiveness when using only the Menter turbulence model. The average velocity calculated in the fluid and on the outlet surface decreases with the installation of the turbulators, which is a sign of a very high turbulence generation. This characteristic is also reflected in the smaller difference between the results obtained with and without the transition model in the case of ribs, which indicates the effective utilization of the latter. The Reynolds number, being greater than the critical value for circular ducts, indicates a turbulent flow which, however, does not undergo transition from the channel inlet, as demonstrated by the difference observed when using the transition model. Finally, the pressure drop, calculated on the total outlet pressure, indicates a greater hydraulic loss when turbulators are used, which was already expected due to the lower velocity at the channel outlet.

The table referring to the third cooling channel indicates its smaller size with a lower Reynolds number, $Re_{D_{hyd}}$. Furthermore, this variable suggests a greater difference between the transitional and fully turbulent models due to the greater distance between the channel inlet and the transition point.

	Smooth Cooling Channel Vane $k-\omega$ *SST* **Model**	**Smooth Cooling Channel Vane** $\gamma-Re_\theta$ **Model**	**Ribbed Cooling Channel Vane** $k-\omega$ *SST* **Model**	**Ribbed Cooling Channel Vane** $\gamma-Re_\theta$ **Model**
Average Outlet Static Temperature [K]	325.798	322.431	334.969	332.377
Average Volume Static Temperature [K]	317.108	315.314	323.948	321.621
Average Outlet Velocity [m/s]	38.116	38.650	30.424	30.400
Average Volume Velocity [m/s]	37.332	38.020	29.830	29.834
Reynolds Number $Re_{D_{hyd}}$	23000	23300	18300	18300
Average Outlet Total Pressure [Pa]	107295	107329	106959	106969
Total Pressure Drop [-]	-0.256%	-0.224%	-0.568%	-0.559%

Table 17: Steady RANS Simulations Results: 2^{nd} Cooling Channel Flow Variables.

	Smooth Cooling Channel Vane $k-\omega$ *SST* **Model**	**Smooth Cooling Channel Vane** $\gamma-Re_\theta$ **Model**	**Ribbed Cooling Channel Vane** $k-\omega$ *SST* **Model**	**Ribbed Cooling Channel Vane** $\gamma-Re_\theta$ **Model**
Average Outlet Static Temperature [K]	341.978	335.509	363.966	367.996
Average Volume Static Temperature [K]	327.563	324.329	347.194	343.189
Average Outlet Velocity [m/s]	35.660	36.365	25.431	24.709
Average Volume Velocity [m/s]	34.435	35.458	24.077	23.871
Reynolds Number $Re_{D_{hyd}}$	12600	12800	9000	8700
Average Outlet Total Pressure [Pa]	107178	107230	106826	106808
Total Pressure Drop [-]	-0.364%	-0.316%	-0.692%	-0.708%

Table 18: Steady RANS Simulations Results: 3^{rd} Cooling Channel Flow Variables.

Figures 4.17 and 4.18 show the clip planes used to study the internal flow in the channels. These planes were chosen to create sections perpendicular to the ribs and, therefore, to better verify their operation and effectiveness. Specifically, the first plane is positioned approximately halfway along the second channel, and the second plane is positioned approximately one-third of the way along the third channel. The plane normals were imposed parallel to the aerodynamic chord of the vane profile.

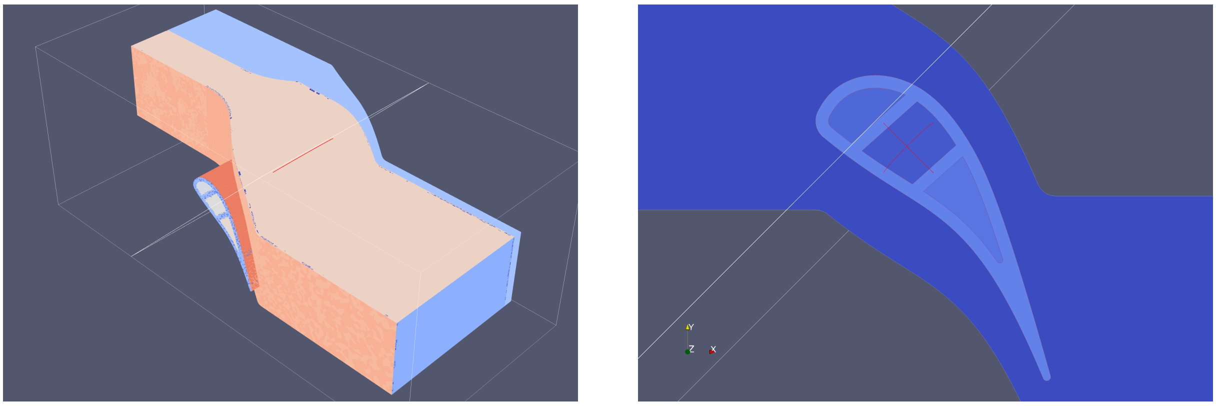

(a) (b)

Figure 4.17: Section Plane Used for 2^{nd} Cooling Channel Analysis: Isometric (a) and Top (b) View.

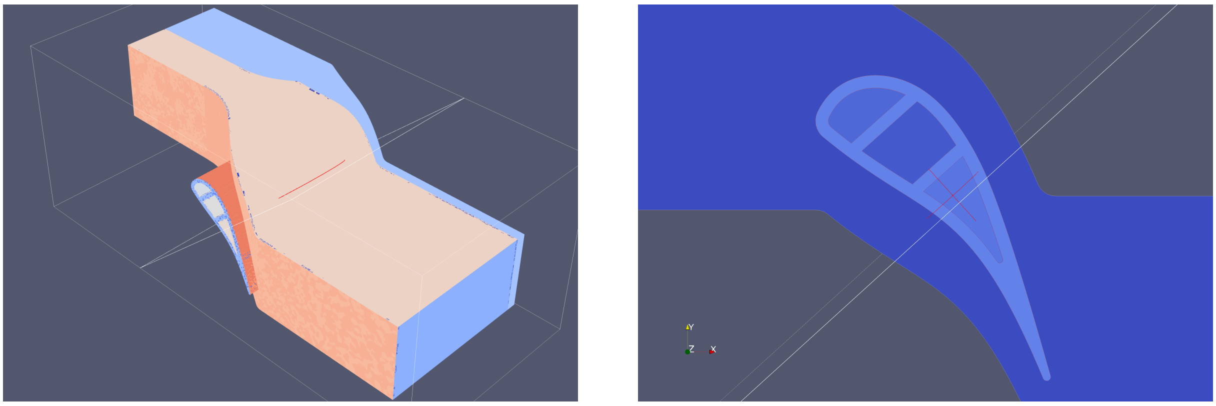

(a) (b)

Figure 4.18: Section Plane Used for 3^{rd} Cooling Channel Analysis: Isometric (a) and Top (b) View.

Figures 4.19, 4.20, and 4.21 show the Mach number distributions on the vane midspan. The first, in order, is the contour referring to the non-cooled vane design; the second refers to the design with smooth cooling channels; and the third refers to the design equipped with ribbed cooling channels. It is noted that the internal design of the vane does not significantly alter the external fluid dynamic field: the variation in the vane's wall temperature does not sufficiently influence the temperature to change the local speed of sound, and consequently, the Mach number. Finally, a sonic shock is noted at the blade row throat, leading to a flow choking condition at the inlet.

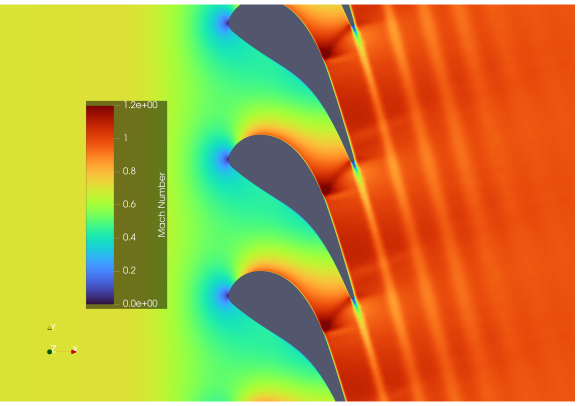

Figure 4.19: Midspan Mach Number Contour for Non-Cooled Vane.

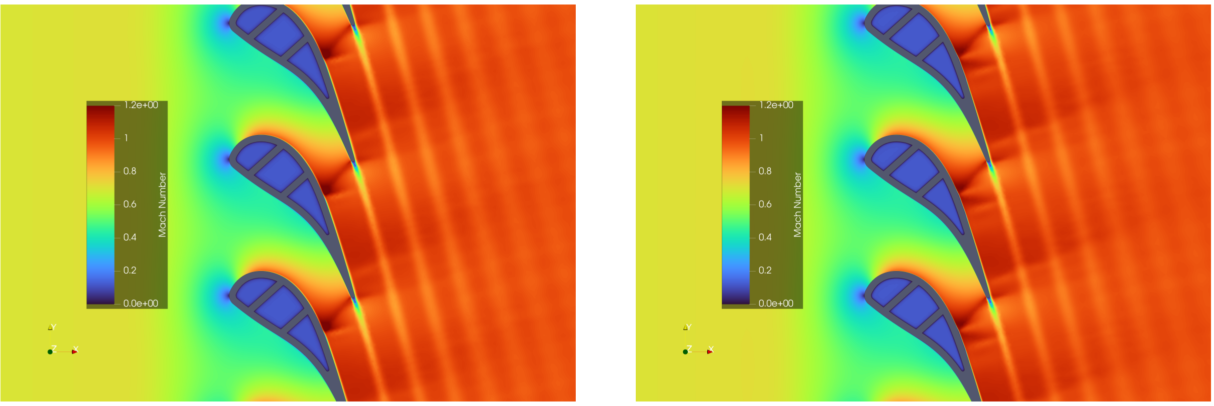

(a) (b)

Figure 4.20: Midspan Mach Number Contour for Smooth Channel Cooled Vane for $k-\omega$ SST Simulation (a) and $\gamma-Re_\theta$ Simulation (b) Results.

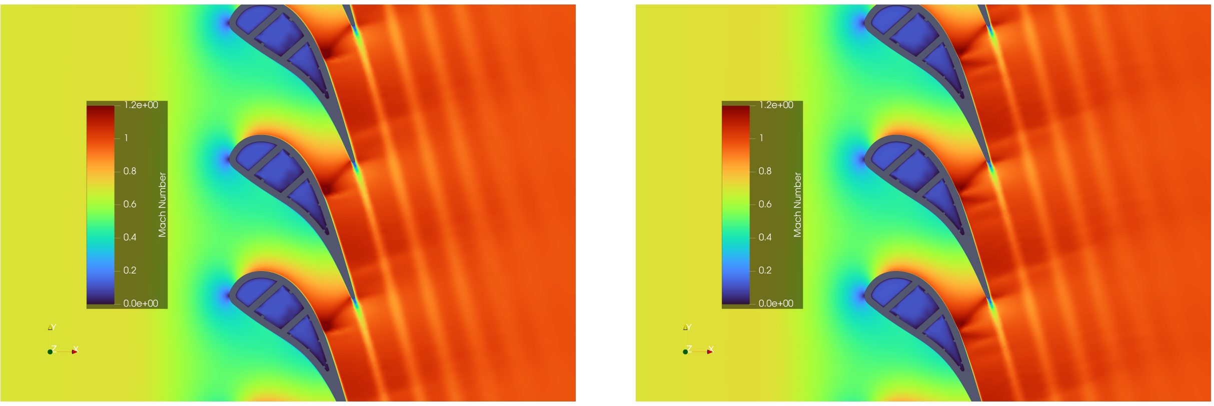

(a) (b)

Figure 4.21: Midspan Mach Number Contour for Ribbed Channel Cooled Vane for $k-\omega$ SST Simulation (a) and $\gamma-Re_\theta$ Simulation (b) Results.

Figures 4.22, 4.23, and 4.24 show the total pressure distributions at the vane midspan. A completely uniform flow field is observed, equal to the total pressure value at the computational domain inlet. The only exceptions are the vane's wake and a small flow separation bubble on the vane suction surface, which result in a wake that crosses the periodic interface and dissipates in the outlet region.

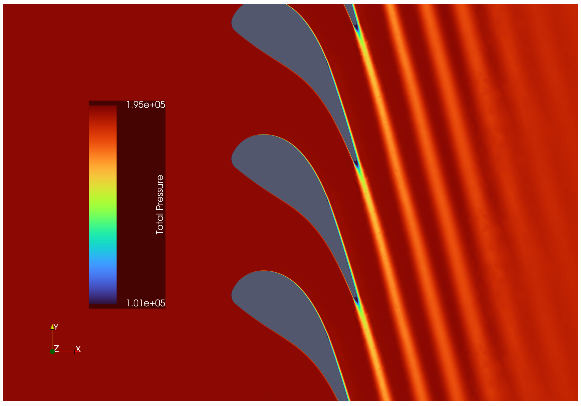

Figure 4.22: Midspan Total Pressure Contour for Non-Cooled Vane.

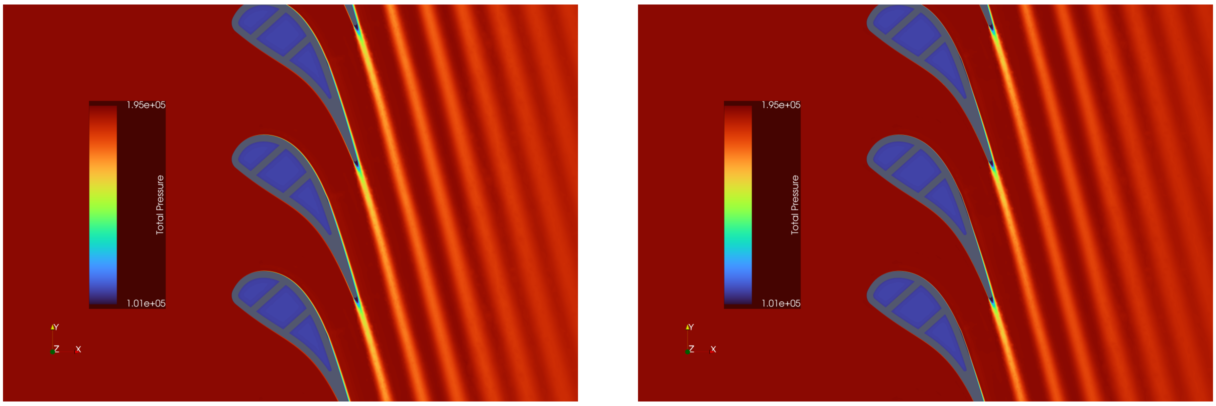

(a)

(b)

Figure 4.23: Midspan Total Pressure Contour for Smooth Channel Cooled Vane for $k-\omega\ SST$ Simulation (a) and $\gamma-Re_\theta$ Simulation (b) Results.

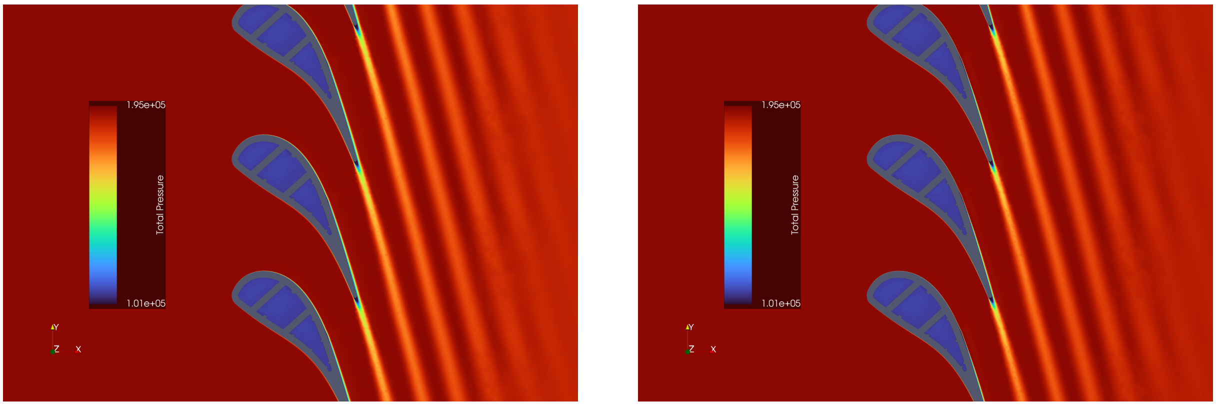

(a) (b)

Figure 4.24: Midspan Total Pressure Contour for Ribbed Channel Cooled Vane for $k-\omega$ SST Simulation (a) and $\gamma-Re_\theta$ Simulation (b) Results.

Figures 4.25, 4.26, and 4.27 show the static temperature distributions on the vane midspan. A substantial equality of the thermal contour in the fluid domain is noted across the various designs and setups used. A substantial difference occurs in the solid domain of the vane, with a significant decrease in the internal metal temperature, favoring the ribbed channel cooled design.

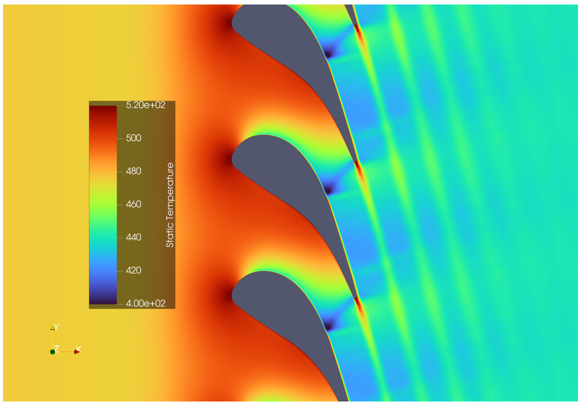

Figure 4.25: Midspan Static Temperature Contour for Non-Cooled Vane.

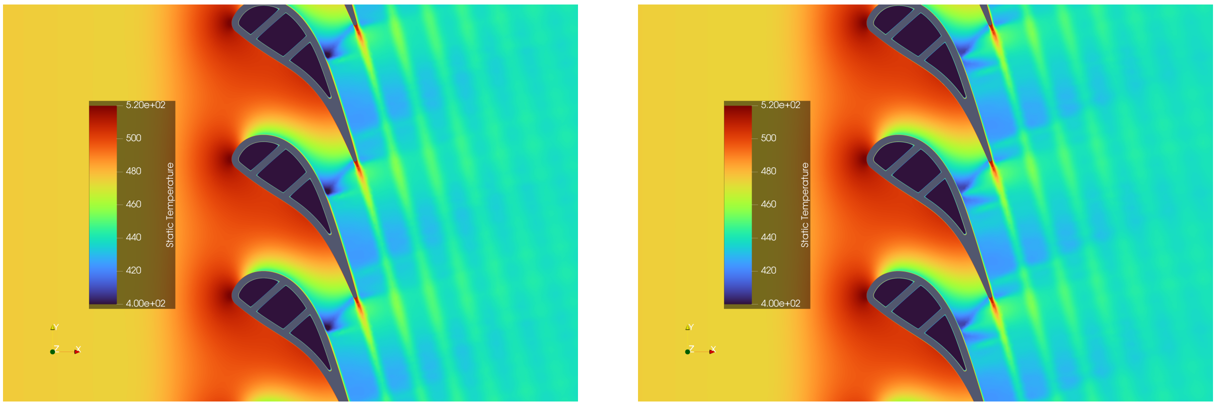

(a)

(b)

Figure 4.26: Midspan Static Temperature Contour for Smooth Channel Cooled Vane for $k-\omega$ SST Simulation (a) and $\gamma-Re_\theta$ Simulation (b) Results.

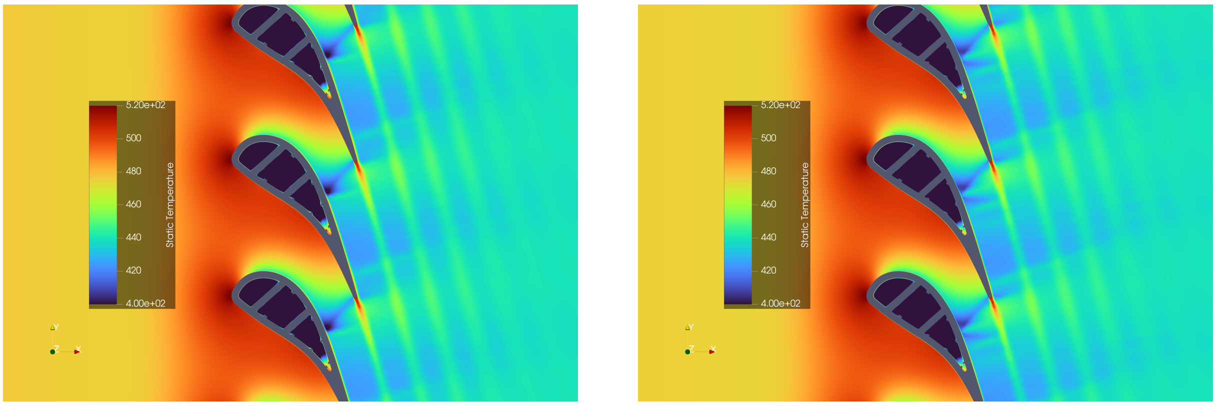

(a)

(b)

Figure 4.27: Midspan Static Temperature Contour for Ribbed Channel Cooled Vane for $k-\omega$ SST Simulation (a) and $\gamma - Re_\theta$ Simulation (b) Results.

Figures 4.28, 4.29, and 4.30 show the static temperature distributions in the solid domain at the vane midspan. The first characteristic is the non-cooled design, which reaches a temperature approximately equal to the inlet stagnation temperature, with a slight temperature decrease near the trailing edge on the suction side. This is attributed to the greater convective heat transfer induced by the flow acceleration and the flow's turbulent transition. The subsequent figures show the static temperature distribution in the smooth channel cooled design. It is noted that the left figure offers a statistically higher average temperature, an effect of the turbulence model lacking the transition model, which is used in the right-hand result. The final figure, showing the case cooled with ribbed channels, also reveals the largest difference in internal temperature between the case with and without the transition model. Due to these visible differences between the two models, the transition model was chosen for the subsequent study of the designs subjected to oscillating boundary conditions.

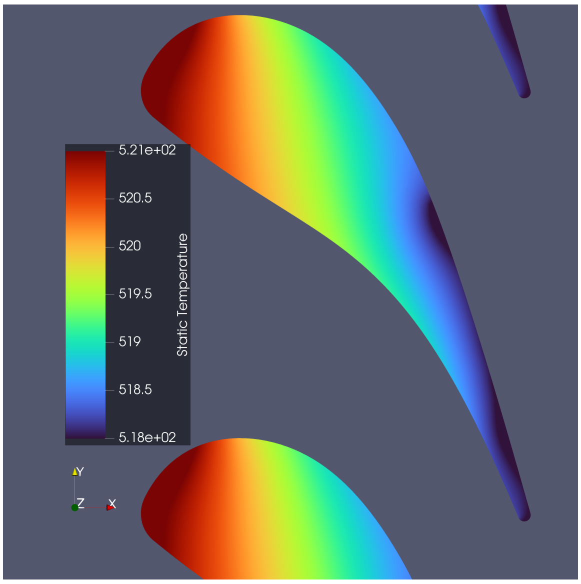

Figure 4.28: Midspan Static Temperature Contour for Non-Cooled Vane: Detail of Solid Vane.

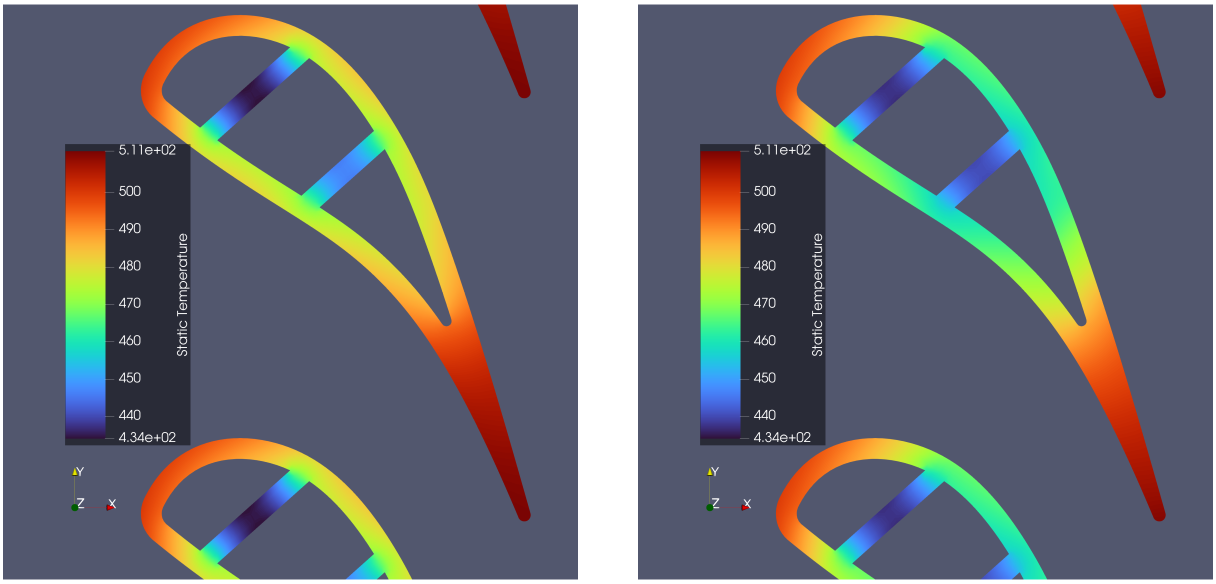

(a) (b)

Figure 4.29: Midspan Static Temperature Contour for Smooth Channel Cooled Vane for $k-\omega$ SST Simulation (a) and $\gamma-Re_\theta$ Simulation (b) Results: Detail of Solid Vane.

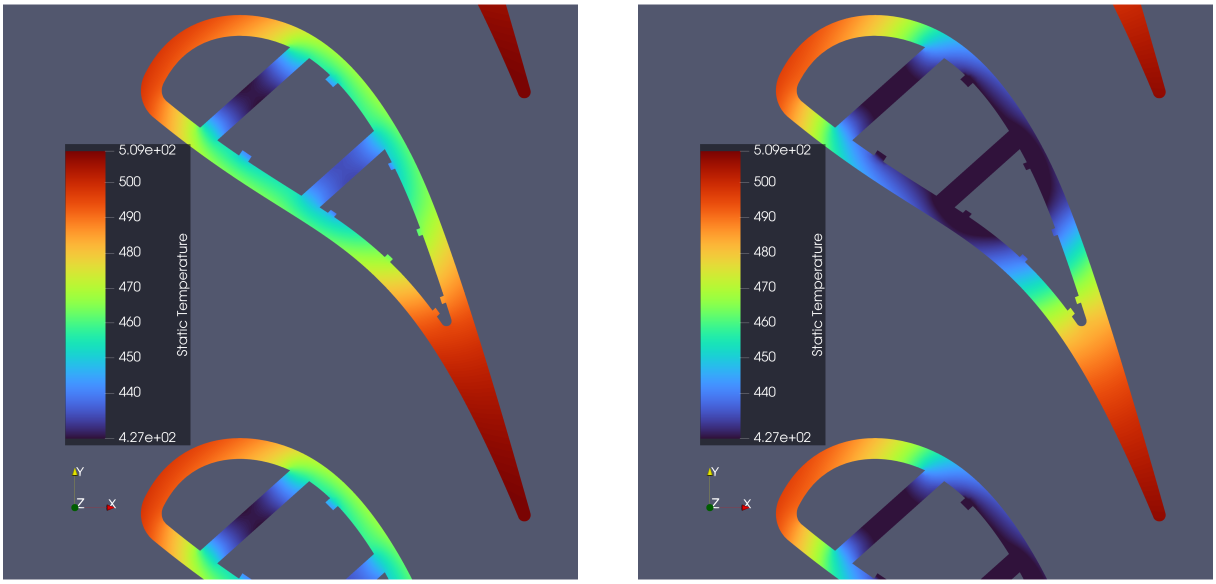

(a)

(b)

Figure 4.30: Midspan Static Temperature Contour for Ribbed Channel Cooled Vane for $k-\omega\ SST$ Simulation (a) and $\gamma-Re_\theta$ Simulation (b) Results: Detail of Solid Vane.

Figures 4.31, 4.32, 4.33, and 4.34 show the static temperature distributions on the sections created to study the second and third cooling channels. In the first figures, which refer to the smooth channel case, a temperature increase very close to the wall is observed, which is attributable to non-convective temperature diffusion perpendicular to the wall. A very different scenario is seen in the ribbed channel case: the ribs lead to very high turbulence levels, resulting in forced mixing and an increase in the bulk flow temperature. This, in turn, leads to better heat removal from the solid and a consequent decrease in the average metal temperature.

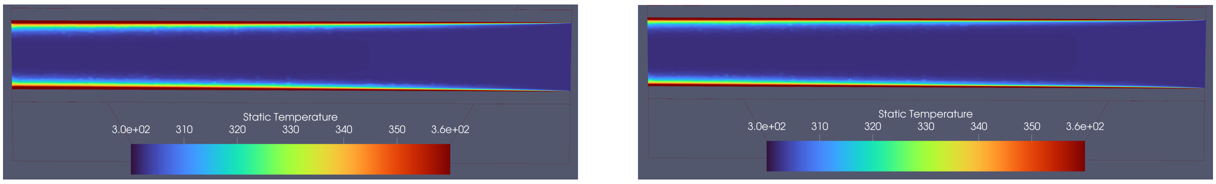

(a) (b)

Figure 4.31: Coolant Fluid Static Temperature Contour in 2^{nd} Smooth Cooling Channel: $k-\omega\ SST$ (a) and $\gamma-Re_\theta$ (b) Model.

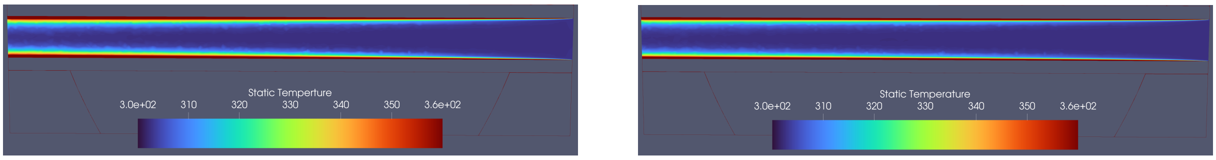

(a) (b)

Figure 4.32: Coolant Fluid Static Temperature Contour in 3^{rd} Smooth Cooling Channel: $k-\omega\ SST$ (a) and $\gamma-Re_\theta$ (b) Model.

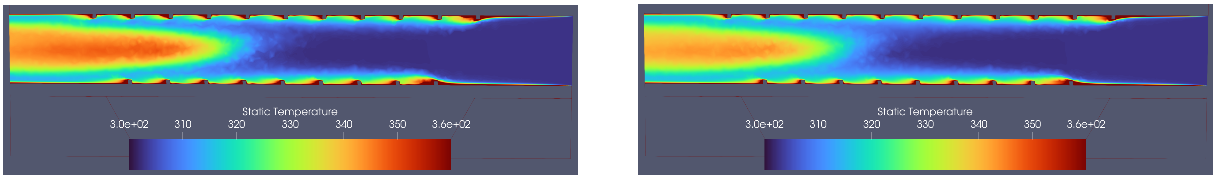

(a) (b)

Figure 4.33: Coolant Fluid Static Temperature Contour in 2^{nd} Ribbed Cooling Channel: $k-\omega\ SST$ (a) and $\gamma-Re_{\theta}$ (b) Model.

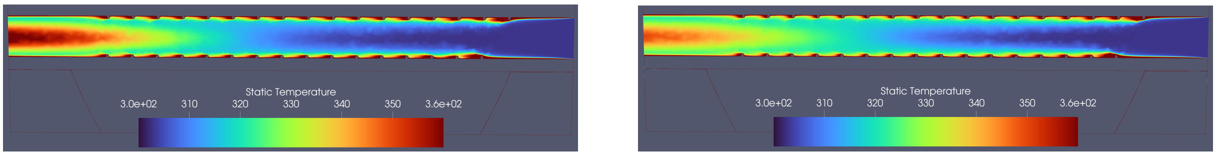

(a) (b)

Figure 4.34: Coolant Fluid Static Temperature Contour in 3^{rd} Ribbed Cooling Channel: $k-\omega\ SST$ (a) and $\gamma-Re_{\theta}$ (b) Model.

Figures 4.35, 4.36, 4.37, and 4.38 show the turbulent kinetic energy distributions in the two channels, for the smooth and then the ribbed case. The first figures show an almost uniform distribution of turbulent kinetic energy, with irregularities concentrated at the wall, in the boundary layer region, which is the sole generator of turbulence. Comparing the fully-turbulent results with those obtained using the transition model, the turbulent transition point of the boundary layer is shifted further downstream, towards the channel outlet. The following figures show the case analyzed with a transition model. The generation of turbulence is observed to be concentrated downstream of the cooling ribs and also develops towards the center of the channel.

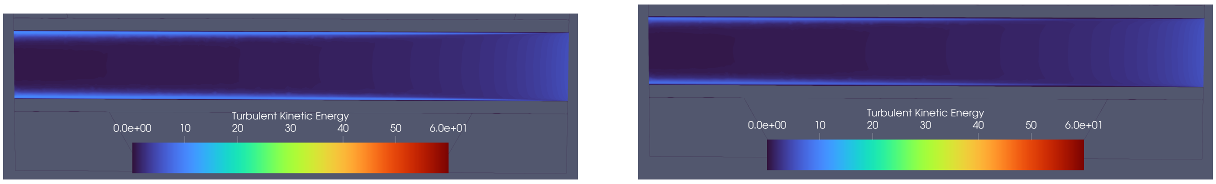

(a) (b)

Figure 4.35: Coolant Fluid Turbulent Kinetic Energy Contour in 2^{nd} Smooth Cooling Channel: $k-\omega\ SST$ (a) and $\gamma - Re_\theta$ (b) Model.

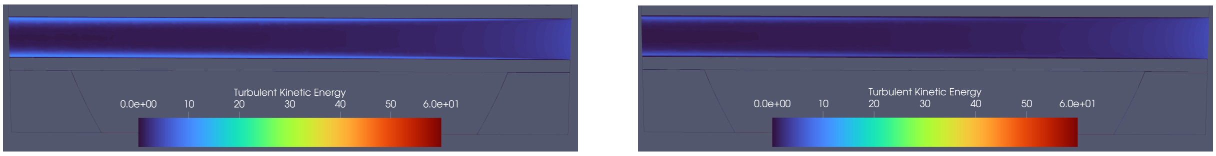

(a) (b)

Figure 4.36: Coolant Fluid Turbulent Kinetic Energy Contour in 3^{rd} Smooth Cooling Channel: $k-\omega\ SST$ (a) and $\gamma - Re_\theta$ (b) Model.

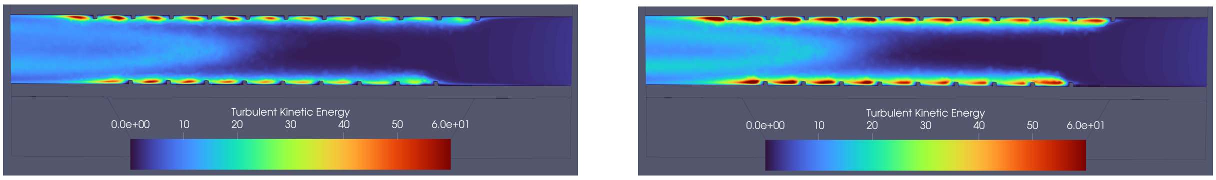

(a) (b)

Figure 4.37: Coolant Fluid Turbulent Kinetic Energy Contour in 2^{nd} Ribbed Cooling Channel: $k-\omega\ SST$ (a) and $\gamma - Re_\theta$ (b) Model.

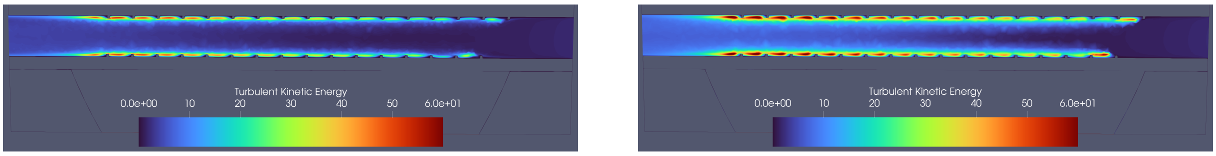

(a) (b)

Figure 4.38: Coolant Fluid Turbulent Kinetic Energy Contour in 3^{rd} Ribbed Cooling Channel: $k-\omega\ SST$ (a) and $\gamma - Re_\theta$ (b) Model.

Figures 4.39, 4.40, 4.41, and 4.42 show the velocity distributions in the second and third cooling channels. In the first figures, a uniform velocity distribution associated with the absence of ribs is observed. The turbulence, previously highlighted by the turbulent kinetic energy distribution, is shown here by the velocity variation downstream of the turbulating ribs and the decrease in the cooling flow velocity in the channel outlet region, leading to a higher local static temperature and greater turbulence.

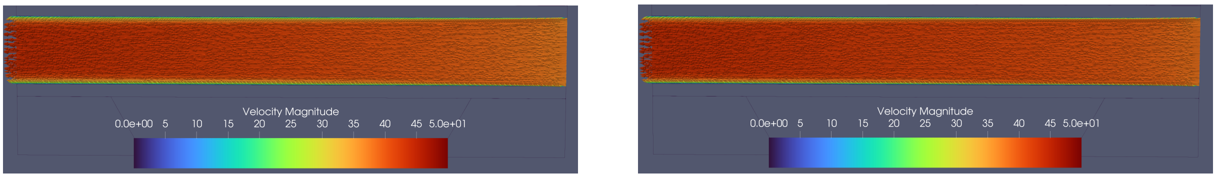

(a) (b)

Figure 4.39: Coolant Fluid Velocity Vectors on Contour in 2^{nd} Smooth Cooling Channel: $k-\omega\ SST$ (a) and $\gamma-Re_\theta$ (b) Model.

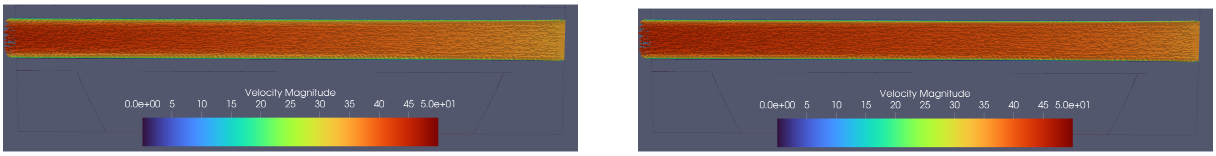

(a) (b)

Figure 4.40: Coolant Fluid Velocity Vectors on Contour in 3^{rd} Smooth Cooling Channel: $k-\omega\ SST$ (a) and $\gamma-Re_\theta$ (b) Model.

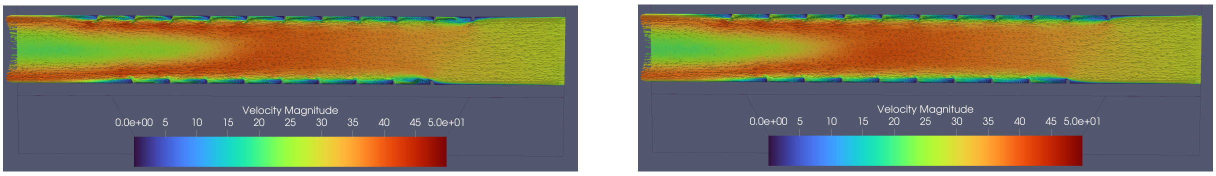

(a) (b)

Figure 4.41: Coolant Fluid Velocity Vectors on Contour in 2^{nd} Ribbed Cooling Channel: $k-\omega\ SST$ (a) and $\gamma-Re_\theta$ (b) Model.

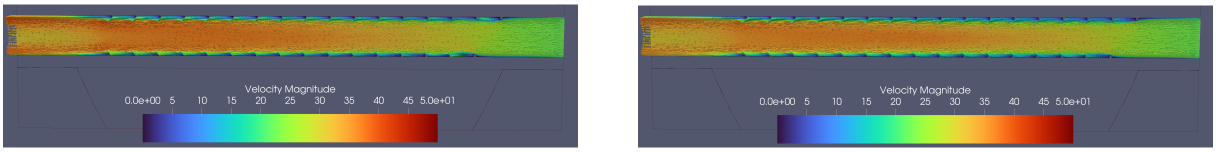

(a) (b)

Figure 4.42: Coolant Fluid Velocity Vectors on Contour in 3^{rd} Ribbed Cooling Channel: $k-\omega\ SST$ (a) and $\gamma-Re_\theta$ (b) Model.

In Figures 4.43, 4.44, 4.45, and 4.46, magnified views of the velocity distributions calculated in the second and third cooling channels are presented. Velocity vectors are superimposed on the simple contours to highlight the local flow direction. The first figures show a well-defined boundary layer that does not undergo variations when the solver setup is modified. The parabolic velocity profile is consistent with theory, demonstrating an excellent resolution of the boundary layer and, therefore, good mesh parameters for boundary layer studies. The subsequent figures show the flow field that develops between two consecutive ribs, highlighting an unclosed recirculation bubble: thus, the design parameters chosen for the ribs were likely optimized for higher Reynolds numbers ($Re_{D_{hyd}}$) than those achieved in the present case. This latter hypothesis leads to a lower heat transfer efficiency for the ribbed structures.

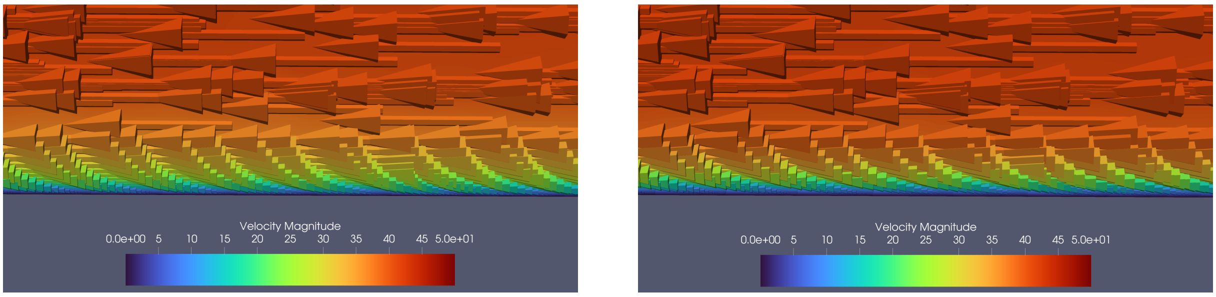

(a)

(b)

Figure 4.43: Coolant Fluid Velocity Vectors Wall Particular on Contour in 2^{nd} Smooth Cooling Channel: $k-\omega\ SST$ (a) and $\gamma-Re_{\theta}$ (b) Model.

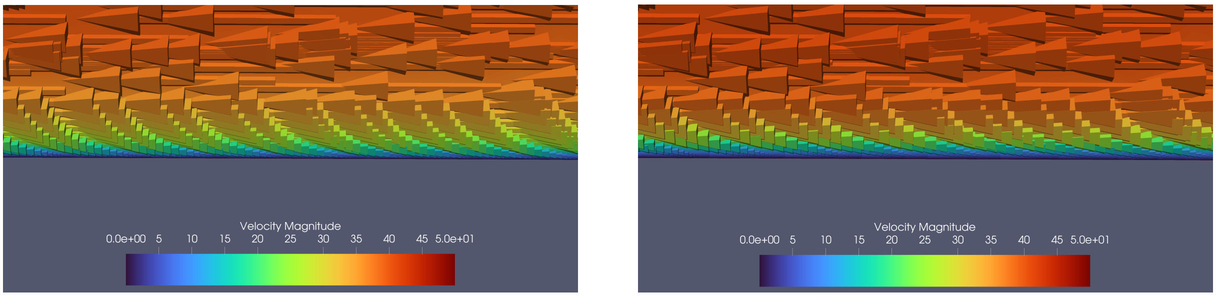

(a) (b)

Figure 4.44: Coolant Fluid Velocity Vectors Wall Particular on Contour in 3^{rd} Smooth Cooling Channel: $k-\omega$ SST (a) and $\gamma-Re_\theta$ (b) Model.

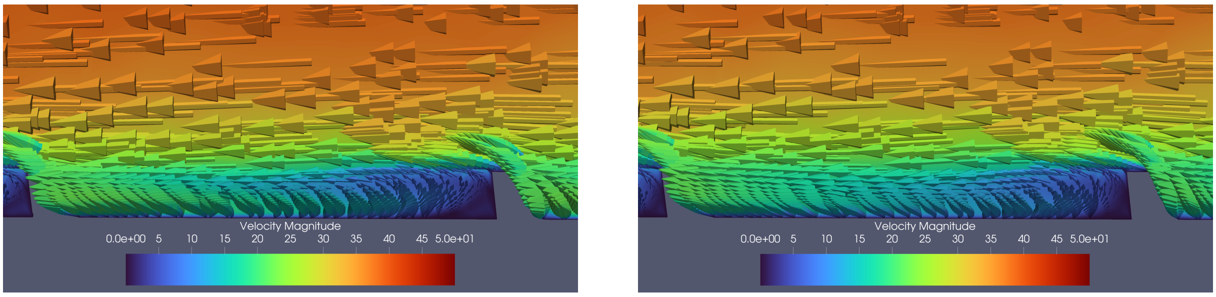

(a) (b)

Figure 4.45: Coolant Fluid Velocity Vectors Wall Particular on Contour in 2^{nd} Ribbed Cooling Channel: $k-\omega$ SST (a) and $\gamma-Re_\theta$ (b) Model.

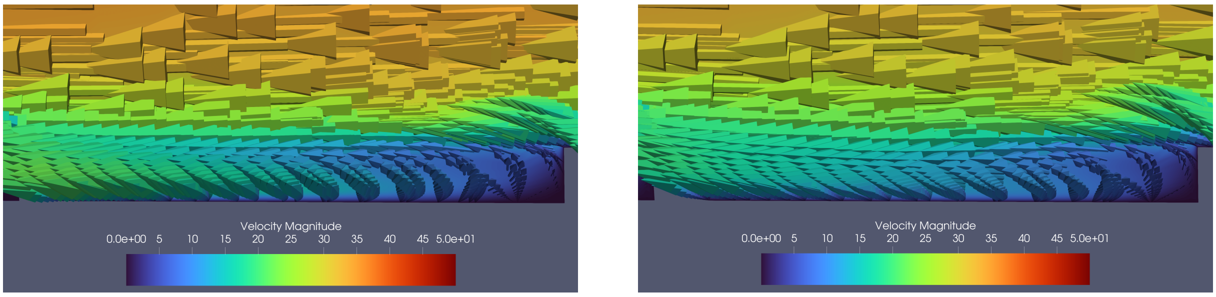

(a)

(b)

Figure 4.46: Coolant Fluid Velocity Vectors Wall Particular on Contour in 3^{rd} Ribbed Cooling Channel: $k-\omega$ SST (a) and $\gamma-Re_{\theta}$ (b) Model.

Figures 4.47 and 4.48 show the distributions of the convective heat transfer coefficient calculated on the wall between two consecutive ribs. It is noted that the heat transfer primarily occurs at a distance from the rib, indicating the presence of a small stagnation zone very close to the wall downstream of the turbulator. In this zone, temperature is transferred very slowly between the solid and the cooling fluid, primarily through diffusion.

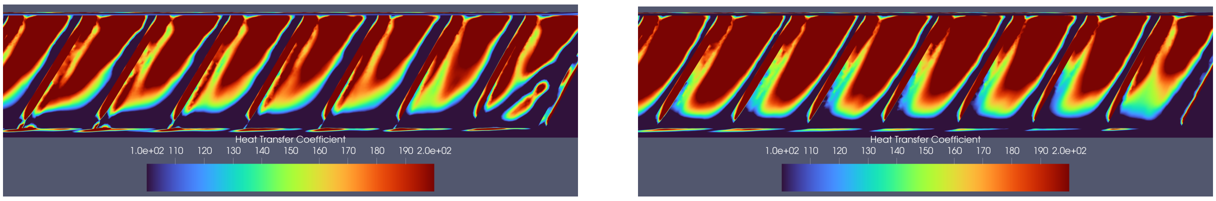

(a) (b)

Figure 4.47: Wall Heat Transfer Coefficient Contour in between Rib Turbolators in 2^{nd} Cooling Channel: $k-\omega$ SST (a) and $\gamma-Re_{\theta}$ (b) Model.

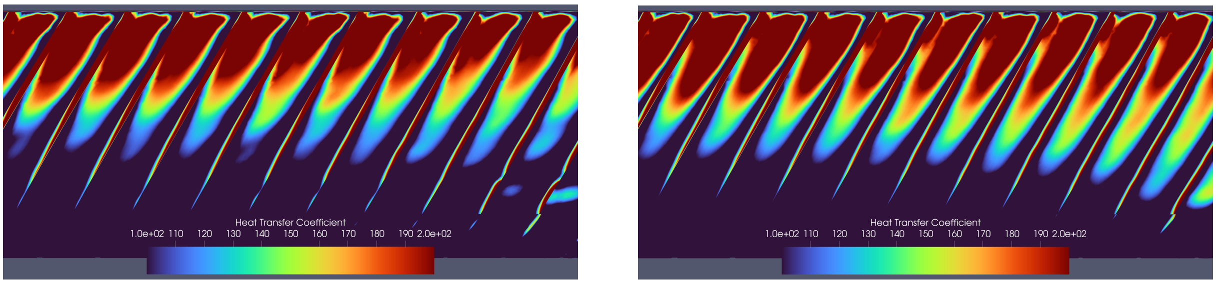

(a) (b)

Figure 4.48: Wall Heat Transfer Coefficient Contour in between Rib Turbolators in 3^{rd} Ribbed Cooling Channel: $k-\omega$ SST (a) and $\gamma-Re_{\theta}$ (b) Model.

4.5 Comparative Analysis with Transition Model

This section presents the comparative results of the $k-\omega\ SST$ and $\gamma-Re_{\theta}$ turbulence models applied to cooled vane designs with smooth and ribbed channels. The distributions of static pressure and static temperature on the external wall, as well as on the internal walls of the cooling channels (where applicable), will be compared. For the analysis of the external wall distribution, cuts were made at 10%, 30%, 50%, 70%, and 90% of the vane span. Since the vane does not have a constant opening, it is sectioned by splines created by considering the local opening at 170 points along the profile.

Figures 4.49, 4.50, and 4.51 show the distributions of static pressure on the external wall of the profile. Each plot presents the distribution for the same span-wise cut, varying the design and the setup used for the analysis. The region of the cascade throat is noticeable, where the relative pressure value drops below 0.5, indicating, almost certainly, the sonicity of the throat and the choking* of the passage. In the sections closer to the endwalls (10% and 90% span), a strong similarity is observed between the profiles obtained with the two-equation and four-equation models, which is an indication of wall-generated turbulence. In the midspan section (50% span), however, the largest difference between the two models is noted, as this is the region where the finite-span effect of the vane is least pronounced.

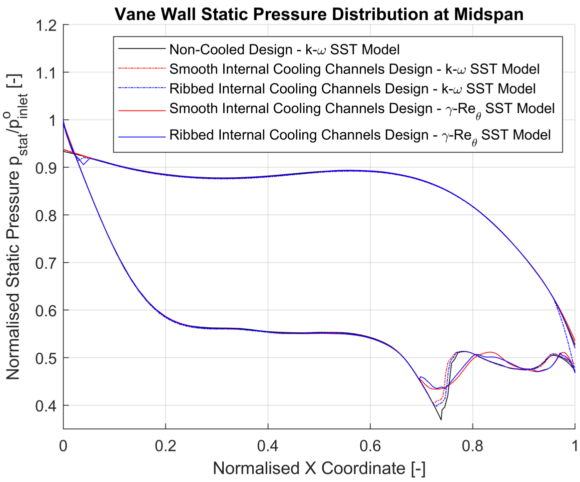

Figure 4.49: Midspan Distribution of Wall Vane Static Pressure.

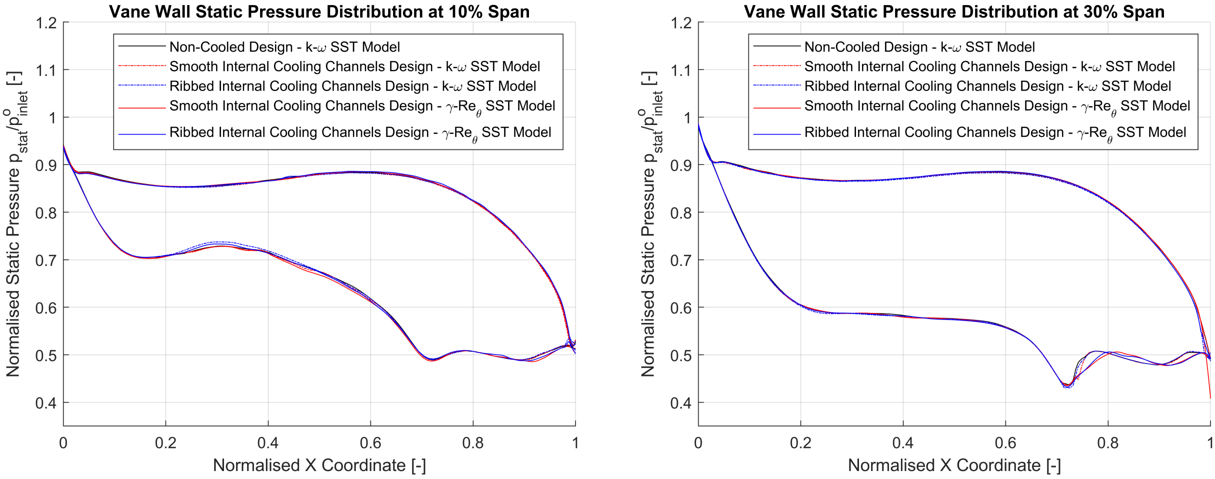

(a) (b)

Figure 4.50: Wall Vane Static Pressure Distribution at 10% of Span (a) and at 30% of Span (b).

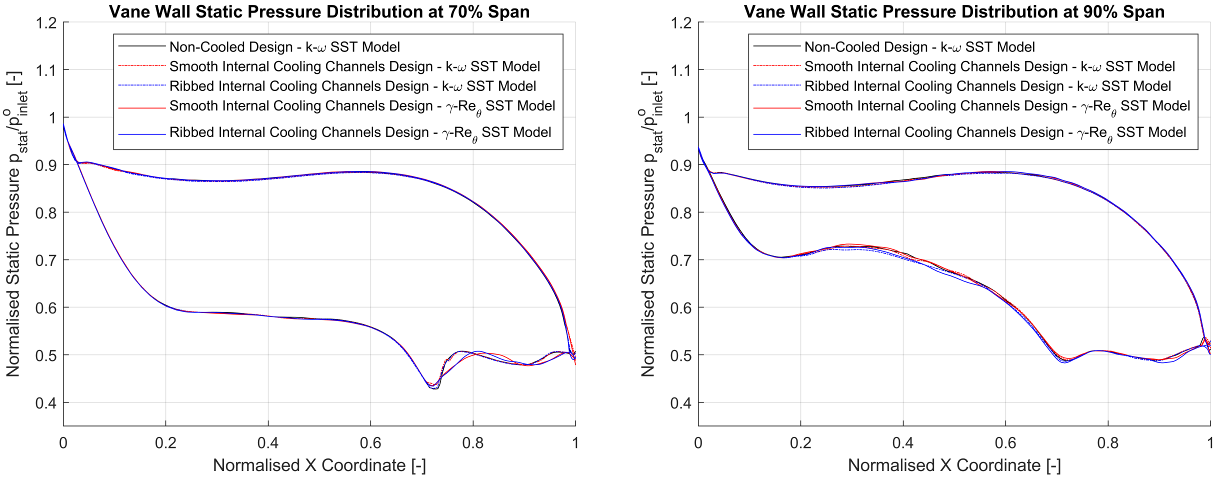

(a) (b)

Figure 4.51: Wall Vane Static Pressure Distribution at 70% of Span (a) and at 90% of Span (b).

Figure 4.52 presents the distribution of wall static pressure on the external profile for a fixed turbulence model ($\gamma - Re_\theta$) and varying analysis section. A radical difference is noted in the suction side of the profile, leading to a smaller flow expansion in the regions near the endwalls, which is attributed to the presence of the endwalls themselves, which render the vane finite and induce secondary flow/endwall effects.

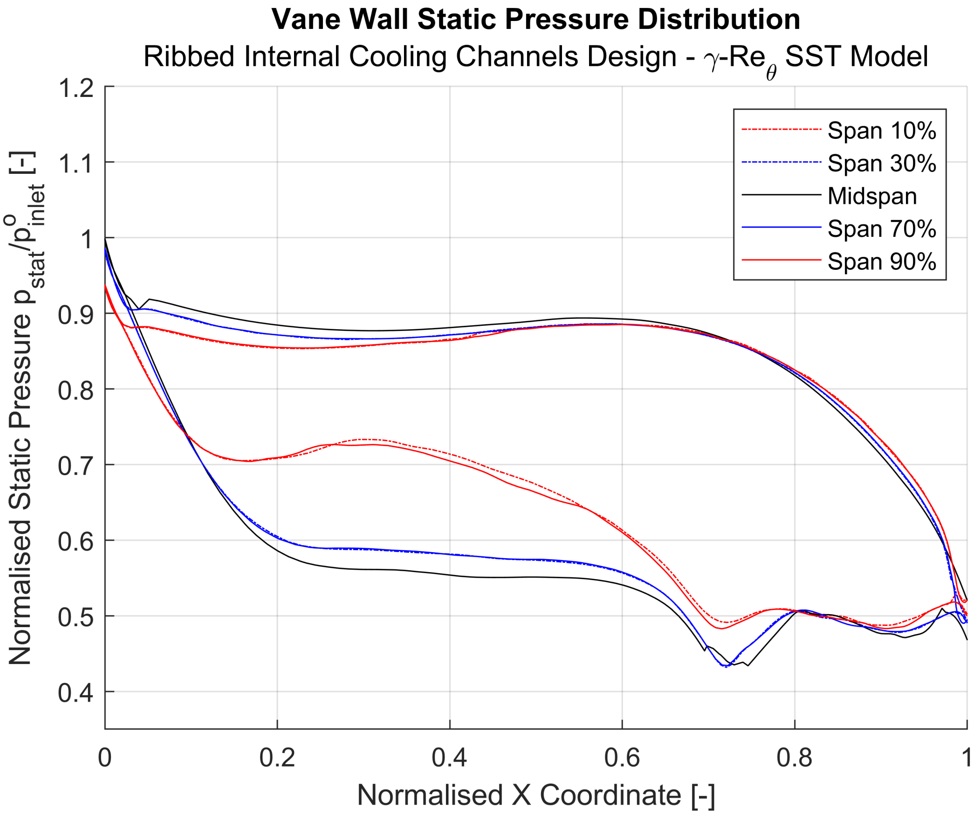

Figure 4.52: Wall Vane Static Pressure Distribution at Different Span Section for $\gamma - Re_\theta$ Transition Model Simulation Results.

Figures 4.53, 4.54, and 4.55 show the distributions of static temperature on the external wall of the profile. Differences are accentuated as the span section changes in the case of the internally cooled vane: as the span-wise position moves towards the midspan, the profile temperature tends to decrease. For the same span-wise position, a temperature decrease is noted as the design changes: the uncooled model reaches the inlet stagnation temperature, while for the cooled models, a temperature drop is observed in correspondence with the zone containing the cooling channels, followed by an increase in the uncooled trailing edge region. For the same design and span section, no differences are evident with the change in the turbulence model used.

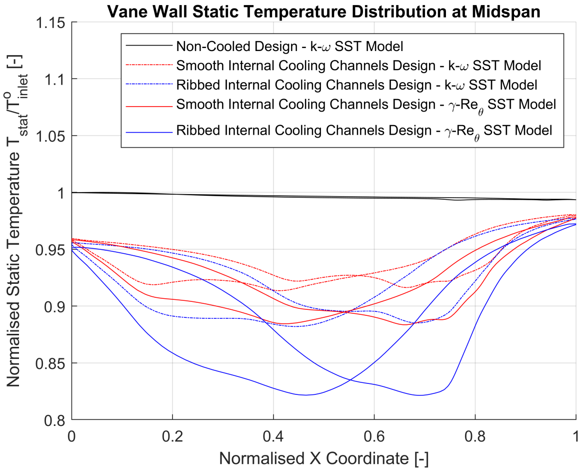

Figure 4.53: Midspan Distribution of Wall Vane Static Temperature.

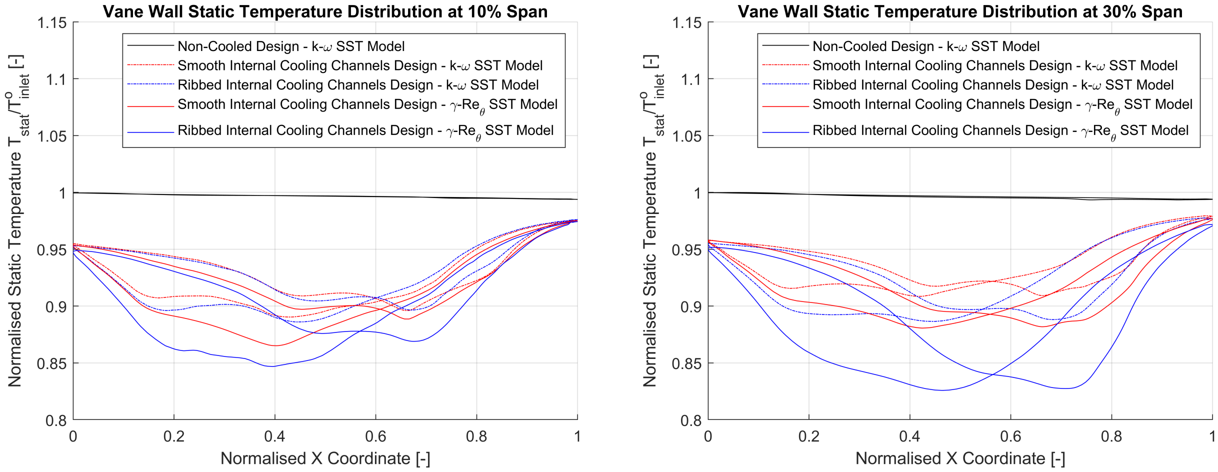

(a) (b)

Figure 4.54: Wall Vane Static Temperature Distribution at 10% of Span (a) and at 30% of Span (b).

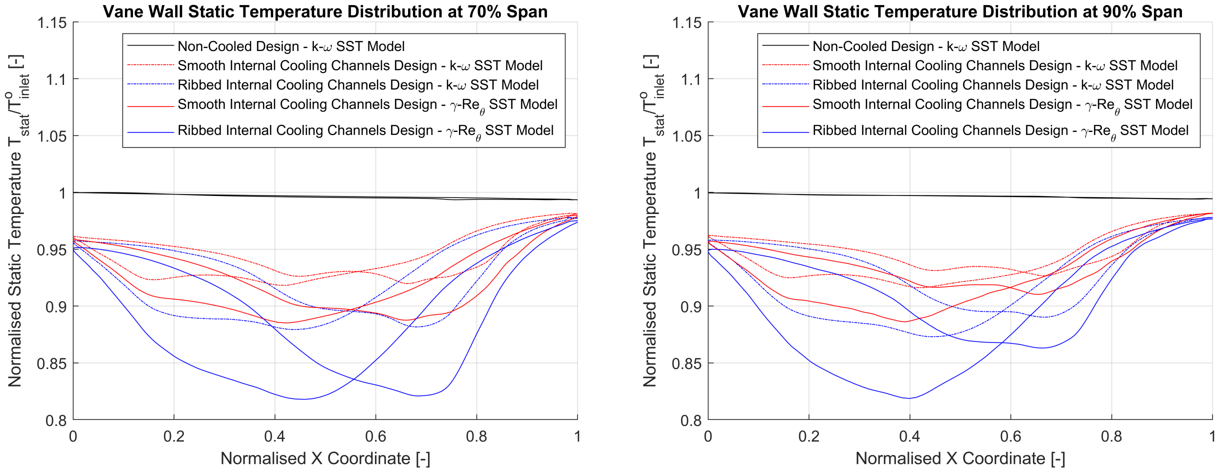

(a) (b)

Figure 4.55: Wall Vane Static Temperature Distribution at 70% of Span (a) and at 90% of Span (b).

Figure 4.56 presents the temperature distribution on the external wall of the profile for the same design and turbulence model, but varying the span section. As previously noted, the average temperature decreases as the span-wise position increases (towards midspan), due to the effect of longer contact time with the cooling fluid.

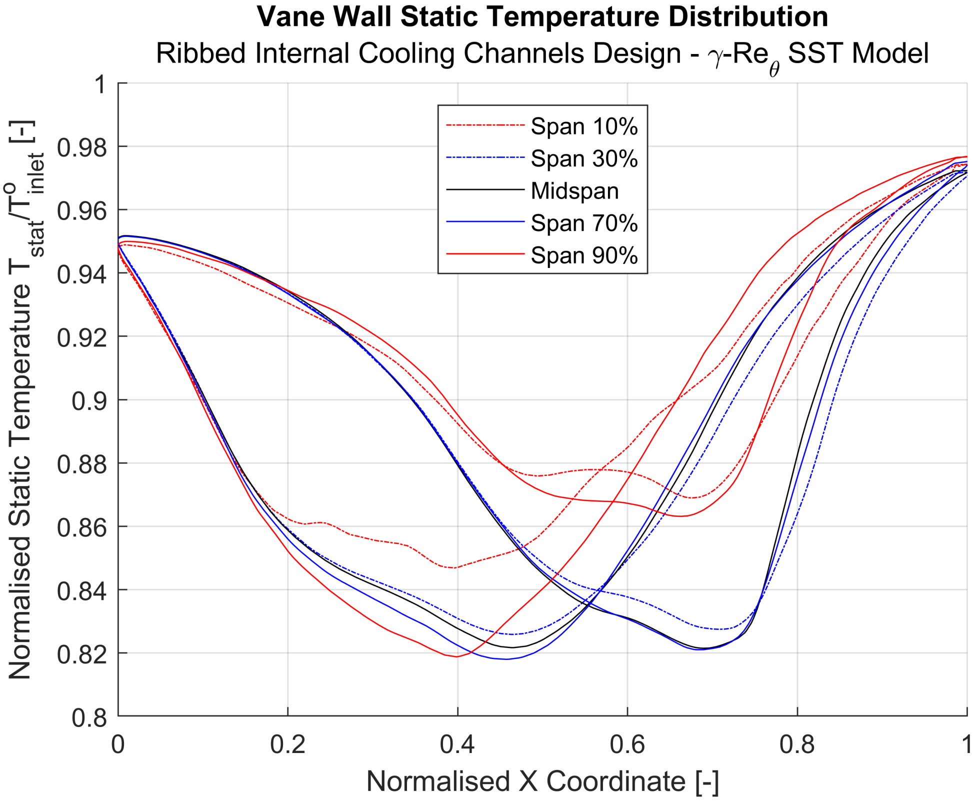

Figure 4.56: Wall Vane Static Temperature Distribution at Different Span Section for $\gamma - Re_\theta$ Transition Model Simulation.

Figure 4.57 presents the wall static temperature distribution calculated in the two cooling channels of interest, varying the design and the computational model used. The average temperature decreases when moving from the smooth channel design to the ribbed channel design. Furthermore, for the same design, a lower temperature is noted with the use of the transition model ($\gamma - Re_\theta$).

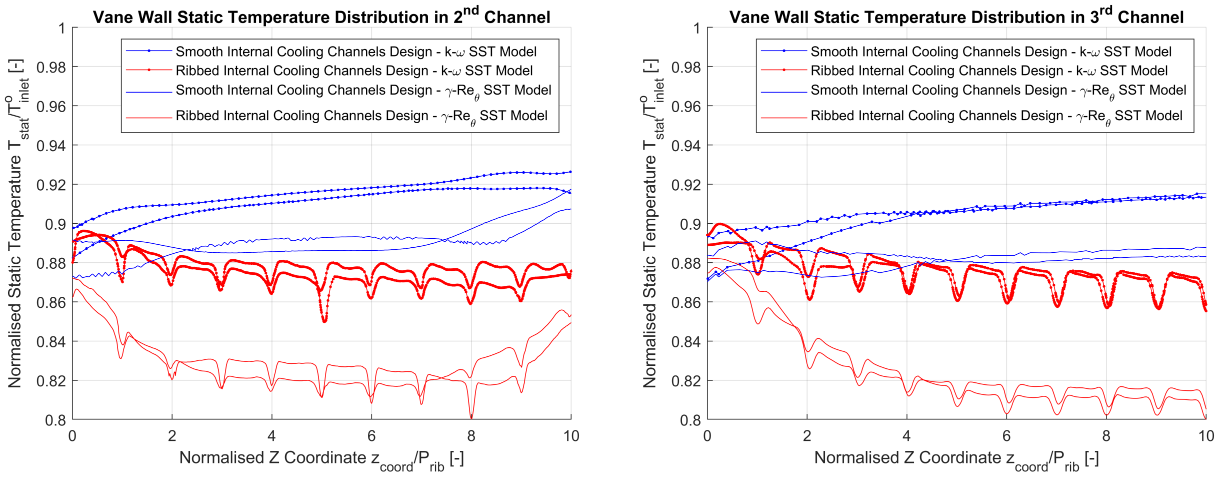

(a) (b)

Figure 4.57: Wall Vane Static Temperature Distribution in 2^{nd} (a) and 3^{rd} (b) Cooling Channel.

Figure 4.58 presents the wall static temperature distribution in the two cooling channels for the same design and computational model used. This demonstrates that cooling is more efficient in the second channel, which, thanks to its larger diameter, leads to a higher turbulence level and a corresponding higher thermal mixing.

Figure 4.59 shows the wall distribution of the heat transfer coefficient in the second and third cooling channels for the ribbed channel case and the four-equation turbulence model ($\gamma - Re_\theta$). It confirms that the maximum heat transfer occurs at a distance from a rib, which is also demonstrated by the contour of the same quantity calculated on the wall between two consecutive ribs.

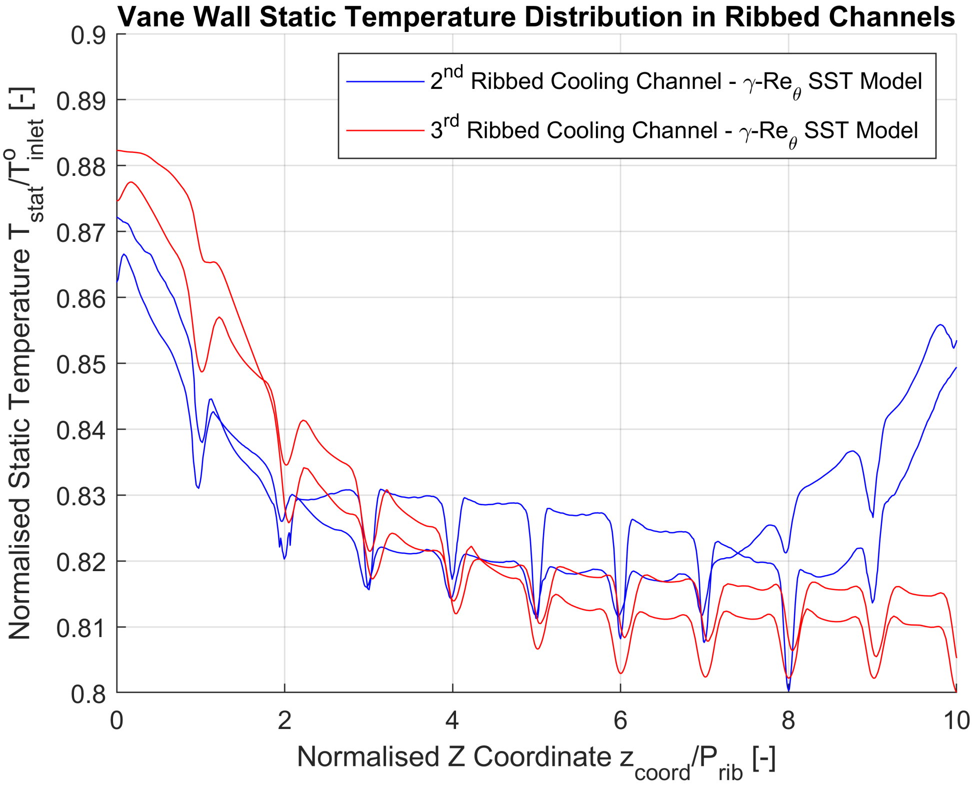

Figure 4.58: Wall Vane Static Temperature Distribution in Ribbed Cooling Channel for$\gamma - Re_\theta$ Transition Model Simulation.

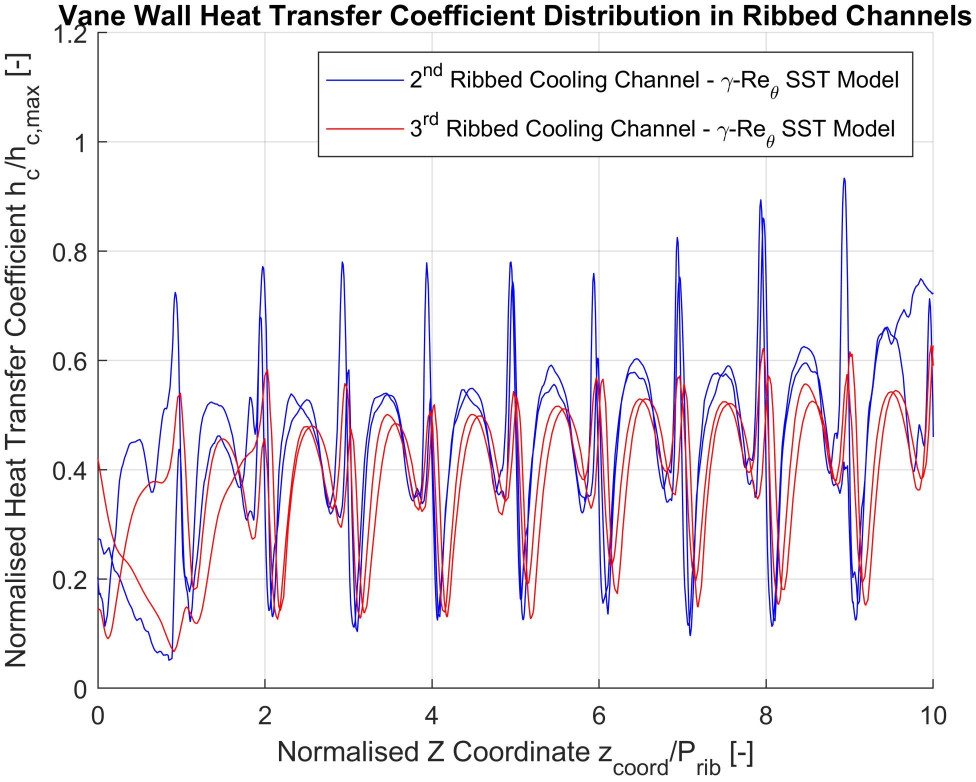

Figure 4.59: Wall Vane Heat Transfer Coefficient Distribution in Ribbed Cooling Channel for$\gamma - Re_\theta$ Transition Model Simulation.

5 Unsteady Simulations

This section details the unsteady-state simulations (also known as transient simulations) performed using the Ansys Fluent 2023 R2 suite. The Unsteady Reynolds-Averaged Navier-Stokes (URANS) equations were employed, specifically adopting the $\boldsymbol{\gamma - Re_\theta}$ transition model. Starting from the three distinct vane designs, the meshing parameters determined by the preceding mesh sensitivity analysis were applied to generate three separate computational meshes. For the non-cooled vane design, only the two-equation turbulence model ($\boldsymbol{k - \omega}$ SST) was utilized. Conversely, to achieve more reliable results within the cooling passages, the subsequent two designs were simulated using the four-equation transition model ($\gamma - \boldsymbol{Re_\theta}$).

5.1 Computational Domain

Figures 5.1, 5.2, and 5.3 illustrate the computational domains employed for the unsteady-state simulations. A plenum has been added to the outlet of the computational domain used for the steady simulations, thereby extending it. This added section, which will be meshed with a coarser grid, serves two main purposes: to control numerical viscosity and to mitigate reverse acoustic waves coming from the outlet. The former, in fact, helps with the numerical stability of the simulations, allowing us to maintain a higher Courant number without compromising residual values. The latter aids in controlling sonic waves originating from the fluid-vane interaction and propagating towards the outlet. The plenum, in fact, will experience high levels of backflow and will simulate wave propagation in calm air with the aid of free-shear stress boundary conditions on the domain limits. The plenum is divided into seven sections, each characterized by its own cell size, to progressively coarsen the mesh resolution approaching the domain outlet.

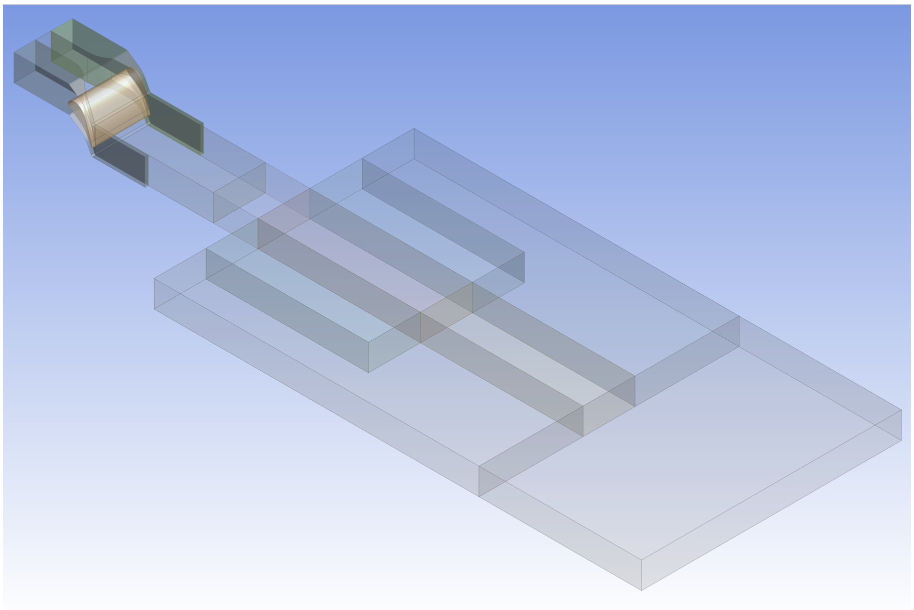

Figure 5.1: Isometric View of the Domain used for Non-Cooled Vane Unsteady URANS Simulation.

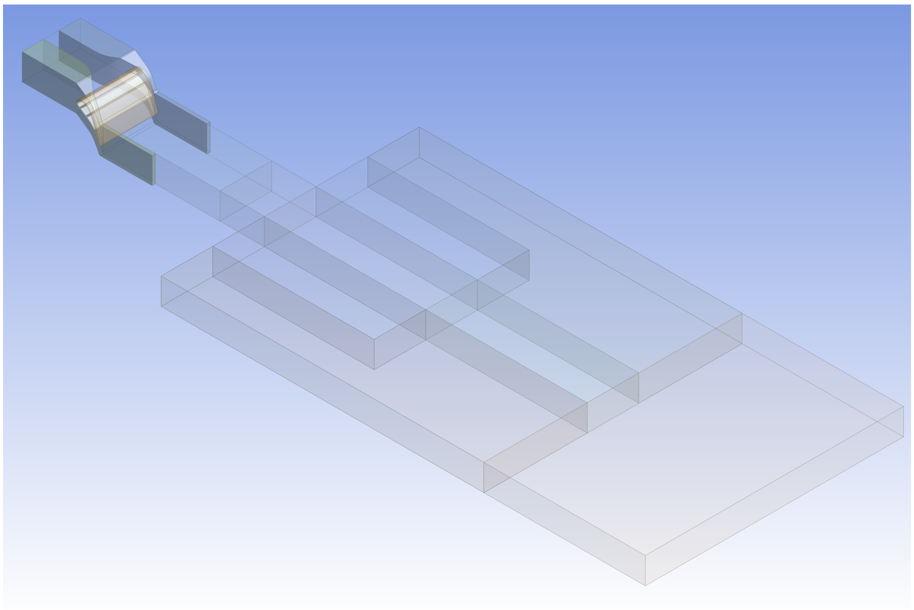

Figure 5.2: Isometric View of the Domain used for Smooth Channel Cooled Vane Unsteady URANS Simulation.

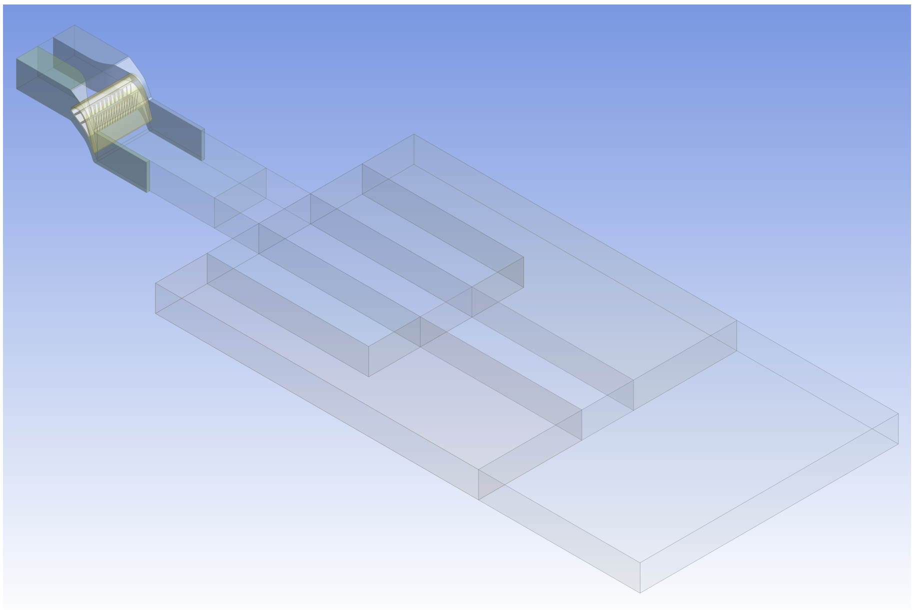

Figure 5.3: Isometric View of the Domain used for Ribbed Channel Cooled Vane Unsteady URANS Simulation.

5.2 Mesh Analysis

The parameters used for the generation of the unstructured mesh in the three cases under examination will now be discussed. Table 19 shows the meshing parameters that lead to the computational grid of the main flow. These parameters, like those used for the steady simulations, stem from the considerations made during the mesh sensitivity analysis. Consequently, the computational grids will be very similar to the previously utilized meshes. Tables 20 and 21 report the specific parameters for the meshing of the solid domain and the fluid cooling channels. The only difference compared to the meshes obtained in the previous chapter lies in the plenum itself. It connects the cell size of the vane domain with a cell size of $l_c = 5\ mm$. This reduction in resolution within the solution is vital for increasing the stability of the calculation and for keeping the number of elements and the associated computational cost approximately constant.

	Main Flow
Method	Tetrahedrons
Element Size [mm]	2
Refinement Size [mm]	1
Leading Edge Surface Element Size [mm]	0.375
Trailing Edge Surface Element Size [mm]	0.150
Suction & Pressure Surface Element Size [mm]	0.700
Inflation Parameters	First Layer Thickness: 0.843 μm Number of Layers: 25 Growth Rate: 1.26

Table 19: Main Flow Mesh Parameters for Unsteady URANS Simulations.

	Cooling Fluid
Method	Tetrahedrons
Element Size [mm]	1
Leading Edge Surface Element Size [mm]	0.375
Trailing Edge Surface Element Size [mm]	0.150
Suction & Pressure Surface Element Size [mm]	0.700
Rib Turbolators Interface Element Size [mm]	0.250
Inflation Parameters	First Layer Thickness: 0.843 μm Number of Layers: 25 Growth Rate: 1.225

Table 20: Cooling Fluid Channels Mesh Parameters for Unsteady URANS Simulations.

	Solid Vane & Endwalls
Method	Automatic
Element Size [mm]	5
Vane Size Refinement [mm]	0.5
Leading Edge Surface Element Size [mm]	0.375
Trailing Edge Surface Element Size [mm]	0.150
Suction & Pressure Surface Element Size [mm]	0.700
Rib Turbolators Interface Element Size [mm]	0.250

Table 21: Solid Domains Mesh Parameters for Unsteady URANS Simulations.

Figure 5.4 shows an isometric overview of the mesh used for the non-cooled vane design simulation. A very coarse mesh is visible in the added plenum section. Figure 5.5 presents the domain cross-section at midspan with a magnification focusing on the transonic vane region. Further increasing the definition in the high curvature regions, Figure 5.6 shows a detailed view of the mesh around the leading edge and the trailing edge, respectively. Figure 5.7 includes a cross-section of the vane and a cross-section of the plenum. The first, obtained by intersecting the walls of the second cooling channel (if present, otherwise this refers to the main flow path) perpendicularly, shows all the walls where the no-slip condition was applied, and consequently, the inflation parameters. The second cross-section, reported on a plane parallel to the periodic boundaries, illustrates the internal composition of the computational grid used for the plenum, highlighting the similarity between the surface and volume mesh.

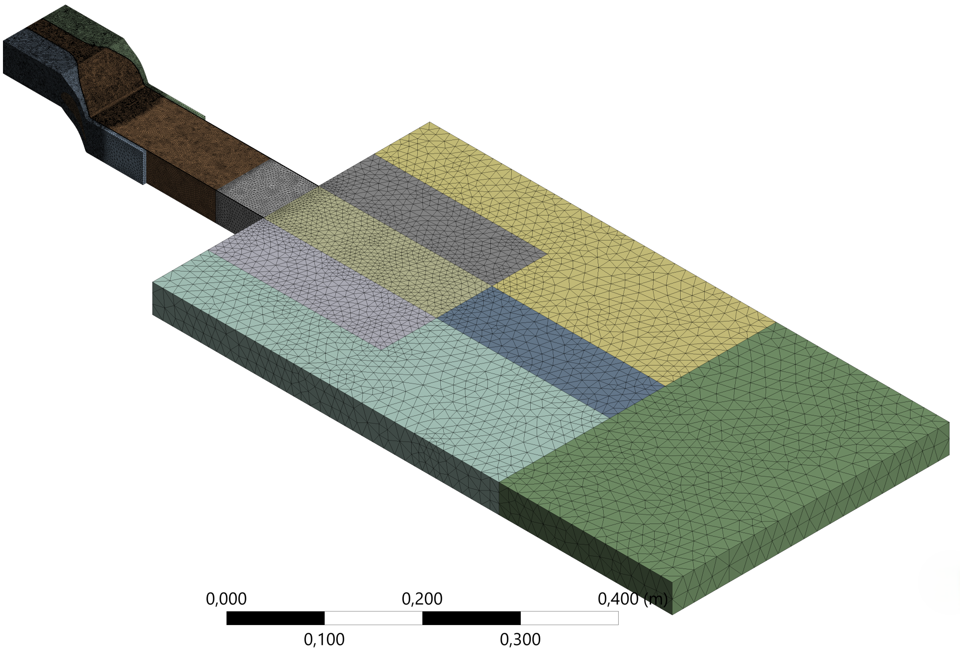

Figure 5.4: Isometric View of the Mesh Used for Unsteady URANS Simulations for Non-Cooled Vane.

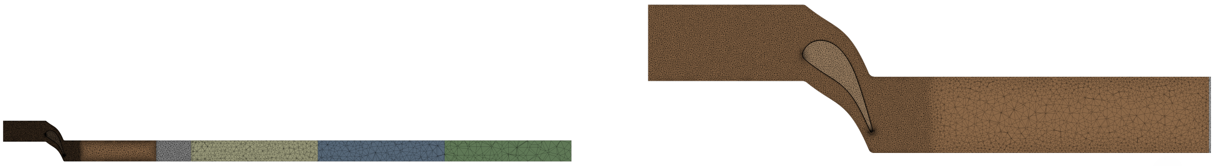

(a) (b)

Figure 5.5: Top View at Midspan of the Full Mesh (a) and Magnification of the Meshed Vane Zone (b) Used for Unsteady URANS Simulations for Non-Cooled Vane.

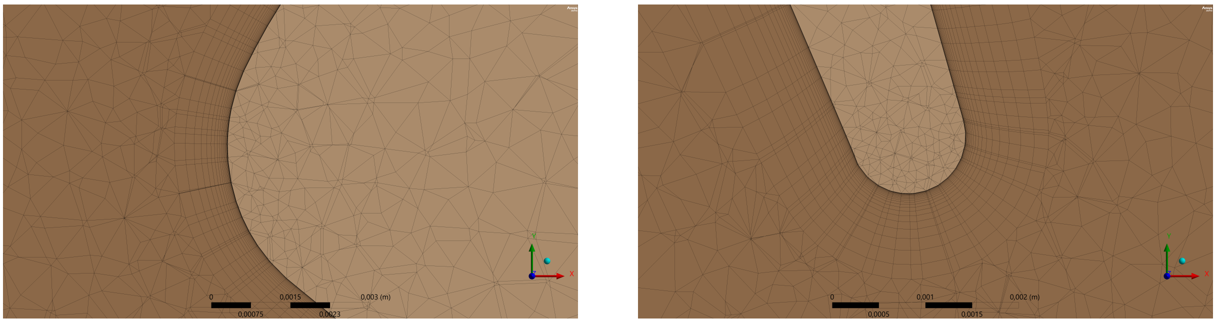

(a) (b)

Figure 5.6: Top View at Midspan of the Leading Edge (a) and Trailing Edge (b) Magnification of the Meshed Vane Zone Used for Unsteady URANS Simulations for Non-Cooled Vane.

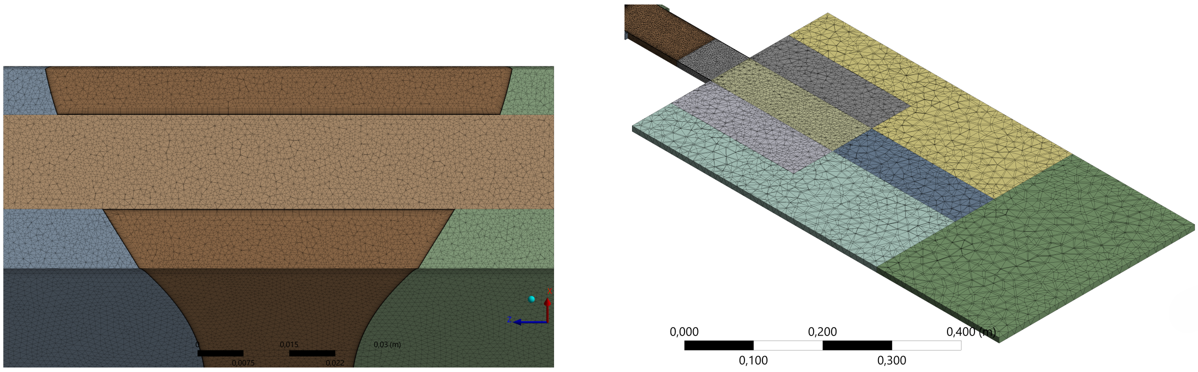

(a) (b)

Figure 5.7: Section View of the Meshed Vane (a) and Isometric View of the Meshed Plenum (b) Used for Unsteady URANS Simulations for Non-Cooled Vane.

Figures 5.8, 5.9, 5.10, and 5.11 present the images corresponding to the computational grid used to analyze the case with the vane cooled by smooth channels. The mesh sizing in the leading and trailing edge regions is noted to propagate onto the inner contact surface between the vane and the cooling fluid. The cross-section cutting through the second cooling channel demonstrates how the inflation parameters were also applied to the internal contact surfaces between the solid and fluid domains.

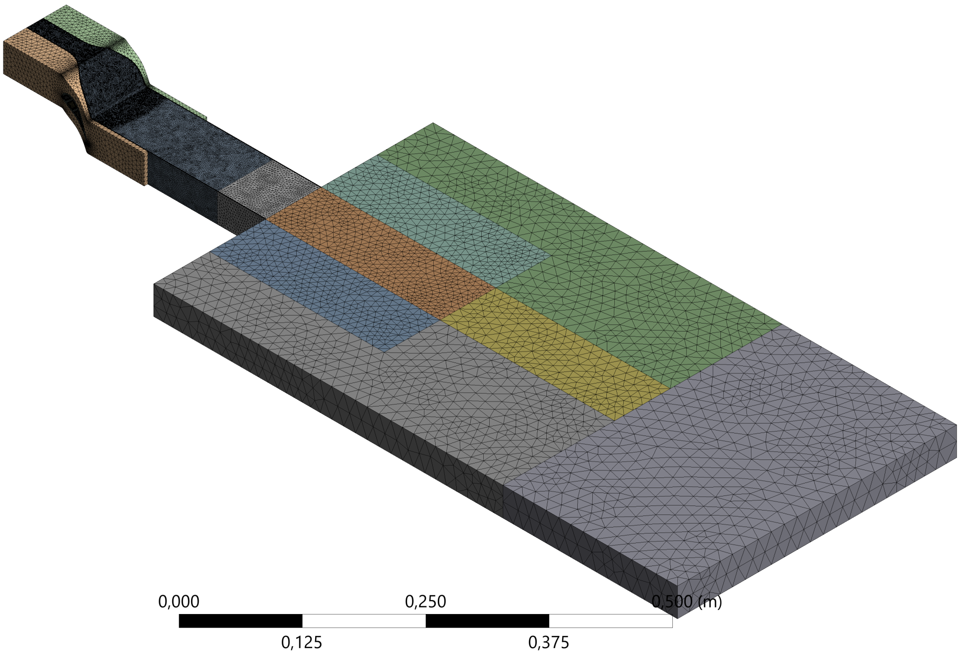

Figure 5.8: Isometric View of the Mesh Used for Unsteady URANS Simulations for Smooth Channel Cooled Vane.

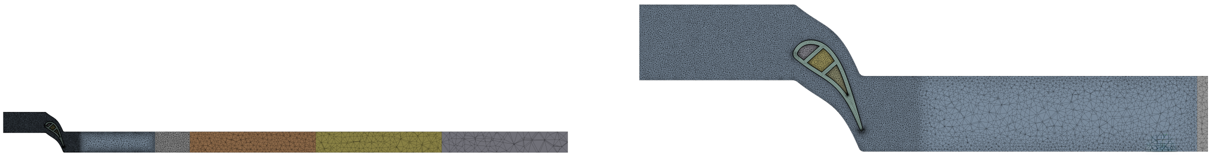

(a) (b)

Figure 5.9: Top View at Midspan of the Full Mesh (a) and Magnification of the Meshed Vane Zone (b) Used for Unsteady URANS Simulations for Smooth Channel Cooled Vane.

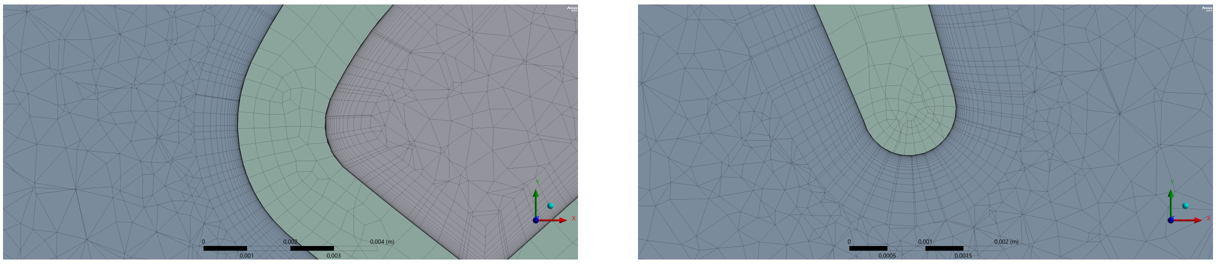

(a) (b)

Figure 5.10: Top View at Midspan of the Leading Edge (a) and Trailing Edge (b) Magnification of the Meshed Vane Zone Used for Unsteady URANS Simulations for Smooth Channel Cooled Vane.

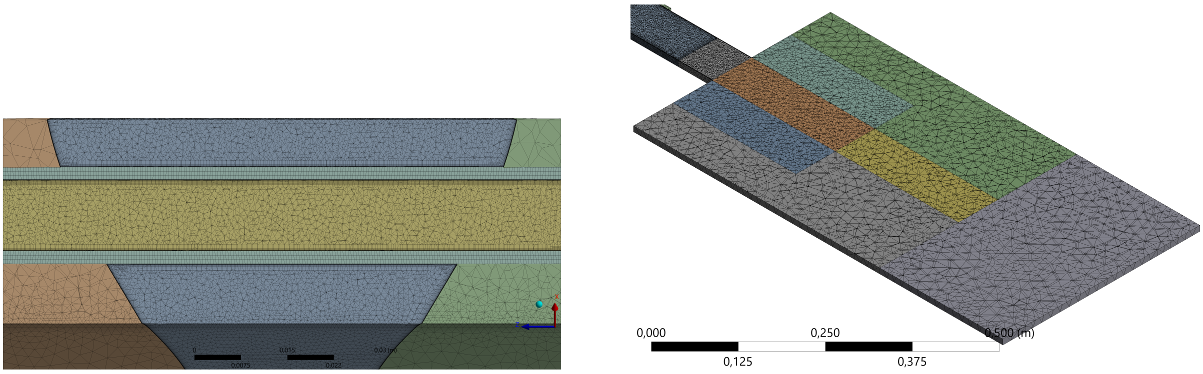

(a)

(b)

Figure 5.11: Section View of the Meshed Channel (a) and Isometric View of the Meshed Plenum (b) Used for Unsteady URANS Simulations for Smooth Channel Cooled Vane.

Figures 5.12, 5.13, 5.14, and 5.15 present the images referring to the computational grid used to analyze the case with the vane cooled by ribbed channels. These channels can be seen in the last graphic, which replaces the plenum section plane. In this last view, in fact, the mesh concentrated around the internal cooling ribs is shown: the layer of prism elements (or quad layers) is notable, which is necessary to accurately study the viscous thermal exchange that occurs in the boundary layer due to temperature gradients.

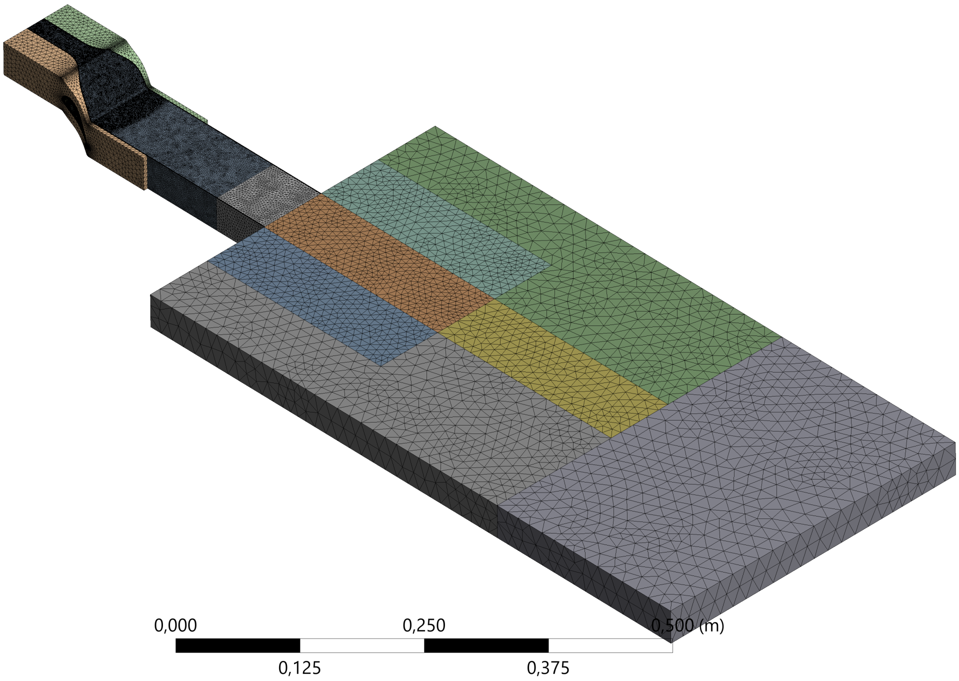

Figure 5.12: Isometric View of the Mesh Used for Unsteady URANS Simulations for Ribbed Channel Cooled Vane.

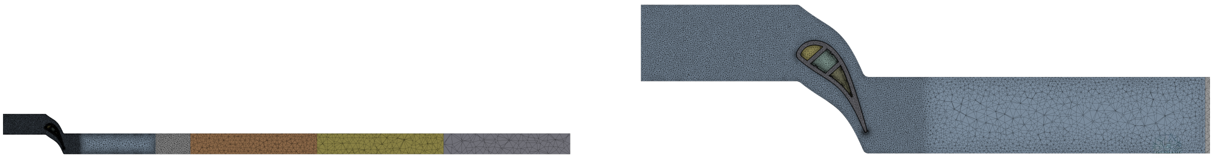

(a) (b)

Figure 5.13: Top View at Midspan of the Full Mesh (a) and Magnification of the Meshed Vane Zone (b) Used for Unsteady URANS Simulations for Ribbed Channel Cooled Vane.

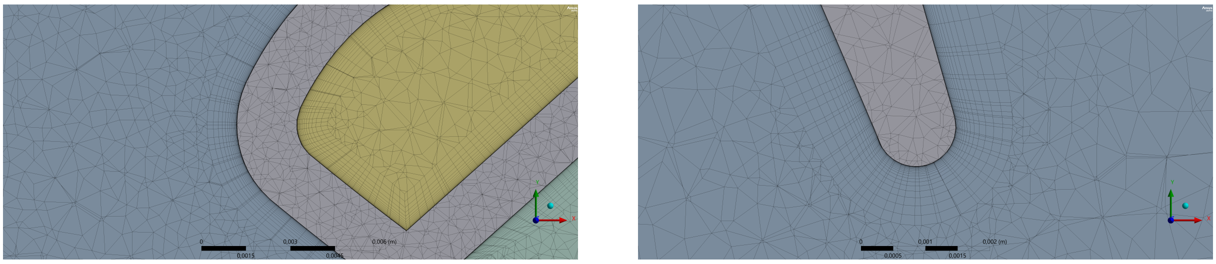

(a) (b)

Figure 5.14: Top View at Midspan of the Leading Edge (a) and Trailing Edge (b) Magnification of the Meshed Vane Zone Used for Unsteady URANS Simulations for Ribbed Channel Cooled Vane.

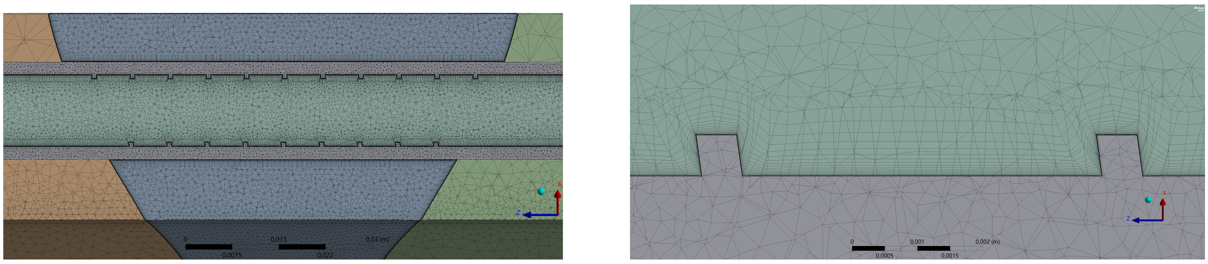

(a) (b)

Figure 5.15: Section View of the Meshed Vane (a) and Magnification of the Meshed Ribs (b) Used for Unsteady URANS Simulations for Ribbed Channel Cooled Vane.

5.3 Boundary Conditions and Setup

Figure 5.16 illustrates the boundary conditions applied at the domain inlet over a single period. These conditions derive from the scaling of the actual conditions calculated at the exhaust of a Rotating Detonation Combustor (RDC). The observed attenuation effect is attributed to the connecting channel between the two components, which damps the oscillations of the inlet variables while leaving their incidence angle unchanged. It can be noted that the oscillation of $\Delta\alpha = 40°$ is a value easily found in RDC literature data. Table 22 lists the boundary conditions, by type and magnitude, that were applied to the solver. The total inlet conditions mentioned as *Unsteady B. C.* refer to the profile shown in the figure above. It is important to note the application of a slip wall condition on the plenum side walls: this condition is necessary for the plenum to effectively simulate a free-shear stress boundary evolution (or far-field evolution). Table 23 reports the solver setup data. The choice that differentiates these simulations from the preceding ones is the selection of the time step: in the URANS case, setting a time marching step is mandatory. By

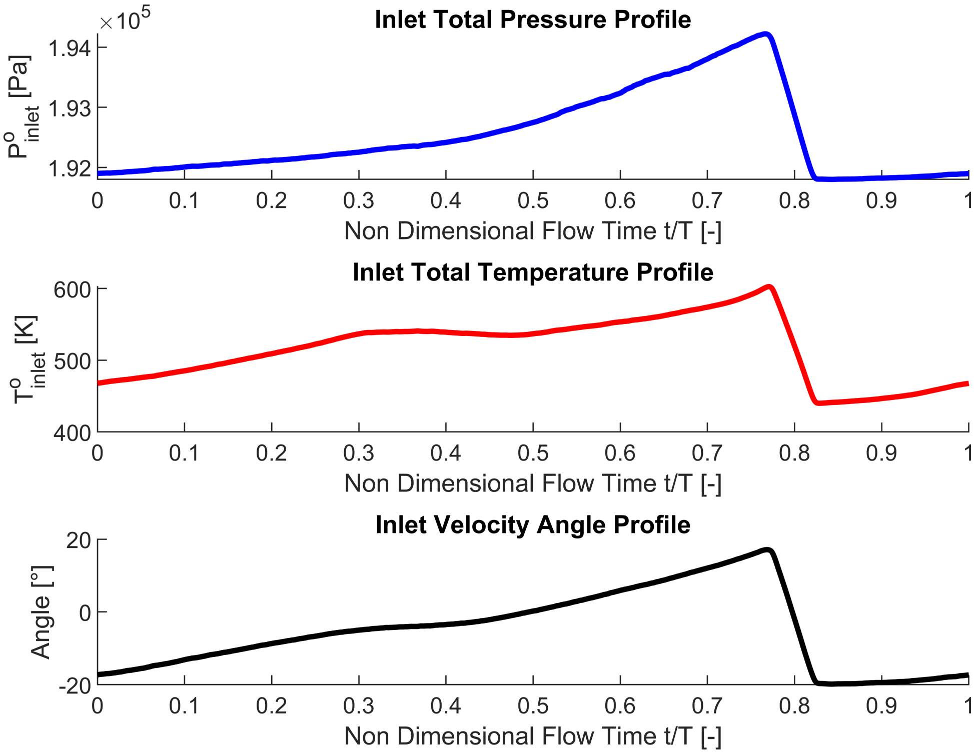

Figure 5.16: Oscillatory Inlet Boundary Conditions Plot over a Period.

	Main Inlet	**Main Outlet**	**Coolant Inlet**	**Coolant Outlet**
Total Pressure [Pa]	**Unsteady B.C.**	-	107570	-
Total Temperature [K]	**Unsteady B.C.**	-	303.15	-
Gauge Pressure [Pa]	-	101325	-	106390
Backflow Temperature [K]	-	440	-	298.15
Periodicity		Superior	Inferior	
No Slip		Vane Surface	Endwalls	
Slip		Plenum Side Walls		
Adiabaticity		Vane Surface	Endwalls	

Table 22: Boundary Conditions Used in Unsteady URANS Simulations.

setting this parameter, given the cell dimensions of the computational mesh, a map of the Courant number can be derived, whose maximum value provides information about the method's stability. Since we are dealing with an implicit solver, the Courant-Friedrichs-Lewy (CFL) condition does not impose severe restrictions. The conditions reported in Table 24 refer to the characteristics of the materials used. For uniformity with the results previously obtained, the same modifications mentioned in the steady-state simulation case were applied.

Solver Type	Implicit Density-Based
Accuracy Order	2^{nd} Order
Initialization	Fluent Hybrid
Time Step Type	Frequency Based
Frequency	$5\ kHz$
Time Steps per Period	100
Save Frequency	Every 5 Time Steps

Table 23: Solver Setup Used in Unsteady URANS Simulations.

	Fluid	**Solid**
Name	Air	CMSX-4
Density ρ $[kg/m^3]$	Ideal Gas Law	8700
Heat Capacity C_p $[J/kg \cdot K]$	NASA 9-Piecewise Polynomial	500
Thermal Conductivity k $[W/m \cdot K]$	0.0242	7.8
Dynamic Viscosity μ $[Pa \cdot s]$	Sutherland Law	-
Molecular Weight $[kg/kmol]$	28.966	-

Table 24: Material Setup Used in Unsteady URANS Simulations.

5.4 Results

This section will reference the solutions of the unsteady simulations run for $T_{max} = 35$ periods. To ensure convergence in time, the cross-correlation method was applied to evaluate the similarity between the distributions of certain monitored variables in two consecutive periods.

The following variables were evaluated: total pressure p^o_{out}, static temperature T_{out}, Mach number Ma_{out}, and flow angle α_{out} at the stator-rotor interface plane. This section is located downstream of the vane at a distance equal to 30% of the vane's true chord. Additionally, the oscillations of the area-averaged static temperature on the external surface and the volume-averaged temperature of the solid vane were evaluated. The cross-correlation method was then applied to three quantities evaluated at three different points. The three reference quantities are density ρ, Mach number Ma, and total temperature T^o, which directly relate to the conserved variables in the governing equations. The three analysis points are a mesh vertex located in the opening area of the convergent duct upstream of the solid vane, denoted as *inlet*; a point located in the passage between the vanes, upstream of the cascade throat, denoted as *passage*; and a point located on the stator-rotor coupling section. All points have a Z coordinate of zero, and are therefore located on the midspan section. The cross-correlation method was subsequently applied to the vane's thermal variables to confirm the heat transfer stability.

To evaluate the information content of the individual signals, the Fast Fourier Transform (FFT) was then applied to the previously obtained signals, followed by a Welch filter, to achieve clearer and less noisy results.

Finally, the contour analyses were conducted at midspan, focusing on the main flow's Mach number, total pressure, and total temperature, as well as the static temperature of the solid in the midspan section.

Non-Cooled Vane Unsteady Simulation

In Figure 5.17, the oscillations of the monitored variables in the fluid dynamics and thermal fields are reported. Visually, the similarity of the waveform tends to increase as the periods elapse. The only anomalous waveform is the one contained in the plot monitoring the volume-averaged temperature. This variable, in fact, tends to increase very slowly. Due to this inconsistency, after achieving convergence of the surface-averaged temperature, it was decided to continue the calculation for approximately the same number of periods already computed. Figures 5.18 and 5.19 show the oscillations of the three quantities considered for the subsequent cross-correlation analysis. At first glance, the signal recorded at the most downstream section (outlet) exhibits a much lower frequency wave than that imposed by the oscillating boundary conditions. This periodic signal could be the result of acoustic waves reflected from the outlet boundary. However, these waves are unable to propagate upstream of the cascade throat due to the presence of a supersonic region in that portion of the domain.

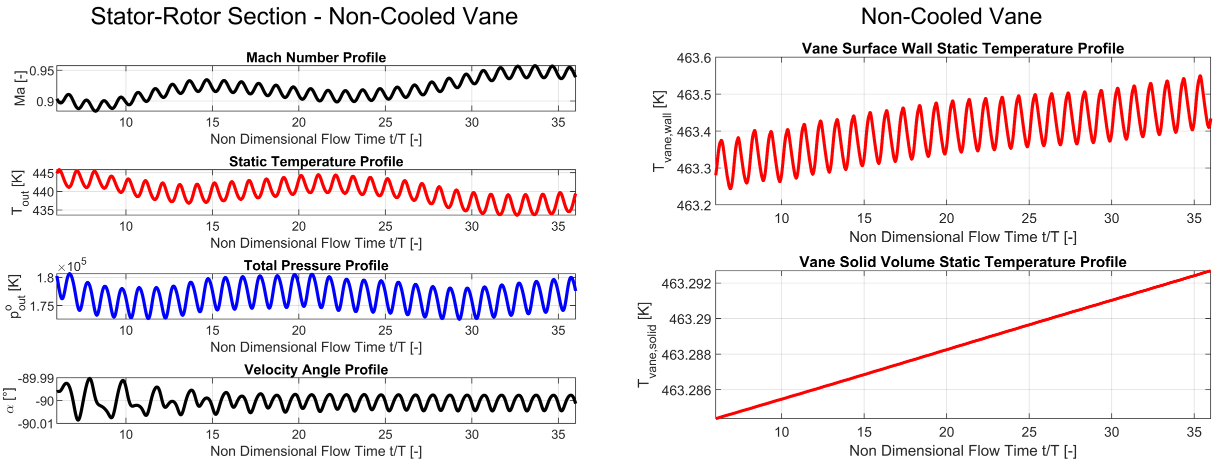

(a) (b)

Figure 5.17: Oscillations of Monitored Variables at Stator-Rotor Coupling Section (a) and on Vane Surface and Volume (b) for the Non-Cooled Design.

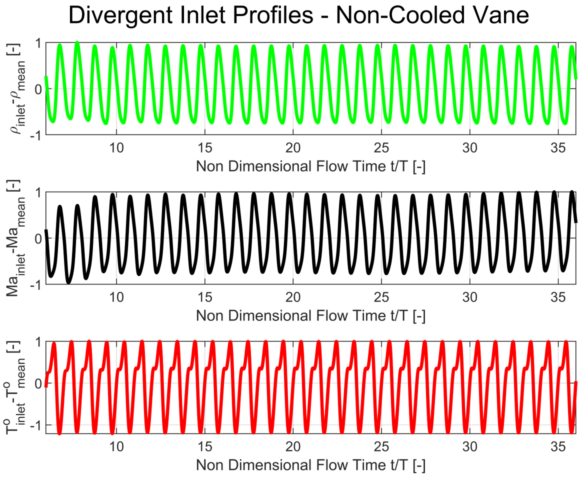

Figure 5.18: Oscillations of Monitored Variables at Inlet Monitor Point for the Non-Cooled Design.

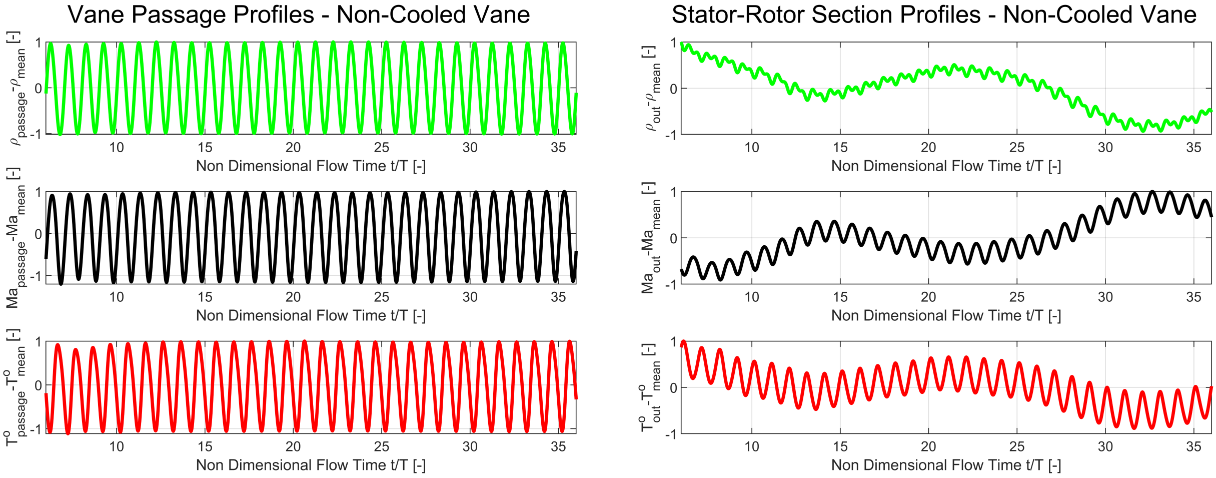

(a) (b)

Figure 5.19: Oscillations of Monitored Variables at Inter-Vanes Passage (a) and Stator-Rotor Coupling Section (b) Monitor Point for the Non-Cooled Design.

Figures 5.20, 5.21, 5.22, and 5.23 present the aforementioned cross-correlation analyses and Fourier Transforms. From the former set of figures, it is observed that the signal tends towards convergence, established at 98% similarity, around the eighteenth period. For the reasons mentioned above, it was deemed preferable to continue the calculation up to the thirty-fifth period to obtain a better estimate of the solid volume temperature. From the second group of figures, and particularly after the application of the Welch filter, peaks of energy corresponding to the oscillation frequency of the boundary conditions and its harmonics are noticeable. Furthermore, the outlet signal presents lower energy compared to the signal recorded at the vane inlet or in the passage: this is the expected oscillation attenuation effect of a turbine stator stage. Finally, the longer period signal was not detected in this analysis, indicating that a greater number of calculated periods is needed to achieve good resolution at low frequencies.

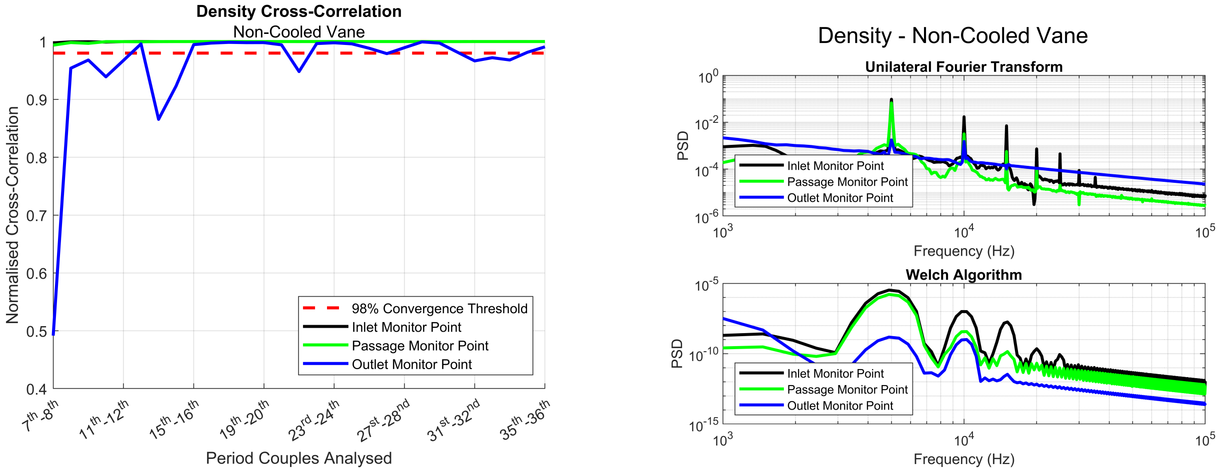

(a)

(b)

Figure 5.20: Cross-Correlation (a) and Fourier Transform with Welch Algorithm (b) of the Density Oscillating Values for the Non-Cooled Design.

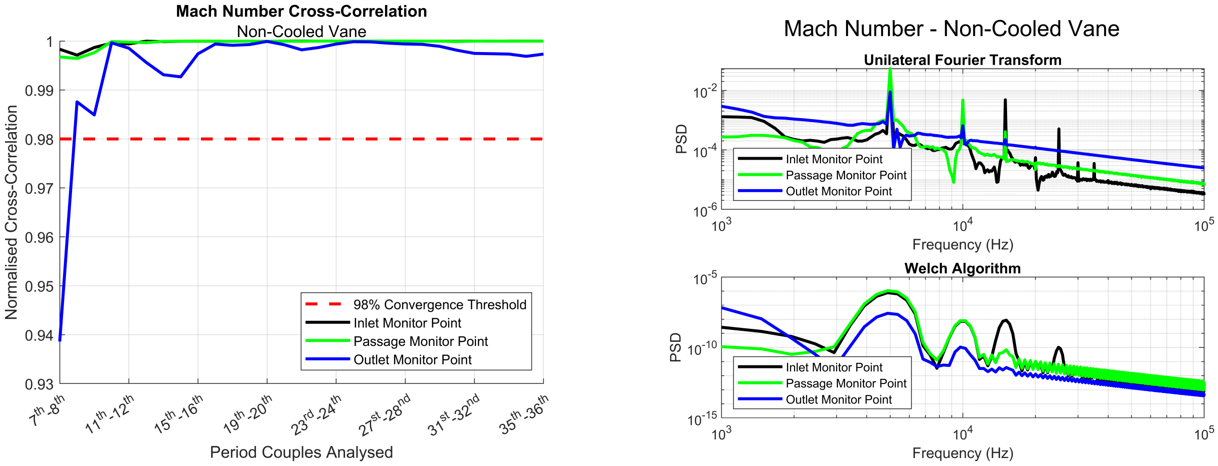

(a) (b)

Figure 5.21: Cross-Correlation (a) and Fourier Transform with Welch Algorithm (b) of the Mach Number Oscillating Values for the Non-Cooled Design.

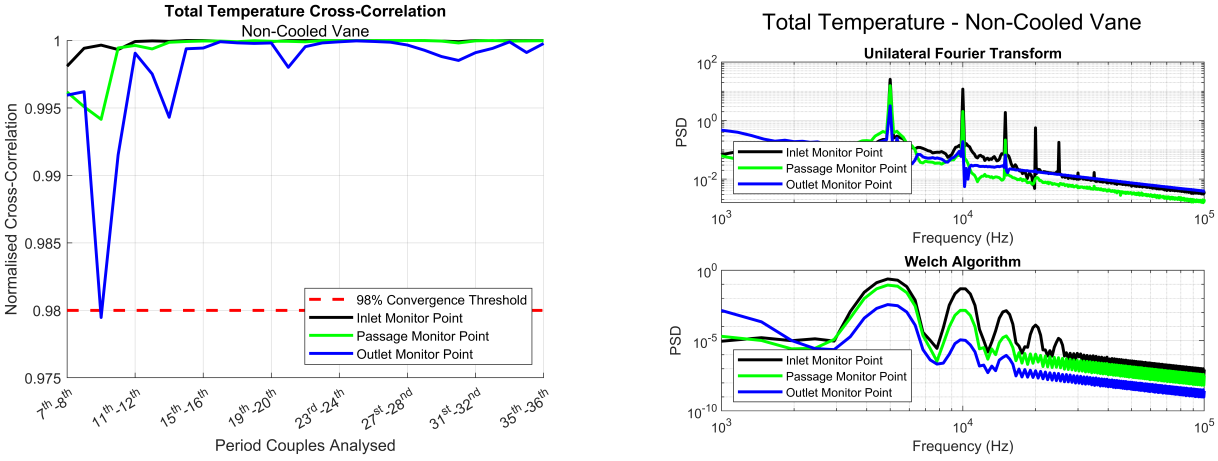

(a) (b)

Figure 5.22: Cross-Correlation (a) and Fourier Transform with Welch Algorithm (b) of the Total Temperature Oscillating Values for the Non-Cooled Design.

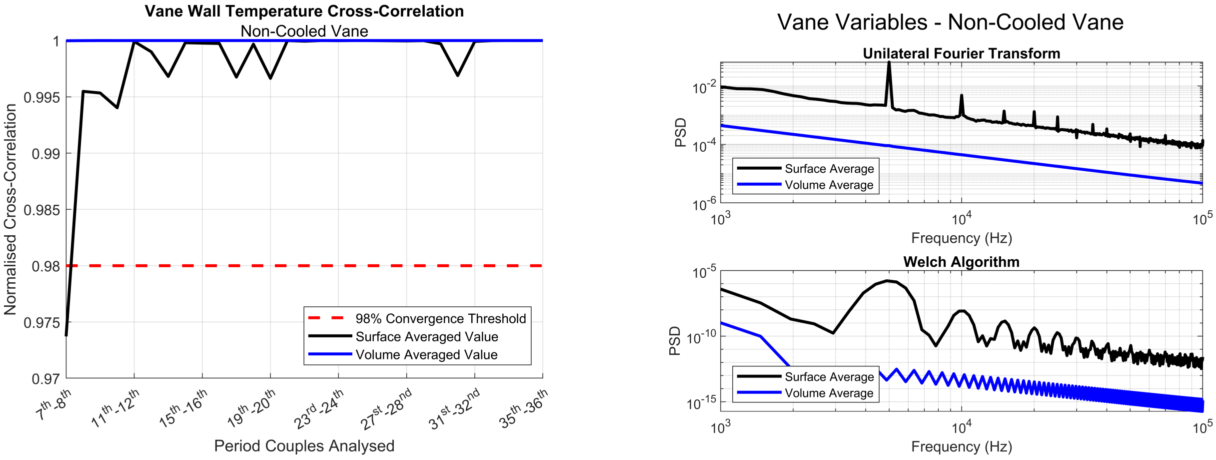

(a) (b)

Figure 5.23: Cross-Correlation (a) and Fourier Transform with Welch Algorithm (b) of the Vane Monitored Variables Oscillating Values for the Non-Cooled Design.

Figures 5.24 and 5.25 show the Mach number distributions of the main flow at different points in the cycle being analyzed. A fundamental use of this contour is to provide an indication of the stagnation point shift relative to the nominal leading edge. Unlike the angle imposed as a boundary condition (which often refers to the pitch angle), this angle measures the flow angle of attack, which does not exhibit a variation as visible as the one induced by the inlet condition. It is also possible to note that the cascade throat remains sonic for all analyzed instants. Figures 5.26 and 5.27 show the total pressure distribution. This quantity, imposed as a boundary condition, highlights the wave front entering the cascade, which is then swallowed by the throat. The most evident total pressure drop is caused by the wake and the gradients generated in the boundary layer that develops along the wall. Figures 5.28 and 5.29 show the total temperature distribution. Here, too, the wave front at the inlet is visible, which, however, is easily dissipated by the solid metallic body immersed in the flow. Figures 5.30 and 5.31 show the static temperature distribution in the solid midspan section. The very narrow legend, as the extremes are only $\Delta T = 10\ K$ apart, highlights the stagnation point shift on the airfoil surface and a cooling zone following the point where the sonic shock is imposed. This structure, in fact, leads to violent boundary layer mixing which, together with the subsequent supersonic expansion, significantly lowers the temperature at that point. The temperature distribution, in any case, does not undergo significant variations between the points of interest.

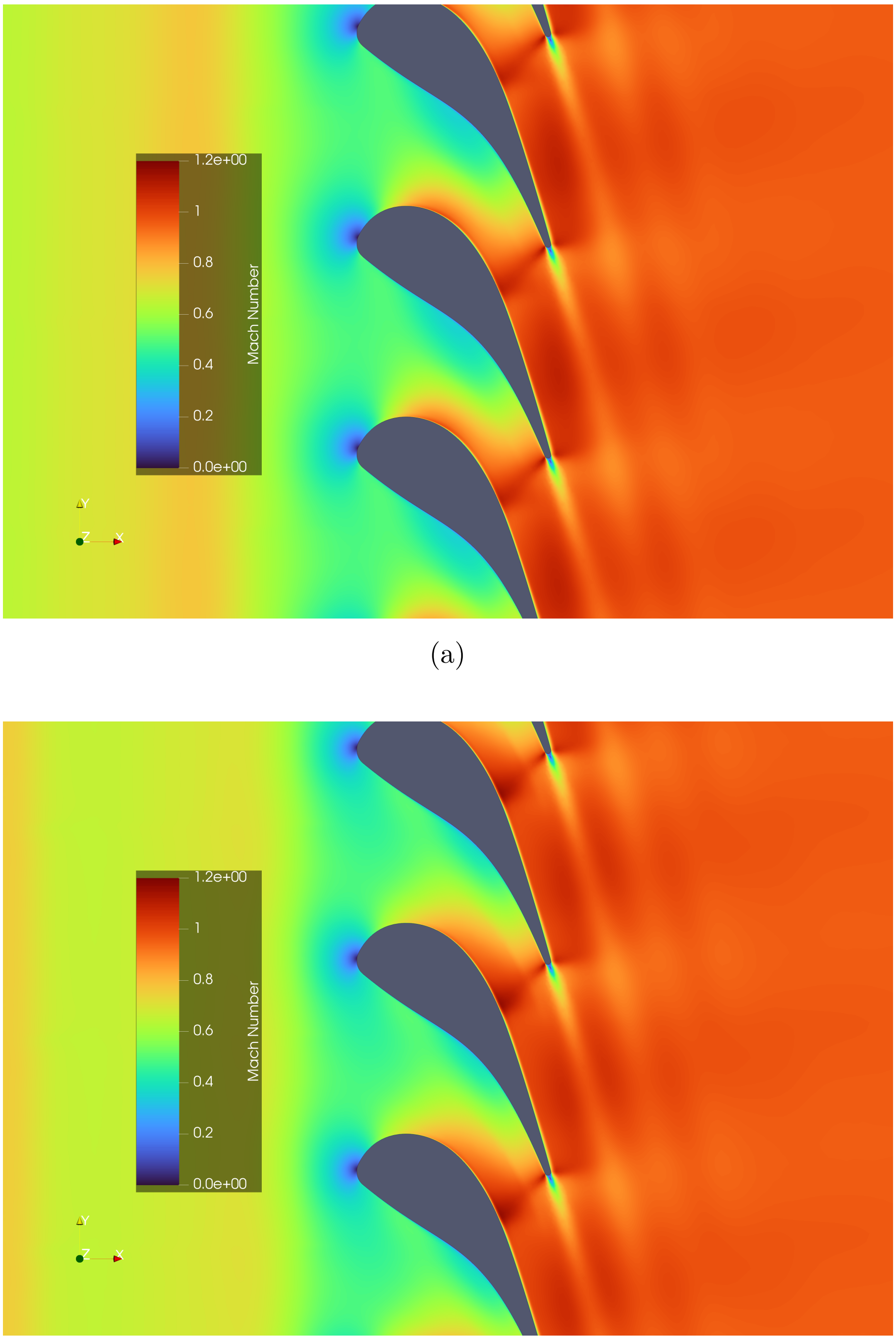

(a)

(b)

Figure 5.24: Main Flow Mach Number Contour at Midspan at 0% (a) and 25% (b) of the Period for Non-Cooled Vane Design.

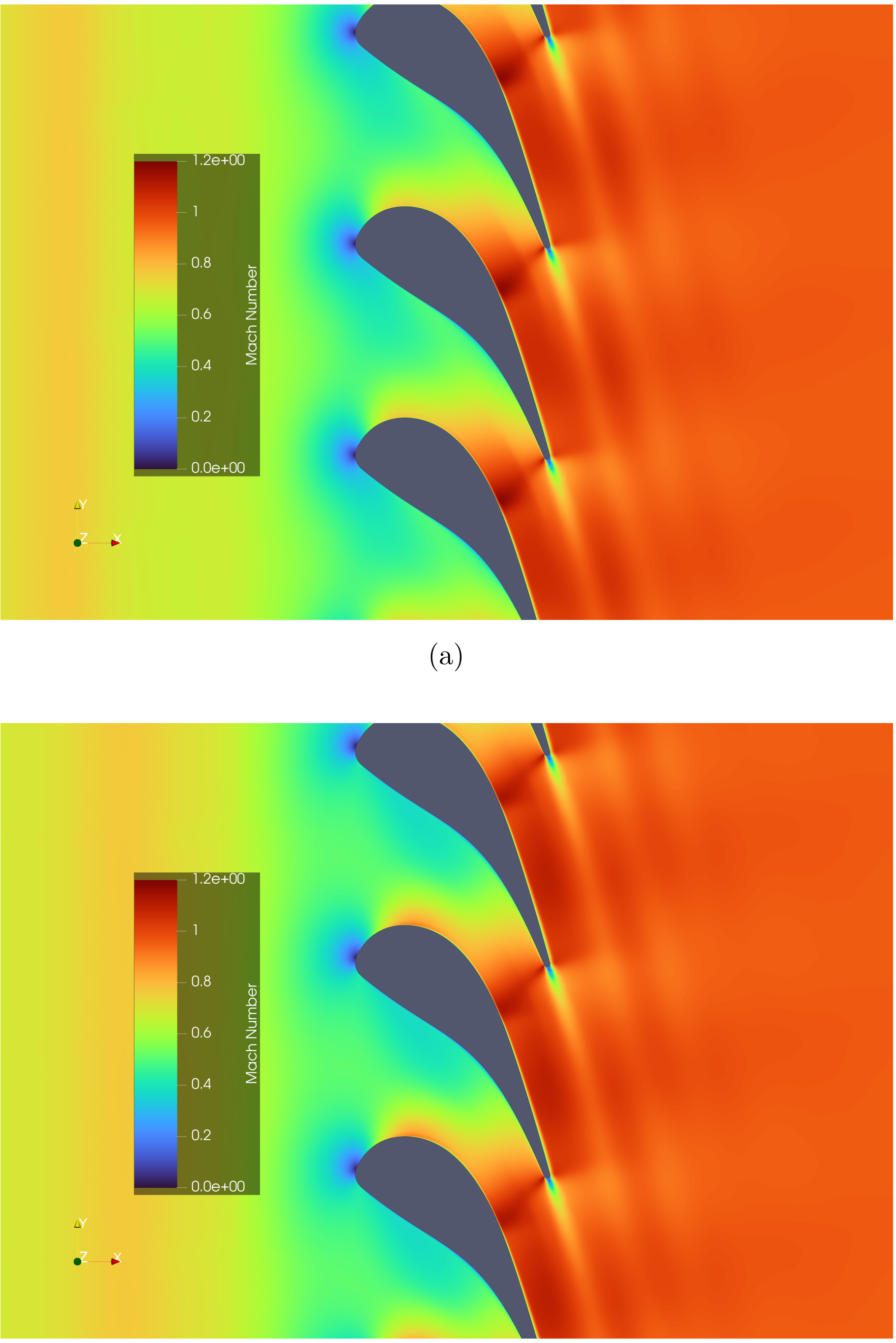

(a)

(b)

Figure 5.25: Main Flow Mach Number Contour at Midspan at 50% (a) and 75% (b) of the Period for Non-Cooled Vane Design.

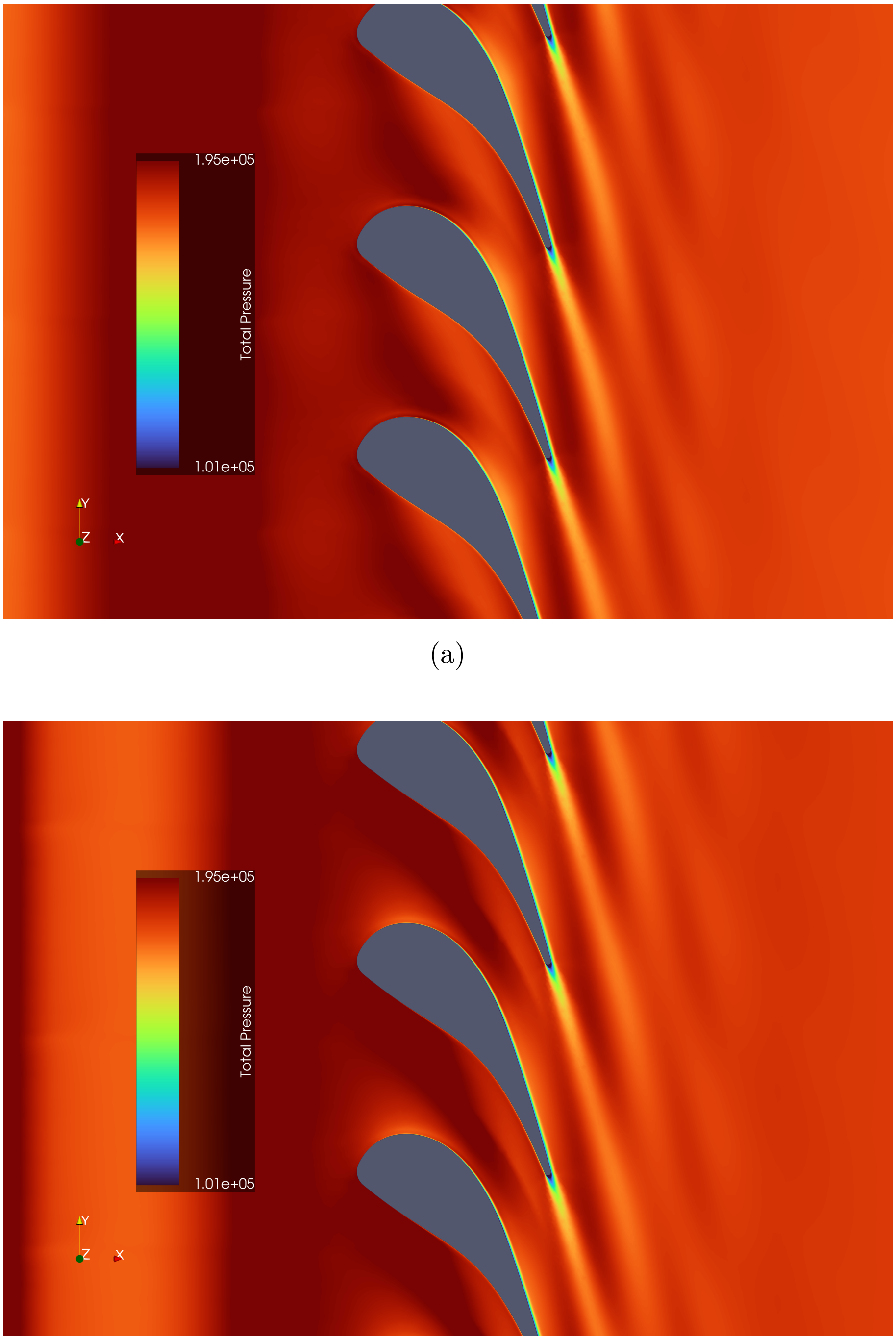

(a)

(b)

Figure 5.26: Main Flow Total Pressure Contour at Midspan at 0% (a) and 25% (b) of the Period for Non-Cooled Vane Design.

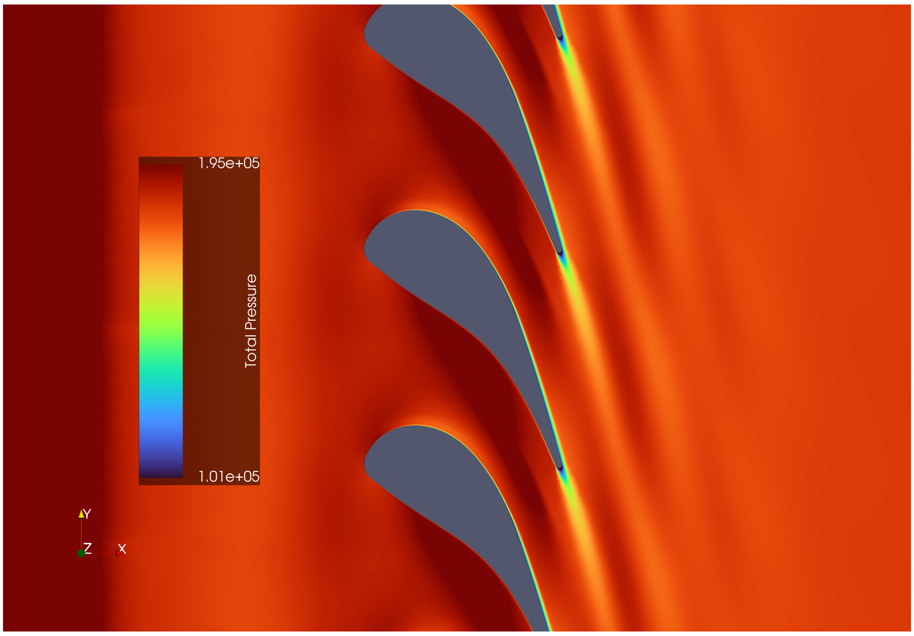

(a)

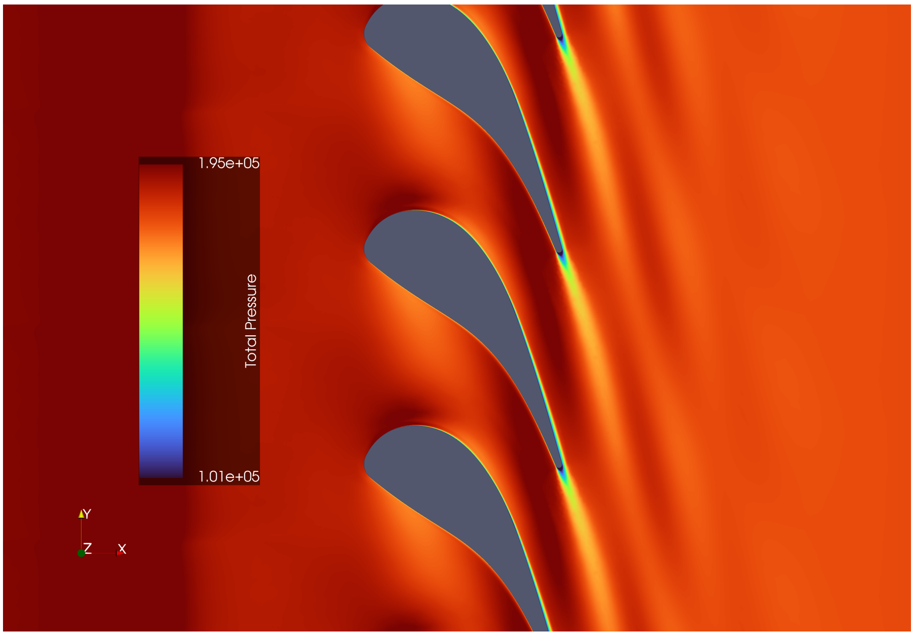

(b)

Figure 5.27: Main Flow Total Pressure Contour at Midspan at 50% (a) and 75% (b) of the Period for Non-Cooled Vane Design.

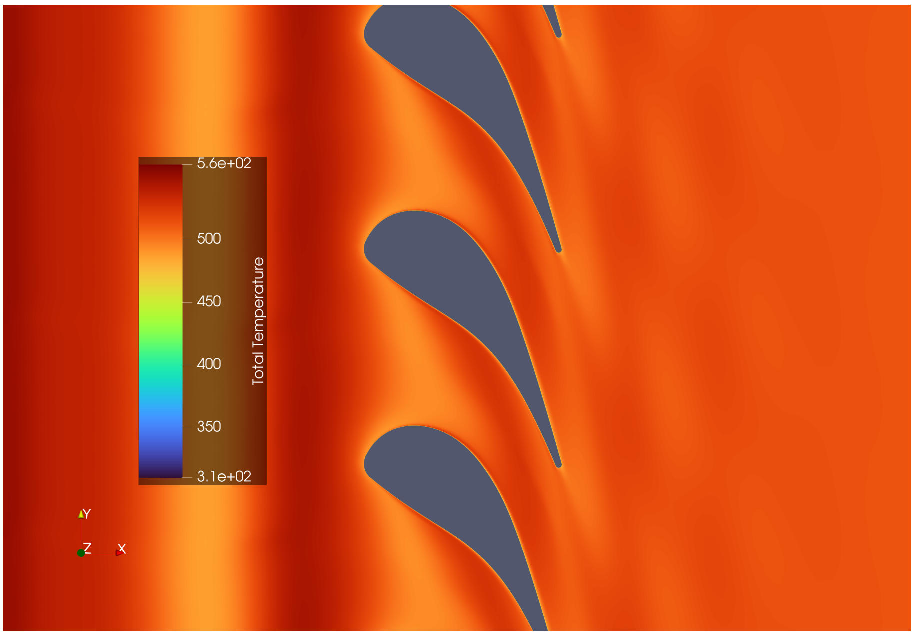

(a)

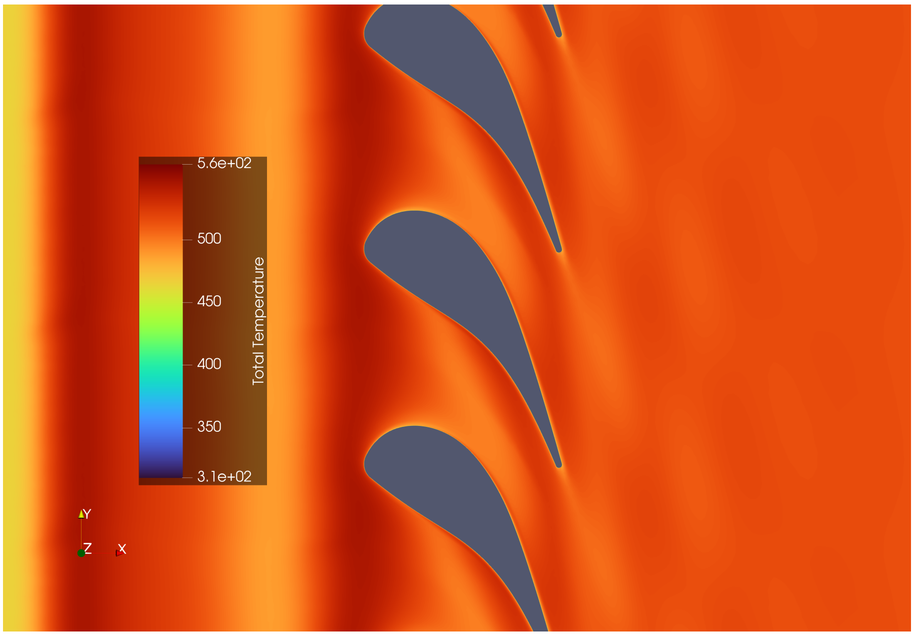

(b)

Figure 5.28: Main Flow Total Temperature Contour at Midspan at 0% (a) and 25% (b) of the Period for Non-Cooled Vane Design.

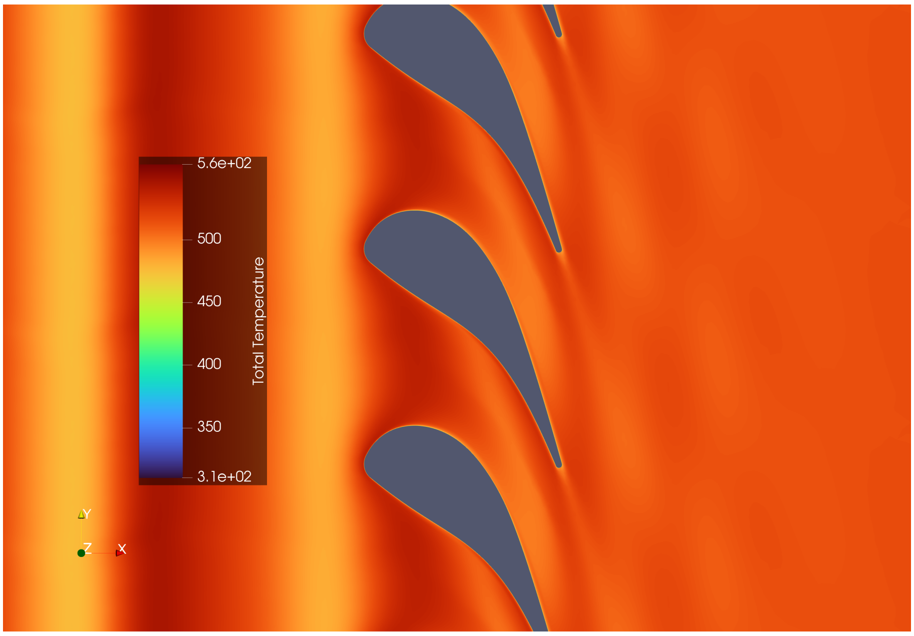

(a)

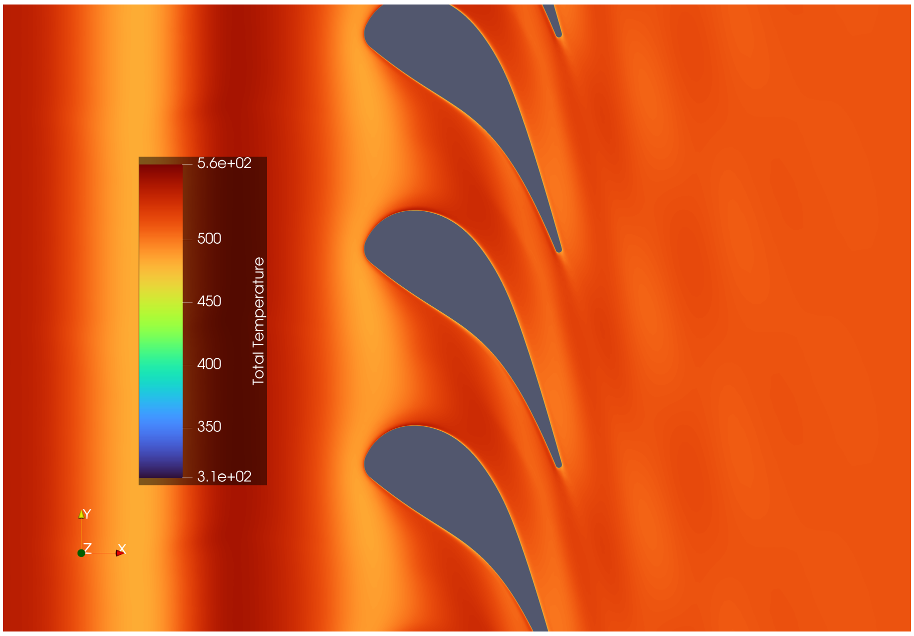

(b)

Figure 5.29: Main Flow Total Temperature Contour at Midspan at 50% (a) and 75% (b) of the Period for Non-Cooled Vane Design.

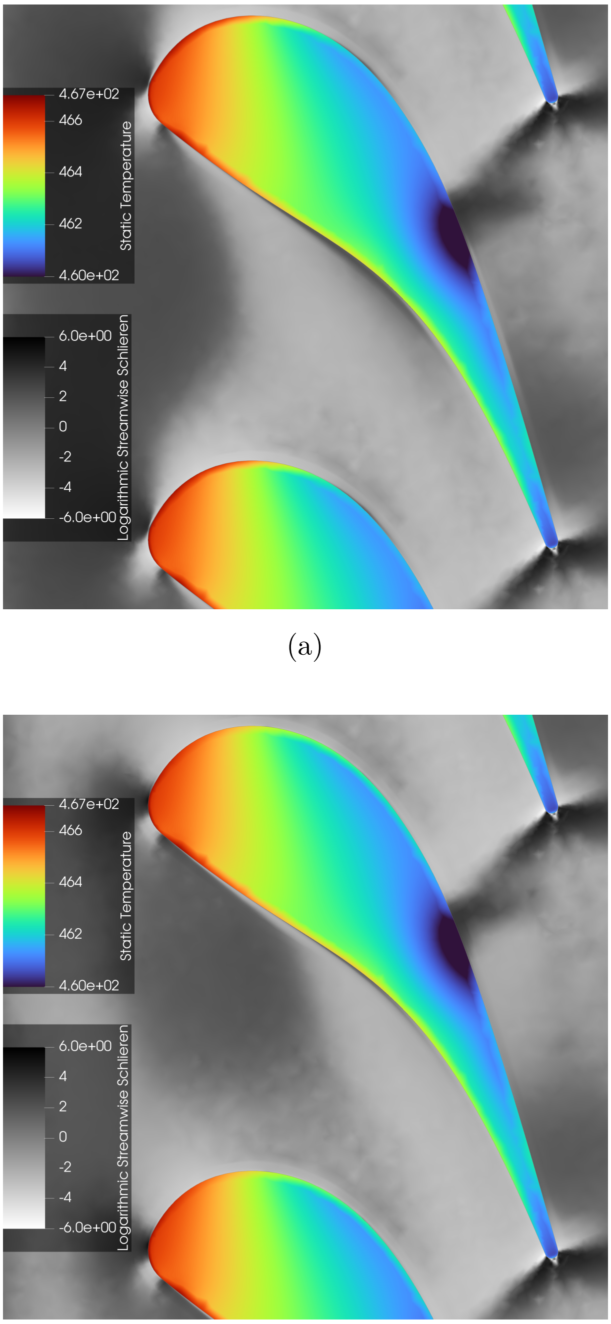

(a)

(b)

Figure 5.30: Solid Vane Static Temperature with the Logarithmic Streamwise Schlieren of the Main Flow Contour at Midspan Section at 0% (a) and 25% (b) of the Period for Non-Cooled Vane Design.

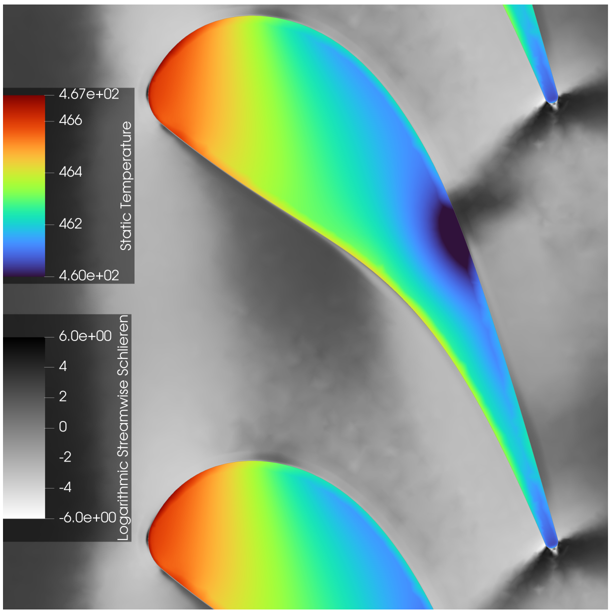

(a)

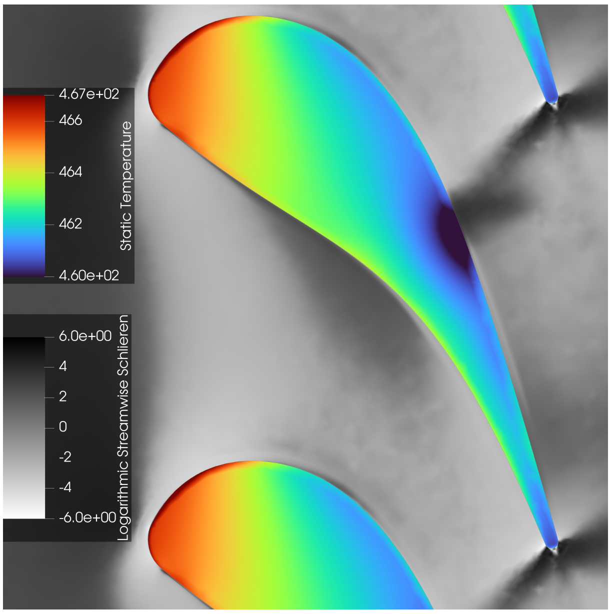

(b)

Figure 5.31: Solid Vane Static Temperature with the Logarithmic Streamwise Schlieren of the Main Flow Contour at Midspan Section at 50% (a) and 75% (b) of the Period for Non-Cooled Vane Design.

Table 25 reports the point-wise values of the quantities used in the cross-correlation study. A variation in the quantities calculated at the stator-rotor interface section is noted, indicating the passage of the wave front. This wave, however, arrives at the section of interest with a phase shift of 25% of the period, suggesting that there is an integer number of wave fronts between the inlet and the coupling section plus a phase shift of a quarter of a period. The plots in Figure 5.32 show the wall distributions of static pressure and temperature measured on the vane surface at the midspan section. Due to the distance from the solid domain walls, the pressure distribution appears smooth. Furthermore, the pressure variation induced by the incident wave front ceases its disturbing effects on the steady-state distribution downstream of the throat. In this section, in fact, the pressure ratio drops below the value of 0.5, leading to a sonic throat and the inability for the flow to transmit information about the downstream zone upstream, thus attenuating the imposed oscillations. The static temperature distribution does not deviate much from the peak value, suggesting that the only effective cooling effects are induced by convective phenomena generated around the solid body, such as in the region of the sonic shock, highlighted by a temperature well (or depression). To better highlight the wall temperature variation, Figure 5.33 shows a differential map of the wall static temperature, created by subtracting the time-step-averaged distribution from the original distribution and dividing it by the latter. This results in a percentage variation of $\Delta T = \pm 1\%$ across the entire surface, effectively drawing attention away from any heat transfer mechanism other than the sonic shock.

	0% of the Cycle	**25% of the Cycle**	**50% of the Cycle**	**75% of the Cycle**
Average S-R Section Total Pressure [Pa]	177594	174171	177197	179973
Average S-R Section Static Temperature [K]	439.439	438.405	434.980	453.310
Average S-R Section Mach Number [-]	0.939	0.938	0.951	0.953
Average Static Wall Vane Pressure [Pa]	126059	127839	129317	127569
Average Static Wall Vane Temperature [K]	463.435	436.530	463.515	463.436
Volume Averaged Static Vane Temperature [K]	463.292	463.292	463.293	463.293

Table 25: Monitored Main flow and Vane Variables at Different Time Steps for Non-Cooled Vane.

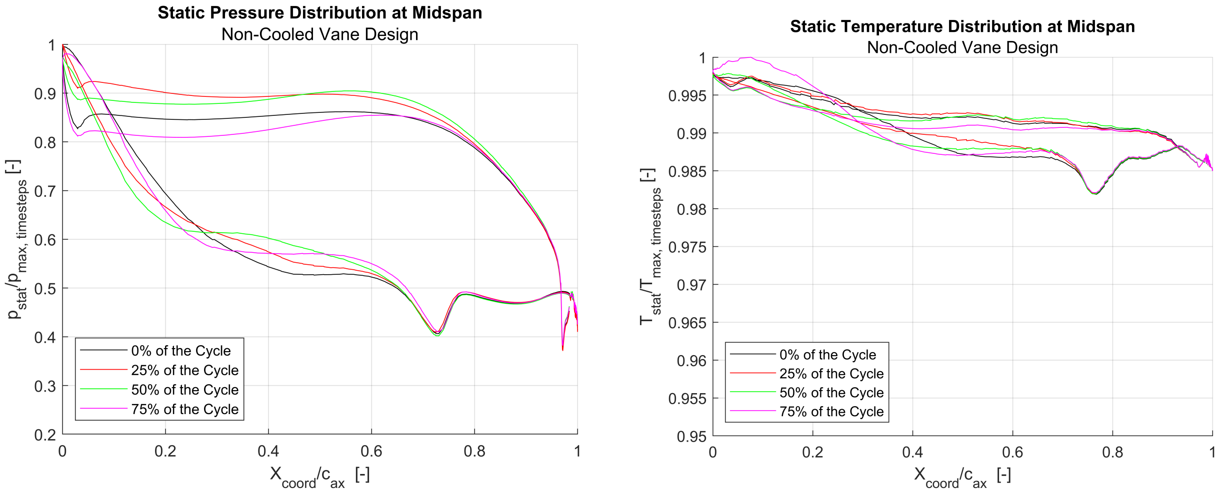

(a) (b)

Figure 5.32: Pressure (a) and Temperature (b) Distribution at Midspan Section of the Vane Surface for the Non-Cooled Vane at Different Time Steps.

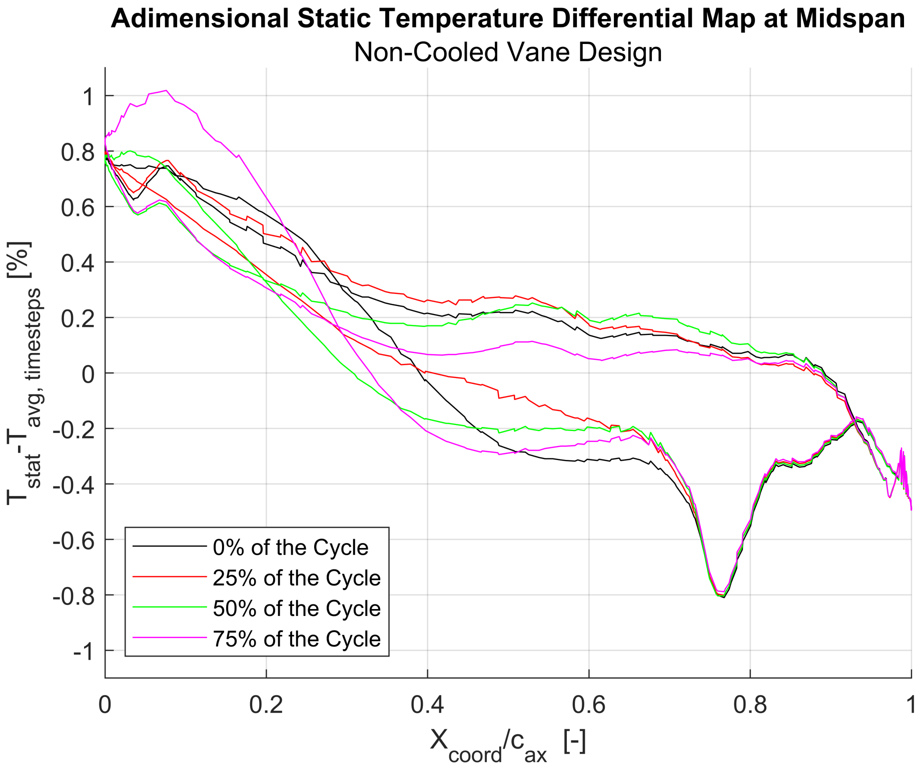

Figure 5.33: Differential Map of the Percentage Wall Temperature Variations on the Vane Surface at Midspan Section for Non-Cooled Vane Design.

Smooth Channel Cooled Vane Unsteady Simulation

Figure 5.34 reports the signals recorded during the simulation over time steps. Observing the oscillation trends, the system clearly originates from a fluid dynamic transient. By the end of the recording window, however, the waveform tends to stabilize. The volume-averaged temperature of the solid is the only variable that does not reach asymptotic convergence, but its range of variation is limited and exhibits a shallow slope. Figures 5.35 and 5.36 show the oscillations of the three variables used in the cross-correlation test evaluated over time at the three monitor points previously illustrated. The zone upstream of the vane shows very fast convergence, driven by the free-stream conditions imposed directly by the boundary conditions. Convergence in the inter-vane passage occurs more rapidly than at the downstream station, demonstrating that the cascade throat is effective in damping the oscillations propagating upstream from the outlet. In the downstream zone, specifically the stator-rotor coupling section, the same cyclic trend shown in the previous simulation is observed.

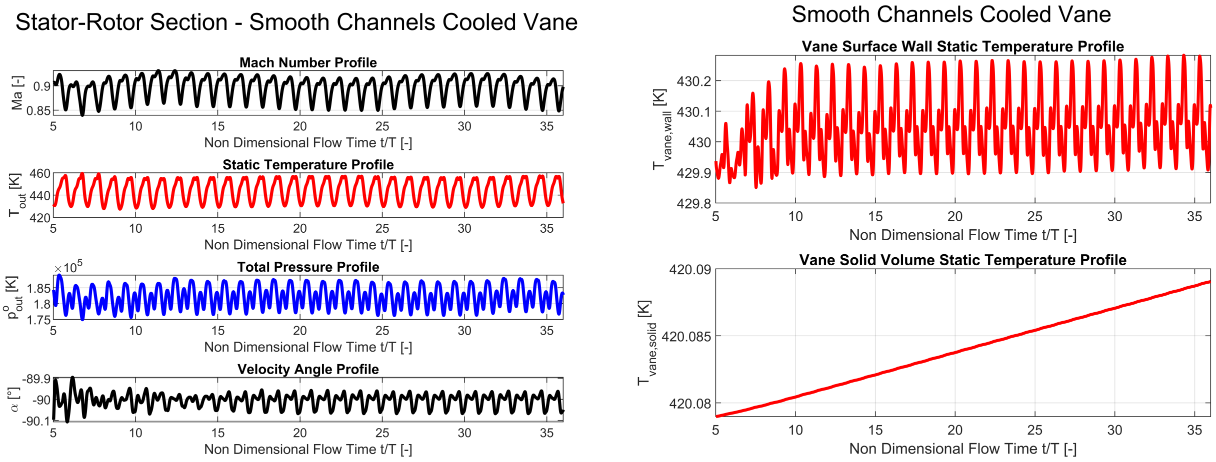

(a)

(b)

Figure 5.34: Oscillations of Monitored Variables at Stator-Rotor Coupling Section (a) and on Vane Surface and Volume (b) for the Smooth Channel Cooled Design.

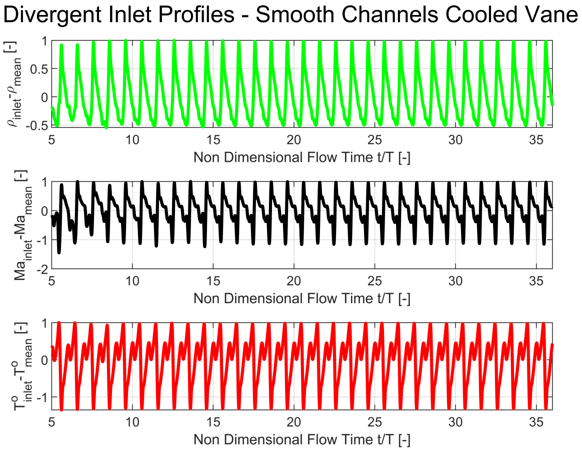

Figure 5.35: Oscillations of Monitored Variables at Inlet Monitor Point for the Smooth Channel Cooled Design.

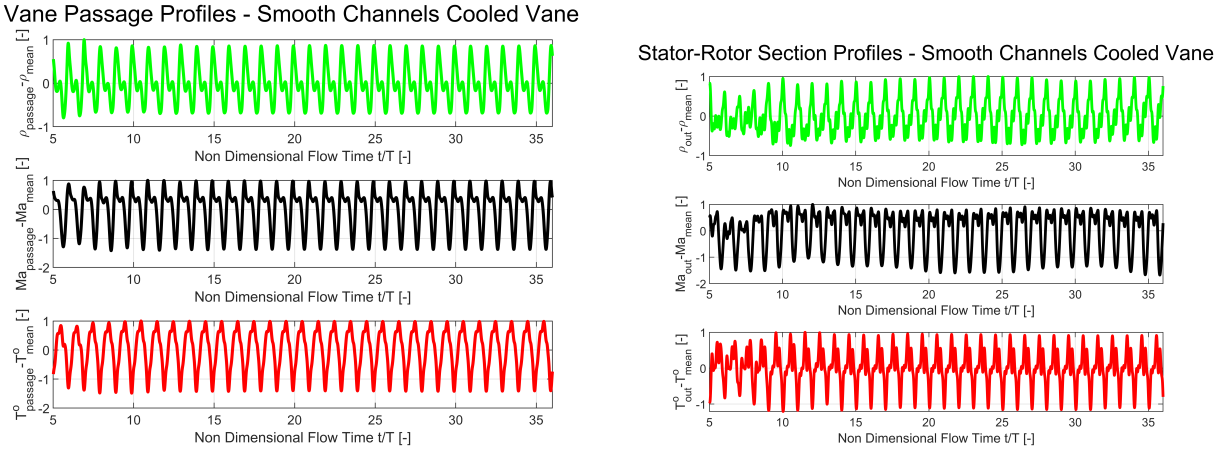

(a)

(b)

Figure 5.36: Oscillations of Monitored Variables at Inter-Vanes Passage (a) and Stator-Rotor Coupling Section (b) Monitor Point for the Smooth Channel Cooled Design.

Figures 5.37, 5.38, 5.39, and 5.40 present the cross-correlation tests of the monitored variables along with the Fourier Transform (FFT), which assesses their informational content. As in the previous case, asymptotic convergence is established around the eighteenth calculated period, but the solver was run up to the thirty-sixth period to ensure a better approximation of the result within the internal solid zones. The information content of the signal tends to decrease from the monitor point located in the inter-vane passage to the one located at the outlet, demonstrating that, even when transitioning from a simpler to a more complex model, the oscillation damping role assumed by the vane persists.

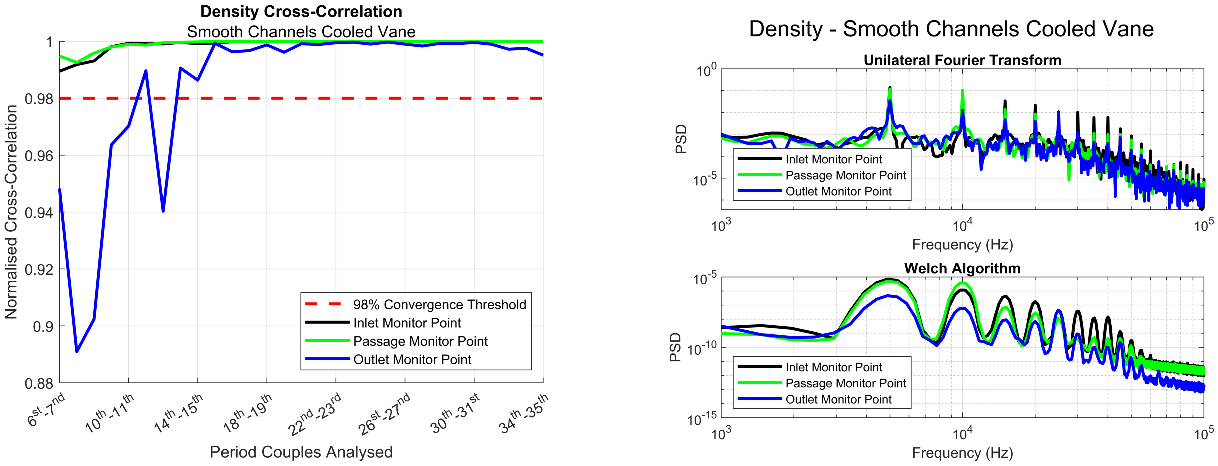

(a) (b)

Figure 5.37: Cross-Correlation (a) and Fourier Transform with Welch Algorithm (b) of the Density Oscillating Values for the Smooth Channel Cooled Design.

Figures 5.41 and 5.42 show the Mach number distributions of the main flow at the midspan section. Comparing these with the results obtained from the fully-turbulent model (the non-cooled case), it is noted that the flow transition point on the external vane wall leads to oscillations in the downstream region. This indicates the presence of a reattachment zone downstream of the recirculation bubble originating from the shock impingement area near the cascade throat. For this reason, the turbulence structures resulting from the application of the two models cannot be directly compared. Figures 5.43 and 5.44 show the total pressure contours in the main flow at the computational domain's midspan section. It is observed that, upon application of the oscillating inlet

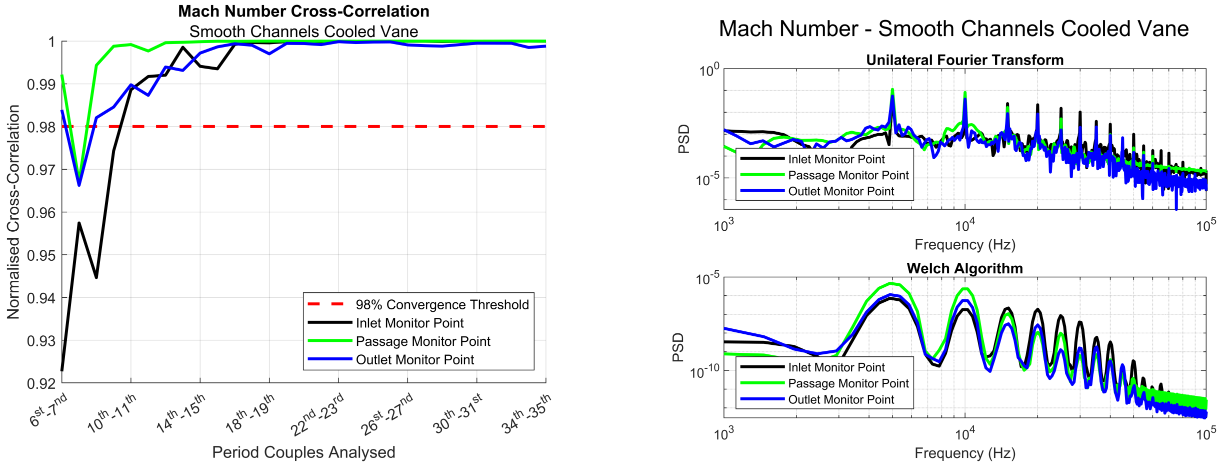

(a) (b)

Figure 5.38: Cross-Correlation (a) and Fourier Transform with Welch Algorithm (b) of the Mach Number Oscillating Values for the Smooth Channel Cooled Design.

conditions, an incident pressure wave is created towards the vane. In this case, too, the transition model highlights turbulent structures downstream of the airfoil's trailing edge.

Figures 5.45 and 5.46 show the total temperature distributions of the main flow at the midspan section. The oscillating total temperature boundary conditions impose a wave front that is swallowed by the passage. Figures 5.47 and 5.48 show the thermal maps of the solid produced at the midspan section. The effectiveness of the smooth channel cooling is evident from the range of values in the legend. A significant temperature decrease is observed in the wall separating two channels. The wall separating the channels from the main flow, however, registers the highest temperature. A critical area to monitor is the trailing edge section, which is subjected to a large heat flux without any installed cooling technique.

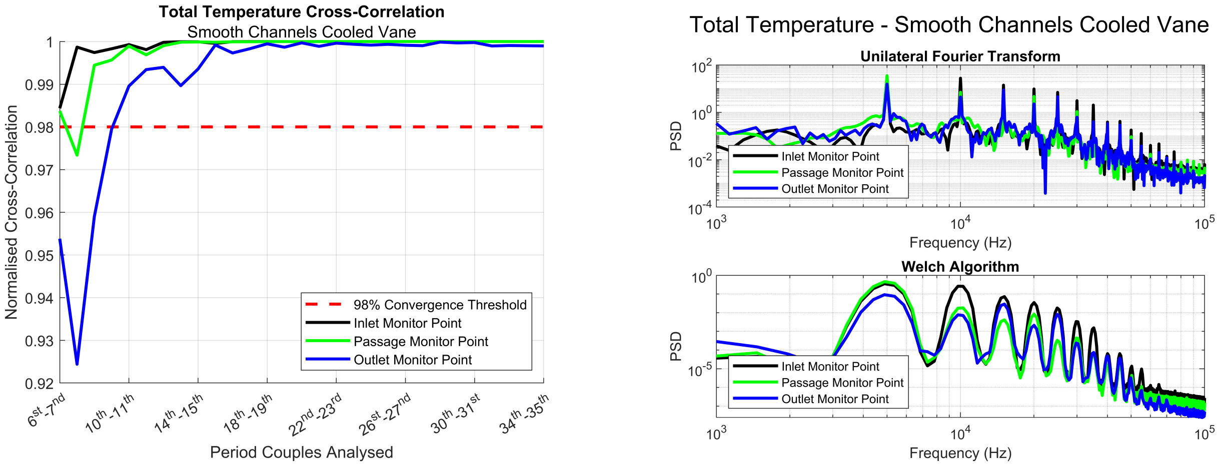

(a) (b)

Figure 5.39: Cross-Correlation (a) and Fourier Transform with Welch Algorithm (b) of the Total Temperature Oscillating Values for the Smooth Channel Cooled Design.

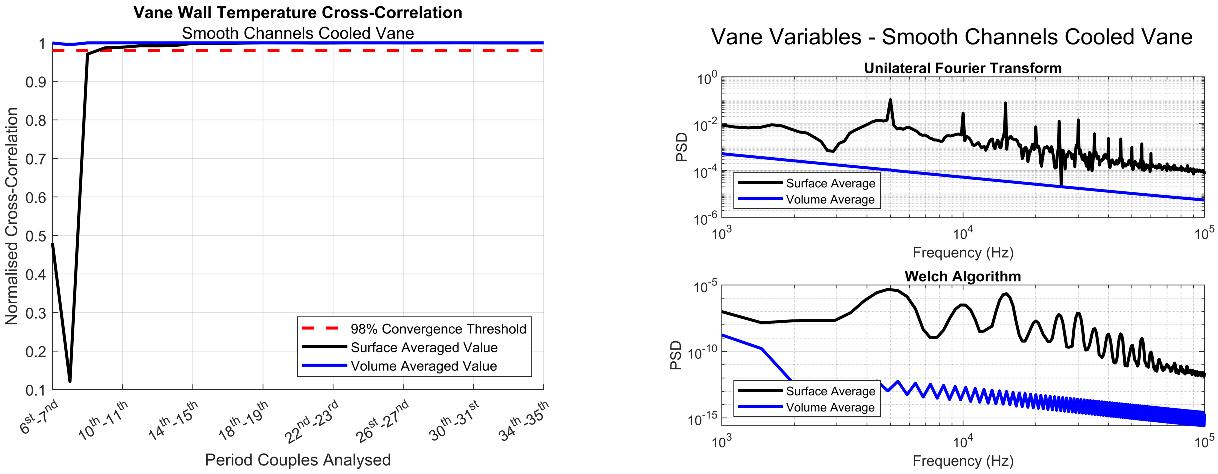

(a) (b)

Figure 5.40: Cross-Correlation (a) and Fourier Transform with Welch Algorithm (b) of the Vane Monitored Variables Oscillating Values for the Smooth Channel Cooled Design.

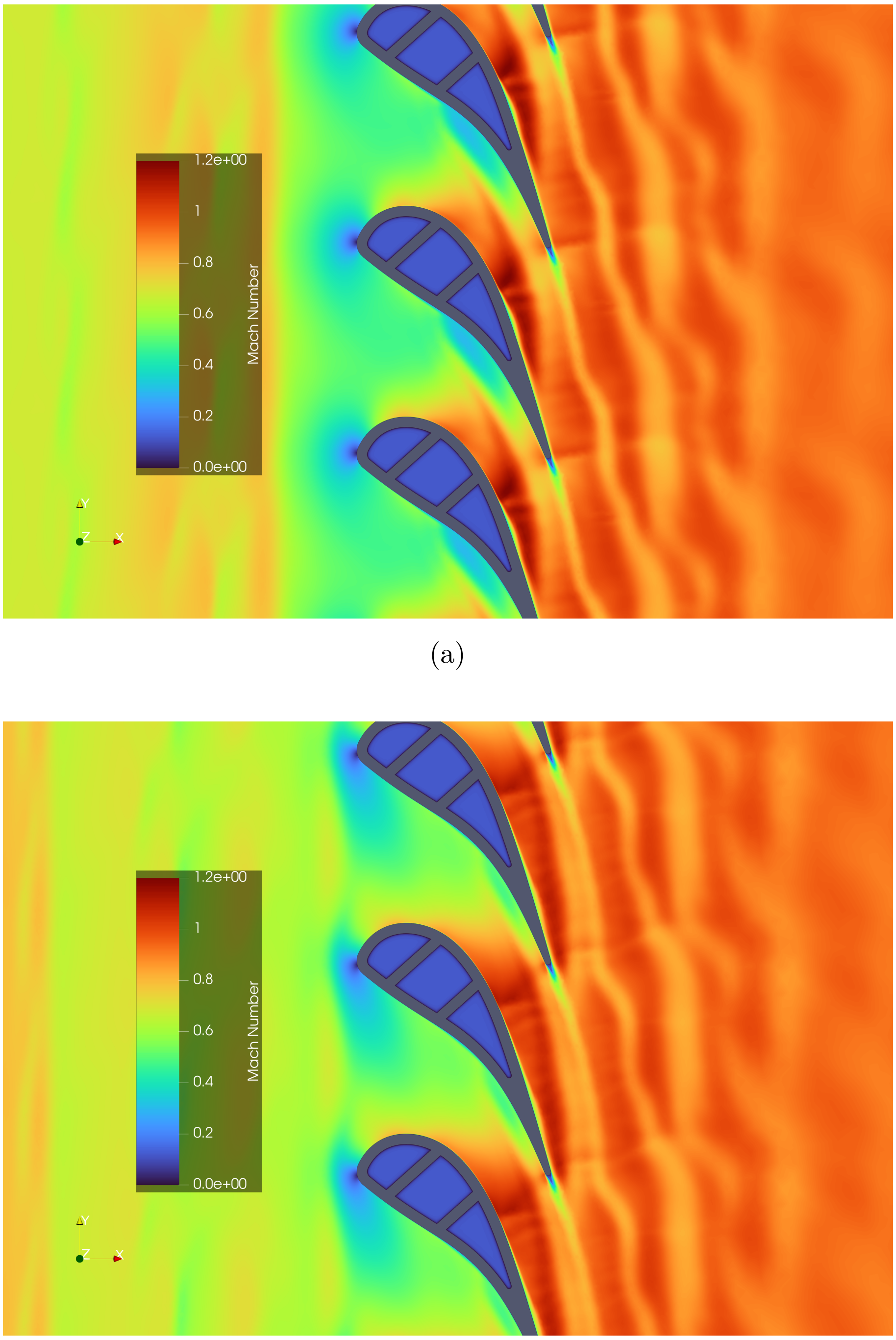

(a)

(b)

Figure 5.41: Main Flow Mach Number Contour at Midspan at 0% (a) and 25% (b) of the Period for Smooth Channel Cooled Vane Design.

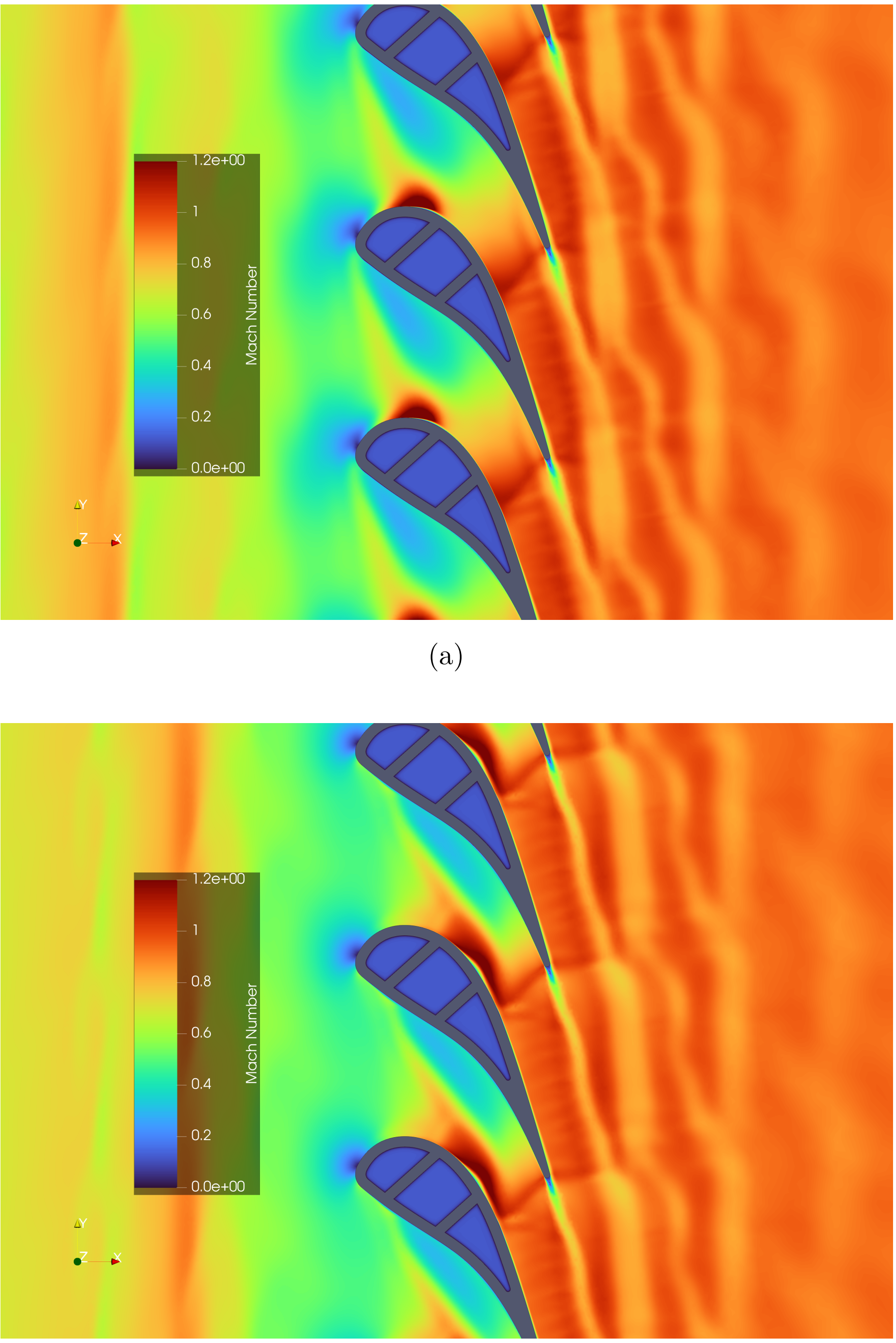

(a)

(b)

Figure 5.42: Main Flow Mach Number Contour at Midspan at 50% (a) and 75% (b) of the Period for Smooth Channel Cooled Vane Design.

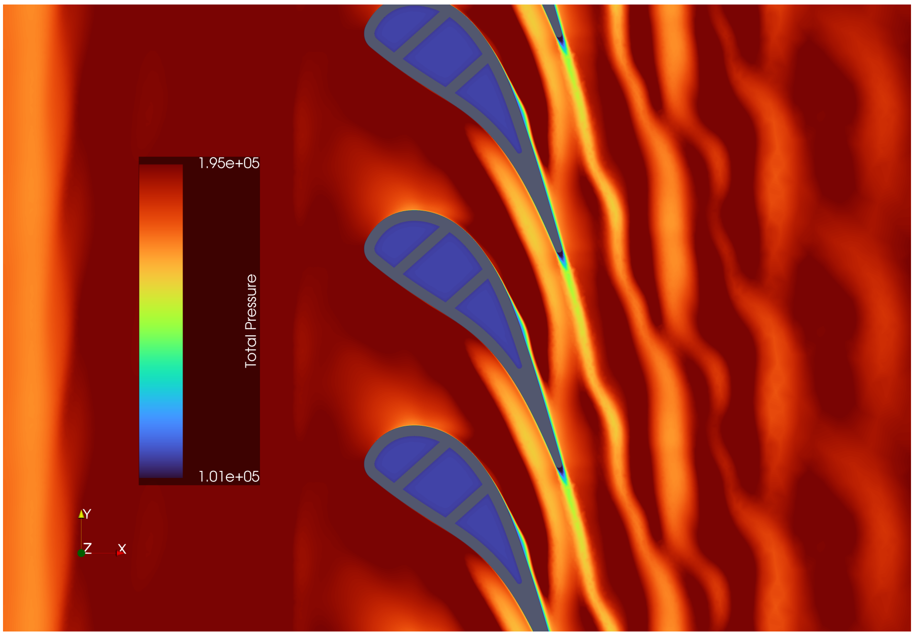

(a)

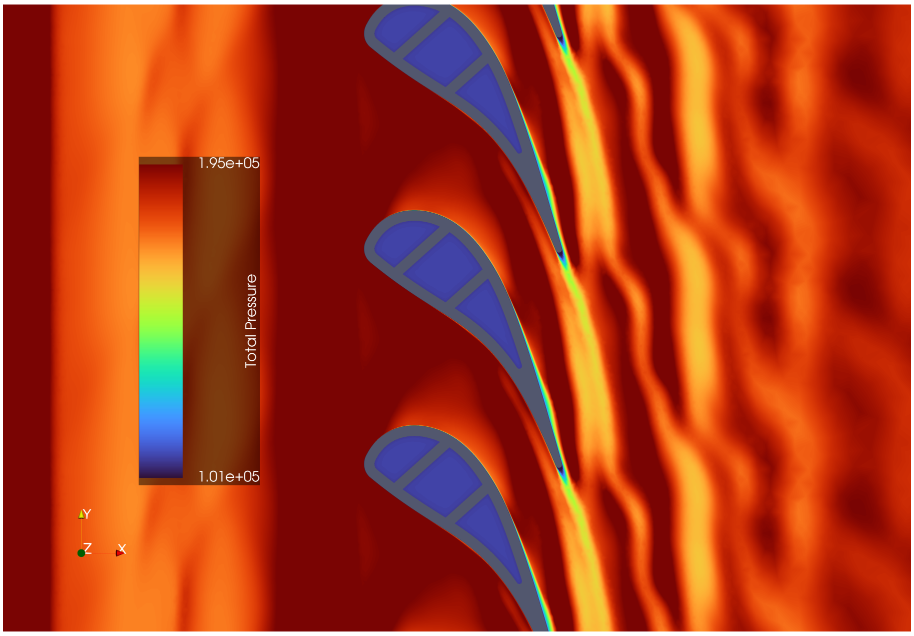

(b)

Figure 5.43: Main Flow Total Pressure Contour at Midspan at 0% (a) and 25% (b) of the Period for Smooth Channel Cooled Vane Design.

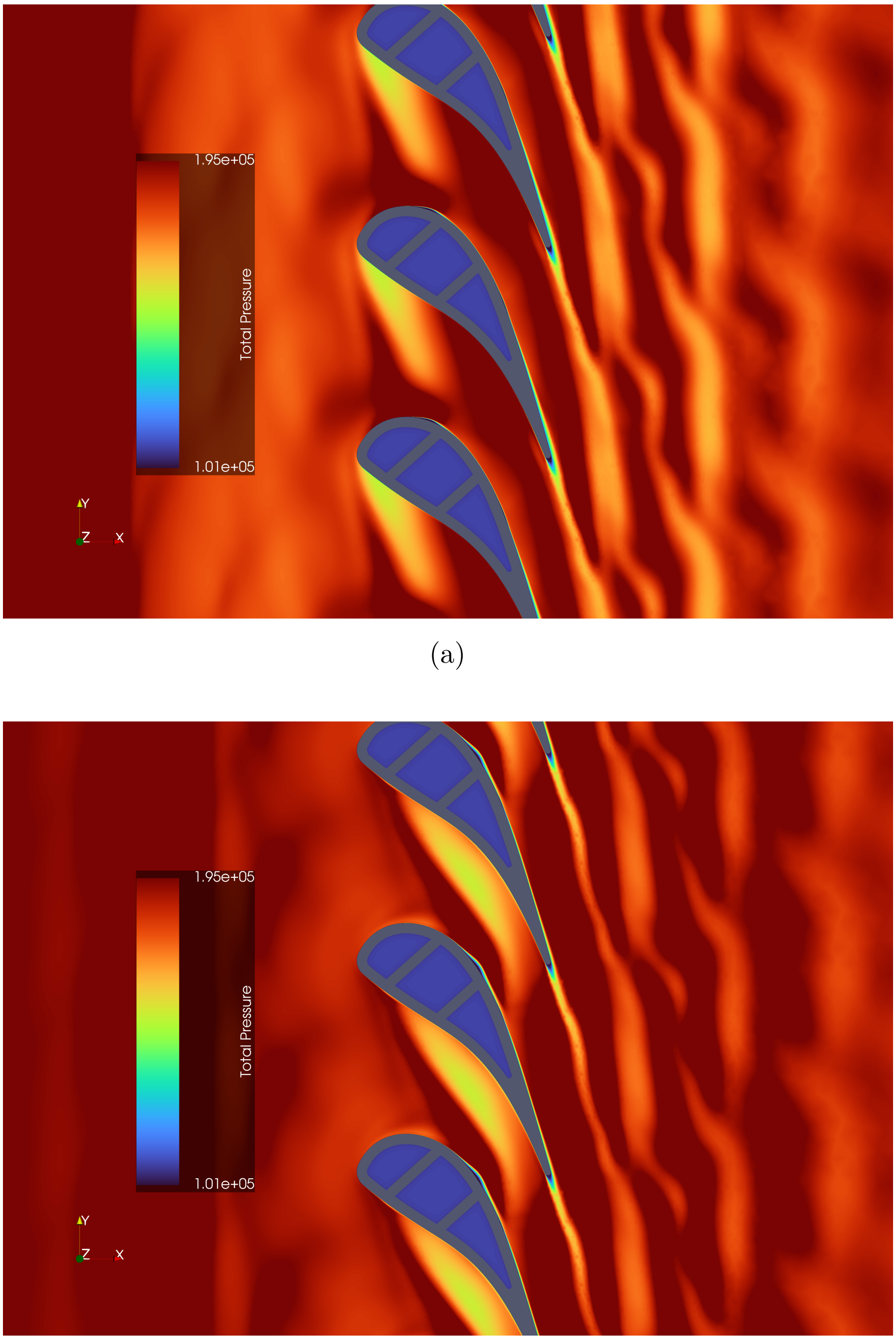

(a)

(b)

Figure 5.44: Main Flow Total Pressure Contour at Midspan at 50% (a) and 75% (b) of the Period for Smooth Channel Cooled Vane Design.

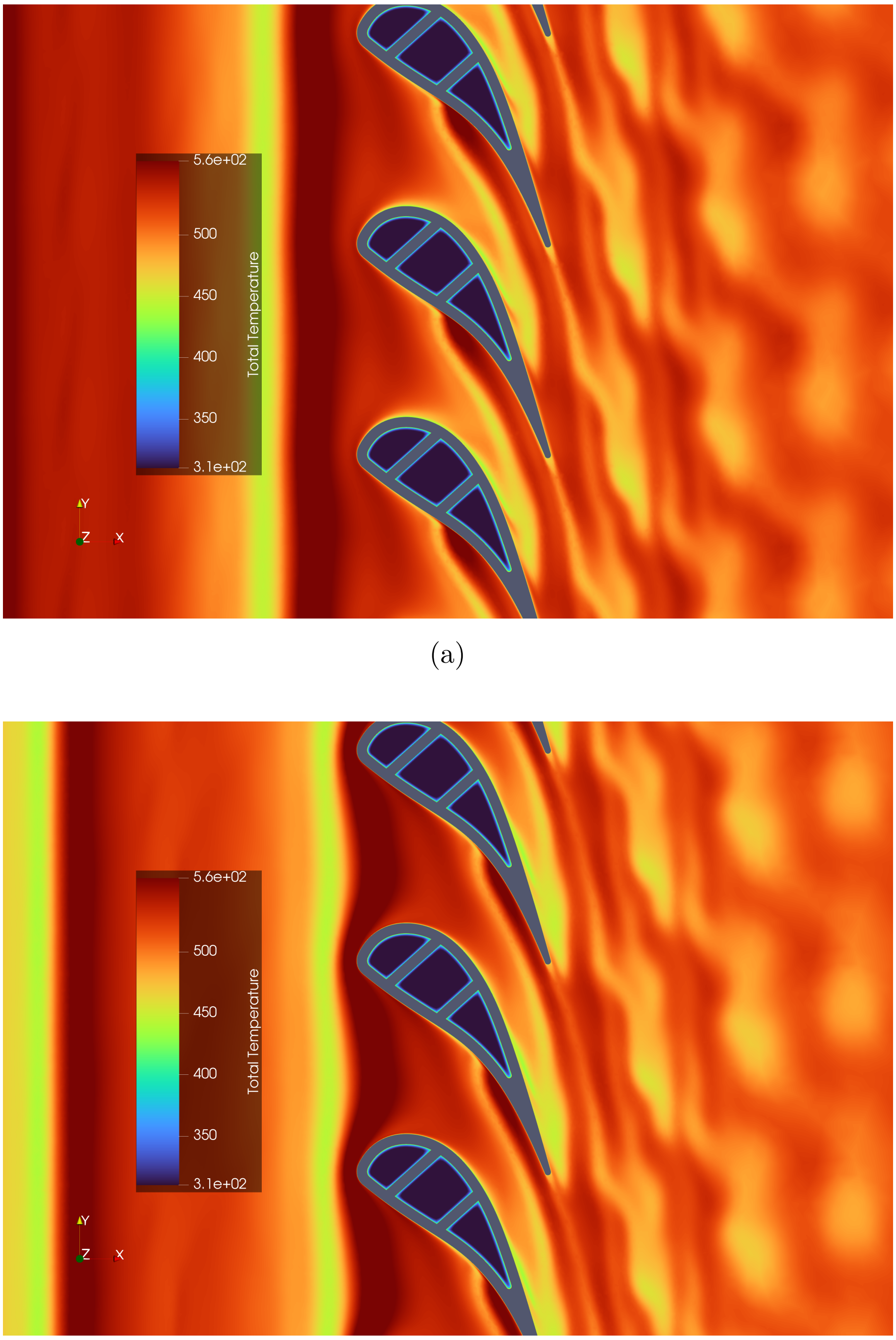

(a)

(b)

Figure 5.45: Main Flow Total Temperature Contour at Midspan at 0% (a) and 25% (b) of the Period for Smooth Channel Cooled Vane Design.

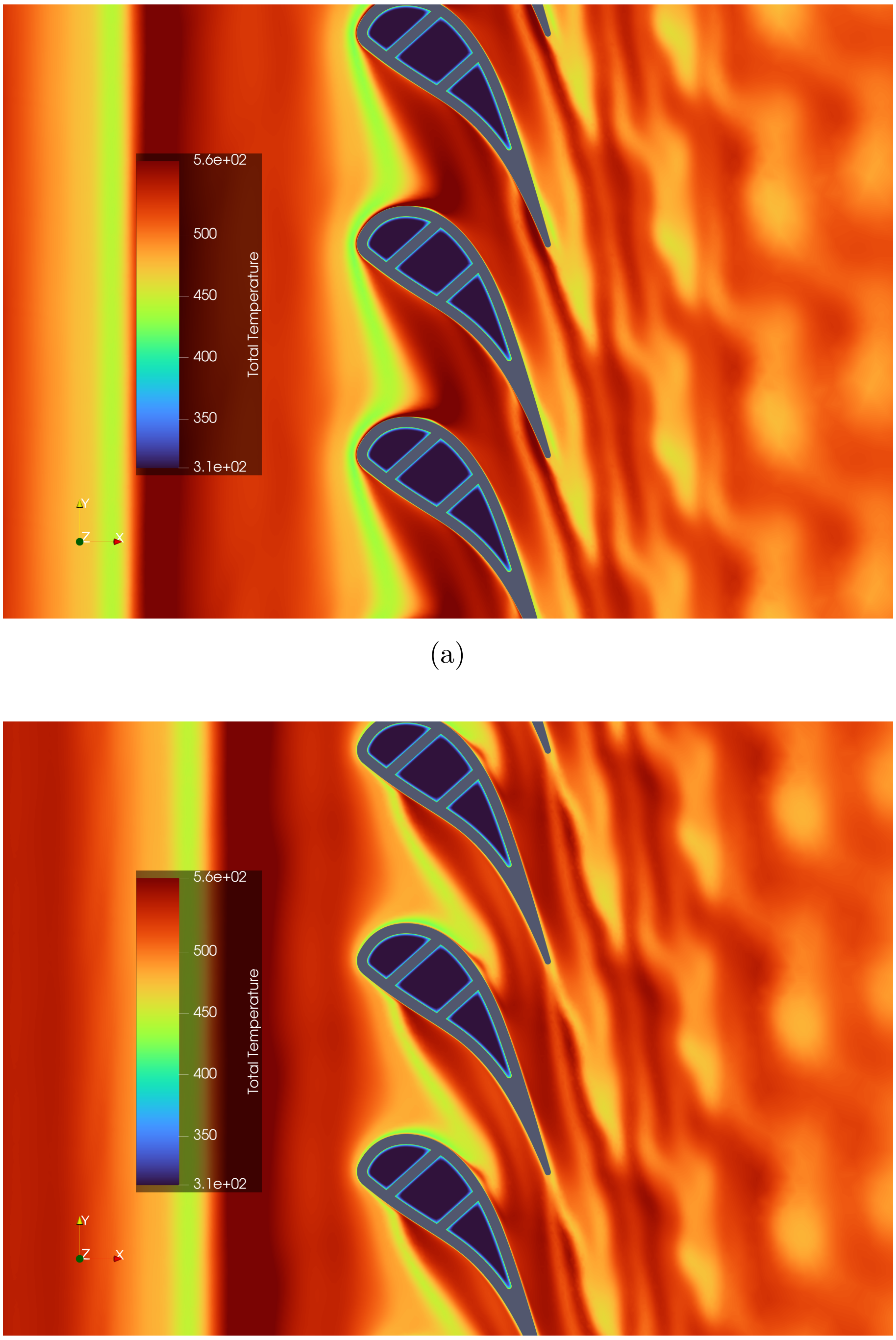

(a)

(b)

Figure 5.46: Main Flow Total Temperature Contour at Midspan at 50% (a) and 75% (b) of the Period for Smooth Channel Cooled Vane Design.

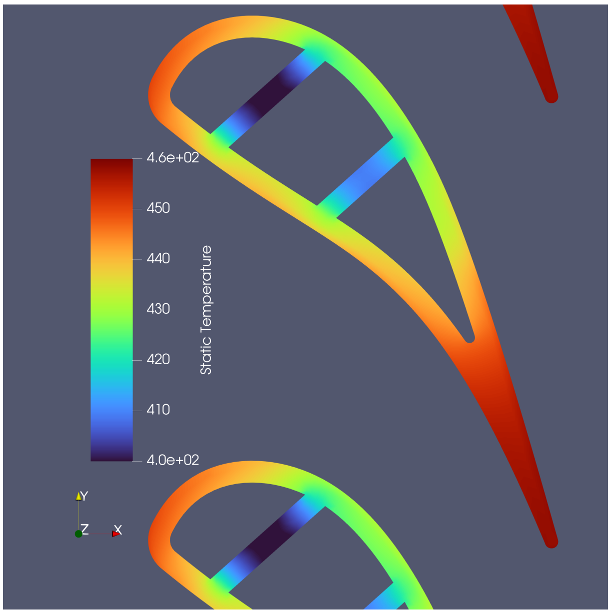

(a)

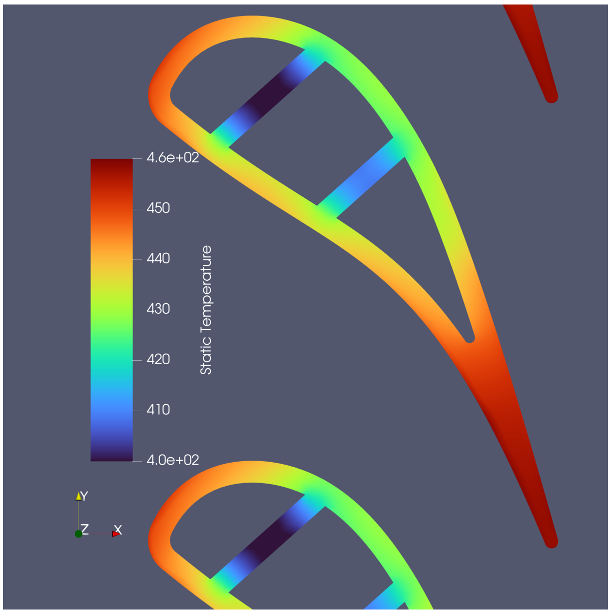

(b)

Figure 5.47: Solid Vane Static Temperature Contour at Midspan Section at 0% (a) and 25% (b) of the Period for Smooth Channel Cooled Vane Design.

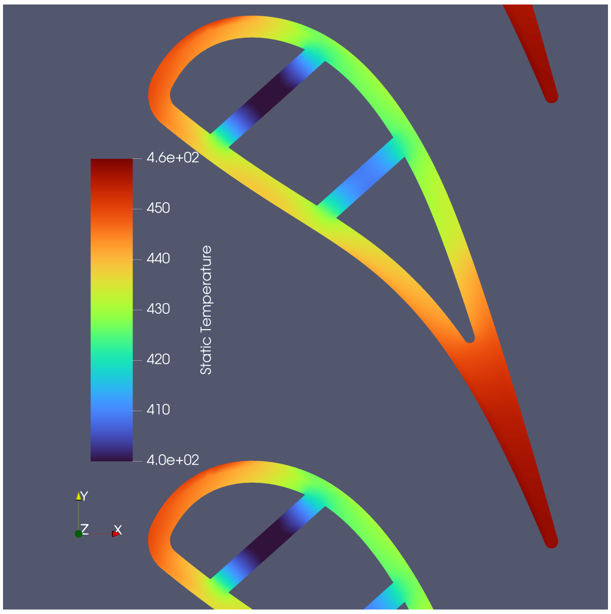

(a)

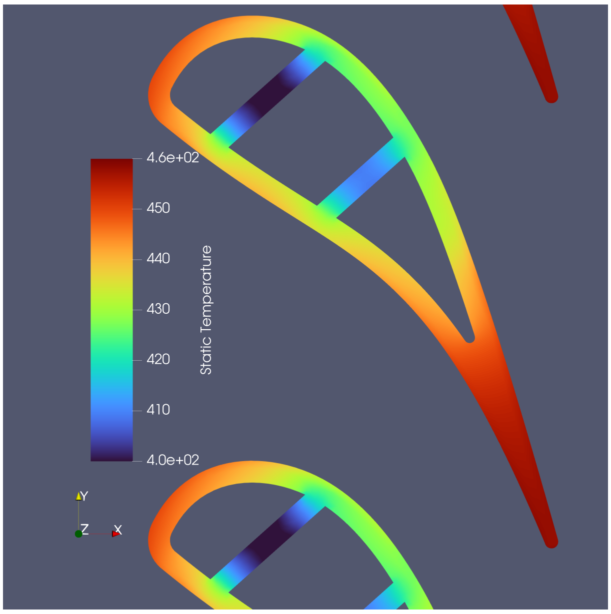

(b)

Figure 5.48: Solid Vane Static Temperature Contour at Midspan Section at 50% (a) and 75% (b) of the Period for Smooth Channel Cooled Vane Design.

Table 26 reports the point-wise values of the monitored quantities at the four instants where the cycle is evaluated. As in the previous case, a phase shift is observed between the peak of the imposed conditions and the peak of the conditions recorded in the stator-rotor coupling section. The volume-averaged temperature of the solid vane undergoes no variation whatsoever, but settles at a temperature lower by $\Delta T_{vol} = 43\ K$ compared to the non-cooled case. Tables 27 and 28 report the variables related to the cooling channels to which the ribs will be applied, namely the second and third channels. The averages evaluated on the outlet surface and the volume of the cooling fluid in the two channels remain constant over time, indicating no correlation between the imposed oscillating conditions outside and the internal channel flow. The pressure drop is lower by 0.1% compared to the steady-state case.

	0% of the Cycle	**25% of the Cycle**	**50% of the Cycle**	**75% of the Cycle**
Average S-R Section Total Pressure [Pa]	182771	183403	186380	17679
Average S-R Section Static Temperature [K]	432.609	439.362	454.391	456.678
Average S-R Section Mach Number [-]	0.898	0.906	0.908	0.849
Average Static Wall Vane Pressure [Pa]	128588	133084	131797	126872
Average Static Wall Vane Temperature [K]	442.373	442.502	442.222	442.170
Volume Averaged Static Vane Temperature [K]	420.089	420.089	420.089	420.089

Table 26: Monitored Main flow and Vane Variables at Different Time Steps for Smooth Channel Cooled Vane.

	0% of the Cycle	**25% of the Cycle**	**50% of the Cycle**	**75% of the Cycle**
Mass Averaged Outlet Static Temperature [K]	309.920	309.920	309.920	309.920
Volume Averaged Static Temperature [K]	310.477	310.477	310.477	310.477
Mass Averaged Outlet Velocity Magnitude [m/s]	40.846	40.842	40.843	40.845
Volume Averaged Velocity Magnitude [m/s]	38.392	38.390	38.391	38.392
Mass Averaged Outlet Total Pressure [Pa]	107418	107418	107418	107418
Total Pressure Drop [%]	-0.141%	-0.141%	-0.141%	-0.141%

Table 27: Second Cooling Channels Variables at Different Time Steps for Smooth Channel Cooled Vane.

	0% of the Cycle	**25% of the Cycle**	**50% of the Cycle**	**75% of the Cycle**
Mass Averaged Outlet Static Temperature [K]	316.388	316.386	316.387	316.387
Volume Averaged Static Temperature [K]	318.082	318.083	318.083	318.082
Mass Averaged Outlet Velocity Magnitude [m/s]	39.658	39.652	39.655	39.657
Volume Averaged Velocity Magnitude [m/s]	35.890	35.888	35.889	35.889
Mass Averaged Outlet Total Pressure [Pa]	107353	107352	107352	107353
Total Pressure Drop [%]	-0.202%	-0.203%	-0.203%	-0.202%

Table 28: Third Cooling Channels Variables at Different Time Steps for Smooth Channel Cooled Vane.

Figures 5.49 and 5.50 show the static pressure and temperature distributions on the external vane wall at the midspan section. The second figure is particularly interesting in highlighting the importance of cooling: although it leads to a lower volume-averaged temperature compared to the non-cooled case, it results in temperature oscillations five times greater than the first case. Furthermore, the differential temperature distribution emphasizes the importance of applying a cooling technique in the trailing edge region.

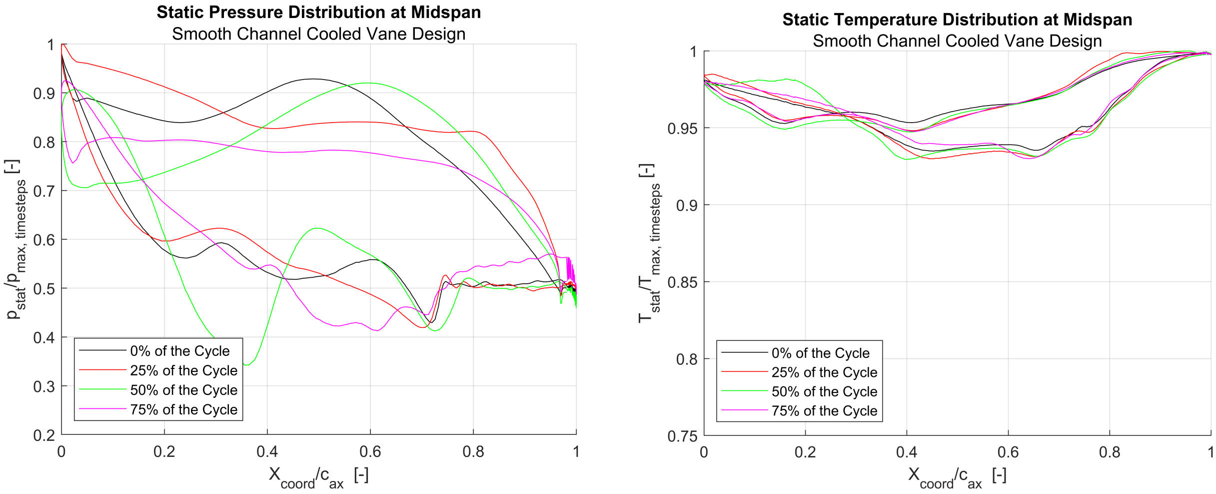

(a) Static Pressure Distribution

(b) Static Temperature Distribution

Figure 5.49: Pressure (a) and Temperature (b) Distribution at Midspan Section of the Vane Surface for the Smooth Channel Cooled Vane at Different Time Steps.

Figures 5.51 and 5.52 show the static pressure and temperature distributions calculated on the walls of the two cooling channels of interest. The data from the unsteady simulations are compared with the steady-state results. From the first figure, there is an almost perfect similarity between the steady and unsteady static pressure distributions. As seen in the previous tables, the oscillating conditions do not vary the flow inside the cooling channels. The difference between the static pressure values and the total pressure (which, instead, varies in the unsteady case) indicates a modification of the mean velocity of the cooling fluid. The static temperature, however, shows a decrease in the unsteady simulation compared to the steady-state case, indicating a lower average solid temperature and, thus, a purely convective heat transfer method between the solid and the surrounding

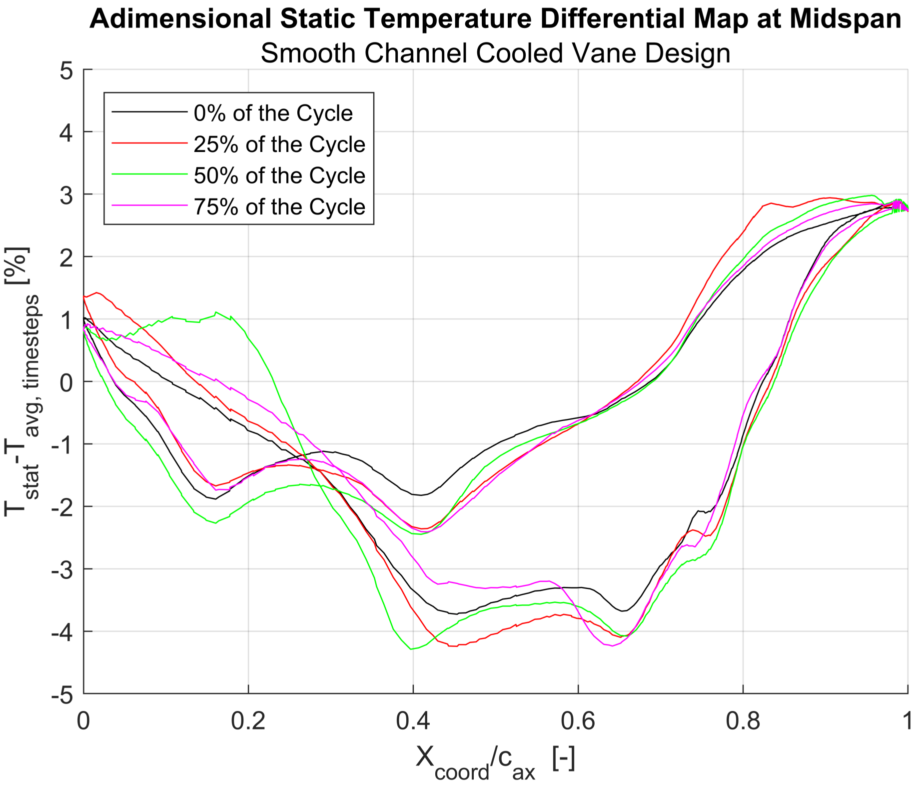

Figure 5.50: Differential Map of the Percentage Wall Temperature Variations on the Vane Surface at Midspan Section for Smooth Channel Cooled Vane Design.

fluid.

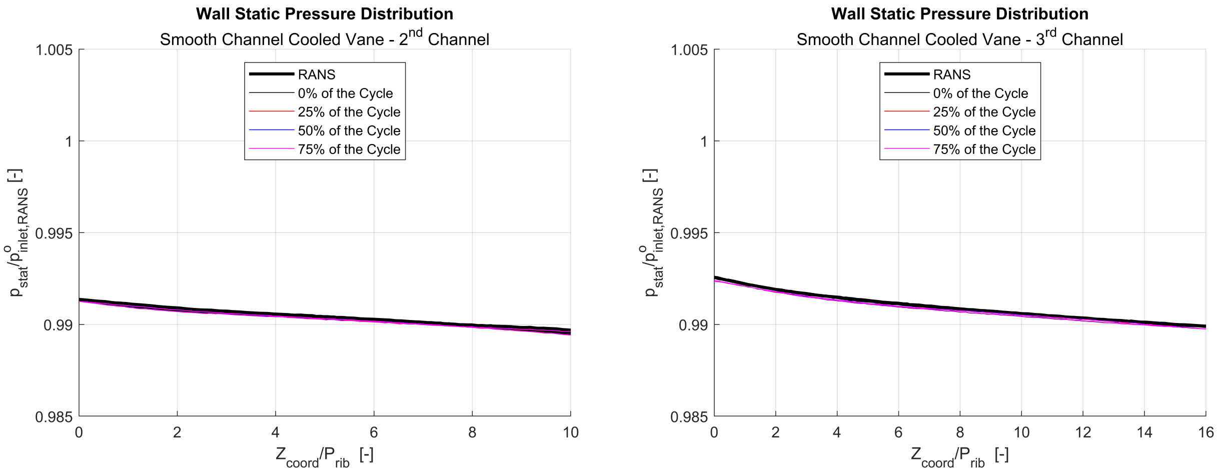

(a)

(b)

Figure 5.51: Wall Static Pressure Distribution in Second (a) and Third (b) for the Smooth Channel Cooled Vane at Different Time Steps.

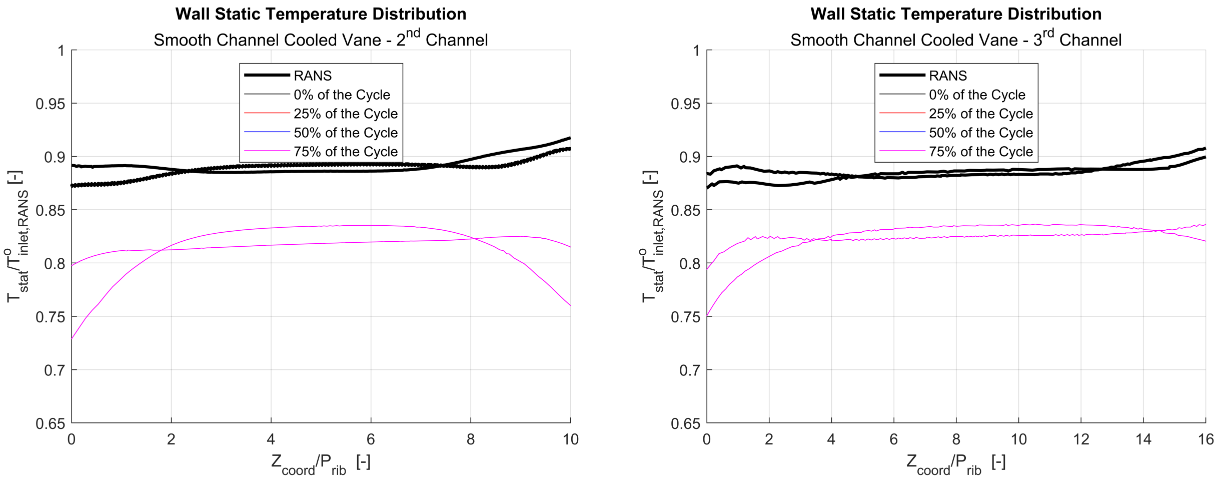

(a)

(b)

Figure 5.52: Wall Static Temperature Distribution in Second (a) and Third (b) for the Smooth Channel Cooled Vane at Different Time Steps.

Ribbed Channel Cooled Vane Unsteady Simulation

Figure 5.53 reports the oscillations of the values monitored in the stator-rotor coupling section and the wall thermal variables. As seen in the previous cases, asymptotic convergence is reached at approximately half the number of periods considered. The volume-averaged static temperature of the vane increases constantly with minor variations, as observed in the study of the other two designs. Figures 5.54 and 5.55 show the oscillations of the monitored variables at the three points of interest. The oscillations at the stator-rotor coupling section continue to oscillate with a much larger period than the oscillations of the imposed inlet conditions.

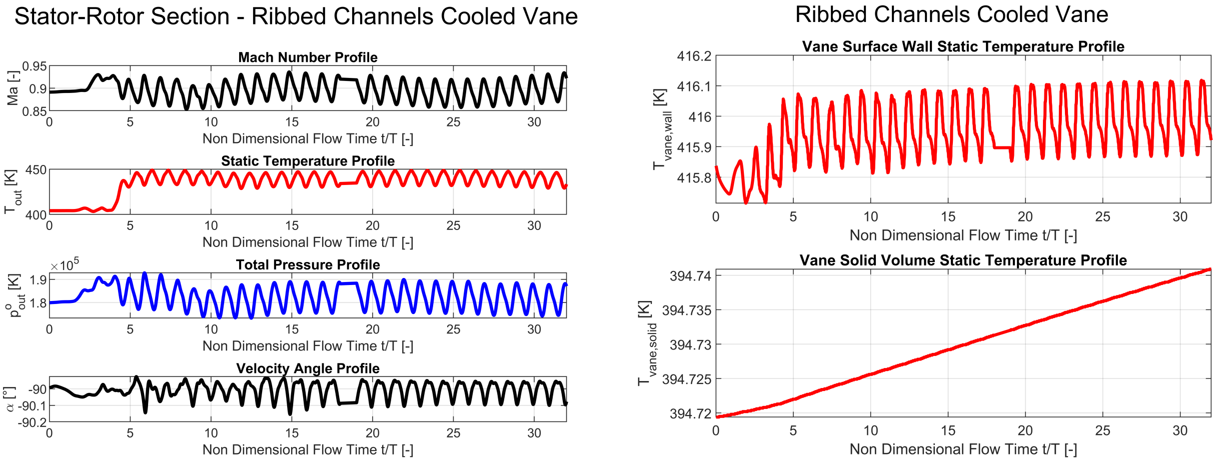

(a) (b)

Figure 5.53: Oscillations of Monitored Variables at Stator-Rotor Coupling Section (a) and on Vane Surface and Volume (b) for the Ribbed Channel Cooled Design.

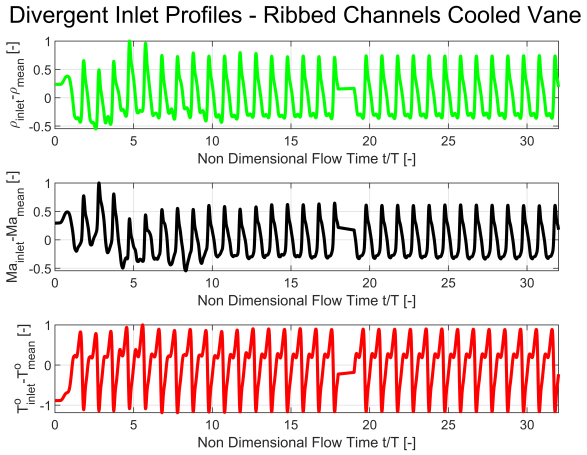
Divergent Inlet Profiles - Ribbed Channels Cooled Vane

Figure 5.54: Oscillations of Monitored Variables at Inlet Monitor Point for the Ribbed Channel Cooled Design.

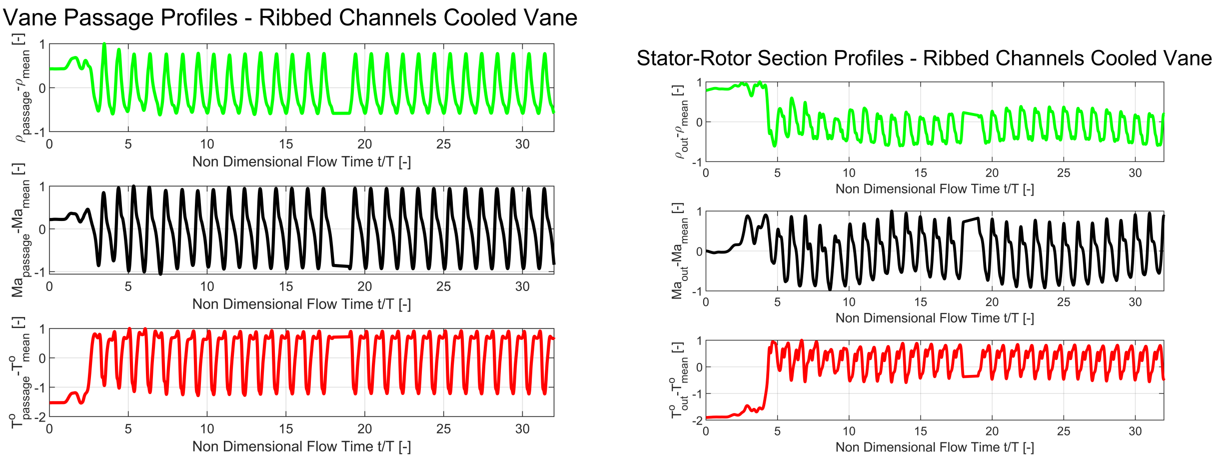
Vane Passage Profiles - Ribbed Channels Cooled Vane

Stator-Rotor Section Profiles - Ribbed Channels Cooled Vane

(a)

(b)

Figure 5.55: Oscillations of Monitored Variables at Inter-Vanes Passage (a) and Stator-Rotor Coupling Section (b) Monitor Point for the Ribbed Channel Cooled Design.

Figures 5.56, 5.57, 5.58, and 5.59 report the results of the cross-correlation tests applied to the three variables related to the governing equations and the two variables related to solid heat exchange. The information provided by the Fourier Transforms once again highlights the importance of the inlet condition oscillations in the system and the attenuation of the information produced by the vane. The informational content related to the volume-averaged solid temperature remains negligible. The average on the external surface of the vane, however, reaches convergence at the eighteenth investigated period.

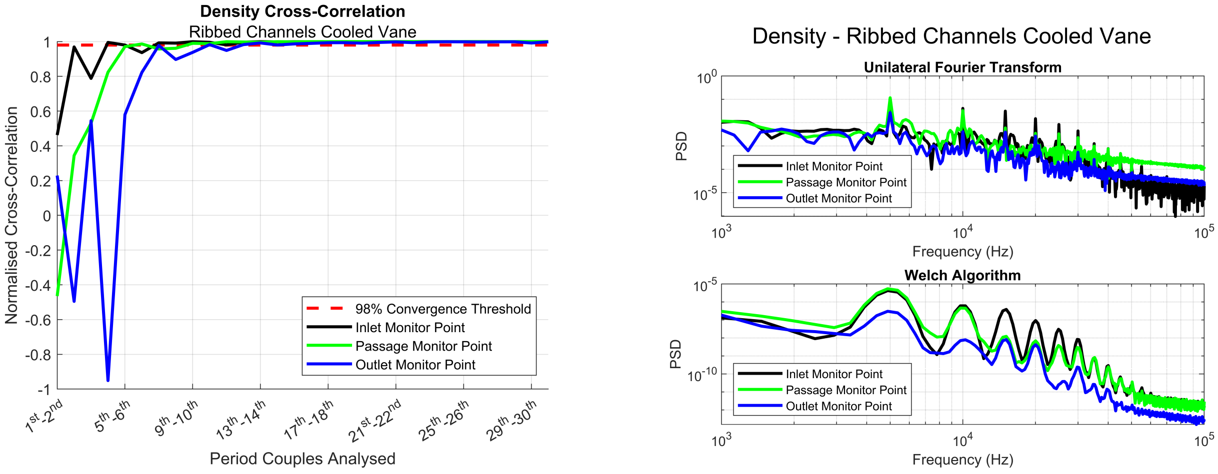

(a) (b)

Figure 5.56: Cross-Correlation (a) and Fourier Transform with Welch Algorithm (b) of the Density Oscillating Values for the Ribbed Channel Cooled Design.

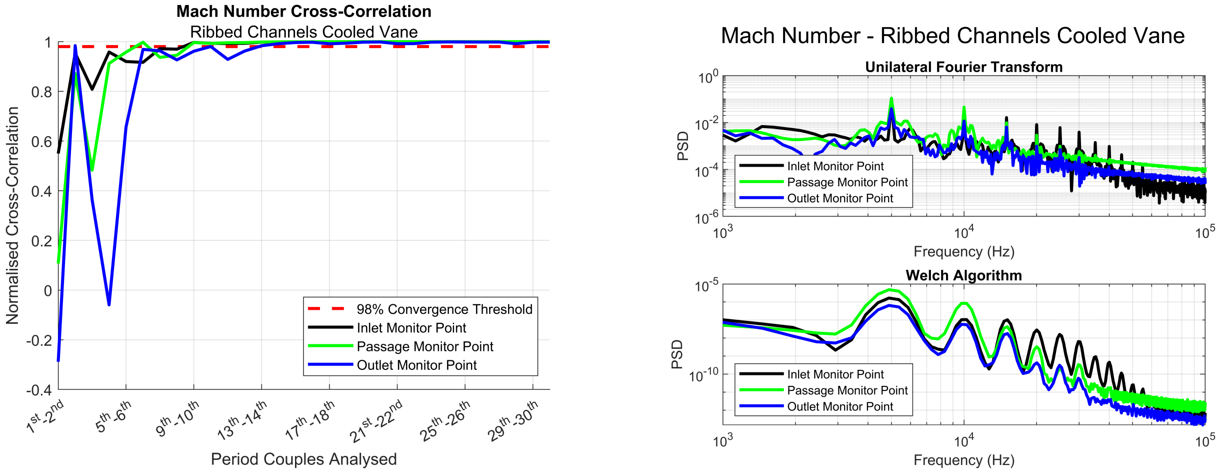

(a) (b)

Figure 5.57: Cross-Correlation (a) and Fourier Transform with Welch Algorithm (b) of the Mach Number Oscillating Values for the Ribbed Channel Cooled Design.

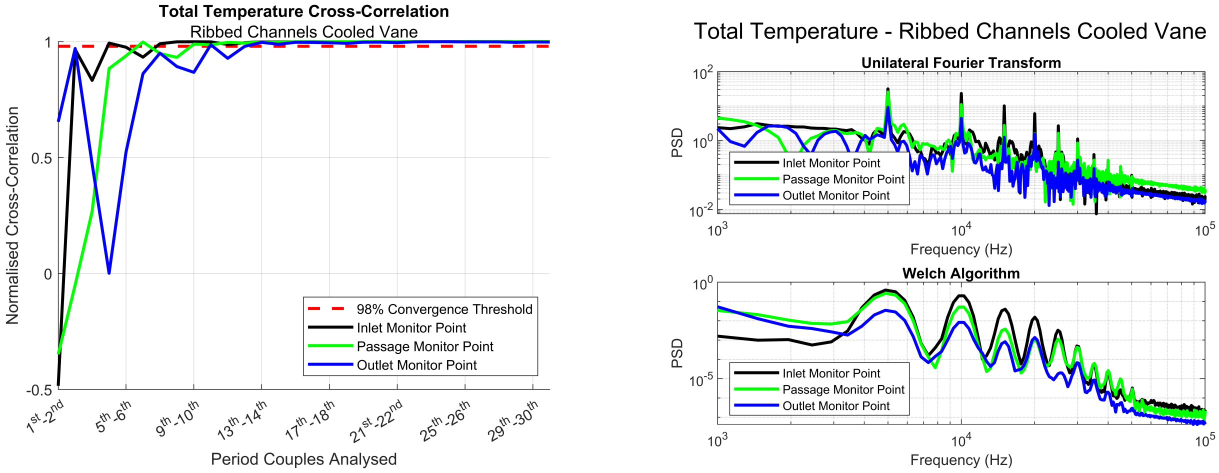

(a) (b)

Figure 5.58: Cross-Correlation (a) and Fourier Transform with Welch Algorithm (b) of the Total Temperature Oscillating Values for the Ribbed Channel Cooled Design.

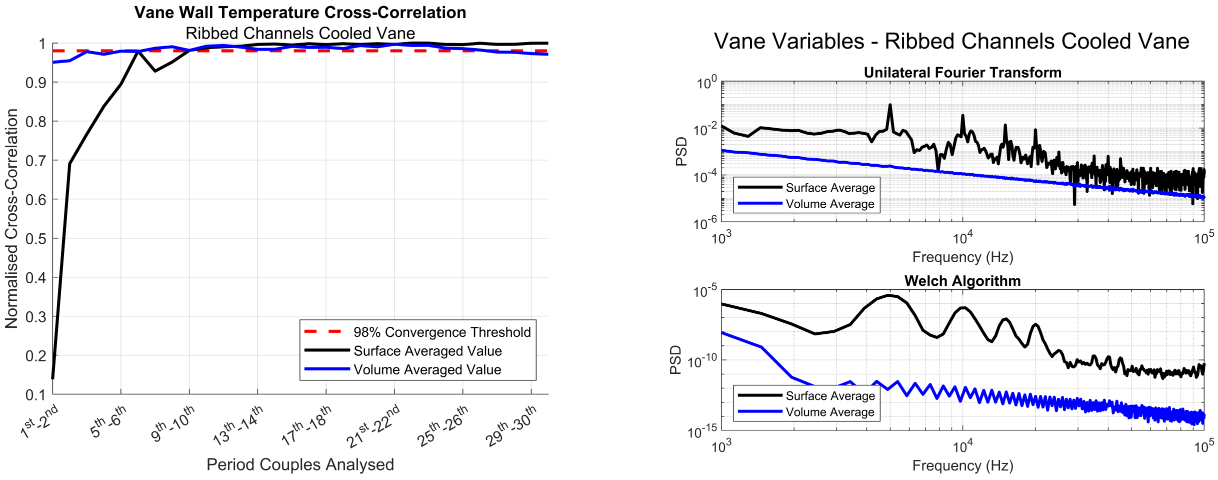

(a) (b)

Figure 5.59: Cross-Correlation (a) and Fourier Transform with Welch Algorithm (b) of the Vane Monitored Variables Oscillating Values for the Ribbed Channel Cooled Design.

Figures 5.60 and 5.61 show the Mach number distributions of the main flow at the midspan section. For this design as well, the transition model provides oscillations of the flow field downstream of the vane that would otherwise be invisible. Having a structure similar to the case of the vane cooled with smooth channels, these last two cases can be compared. Figures 5.62 and 5.63 report the total pressure contours in the main flow at the computational domain's midspan section. It is observed that, upon application of the oscillating inlet conditions, an incident pressure wave is created towards the vane. In this case, too, the transition model highlights turbulent structures downstream of the airfoil's trailing edge. Figures 5.64 and 5.65 show the total temperature distributions of the main flow at the midspan section. The oscillating total temperature boundary conditions impose a wave front that is swallowed by the passage. Figures 5.66 and 5.67 show the thermal maps of the solid produced at the midspan section. The effectiveness of the ribbed channel cooling is notable from the range of values in the legend. The temperature decrease already observed in the smooth channel case is accentuated here, with a minimum temperature reached in the wall separating the first and second cooling channels that is lower by $\Delta T_{vol} = 70\ K$. Furthermore, the map highlights the cooling capability of the ribs even in the presence of oscillating conditions at the outlet.

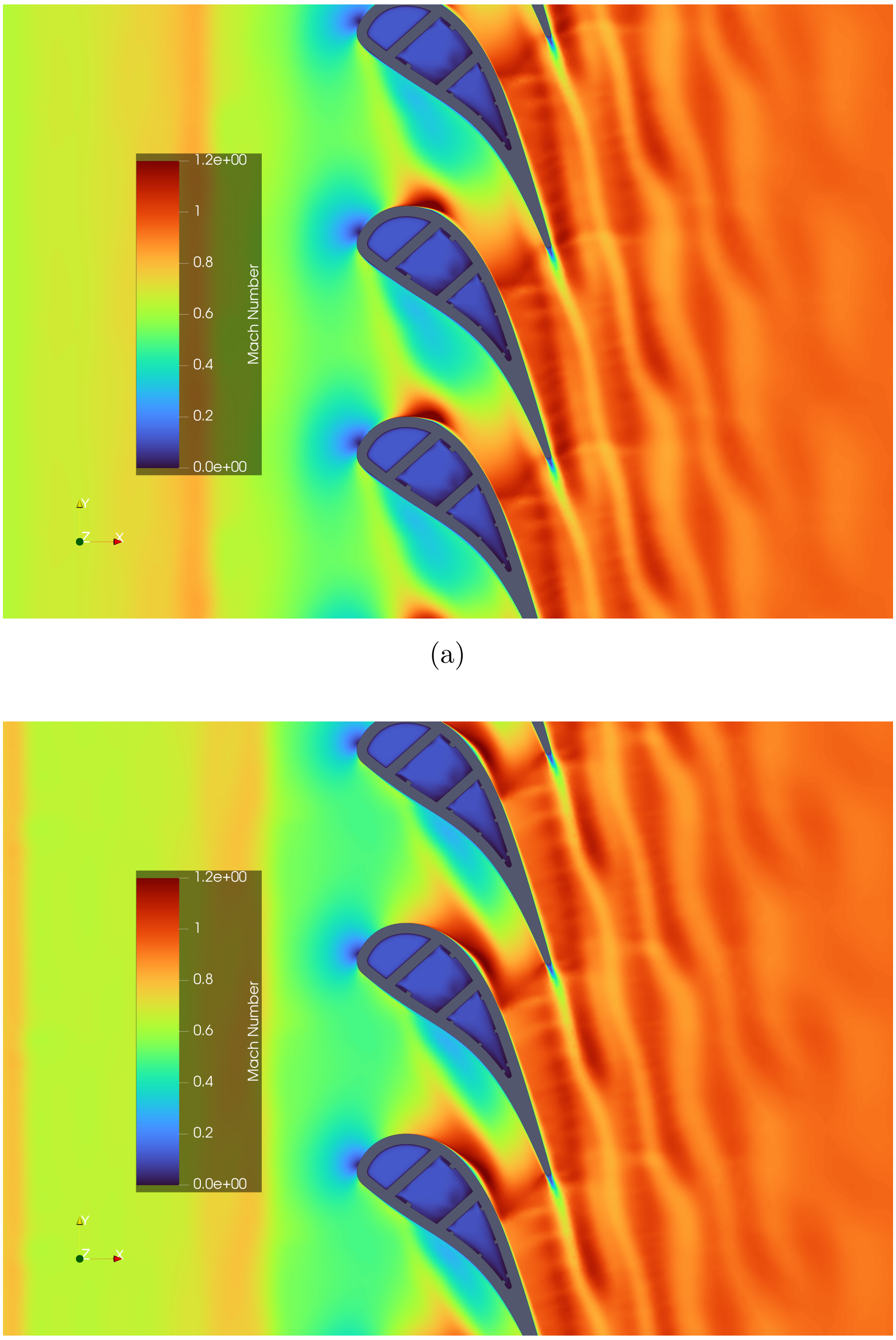

(a)

(b)

Figure 5.60: Main Flow Mach Number Contour at Midspan at 0% (a) and 25% (b) of the Period for Ribbed Channel Cooled Vane Design.

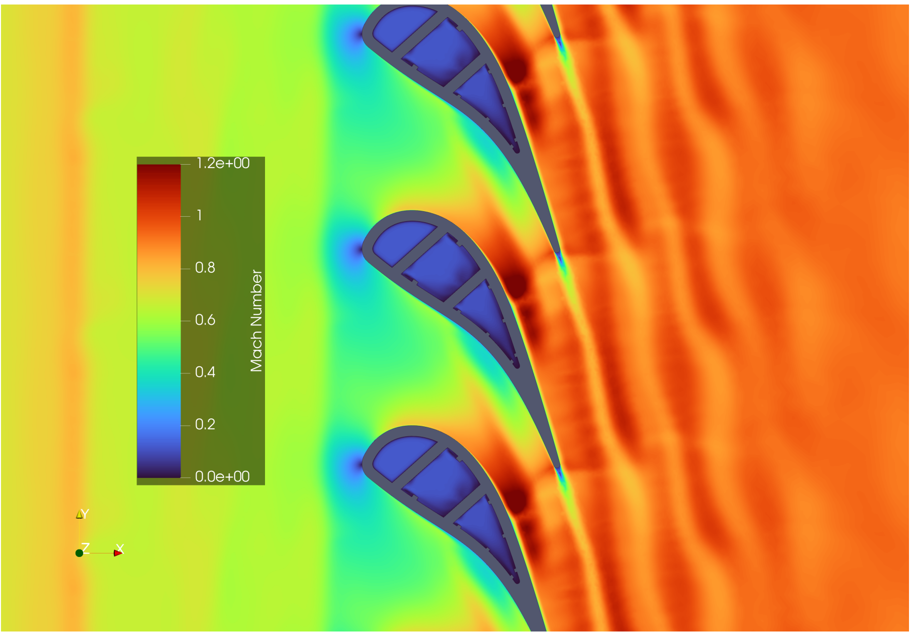

(a)

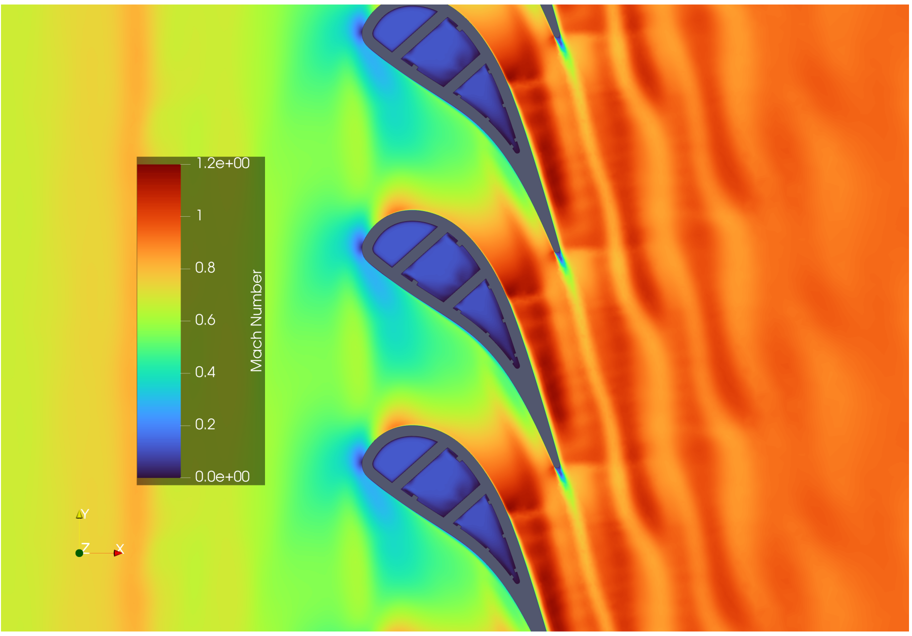

(b)

Figure 5.61: Main Flow Mach Number Contour at Midspan at 50% (a) and 75% (b) of the Period for Ribbed Channel Cooled Vane Design.

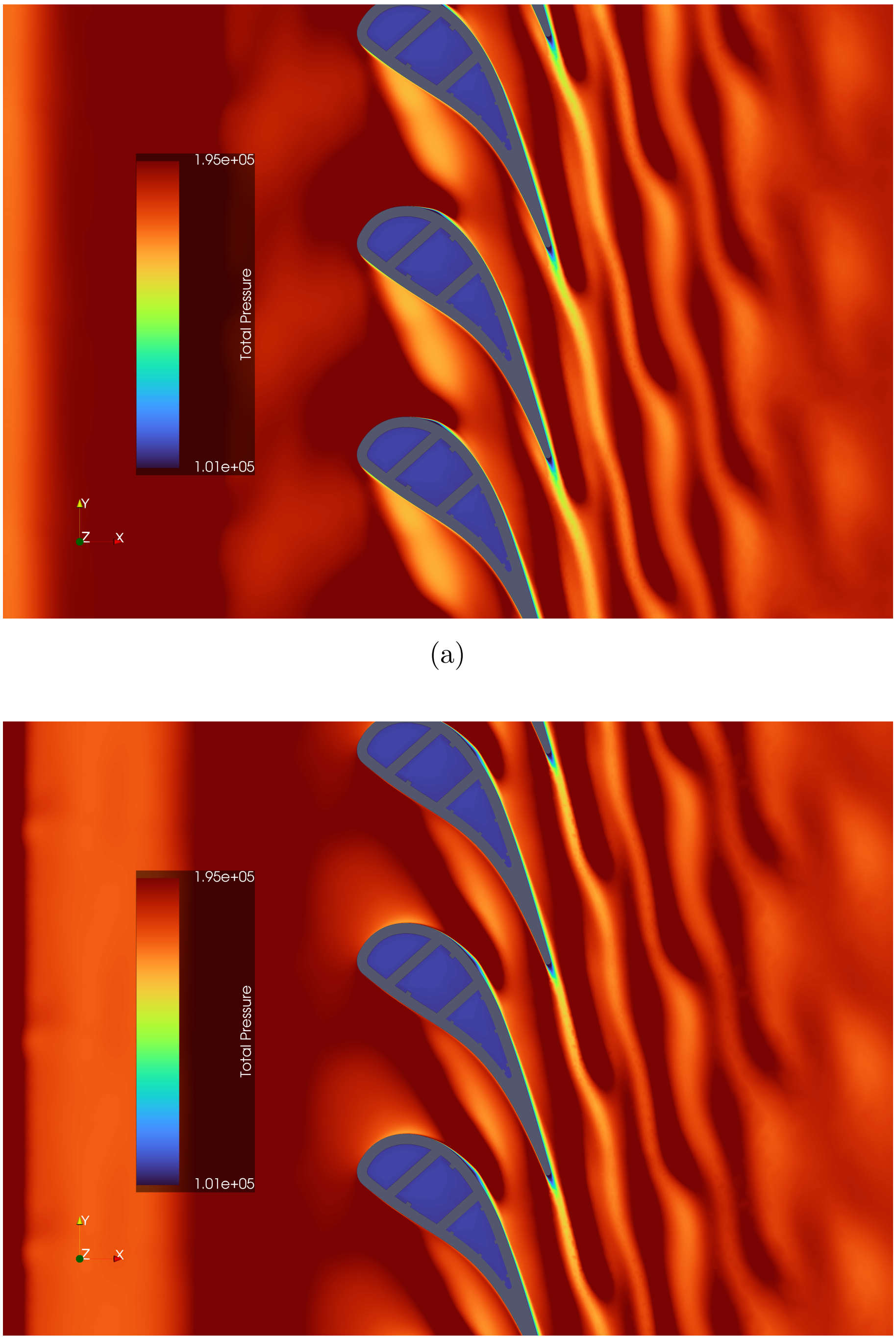

(a)

(b)

Figure 5.62: Main Flow Total Pressure Contour at Midspan at 0% (a) and 25% (b) of the Period for Ribbed Channel Cooled Vane Design.

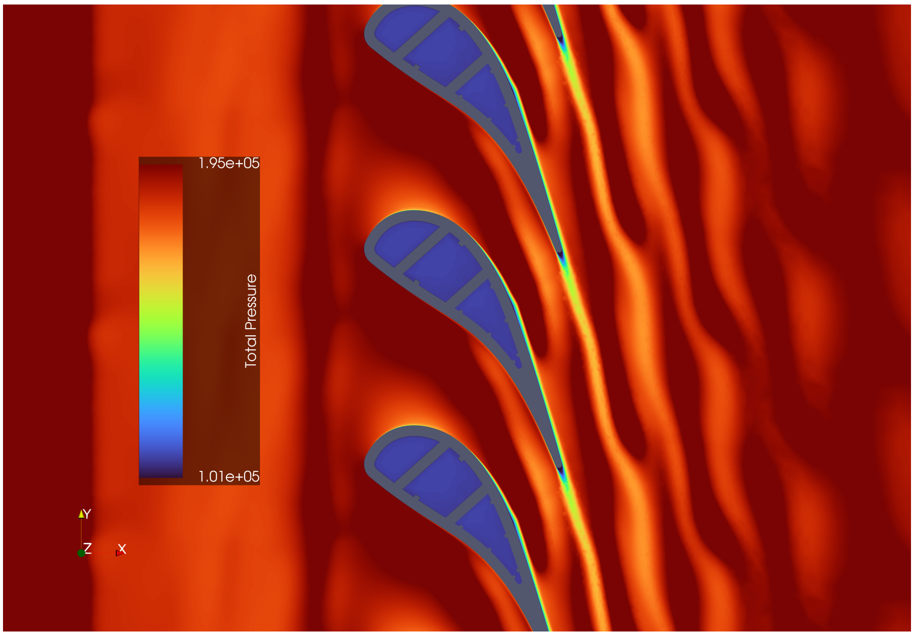

(a)

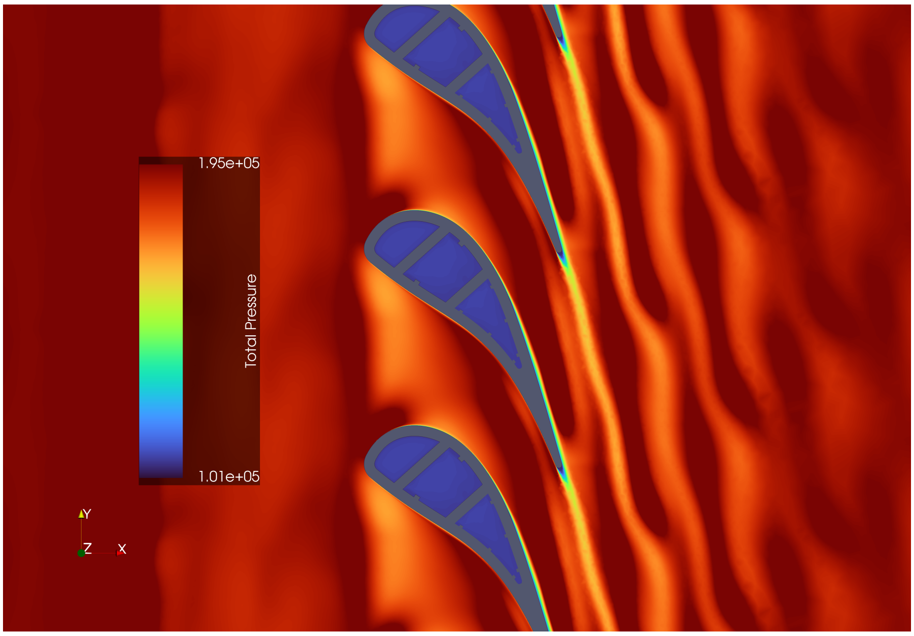

(b)

Figure 5.63: Main Flow Total Pressure Contour at Midspan at 50% (a) and 75% (b) of the Period for Ribbed Channel Cooled Vane Design.

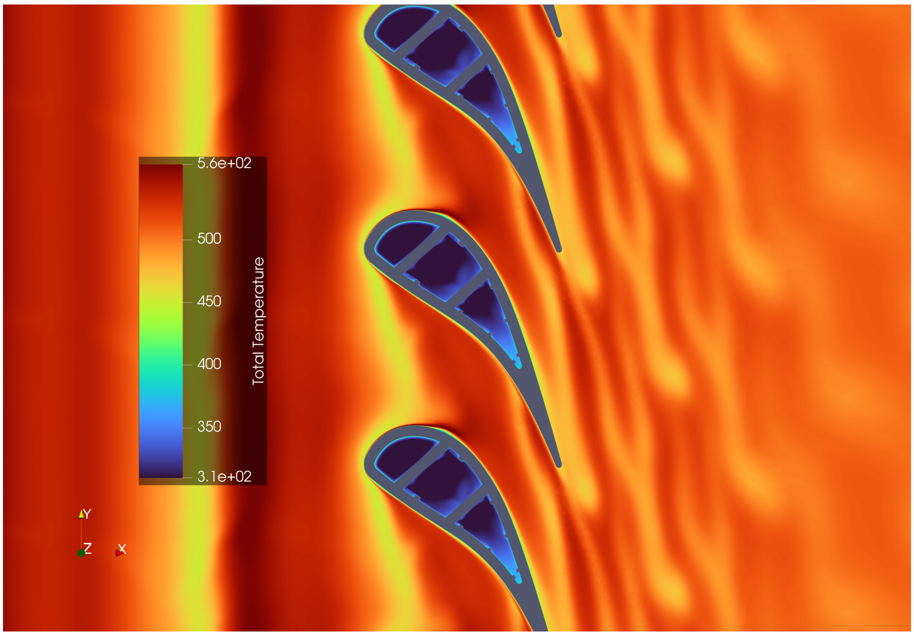

(a)

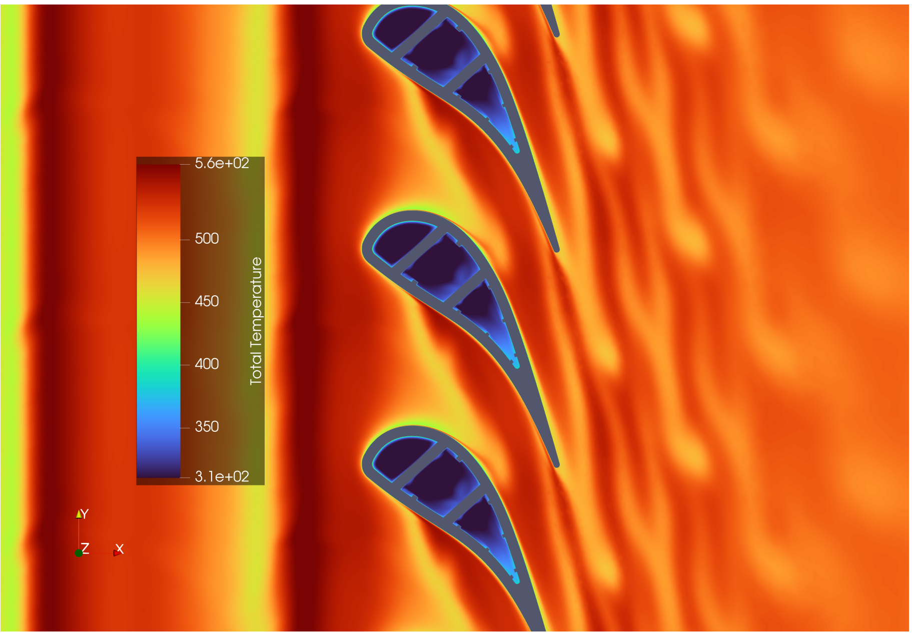

(b)

Figure 5.64: Main Flow Total Temperature Contour at Midspan at 0% (a) and 25% (b) of the Period for Ribbed Channel Cooled Vane Design.

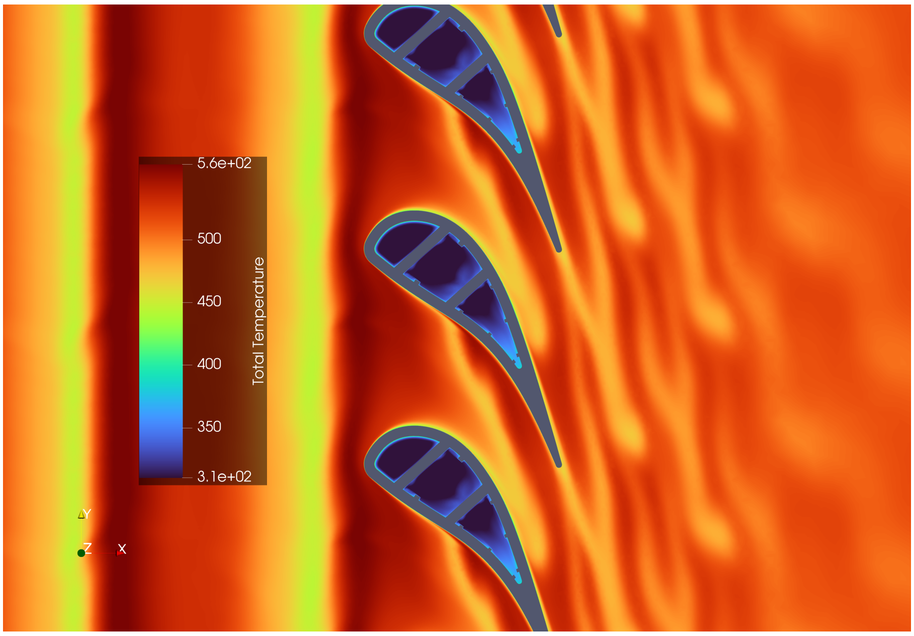

(a)

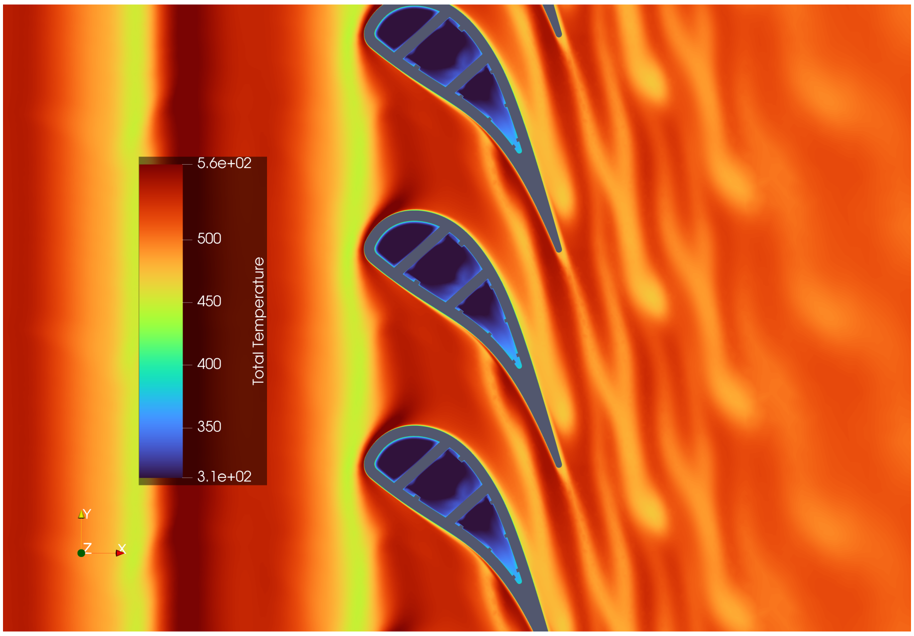

(b)

Figure 5.65: Main Flow Total Temperature Contour at Midspan at 50% (a) and 75% (b) of the Period for Ribbed Channel Cooled Vane Design.

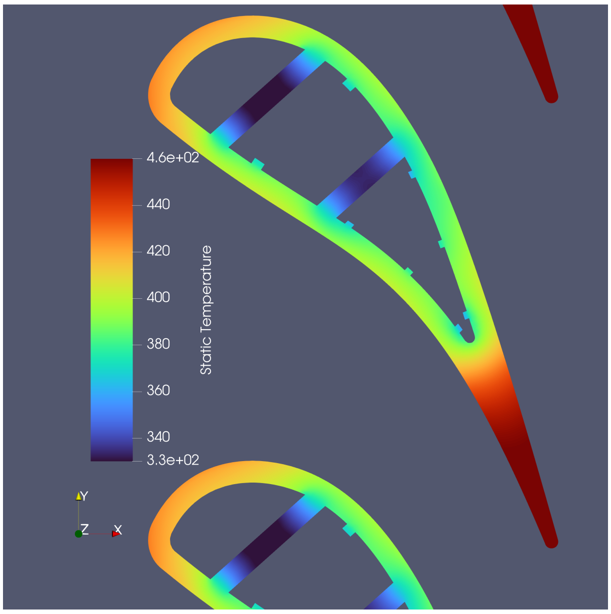

(a)

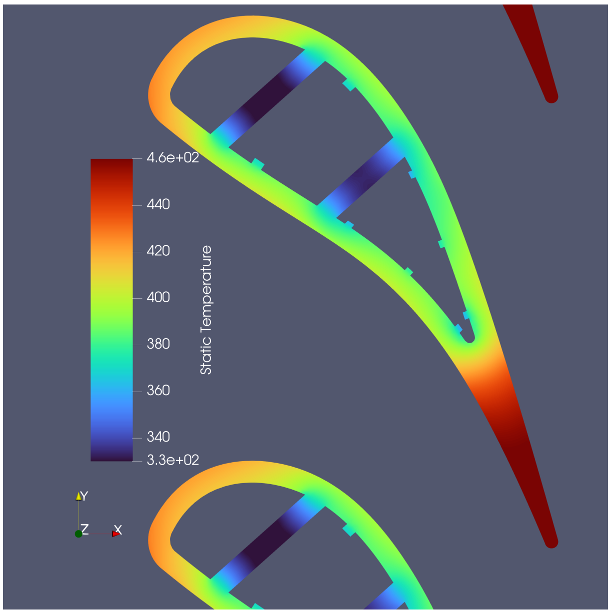

(b)

Figure 5.66: Solid Vane Static Temperature Contour at Midspan Section at 0% (a) and 25% (b) of the Period for Ribbed Channel Cooled Vane Design.

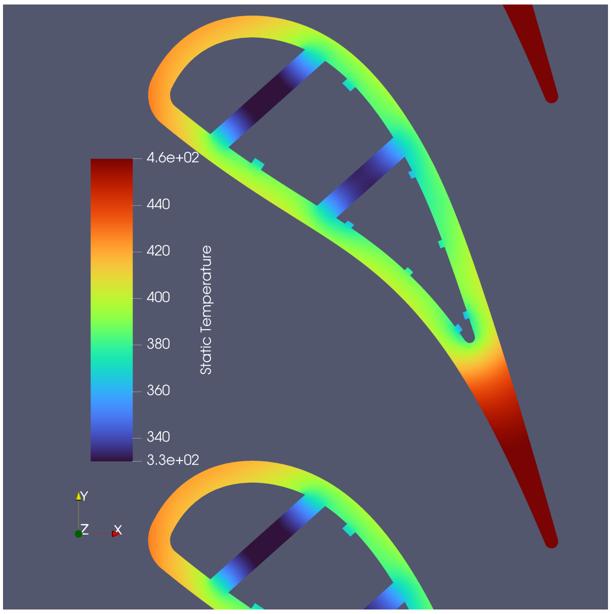

(a)

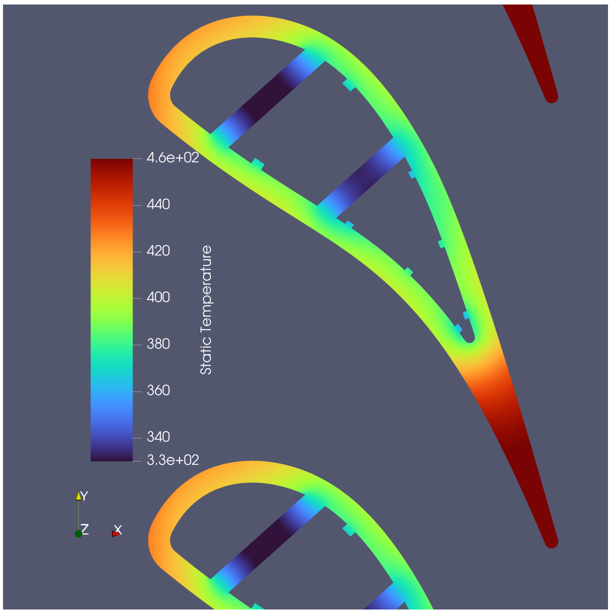

(b)

Figure 5.67: Solid Vane Static Temperature Contour at Midspan Section at 50% (a) and 75% (b) of the Period for Ribbed Channel Cooled Vane Design.

Table 29 reports the point-wise values of the monitored quantities at the four time steps where the cycle is evaluated. As in the previous case, a phase shift is present between the peak of the imposed conditions and the peak of the conditions recorded in the stator-rotor coupling section. The volume-averaged temperature of the solid vane undergoes no variation whatsoever, but is lower by $\Delta T_{vol} = 26\ K$ compared to the smooth channel cooled case. The use of ribs is therefore advisable even in the presence of oscillating conditions that cause shock waves. Tables 30 and 31 report the variables referring to the cooling channels where the ribs were applied, namely the second and third. The averages evaluated on the outlet surface and the volume of the cooling fluid in the two channels remain constant over time, indicating no correlation between the oscillating conditions imposed externally and the flow inside the channel. The pressure drop is lower by 0.1% for the second and lower by 0.15% for the third cooling channel, compared to the steady-state case.

	0% of the Cycle	**25% of the Cycle**	**50% of the Cycle**	**75% of the Cycle**
Average S-R Section Total Pressure [Pa]	189095	181885	175691	185372
Average S-R Section Static Temperature [K]	434.741	444.962	445.554	434.624
Average S-R Section Mach Number [-]	0.918	0.889	0.868	0.918
Average Static Wall Vane Pressure [Pa]	129552	127938	131439	131007
Average Static Wall Vane Temperature [K]	419.734	419.847	419.982	419.802
Volume Averaged Static Vane Temperature [K]	394.744	394.743	394.743	394.743

Table 29: Monitored Main flow and Vane Variables at Different Time Steps for Ribbed Channel Cooled Vane.

	0% of the Cycle	**25% of the Cycle**	**50% of the Cycle**	**75% of the Cycle**
Mass Averaged Outlet Static Temperature [K]	313.567	313.611	313.593	313.576
Volume Averaged Static Temperature [K]	311.820	311.818	311.818	311.819
Mass Averaged Outlet Velocity Magnitude [m/s]	33.094	33.095	33.093	33.093
Volume Averaged Velocity Magnitude [m/s]	30.124	30.122	30.123	30.124
Mass Averaged Outlet Total Pressure [Pa]	107085	107085	107085	107085
Total Pressure Drop [%]	-0.453%	-0.453%	-0.453%	-0.453%

Table 30: Second Cooling Channels Variables at Different Time Steps for Ribbed Channel Cooled Vane.

	0% of the Cycle	**25% of the Cycle**	**50% of the Cycle**	**75% of the Cycle**
Mass Averaged Outlet Static Temperature [K]	325.319	325.341	325.334	325.327
Volume Averaged Static Temperature [K]	323.630	323.627	323.627	323.629
Mass Averaged Outlet Velocity Magnitude [m/s]	30.238	30.242	30.242	30.241
Volume Averaged Velocity Magnitude [m/s]	23.899	23.900	23.899	23.899
Mass Averaged Outlet Total Pressure [Pa]	106974	106974	106974	106974
Total Pressure Drop [%]	-0.557%	-0.557%	-0.557%	-0.557%

Table 31: Third Cooling Channels Variables at Different Time Steps for Ribbed Channel Cooled Vane.

Figures 5.68 and 5.69 show the static pressure and temperature distributions on the external vane wall at the midspan section. The second figure shows the differential map of the vane's wall static temperature at the midspan section. As in the smooth channel cooled case, the static temperature is minimal in the area where the cooling channels are present and increases toward the trailing edge. The temperature oscillation is ten times higher than in the non-cooled vane case. Figures 5.70 and 5.71 show the static pressure and temperature distributions calculated on the walls of the two cooling channels of interest. Data from the unsteady simulations are compared with the steady-state results. From the first figure, an almost perfect similarity between the steady and unsteady static pressure distributions is noted. The static temperature, however, presents a decrease in the unsteady simulation compared to the steady-state case, indicating a lower average solid temperature and, thus, a purely convective heat transfer method between the solid and the surrounding fluid.

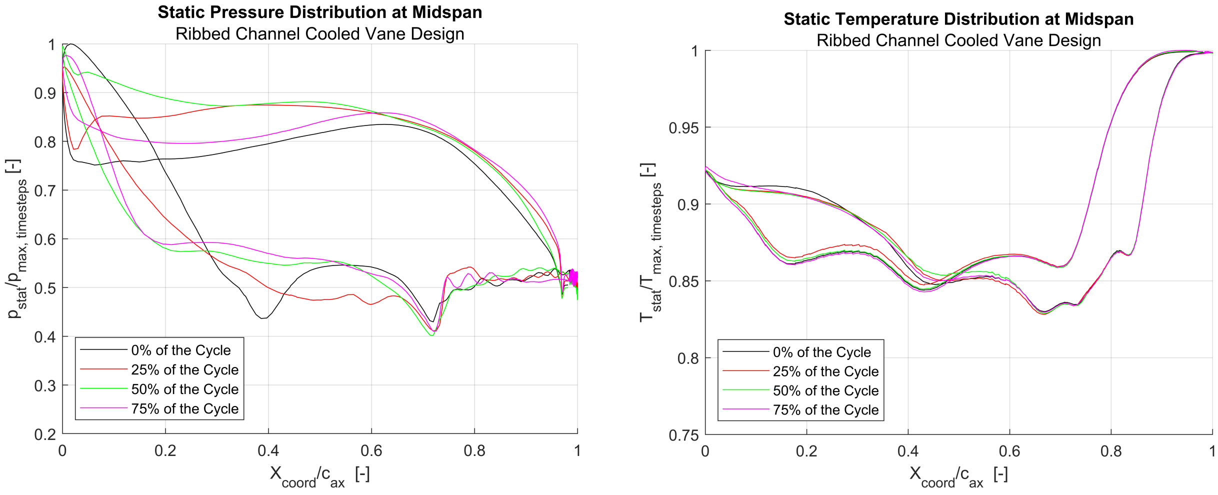

(a) (b)

Figure 5.68: Pressure (a) and Temperature (b) Distribution at Midspan Section of the Vane Surface for the Ribbed Channel Cooled Vane at Different Time Steps.

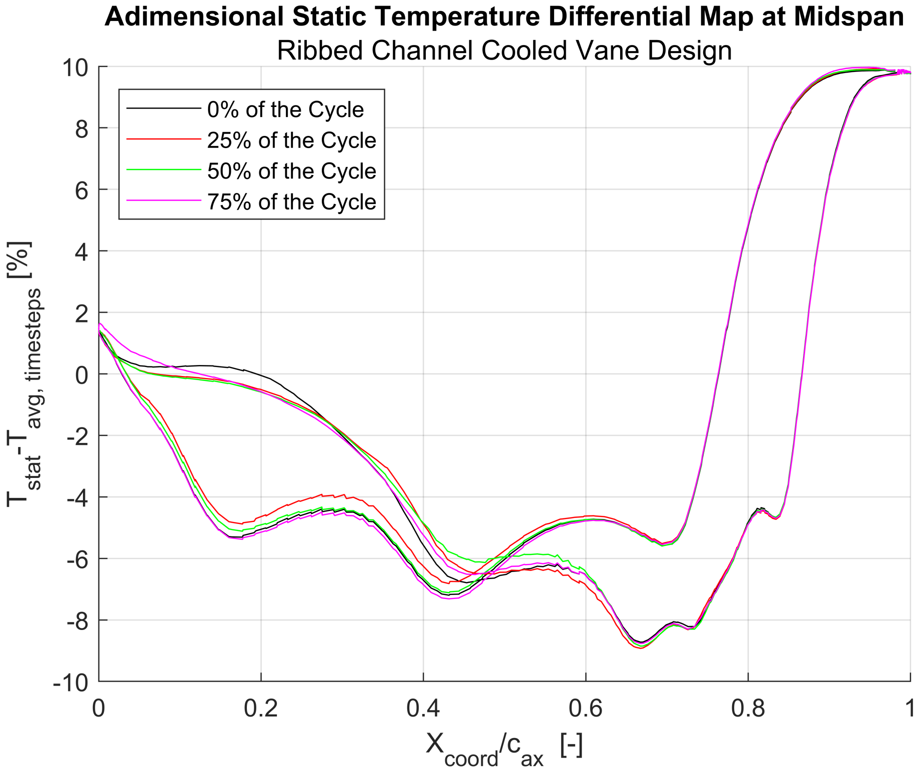

Figure 5.69: Differential Map of the Percentage Wall Temperature Variations on the Vane Surface at Midspan Section for Ribbed Channel Cooled Vane Design.

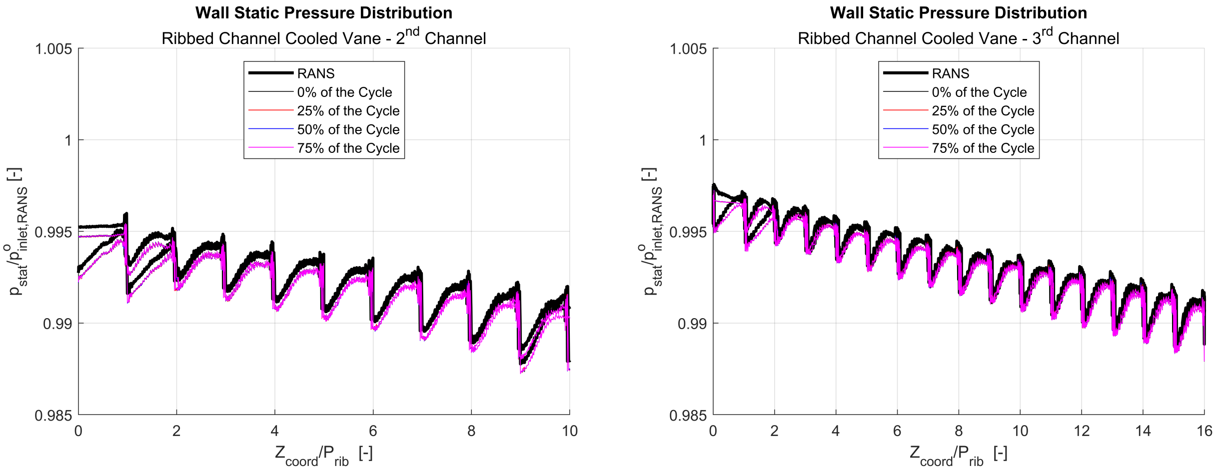

(a) (b)

Figure 5.70: Wall Static Pressure Distribution in Second (a) and Third (b) for the Ribbed Channel Cooled Vane at Different Time Steps.

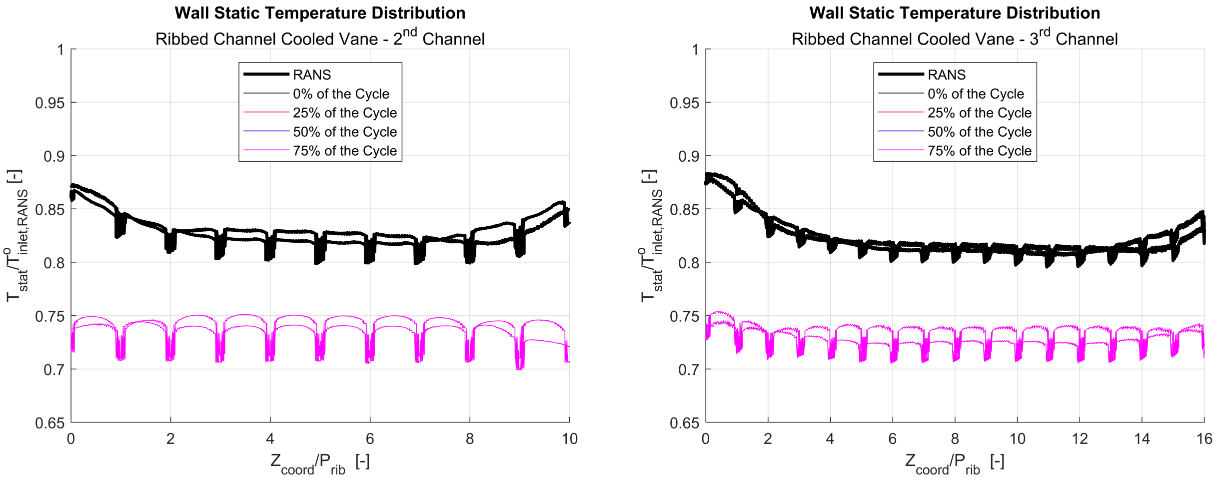

(a) (b)

Figure 5.71: Wall Static Temperature Distribution in Second (a) and Third (b) for the Ribbed Channel Cooled Vane at Different Time Steps.

6 Conclusions

The results obtained from the present thesis can be summarized in three key points: the influence of a transition model on the specific case under examination, how the vane manages to attenuate the oscillating inlet conditions, and the influence of these conditions on the flow inside the cooling channels.

The transition model, whose comparative study with Menter's fully-turbulent model was performed on the sample of steady-state simulations, leads to a substantial modification of the flow field inside the cooling channels. The hypothesis of an entirely turbulent flow, suggested by the use of the $k-\omega\ SST$ model, is in fact poorly suited for the study of flows in smooth channels which, on the contrary, exhibit a transition point upstream of which the flow is laminar. This variation in the flow field induces a poorer thermal mixing and, consequently, a reduced wall heat transfer, leading to an overestimation of the cooling efficiency of the channels themselves. This overestimation, caused by the poorer diffusive heat transfer occurring at the wall, is not in line with a conservative design philosophy that leads us to operate in the worst-case scenario. For these reasons, the turbulence model alone is not suitable for studying this internal heat transfer, but it is well-suited for calculating the heat transfer occurring on the external wall of the airfoil.

Of paramount importance in the study of the stator vane downstream of the combustor is the influence it has on the flow entering the subsequent rotor. This effect is even more significant when dealing with the coupling study with a rotating detonating combustor (RDC), which induces high temperature and pressure fluctuations. These quantities, in fact, were analyzed using the Fourier transform, which yielded encouraging results. The total temperature and pressure signals, in fact, traverse the airfoil, losing energy: there is an average loss of $\Delta PSD_{T^o} = 200$ on the total temperature signal alone. This energy loss is visible in the maps showing the oscillations of the variables of interest as the resolved time steps vary: they exhibit an oscillation within a smaller range of values. The influence of the airfoil on the fluid is also indicated by the effects that traverse the stator-rotor interface in an integer number of periods starting from the inlet of the computational domain, which points to the relationship existing between the frequency of the inlet boundary conditions and the characteristic frequency of the fluid domain. The specific frequency of the domain, in fact is $f_{avg,dom} = \frac{|v_{avg,dom}|}{l_c} = 6\ kHz$, slightly higher than the inlet boundary conditions frequancy of $f_{inlet} = 5\ kHz$.

Finally, the periodic inlet conditions induce a decrease in the temperature within the solid volume of the airfoil. By comparing the results, it is demonstrated that, with the same setup, the introduction of the aforementioned oscillating boundary conditions leads the solid to a lower temperature compared to the case analyzed with steady-state conditions. The latter, derived as the arithmetic mean of the oscillating conditions, in fact, represent a study scenario that overestimates the temperature of the solid under examination. This result is confirmed by the averages taken on the internal surfaces of the cooling channels: compared to the case where the RANS model was implemented, the unsteady results drop to a lower value throughout the channel, with a difference of $\Delta T_{wall,cool} = 0.1\%$ in the ribbed cooling channels design.

Bibliography

[1] V. N. Afanasyev, Ya P. Chudnovsky, A. I. Leontiev, and P. S. Roganov. Turbulent flow friction and heat transfer characteristics for spherical cavities on a flat plate. *Experimental Thermal and Fluid Science*, 7(1):1–8, 1993.

[2] M. Al-Qahtani, Y. J. Jang, H. C. Chen, and J. C. Han. Flow and heat transfer in rotating two-pass rectangular channels (ar=2) by reynolds stress turbulence model. *International Journal of Heat and Mass Transfer*, 45:1823–1838, 2002.

[3] Arunkumar G. L., P. Balachandra Shetty, Madhusudhan Acharya, Srikanth H. V., Chethan S., and Praveena B. A. Conjugate heat transfer analysis of stationary rib turbulated system in nozzle guide vane. In *AIP Conference Proceedings*, volume 2659, page 040009. AIP Publishing, 2022.

[4] J C Bailey and R S Bunker. Gt-2002-30 of dense and sparse extent. In *ASME Turbo Expo*, pages 1–10, 2002.

[5] Martin Bruschewski, Carolin Wüstenhagen, Clemens Domnick, Robert Krewinkel, Chao-Cheng Shiau, Sven Grundmann, and Je-Chin Han. Assessment of the Flow Field and Heat Transfer in a Vane Cooling System Using Magnetic Resonance Velocimetry, Thermochromic Liquid Crystals, and Computational Fluid Dynamics. *Journal of Turbomachinery*, 145(3), oct 20 2022.

[6] S W Chang, T Liou, and T Lee. Gt2012-6 array at high rotation numbers. In *ASME Turbo Expo*, pages 1–10, 2012.

[7] M. K. Chyu and V. Natarajan. Heat transfer on the base surface of three-dimensional protruding elements. *International Journal of Heat and Mass Transfer*, 39(14):2925–2935, 1996.

[8] M. K. Chyu, C. H. Yen, and S. Siw. Comparison of heat transfer from staggered pin fin arrays with circular, cubic and diamond shaped elements. In *Volume 4: Turbo Expo 2007, Parts A and B*, pages 991–999, 2007.

[9] Jason E. Dees, David G. Bogard, Gustavo A. Ledezma, Gregory M. Laskowski, and Anil K. Tolpadi. Experimental Measurements and Computational Predictions for an Internally Cooled Simulated Turbine Vane With 90 Degree Rib Turbulators. In *Volume 4: Heat Transfer, Parts A and B*, pages 447–456. ASMEDC, oct 10 2010.

[10] W Döring. Über den detonationsvorgang in gasen. *Annalen der Physik*, 435(6-7):421–436, 1943.

[11] Bruno Facchini, Andrea Magi, and Alberto Scotti Del Greco. Conjugate Heat Transfer Simulation of a Radially Cooled Gas Turbine Vane. In *Volume 3: Turbo Expo 2004*, pages 951–961. ASMEDC, jan 1 2004.

[12] Mostafa Fathi and Amir Nejat. Conjugate heat transfer investigation of impingement cooling for ribbed internal passage of a turbine vane. *International Journal of Thermal Sciences*, 178:107589, 8 2022.

[13] Kurt R Glaesemann and Laurence E Fried. Improved woodkirkwood detonation chemical kinetics. In *Theoretical Chemistry Accounts*, volume 120, pages 37–43. Springer, 2007.

[14] Je-Chin Han and Hamn-Ching Chen. Turbine blade internal cooling passages with rib turbulators. *Journal of Propulsion and Power*, 22(2):226–248, 2006.

[15] K. Hu, Y. Ju, Y. Feng, and C. Zhang. A dimension reduction-based multidisciplinary design optimization method for high pressure turbine blades. *J. Eng. Gas Turbines Power*, 144(9):091011, 2022.

[16] L. Hylton, M. Mihelc, E. Turner, D. Nealy, and R. York. Analytical and experimental evaluation of the heat transfer distribution over the surfaces of turbine vanes. *NASA Sti/Recon Technical Report N*, 1983.

[17] N. Kaewchoothong and C. Nuntadusit. Flow and heat transfer behaviors in a two-pass rotating channel with rib turbulators using computational fluid dynamics. *Heat Transfer Engineering*, 44(2):175–195, 2022.

[18] Mohamad Sadeq Karimi, Mehrdad Raisee, Saeed Salehi, Patrick Hendrick, and Ahmad Nourbakhsh. Robust optimization of the nasa c3x gas turbine vane under uncertain operational conditions. *International Journal of Heat and Mass Transfer*, 164:120537, 2021.

[19] A. Kumar and M. Pathak. Convective heat transfer enhancement in a turbine blade channel with dimple, rib and hybrid rib-dimple structures. *J Therm Anal Calorim*, 2024.

[20] Eungsuk Lee, Lesley M Wright, and Je-chin Han. Gt2003-38900. In *ASME Turbo Expo*, pages 1–10, 2017.

[21] L. Lei, Z. Yifeng, S. Bengt, Q. Dandan, W. Songtao, and Z. Xinghong. Computational investigation of curvature effects on jet impingement heat transfer at internally cooled turbine vane leading edge regions. *Heat Transfer Research*, 2020.

[22] Phil Ligrani. Heat transfer augmentation technologies for internal cooling of turbine components of gas turbine engines. *International Journal of Rotating Machinery*, 2013, 2013.

[23] Jiang Luo and Eli H. Razinsky. Conjugate Heat Transfer Analysis of a Cooled Turbine Vane Using the V2F Turbulence Model. *Journal of Turbomachinery*, 129(4):773–781, jul 24 2006.

[24] Peter W. Mcfadden and Tony R. Brown. Evaluation of internal heat-transfer coefficients for impingement-cooled turbine airfoils. *Journal of Aircraft*, 6(3):203–208, 1969.

[25] D. E. Metzger and R. S. Bunker. Local heat transfer in internally cooled turbine airfoil leading. *Journal of Turbomachinery*, 112(July 1990):459–466, 1990.

[26] Soma Nakagami, Ken Matsuoka, Jiro Kasahara, M Arai, T Fujimoto, and K Ohtsuka. Experimental visualization of the structure of rotating detonation waves in a disk-shaped combustor. *Journal of Propulsion and Power*, 36(4):707–717, 2020.

[27] S. Norheim and S. Amzin. Numerical investigation of a radially cooled turbine guide vane using air and steam as a cooling medium. *Computation*, 9(6):63, 2021.

[28] Jason K. Ostanek. Improving pin-fin heat transfer predictions using artificial neural

networks. *Journal of Turbomachinery*, 136(5):051010, 2013.

[29] J. S. Park, Je-chin Han, Y. Huang, and S. Ou. Heat transfer performance comparisons of five different rectangular channels with parallel angled ribs. *International Journal of Heat and Mass Transfer*, 35(11):2891–2903, 1992.

[30] D. E. Paxson. A preliminary assessment of the performance of a rotating detonation engine. *Journal of Propulsion and Power*, 30(4):1018–1025, 2014.

[31] Bharath Viswanath Ravi, Prashant Singh, and Srinath V. Ekkad. Numerical investigation of turbulent flow and heat transfer in two-pass ribbed channels. *International Journal of Thermal Sciences*, 112:31–43, 2017.

[32] Douglas Schwer and Kailas Kailasanath. Feedback into mixture plenums in rotating detonation engines. *50th AIAA Aerospace Sciences Meeting including the New Horizons Forum and Aerospace Exposition*, pages AIAA–2012–0545, 2012.

[33] M. A. R. Sharif and K. K. Mothe. Evaluation of turbulence models in the prediction of heat transfer due to slot jet impingement on plane and concave surfaces. *Numerical Heat Transfer, Part B: Fundamentals*, 55(4):273–294, 2009.

[34] V. P. Singh, Dharamveer Singh, and A. Yadav. Analytical Investigation of Ribbed Channels for Gas Turbine. 2022.

[35] Peter A Strakey, Clinton R Bedick, and Donald H Ferguson. Computational fluid dynamics combustion modeling for rotating detonation engines. *SAE International Journal of Aerospace*, 13(2):319–328, 2020.

[36] B. Sundén and M. Faghri. Heat Transfer in Gas Turbines. 2001.

[37] K Takeishi, Y Oda, Y Miyake, and Y Motoda. Experimental and numerical study on the convective heat. In *ASME Turbo Expo*, pages 1–12, 2012.

[38] Gregory Uhl, Holger Wulz, Christopher Heuser, and Michael Oschwald. Numerical analysis of an ejector under pulsating inflow characteristic of rdc exhaust conditions. *Aerospace*, 10(10):843, 2023.

[39] J von Neumann. Theory of detonation waves. In A H Taub, editor, *John von Neumann: Collected Works, 19031957*, volume 6, pages 203–218. Pergamon Press, 1963.

[40] P. Wolaski. Propulsive performance of a continuously rotating detonation engine. *Journal of Propulsion and Power*, 27(1):155–164, 2011.

[41] William D. York and James H. Leylek. Three-Dimensional Conjugate Heat Transfer Simulation of an Internally-Cooled Gas Turbine Vane. In *Volume 5: Turbo Expo 2003, Parts A and B*, pages 351–360. ASMEDC, jan 1 2003.

[42] Amin Yousefi, Amir Nejat, and Mohammad H. Sabour. Ribbed channel heat transfer enhancement of an internally cooled turbine vane using cooling conjugate heat transfer simulation. *Thermal Science and Engineering Progress*, 19:100641, 10 2020.

[43] Y. B. Zel'dovich. On the theory of the propagation of detonation in gaseous systems. *Zhurnal Éksperimentalno i Teoretichesko Fiziki*, 10:542–568, 1940.